1-1-2019

Protection of High-Voltage Transformer Bushings and Other Brittle Structures Against Impact

Christine Nichole Henderson
University of Denver

Recommended Citation

Henderson, Christine Nichole, "Protection of High-Voltage Transformer Bushings and Other Brittle Structures Against Impact" (2019). *Electronic Theses and Dissertations*. 1661.
https://digitalcommons.du.edu/etd/1661

PROTECTION OF HIGH-VOLTAGE TRANSFORMER BUSHINGS AND OTHER BRITTLE STRUCTURES AGAINST IMPACT

A Dissertation

Presented to

the Faculty of the Daniel Felix Ritchie School of Engineering and Computer Science

University of Denver

In Partial Fulfillment

of the Requirements for the Degree

Doctor of Philosophy

---

by

Christine Henderson

November 2019

Advisor: Dr. Maciej Kumosa

Author: Christine Henderson
Title: PROTECTION OF HIGH-VOLTAGE TRANSFORMER BUSHINGS AND OTHER BRITTLE STRUCTURE AGAINST IMPACT
Advisor: Dr. Maciej Kumosa
Degree Date: November 2019

ABSTRACT

This dissertation contributes unique approaches to improve the fundamental understanding of the impact behavior of porcelain high-voltage (HV) transformer bushings under high-velocity impact, with a focus on their protection with feasible methods which could be quickly applied in service to prevent vandalism and other undesirable impact situations. The bushings are brittle and pressurized; prone to explosive damage when hit by a high-velocity projectile. Damaged bushings can destroy transformers and entire substations in complex fashions. This can put the power grid at risk for cascading failures and electrical blackouts, affecting consumers. Therefore, suggesting practical approaches which could be used to protect the bushings against impact is of paramount importance.

Testing of impact protection concepts on a full-scale bushing without exploratory study is expensive. Therefore, this research focused heavily on the development of new laboratory based experimental and numerical approaches for pressurized borosilicate glass cylinders and flat plates using both ballistic and low-velocity impact techniques, to best represent a bushing under high-velocity impact. The laboratory-based testing approaches were further verified by full-scale impact tests with a .308 caliber Winchester rifle cartridge. It was discovered from the laboratory and full-scale tests that an unprotected bushing would display an explosive symmetrical distribution of fragments, potentially destroying transformers, other neighboring equipment, and personnel. It was also demonstrated for the first time that a protective elastomeric coating can be used on the surface of a bushing to absorb an explosive blast from a combined effect of high-velocity impact and internal pressure. Nature was used as a guide to select an appropriate polymer coating for blast mitigation. It turned out that small amounts of Line-X XS-100 applied on the surface of the cylinders, plates, and bushings dramatically changed their failure modes from brittle to ductile. Most importantly, Line-X XS-100 successfully confined fragments on pressurized borosilicate cylinders and full-scale transformer bushings.

This research successfully used an extensive combination of engineering and scientific approaches to recommend a solution to a potentially serious engineering problem created by an explosion of an unprotected bushing in the middle of a HV substation.

ACKNOWLEDGEMENTS

I am immensely grateful for the opportunity to perform a unique and inspiring work. In this process many people have contributed guidance and support. My deepest acknowledgment is to my advisor, Dr. Maciej Kumosa for his continued support, expert guidance, and encouragement throughout this long but fruitful journey.

I want to give a special thank-you to my boss at Reclamation, Dr. William Kepler, for giving me the freedom to pursue this dream while working full time. He repeatedly told me that he hired me because I was smart, driven to succeed, and great! I am immensely thankful for his encouragement and patience.

I would like to thank my “partner in crime,” Stephen DeFrance. Without him ballistic testing would not have been possible. I especially enjoyed hearing his work stories about life in the field.

I would like to thank Dr. Paul Predecki, for all his valuable insight and continual help in each of my publication efforts. He is a wealth of knowledge and I was grateful to gleam from his experience.

I would like to thank all my lab colleagues for their valuable guidance and insight, especially Dr. Euripides Solis-Ramos, Dr. Eva Hakansson and Dr. Bill Dube. I will cherish the friendships we developed.

I would like to thank Dr. Gregory Odegard, Dr. Iwona Jasiuk, and Roman Koltuniuk for their collaborative work and for lending me their expertise and time.

Lastly, I want to give thanks to a special someone in my life that has been with me from the very beginning, helped to open doors making this all possible, and provided me with the means to achieve my heart’s desire for this PhD.

TABLE OF CONTENTS

Chapter 1 Introduction 1
  1.1 Introduction 1
  1.2 Research objectives 3
  1.3 Outline of dissertation 3
  1.4 Research sponsors 5
  1.5 Publications related to this PhD 5

Chapter 2 Power grid and bushing background 8
  2.1 The power grid 8
  2.2 Power transformers and key components 10
  2.3 Key vulnerabilities in component selection 13
  2.4 Transformer bushing design 15
    2.4.1 Bushing types 15
    2.4.2 Bushing profile 17

Chapter 3 Investigation of Bushing Models under Air Gun impact 20
  3.1 Materials and methods 23
    3.1.1 Air gun testing on pressurized borosilicate glass cylinders 23
      3.1.1.1 Test set-up 23
      3.1.1.2 Velocity profiles 29
      3.1.1.3 Fragment size 30
      3.1.1.4 Fragment dynamics 31
    3.1.2 Air gun testing of neighbor effect 32
  3.2 Results and discussion 34
    3.2.1 Preliminary visual observations 34
    3.2.2 Pressure effect on velocity profiles 36
    3.2.3 Pressure effect on fragment size 43
    3.2.4 Fragment dynamics 48
      3.2.4.1 Fragment velocities and ejection times 48
      3.2.4.2 Estimation of impact range of airborne fragments 52
    3.2.5 Cascading damage effect in borosilicate glass bushing models 60
  3.3 Summary 65

Chapter 4 Nature’s version of impact protection through abalone Nacre 67
  4.1 Abalone nacre “brick and mortar” tile structure 68
  4.2 Abalone nacre protein layer 71
  4.3 Abalone biomimetics 75
  4.4 Experimental materials and methods 78
    4.4.1 Abalone characterization 78
    4.4.2 Abalone hydration 81
    4.4.3 Brick and mortar structure 83
    4.4.4 Abalone composites 86
  4.5 Experimental results and discussion 88
    4.5.1 Abalone characterization 88

4.5.2 Abalone hydration ... 91
4.5.3 Brick and mortar structure ... 96
4.5.4 Abalone composites ... 100
4.6 Summary ... 102

Chapter 5 Correlative drop weight and ballistic testing of an elastomeric coating ... 105
5.1 Materials ... 107
5.2 Testing set-up and methods ... 107
5.2.1 Air gun ballistic testing ... 107
5.2.2 Non-instrumented drop weight testing for linear extrapolations ... 109
5.2.3 Ballistic testing at higher impact energies ... 110
5.3 Results and discussion ... 111
5.3.1 Coating effectiveness for air gun impacted cylinders ... 111
5.3.2 Mass loss examination of non-instrumented drop weight testing of borosilicate glass plates ... 114
5.3.3 Refinement of fragment confinement predictions using higher caliber impact energies. ... 118
5.4 Summary ... 121

Chapter 6 Instrumented drop weight testing of cOated borosilicate glass plates ... 123
6.1 Materials ... 124
6.2 Testing set-up and method ... 124
6.2.1 Visual examination of instrumented drop weight samples ... 124
6.2.2 Instrumented drop weight testing using an accelerometer ... 124
6.2.2.1 Accelerometer data filtering ... 126
6.2.2.2 Numerical integration ... 128
6.2.2.3 Collected impact data ... 129
6.3 Results and discussion ... 131
6.3.1 Visual results of sample failure behavior ... 131
6.3.1.1 Impact damage to glass samples on their bottom side ... 131
6.3.1.2 Impact damage to coated sides of samples ... 133
6.3.2 Analysis of accelerometer responses as a function of coating thickness ... 135
6.3.2.1 Time history plots for unfractured samples ... 135
6.3.2.2 Impact energy effect on tested samples ... 139
6.3.3 Critical impact parameters at failure ... 145
6.4 Summary ... 151

Chapter 7 Finite element modeling of instrumented drop weight testing of coated borosilicate glass plates ... 153
7.1 Processing ... 154
7.1.1 TrueGrid ... 154
7.1.2 LS-DYNA ... 158
7.1.3 Finite element formulation ... 159
7.1.4 Explicit method ... 160
7.2 Model generation ... 161

7.2.1 Drop weight, indenter pin and cylindrical die 163
7.2.2 Glass plate.. 165
7.2.3 Polymer coating layer 166
7.3 Checks and issues 167
7.3.1 Convergence study check 167
7.3.2 Hourglass control check.. 168
7.3.3 Issues... 169
7.4 Experimental testing for polymer properties 170
7.5 FEM model results and discussion 172
7.5.1 Numerical method... 172
7.5.2 Time history plots 172
7.5.3 Maximum contact force and impulse comparisons 176
7.6 Summary..181

Chapter 8 full-scale Testing of transformer bushings..................................... 183
8.1 Materials and methods 183
8.2 Results and discussion 188
8.2.1 Impact characteristics of uncoated bushings.................................. 188
8.2.2 Impact characteristics of coated bushings...................................... 193
8.2.3 Comparison of coating efficiency from full-scale testing with previous estimates in Chapter 5. 196
8.2.3.1 Linear extrapolation estimates for full-scale bushings 197
8.2.3.2 Power fit estimates for full-scale bushings 199
8.2.3.3 Actual results for full-scale testing in comparison to previous estimates 199
8.3 Summary..200

Chapter 9 Summary discussion and concluding remarks 202
9.1 Unprotected bushing models...203
9.2 Natural solutions for impact protection 206
9.3 Elastomeric coating protection at low- and high-velocity impact 207
9.4 Coating effectiveness in low-velocity impact..................................210
9.5 Full-scale testing 213
9.6 Final observations and recommendations.......................................214
9.7 Future testing recommendations...216

References 217

Appendix A Acronyms 227
Appendix B Ballistics terminology.. 232
Appendix C Amino acids. Reproduced from ref. (60)....................................... 243
Appendix D “Brick and mortar” drop weight data 245
Appendix E Non-instrumented drop weight data 250
Appendix F Instrumented drop weight data.. 252
Appendix G Finite element model impact parameter data 253

LIST OF FIGURES

Figure 1-1: Middle age plate armor. Reproduced from ref. (5). 2

Figure 2 1: U.S. power grid as of 2013. Reproduced from ref. (1)....................................9
Figure 2 2: Components of a transformer. Reproduced from ref. (11). 11
Figure 2 3: Schematic of a transformer core & windings. Reproduced from ref. (13)......11
Figure 2 4: Damaged bushings. Reproduced from ref. (18). 14
Figure 2 5: OIP bushing schematic. Reproduced from ref. (22). 16
Figure 2 6: Standard elements of a bushing. Reproduced from ref. (17)..........................18
Figure 2 7: Capacitance grading vs. without grading of a bushing. Reproduced from ref. (23). 19

Figure 3 1: High-velocity impact damage to transformer bushings. 21
Figure 3 2: Schematic of ballistic testing layout with camera 1 located in the Z-direction and camera 2 located in the Y-direction. 24
Figure 3 3: Pressure containment box prior to assembly. 26
Figure 3 4: Top view of full set-up. 26
Figure 3 5: Side view of full set-up. 27
Figure 3 6: Testing set-up (a) safety containment and (b) air gun with reservoir tank......28
Figure 3 7: Method for surface area measurements of spray painted large curved fragments..31
Figure 3 8: Top view of air gun ballistic test cylinder arrangement. 33
Figure 3 9: Impact sequences for the 0 kPa and 690 kPa pressure tests. 35
Figure 3 10: Velocity profiles of the fragments at a) 0, (b) 69, (c) 207, (d) 345, (e) 448, (f) 517 and (g) 690 kPa. Zero degrees is where the pellet exited the cylinder. Results for one experimental shot at each pressure are shown. 40
Figure 3 11: Profile velocity at tested pressures. 41
Figure 3 12: Polar plot of deviations occurring in symmetry of radial velocity during tested cylinder pressures a) in full-scale and b) zoomed in to show small deviations in the radial velocity. 42
Figure 3 13: Average deviations in symmetry determined for the blast profiles at tested pressures...43
Figure 3 14: Fragmentation for tests at (a) 0, (b) 270 and (c) 690 kPa. 44
Figure 3 15: Fragment size of collected spray painted fragments (a) 0, (b) 345 and (c) 690 kPa..45
Figure 3 16: Percent recovery of fragments vs. pressure. 46
Figure 3 17: Histogram of collected fragments for 0, 207, and 690 kPa. 47
Figure 3 18: Fragment size versus pressure (kPa). 48
Figure 3 19: Fragment velocities and masses for a) 0 kPa and b) 207 kPa. 49
Figure 3 20: Initial velocities versus ejection times for a) 0 kPa and b) 207 kPa.............51
Figure 3 21: Fragment force diagram for air resistance of a flying fragment after ejection from cylinder...53

Figure 3 22: Predicted velocities of ejected fragments with time for nine combinations of mass and initial velocity......55
Figure 3 23: Experimental and calculated fragment velocities for three selected categories; a and b) decreasing velocities, c and d) increasing velocities, and e and f) semi-stationary velocities with best fits for the experimental data. 58
Figure 3 24: Visual observation of failure sequence at (a) impact flash, (b) primary reaction at 600 µs, (c) secondary reaction at 11,200 µs, and (d) tertiary reaction at 32,300 µs......62
Figure 3 25: Probability of neighboring damage initiated by a single cylinder failure. 63
Figure 3 26: Probability of damage based on distance from center to center of cascading cylinder pairs......63

Figure 4 1: Abalone nacre macro-layer arrangement consisting of the hard outer prismatic calcite layer and soft inner nacreous layer. Reproduced from ref. (48)...........69
Figure 4 2: Depiction of abalone hexagonal tile arrangement a) schematic representation b) back scattered SEM image of hexagonal tiles on inner surface of shell. Reproduced from ref. (49). 70
Figure 4 3: Lustrin A protein sequence: a) amino acid sequences of interest split out by domains and b) Lustrin A schematic of domain morphology. Reproduced from ref. (55)......73
Figure 4 4: β-turn representation with the CO group of residue (i) hydrogen bonded to the NH group of residue (i+3). Reproduced from ref. (60). 75
Figure 4 5: PMMA composite, mimicking nacre tile locking, after assembly. Reproduced from ref. (50)......77
Figure 4 6: Loaner large red shell from Monterey Abalone Company......78
Figure 4 7: Photogrammetry dense point cloud model of large red shell with scale markers......79
Figure 4 8: Photogrammetry dense point cloud greyscale model of small green shell. 80
Figure 4 9: Density determination set-up, USBR Geotech lab......80
Figure 4 10: Abalone testing ballistic set-up. 82
Figure 4 11: Abalone shell target fixture......82
Figure 4 12: Tile layering scheme for drop weight testing. Repeat pattern......84
Figure 4 13: Drop weight testing set-up for the samples: 1) drop weight with accelerometer attached, 2) indenter pin, 3) protective material, 4) glass plate sample, and 5) cylindrical die. 85
Figure 4 14: Representative stacking arrangement of abalone shell fragments......86
Figure 4 15: Vacuum bagging of abalone composites......87
Figure 4 16: Oregon Ballistics test set-up for vacuum bagged abalone composite. Front view (left) and back view (right). 88
Figure 4 17: Scanning electron micrographs of abalone shell microstructure......89
Figure 4 18: Growth pattern of red and green abalone......90
Figure 4 19: Density of red and green abalone......91
Figure 4 20: Abalone multiaxial impact test for various stages of hydration......92
Figure 4 21: Kinetic energy dissipation of live, saturated and dried abalone shells..........93

Figure 4 22: Visual ballistic damage results of post-impacted live versus dried abalone nacre shell. 94
Figure 4 23: Pellet deformation responses: a) original undamaged (.22 caliber) 1.66 g pellet, b) live abalone impact and c) dried abalone impact....95
Figure 4 24: Normalized hole diameters after pellet penetration through live, saturated, and dried abalone shells. 95
Figure 4 25: Critical energies of glass tiles with different adhesives. 98
Figure 4 26: Critical energies of PVC tiles with different adhesives. 99
Figure 4 27: Ballistic limit kinetic energy results for abalone composites. 102

Figure 5 1: Set-up of coated cylinders. 109
Figure 5 2: Side rupture of 1.43 mm thick coated cylinder. 112
Figure 5 3: Measured mass loss at 95J for all coating thicknesses on glass cylinders. ...113
Figure 5 4: Mass loss as a function of coating thickness; (a) all data, (b) damaged samples. 116
Figure 5 5: Average and upper limit energies for the drop weight samples as a function of coating thickness. 118
Figure 5 6: Images of post impact response from the 9x19 mm IMI FMJ test demonstrating fragmentation containment for coated cylinders: (left) bullet exit (right) bullet entrance. 119
Figure 5 7: Measured mass loss for borosilicate cylinders at different bullet kinetic energies for 3.05 mm thick coating with a best fit power curve. 120

Figure 6 1: Accelerometer mounting details. 126
Figure 6 2: 10th order Butterworth 1800 Hz low pass filter bode magnitude plot 127
Figure 6 3: Smoothed vs. noisy raw acceleration data for 3.11 mm coated sample at 15.6 J of impact energy. 128
Figure 6 4: Numerical method comparison for a single accelerometer data set. 129
Figure 6 5: Coated sample failure modes: (a) radial cracking with significant spalling for 2.33 mm thick sample impacted at 19.9 J and (b) radial cracking with reduced spalling for 5.64 mm thick sample impacted at 23.4 J. 132
Figure 6 6: Number of cracks for all failed samples. 133
Figure 6 7: Optical images of typical damage to the coatings on the impacted side of the specimens with (a) 1.32 mm at 17.3J, (b) 2.33 mm at 18.6J, (c) 3.11 mm at 16.4 J and (d) 5.64 mm at 26 J of coating. 134
Figure 6 8: 3.11 mm thick coating sample: (a) Schematic of the coating cross section and impactor location with internal voids represented by dashed circles, (b) SEM image of non-impacted surface, (c) and (d) damage modes on the impact area, i.e. crushing, tearing and radial stretching marks. 135
Figure 6 9: Time history plot for uncoated sample at 0.19 J of impact energy. 137
Figure 6 10: Time history plots for 1.32 mm coating at 8.65 J of impact energy. 137
Figure 6 11: Time history plots for 5.68 mm coating at 8.65 J of impact energy. 138
Figure 6 12: Maximum contact force with respect to thickness and impact energy for all tested samples. 140

Figure 6 13: Maximum normalized displacement vs. impact energy for un-failed samples. 141
Figure 6 14: Impact duration and time to maximum contact force with respect to coating thickness....................142
Figure 6 15: Maximum energy transferred, and specific energy transferred with respect to coating thickness and impact energy for all tested samples. 144
Figure 6 16: Relationship between impulse and impact energy. 145
Figure 6 17: Critical parameters at failure with respect to coating thickness. 149

Figure 7 1: TrueGrid mesh generation steps: (a) initial block, (b) deletion of center and corner indices, (c) cylindrical surface definition and corner shifting, and (d) final meshed cylindrical die. 157
Figure 7 2: Final model mesh generation in TrueGrid. 158
Figure 7 3: LS-DYNA graphical representation of master and slave contact surface for the cylindrical die and glass plate. 162
Figure 7 4: Representation of a fully integrated 8-noded solid element. Reproduced from ref. (134). 163
Figure 7 5: Representative stress vs. strain curve for glass. Reproduced from ref. (140). 166
Figure 7 6: Mesh convergence test. 168
Figure 7 7: Hourglass energy check....................169
Figure 7 8: Elastomeric coating dogbone sample. 171
Figure 7 9: Stress vs. strain curve for elastomeric coating sample. 171
Figure 7 10: Time history plot for FEM simulation of uncoated sample at 0.23 J of impact energy....................175
Figure 7 11: Time history plot for FEM simulation of 1.33 mm coating at 8.6 J of impact energy....................175
Figure 7 12: Time history plot for FEM simulation of 5.64 mm coating at 8.6 J of impact energy....................176
Figure 7 13: Maximum force (a) uncoated samples and (b) coated samples....................177
Figure 7 14: Numerical and experimental normalized maximum displacements....................178
Figure 7 15: Numerical and experimental results for impact duration and time to maximum contact force....................179
Figure 7 16: Impulse (a) coated samples and (b) uncoated samples....................181

Figure 8 1: Two types of bushings used in this research. (a) bolt-mount and (b) rod-mount. 185
Figure 8 2: Pre-test condition of coated bushings (a) bolt-mount and (b) rod-mount. 186
Figure 8 3: Bushing mounting style for bolt-mount (left) and rod-mount (right). 187
Figure 8 4: High-speed images of the bolt-mounted uncoated bushing impact event. 188
Figure 8 5: High-speed images of the rod-mounted uncoated bushing impact event....................189
Figure 8 6: Fragmentation distribution for (a) bolt-mounted bushing and (b) rod-mounted bushing. 190
Figure 8 7: Fragment masses collected for the pressurized bushings. 191

Figure 8 8 Pictures of (a) top and (b) bottom intact portions from bolt-mounted bushing. 192
Figure 8 9: Mass vs. distance of fragments for (a) bolt-mounted bushing and (b) rod-mounted bushing. 193
Figure 8 10: High-speed imagery of bolt-mounted coated bushing response. 194
Figure 8 11: Damage of bolt-mounted and coated bushing (a) on outside petticoat and (b) inside the bushing. 195
Figure 8 12: High-speed imagery of rod-mounted and coated bushing responses. 195
Figure 8 13: Damage of rod-mounted and coated bushing (a) on outside of petticoat and (b) inside the bushing. 196

Figure 9 1: Summary diagram. 203
Figure 9 2: Schematic representation of coating effectiveness and usefulness. 213

Figure B 1: Common impact failure modes. Reproduced from ref. (151). 237
Figure B 2: Schematics of brittle ceramic impact modes of failure. Reproduced from refs (34, 35).. 240

LIST OF TABLES

Table 3-1: Best fit parameters for all fragments. 59

Table 4-1: Sample testing rubric. 84
Table 4-2: Weight fraction of shells for abalone composites. 101

Table 5-1: Cartridges and projectiles used in coated borosilicate cylinder testing......... 111
Table 5-2: Best fit parameters for the data in Figure 5-3. 113
Table 5-3: Best fit parameters for the data in Figure 5-4. 116
Table 5-4: Best fit parameters for the data in Figure 5-5. 118

Table 6-1: Average normalized maximum displacements... 141
Table 6-2: Critical impact parameter method for (a) impact energy (J), (b) maximum contact force (kN), and (c) impulse (Ns). 147
Table 6-3: Average critical impact parameters and coating effectiveness. 151

Table 7-1: Drop weight, indenter pin and cylindrical die model geometry. 164
Table 7-2: Drop weight, indenter pin and cylindrical die material properties. 164
Table 7-3: Glass plate material properties. 165
Table 7-4: Polymer coating material properties. 167

Table B-1: Velocity regime characterization. 234
Table B-2: Kinetic energy for NIJ classifications. 235
Table C-1: Amino acid acronyms and letters. 244

CHAPTER 1 INTRODUCTION

1.1 Introduction

Individuals with a basic knowledge of transmission operations and transformer components, can identify critical High-Voltage (HV) transformer locations and plan an attack on power grid facilities (1). It is fairly simple to obtain the necessary information from news events, publicly available documents, and the internet.

The 1990 Physical Vulnerability Office of Technology (OTA) report states “that the most common threat consists of ordinary vandals who shoot at transmission lines or transmission line bushings” (2). This also applies to individuals randomly targeting substation components. This type of threat would likely be identified as transmission line destruction, arson, and random shots at transformer bushings, holding tanks, radiators, and other components.

A 2010 North American Reliability Organization (NERC) report, “High Impact, Low frequency Event Risk to the North American Bulk Power System” states that most sophisticated attacks are a high-impact low-frequency risk (3). These risks are harder to mitigate against and are fortunately less common. This type of attack would be considered a highly coordinated, well-planned attack against multiple assets designed to inflict as much damage as possible (3). The high-impact low-frequency event experienced on April 16, 2013 is the reason for this research. The Metcalf California transmission substation in Silicon Valley was attacked by a highly sophisticated team of individuals. They destroyed 17 transformers, crippled the substation for a month and caused $15 million in damage (4). This attack generated congressional interest in the physical security of high-voltage transformers, which prompted additional grid security initiatives by utilities and government agencies (1). Although this paper does not include risk assessment research, it is still relevant to the reasoning behind this research.

When examining impact protection designs, creative solutions are necessary. Often armor systems must evolve with ever increasing threat types, especially as technology changes. As far back as the middle ages, armory designers struggled to develop protections capable of defending against ballistics. This same problem has not changed, but the type of weapons and strategies have. For example, Figure 1-1 shows an image of medieval plate armor, which was sophisticated for the era. It essentially made the wearer impact resistant to the impact threats, but advances in technology made the armor obsolete (5). Modern materials have been studied for impact resistant applications, such as: natural materials, composite systems, foams, coatings, multi component systems, fabrics, nanoparticles, and many other materials (6).

Figure 1-1: Middle age plate armor. Reproduced from ref. (5).

Standard methodologies for testing of materials is infrequently available due to the highly creative nature of change and ideas that can arise from impact design. The ideas presented in this research required unique approaches for assessing protection effectiveness. Novel methodologies for this research on transformer bushings and comparable brittle structures will be further discussed in the following chapters. A review of ballistics terminology is present in Appendix B.

1.2 Research objectives

The primary objective of this research was to recommend a viable impact protection for transformer bushings subjected to high-velocity impact. The secondary objectives were to:

1. Understand how bushings behave under impact by simulating the behavior of a bushing under laboratory conditions using simple geometries.
2. Use nature as a guide in developing a protection concept.
3. Develop experimental and numerical techniques that could be used to analyze and explore impact protection.
4. Make recommendations on how to use the techniques and methods used in this research to protect other brittle structures.

1.3 Outline of dissertation

This dissertation is organized into nine chapters. Chapter 1 introduces this research, objectives, sponsors, and provides a review of all related publication efforts.

Chapter 2 provides a review of the power grid and power transformers. Key vulnerabilities are identified, as applied to transformer bushing components. Transformer bushing design is discussed.

Chapter 3 focuses on the initial investigations of this research by using scaled transformer bushing models. Testing methods are introduced that provided insight into the fundamental understanding of pressurized cylinder explosion response, fragment dynamics, and cascading damage effects when more than one cylinder is in close proximity to another.

Chapter 4 discusses concepts of impact protection using nature as a guide. When trying to find ways to protect a brittle material the first place to look is how nature does it; one of its most impact resistant organisms is the abalone. The microstructure and protein layer are discussed towards their potential as impact protection concepts.

Chapter 5 discusses the use of an elastomeric coating called Line-X XS-100, as an impact protection option. Ballistic and low-velocity testing methods are introduced and analyzed to further examine the coating protection response of brittle materials, like pressurized cylinders and flat glass plates. This chapter presented the first ever predictions of coating thickness, fragmentation confinement and energy prior to failure that would be needed to protect the borosilicate cylinders at rifle impact energies.

Chapter 6 further delves into the elastomeric coating behavior during impact using a refined drop weight testing method utilizing instrumentation through an accelerometer. Chapter 7 describes using finite element modeling (FEM) to verify results from Chapter 6. An overview of FEM and the use of two software packages is discussed.

Model generation and analysis results are reviewed in comparison with experimental results.

Chapter 8 discusses full-scale testing of transformer bushings with and without the coating from Chapter 5 and Chapter 6. Linear and power fit predictions from Chapter 5 are compared to full-scale results. Chapter 9 summarizes the research and additional concluding remarks are provided.

1.4 Research sponsors

This research was funded by the NSF I/UCRC Center for Novel High Voltage/Temperature Materials and Structures under #IIP 1362135 and by the Bureau of Reclamation's Security, Safety and Law Enforcement (SSLE) office. The work was performed at the University of Denver and the Bureau of Reclamation over the period 2015-2019.

1.5 Publications related to this PhD

Published Journal Articles

1. **Henderson CN**, DeFrance CS, Predecki P, Kumosa M. *Damage prevention in transformer bushings subjected to high-velocity impact*. International Journal of Impact Engineering, 2019. 130: p. 1-10.
2. **Henderson CN**, DeFrance CS, Predecki P, McCloskey TV, Truitt E, Hoffman J, Kumosa M. *Ballistic Fragmentation Confinement of Coated Brittle Transformer Bushing Models*. International Journal of Impact Engineering, 2018. 122: p. 363-373.

3. Bakir M, **Henderson CN**, Meyer JL, Oh J, Miljkovic N, Kumosa M, Economy J, Jasiuk I. *Effects of environmental aging on physical properties of aromatic thermosetting copolyester matrix neat and nanocomposite foams*. Polymer Degradation and Stability, 2018. 147: p. 49-56.

Submitted Journal Articles

1. **Henderson CN**, Monteith J, Solis-Ramos E, Godard R, Predecki P, Kumosa M. *Impact Protection of Borosilicate Glass Plates with Elastomeric Coatings in Drop Tower Tests*. International Journal of Impact Engineering, Submitted June 2019.
2. **Henderson CN**, Bhumkar O, DeFrance CS, Kumosa M, Odegard G. *Fragmentation of Brittle Transformer Bushing Models Under High velocity Impact and Internal Pressure*. International Journal of Solids and Structures, Ready for submission.

Reports

1. **Henderson CN**. *Proposed research on composite materials and designs to protect transformer bushings from high velocity impact.* Department of the Interior. Bureau of Reclamation. 2015. Technical Memorandum No. MERL-2015-098.
2. Waters D, **Henderson CN**, Pang S, Raviprasad S, Abueidda D, Hakansson E, Hoffman J, Kumosa M, Ostoja-Starzewski M, Jasiuk I. *Physical damage to HV transmission infrastructure.* Annual Report. Presented to NSF I/UCRC Novel High Voltage/High Temperature Materials and Structures. May 2016.

3. **Henderson CN**, Kumosa M, DeFrance CS, Solis-Ramos E, Odegard G, Roehm P, Pang S. *Prevention of high velocity impact damage to substations.* Annual Report. Presented to NSF I/UCRC Novel High Voltage/High Temperature Materials and Structures. May 2017.
4. **Henderson CN**, DeFrance CS, Kumosa M. *Critical infrastructure review of transformer bushing protection.* Presented to Federal Bureau of Investigation. Stapleton, CO. August 2017.
5. **Henderson CN**, DeFrance CS, Solis-Ramos E, Odegard G, Kumosa M, Hoffman J, Predecki P. *Prevention of high velocity impact damage to substations.* Annual Report. Presented to NSF I/UCRC Novel High Voltage/High Temperature Materials and Structures. May 2018.
6. **Henderson CN**. *Transformer bushing protection.* Presented to Security, Safety, and Law Enforcement Office. Bureau of Reclamation. Denver, CO. March 2019.
7. **Henderson CN**, Kumosa M. *Protecting transformer bushings against high velocity impact.* Presented to Tri-State. Denver, CO. May 2019.

CHAPTER 2 POWER GRID AND BUSHING BACKGROUND

Power grids are made up of many components. This chapter focuses on a literature review with regards to the power grid, the selection of components, and transformer bushing components and design.

2.1 The power grid

The electrical transmission network includes large electric power transformers that distribute large volumes of electricity. Fewer than three percent of the transformers in substations are HV power transformers, but they carry 60-70 percent of the nation's electricity (7). HV transformers are listed as critical assets within the U.S. electrical transmission network by a 2014 congressional physical security report (1). NERC defines a critical asset as a

> *"facility, system, and equipment which, if destroyed, damaged, degraded, or otherwise rendered unavailable, would have a significant impact on the ability to serve large quantities of customers for an extended period of time, would have a detrimental impact on the reliability or operability of the electrical grid, or would cause significant risk to public health and safety (8)."*

The United States power grid is dependent on its many connections to deliver power. Some connections can be severed without significant impact to power delivery, while destroying others would lead to major disruptions. Figure 2-1 identifies the many substations and transmission lines in the power grid, as of 2013. The loss of certain key substations would leave a regional network crippled and highly susceptible to cascading failure (1). Facilities with system redundancy that carry less load may be considered less critical, because power can be diverted through other substation delivery paths. Some components can be replaced quickly, on-line backup equipment can be used, or other measures can be enacted to transfer power. Utilities typically develop contingency plans based on failure of equipment rather than damage to multiple pieces of critical equipment at any given location (9).

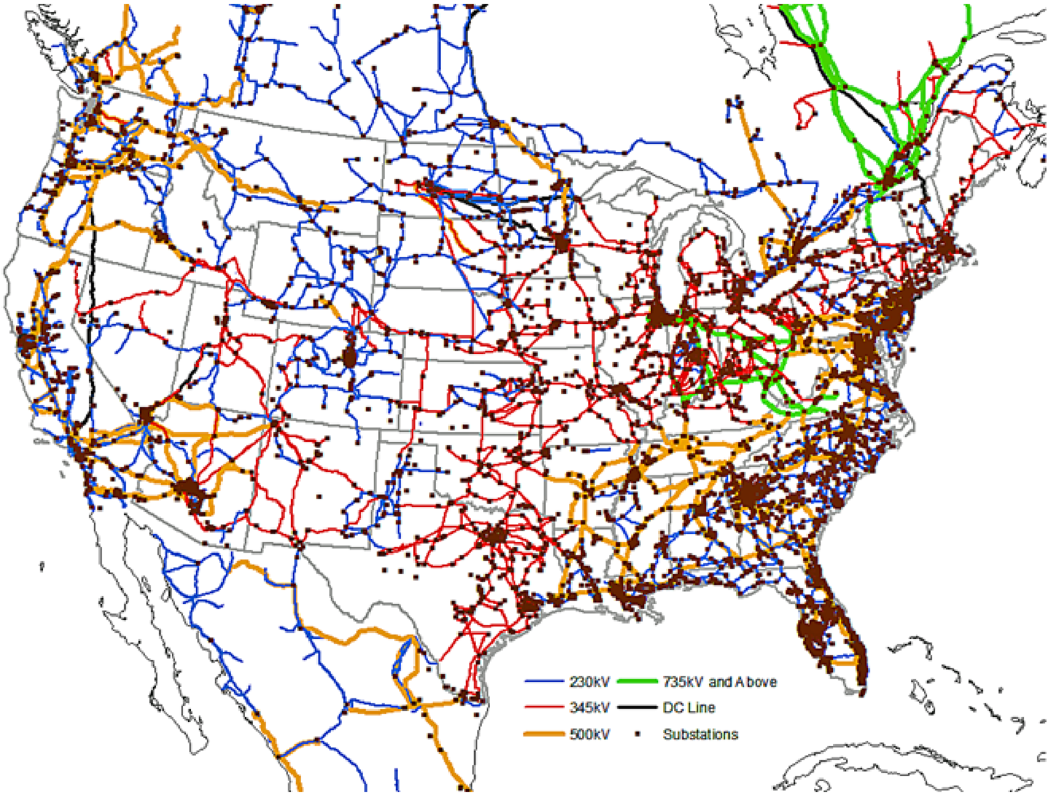

Figure 2-1: U.S. power grid as of 2013. Reproduced from ref. (1).

A substation serves the primary goal of increasing or decreasing voltage to meet the needs of the network. To do this, substations are equipped with transformers which perform the actual voltage level conversion. There can be one transformer or many, depending on the size of a substation. Along with transformers, a substation can contain switching, protection, and control equipment. These can include such things as: lightning rods, circuit breakers, capacitors, voltage regulators, and other electrical components necessary for the functioning of the substation (10). Many of these components may be present in a substation, but most of them, if damaged, would not cause costly disruptions to the power grid, and can be replaced quickly. Damaged transformers within substations are components that can cause significant damage to the network and are vital for functionality.

After discussing the importance of the power grid and the substation transformers that serve to distribute power, the following sections in this chapter will describe components of power transformers.

2.2 Power transformers and key components

Power transformers use electromagnetic induction to increase or decrease the output voltage levels (11). The transformer system consists of several key parts that allow it to transfer output voltages from high to low, or vice versa. Figure 2-2 shows the primary components of a transformer: core & windings, tank, bushings, oil conservator, and the radiator and fan. Since each of these components provides a specific function, damage to any of them will have a different impact on the transformer system.

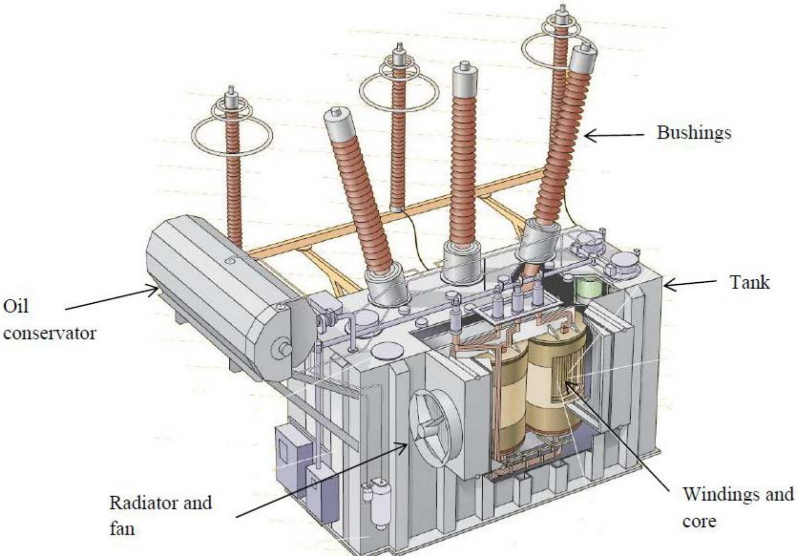

Figure 2-2: Components of a transformer. Reproduced from ref. (11).

The core and windings together make up the power source for the transformer system, based on the principles of magnetic induction. A changing magnetic field within a coil of wire induces a voltage across the coil (12). There can be many different shapes for cores, but a common shape is square with windings on opposite sides, as shown in Figure 2-3.

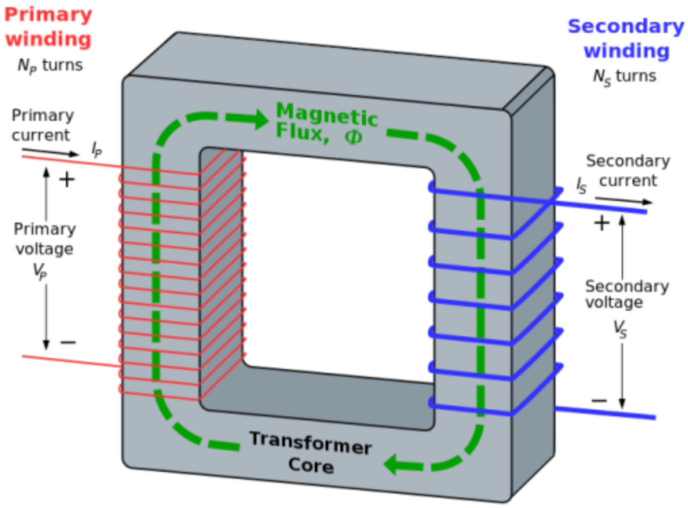

Figure 2-3: Schematic of a transformer core & windings. Reproduced from ref. (13).

The windings provide the increase or decrease in voltage function. Higher voltage corresponds with a larger number of windings. The voltage to number of turns in the winding ratio is mathematically defined by Equation (1). Ns,p is the number of turns, and Vs,p is the voltage in the secondary and primary windings (14).

$$\frac{N_p}{N_s} = \frac{V_p}{V_s} \tag{1}$$

The core and windings are contained in a holding tank, which protects the active parts of the power transformer. The tank is usually filled with oil for cooling and insulation (11). Tanks are constructed of steel and are designed to be strong with variable wall thicknesses according to operating pressures (15).

Bushings are used to safely transmit power into and out of a device via insulating material. Bushings are described as “rabbit ears” because they are the spiked protrusions seen coming from the tops or sides of transformer holding tanks and buildings. Bushings allow an electrical conductor, such as a transmission line, to pass safely through a grounded barrier. A bushing must be able to insulate conductors carrying HV through a grounded enclosure without causing an explosive event (16). The insulating material is selected and designed to withstand the electrical energy that is passing through the conductor along with any large electrical surge events that could occur. Many different styles and designs exist for bushings, depending on their application.

The oil conservator system is designed to maintain the insulating oil for the core and windings of the transformer. It helps to act as a coolant to dissipate heat generated by the transformer (12) and is a reservoir that allows for expansion of the oil during increases in operation (17).

The radiator & fan make up the cooling equipment necessary for keeping the transformer from overheating. Heat is transferred from the core and windings through the oil and then dissipated by the radiator fins to the surrounding air through convection (12).

2.3 Key vulnerabilities in component selection

Key vulnerabilities are selected in terms of primary and secondary failure. A primary failure is essentially a failure that does not allow time for intervention, is immediate, or is extremely expensive and damaging to the system if it occurs.

A secondary failure is one where enough lead time allows for detection and intervention, the component is not too expensive to replace, or the resulting damage does not result in costly damage or failure. Secondary failures can become primary failures in certain situations, which will be important in our case.

Damage to the core and windings would cause immediate failure to the transformer system. These are not the primary components for the focus in this research, even though they can be a primary target of attackers. Unless attackers are knowledgeable about the transformer, it would be difficult for them to locate the core which is protected by the exterior tank and insulating oil. Damage to the core would need to be accomplished indirectly through damage to the tank or directly through a precise hit with a projectile. If the tank is properly protected, then the core and windings will remain operational.

The tank is a holding container for the core & windings. It will be a primary failure if the projectile penetrates through to the core and windings. A more common scenario would create a secondary failure if the penetration of the tank results in draining of insulating oil. The draining oil may lead to arcing and delayed failure of the transformer (12), which allows time for detection.

Transformer bushings are open and exposed on top of the tank. They are visible from long distances and may be an easy target. Damage to the bushing component can produce disastrous primary failure of the transformer. In Figure 2-4, a bushing failure from lack of maintenance resulted in catastrophic damage to a neighboring bushing and sent shock waves through the transformer holding tank.

Figure 2-4: Damaged bushings. Reproduced from ref. (18).

Several possible consequences exist when a bushing is damaged, either intentionally or accidently. The bushing could crack and leak oil and/or lose its insulating material, resulting in eventual arcing and explosive destruction; a secondary failure event. The bushing can be destroyed, exposing open ends of the conductor, which can touch the metallic holding tank. A live conductor touching the holding tank can result in an explosion; a primary failure event. Transformer bushings were the focus of this research since a primary failure is likely, during a high-velocity impact.

2.4 Transformer bushing design

Transformer bushings are tailored specifically to meet the transformer's electrical needs. Requirements and limitations of bushings are specified in the Institute of Electrical and Electronics Engineers standards IEEE C57.19.00 and IEEE C57.19.01 (19). An evaluation of the different types of bushings along with the specifics of the bushing design profile has been performed in this section.

2.4.1 Bushing types

Transformer bushings can be classified into the following major types: solid ceramic, oil impregnated paper (OIP), resin impregnated paper (RIP), and silicone rubber insulator (SRI). Other types of bushing classifications exist but will not be discussed further in this chapter.

Solid ceramic bushings are the simplest design and consist of a central conductor surrounded by the ceramic insulator. These types of bushings were more common before power demands increased. Solid ceramic bushings had to become much larger in diameter to account for stronger electrical fields.

OIP bushings (sometimes called condenser bushings) are commonly used in power transformers today. These bushings utilize insulating paper impregnated with transformer oil. OIP bushings are nearly partial discharge free, have longer service lives, and lower production cost (20). Partial discharge (PD) is essentially the breakdown of the insulating material over time, which can spread out and form channels. PD causes further damage and allows the electricity within the conductor to spread into the insulating medium, instead of remaining in the conductor (21). The use of transformer oil has drawbacks, such as susceptibility to moisture ingress and leakage. OIP bushing are susceptible to an explosive failure mechanism (22). Figure 2-5 is a schematic of an OIP bushing, which shows the regions of oil insulation along with the area where the resin impregnated paper resides. An OIP bushing can be made of ceramic or composite materials.

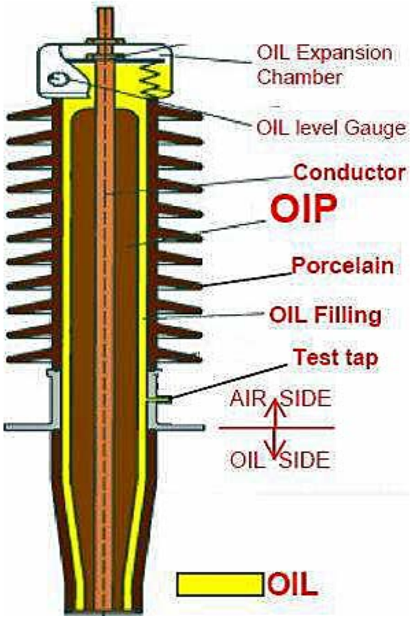

Figure 2-5: OIP bushing schematic. Reproduced from ref. (22).

RIP bushings combine a resin impregnated insulating paper and a small amount of mineral oil as an insulator (23). Despite the mineral oil, these bushings are still identified as oil-free and can be mounted at any angle. RIP bushings are more expensive than OIP bushings but require less maintenance costs. The use of RIP bushings for high-voltage applications is common and can be used in ceramic or composite form (24). The composite form of RIP bushings are gaining popularity and replacing ceramic OIP bushings (22).

SRI bushings are the modern day composite alternative to ceramic bushings. The insulator consists of a fiberglass tube with silicone rubber sheds. They offer advantages in shatter resistance with no collateral damage in an impact event. A projectile penetration through the SRI bushing core will probably cause electrical breakdown. The lack of insulating oil and ceramic exteriors means there is no risk of flammable explosions or shattering (22). SRIs cannot match some of the transformer voltage capabilities of OIP bushings and do not always offer a viable replacement. SRIs are an option in some applications but they will not be discussed further in this research.

2.4.2 Bushing profile

Protection materials and designs need to consider the external profile of a transformer bushing. The bushing profile design ensures that the electrical strength of the insulated material is capable of withstanding the energy passing through the conductor (24). Leakage paths develop within the insulation as the strength of the electrical field increases. The energy of the leakage path can overcome the dielectric strength of the insulation. It may puncture the insulation and allow the electrical energy to travel to the nearest ground, causing burning and arcing (24).

A standard bushing schematic, as shown in Figure 2-6, identifies the location of the shed profile typically found in transformer bushings. The sheds are present on the bushing outside of the transformer tank, and are the parts exposed to weather, insects, moisture, sunlight, and targets for shooters.

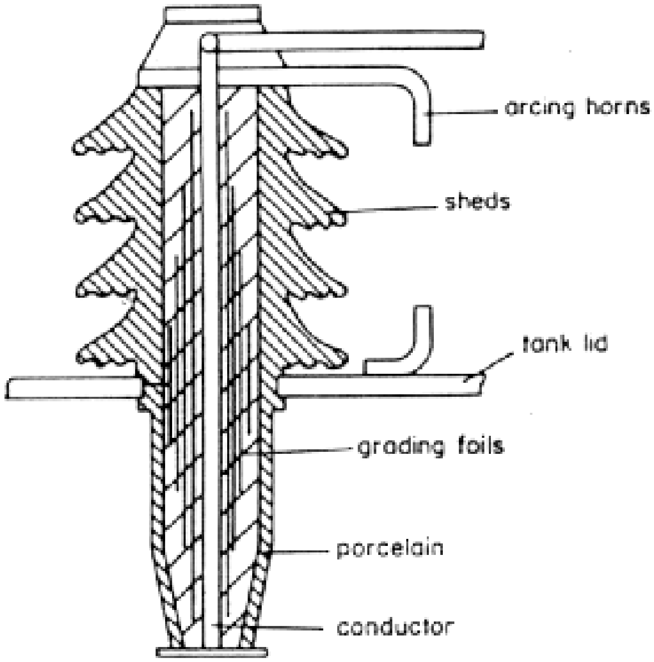

Figure 2-6: Standard elements of a bushing. Reproduced from ref. (17).

The sheds, shown in Figure 2-7 are used to increase the creepage distance and break up the flashover path (17). Creepage distance is considered the shortest path between two conductive parts measured along the surface of the bushing. The shed profile adds surface area to decrease the size of the bushing and creates a longer electric flow path. Without the shed profile, older bushings had to be very large to accommodate rising power demands (25).

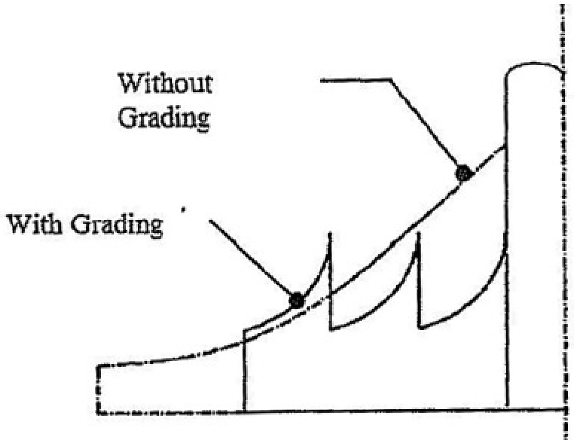

Figure 2-7: Capacitance grading vs. without grading of a bushing. Reproduced from ref. (23).

Designs in this research utilize and maintain the shed profile of the transformer bushings. If a protection design or material does not follow the shed profile, the leakage current follows the new creepage distance.

CHAPTER 3 INVESTIGATION OF BUSHING MODELS UNDER AIR GUN IMPACT

Transformer bushings behave like pressure vessels in service. Traditionally, metallic pressure vessels are designed with a leak-before-break (LBB) concept. LBB entails a slow dispersing of pressure without tearing the material apart. If a high-pressure metallic gas bottle bursts, without following LBB, the resulting explosion can destroy surrounding structures and cause severe injuries to personnel (26). This concept would also be the case for brittle structures such as bushings; the energy required to create an explosive reaction is much smaller than for metallic pressure vessels. Ceramic bushings present an intrinsically difficult problem: they are fragile and prone to extensive damage when impacted, differing from metallic pressure vessel behavior. When ceramic cracks propagate faster than leaks created by the initial opening from a projectile impact, a pressurized vessel will explode and generate fragments; whose sizes and velocities depend on the material type (27). The above LBB concept does not apply to brittle materials.

An explosive reaction of a ceramic transformer bushing can be described by four steps, demonstrated in Figure 3-1. The first step involves the initial impact. Step 2 consists of the development of fragments during the initial blast response. Step 3 involves the dynamic behavior of flying fragments. Step 4 is the “domino effect” on surrounding equipment and personnel. This last step, step 4, involves a reactionary component to the explosion, where neighboring bushings or equipment become part of the cascading reaction. The best protection strategy against high-velocity impact damage to a HV bushing would involve preventing damage initiation in the first step, which is often the hardest to implement. Since bushings are relatively inexpensive it may be a better option to design a protection measure for fragmentation confinement. This would prevent damage to neighboring personnel and equipment and would also allow time for the problem to be detected and the bushing replaced. This chapter will focus on understanding the behavior of brittle pressurized cylinders in steps 2 -4.

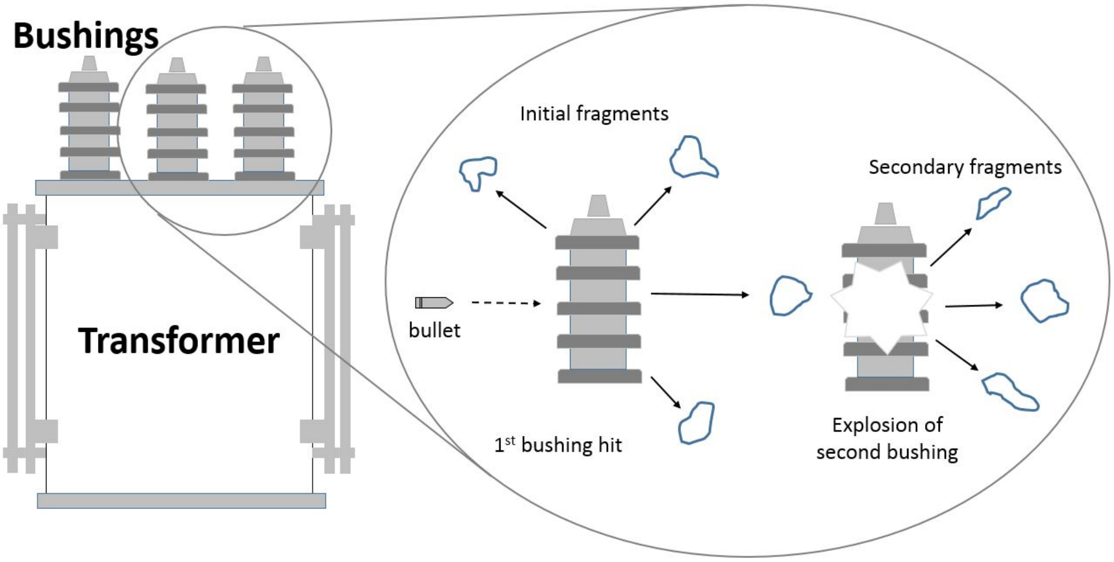

Figure 3-1: High-velocity impact damage to transformer bushings.

In this research, unique testing methods are suggested and applied to investigate high-velocity impact failures of small glass pressurized cylinders representing full-scale porcelain HV transformer bushings. Impact testing of full-scale transformer bushings is an expensive endeavor. Therefore, this research utilizes a simplified and less expensive scale model of the bushings subjected to an air gun with .22 lead pellets at an impact energy of about 95J. Groups of scale models were used together under pressure and high-velocity impact from an air gun to ascertain the likelihood of cascading damage, which represents a set of porcelain bushings on top of a transformer. The premise being that multiple bushings, in service, can experience cascading failure if just one bushing is impacted. In a real full-scale scenario, the bushings would be made of C-120 porcelain and the projectiles would be of a higher caliber than the lead pellets.

The most commonly used materials for HV bushings are porcelain, glass or glass fiber reinforced polymers (28). Borosilicate glass is less expensive and more widely available than C-120 porcelain, therefore it was chosen as the material model of choice for this research. The borosilicate glass tested in this study and C-120 porcelain have similar density, 2.4 g/cm^3 for porcelain and 2.23 g/cm^3 for glass , a stiffness of 67-150 GPa for porcelain and 67-80 GPa for glass, and a strength of about 130 MPa for porcelain and 280 MPa for glass (29, 30). Protecting borosilicate glass against high-velocity impact could be more difficult than for porcelain. Therefore, the impact predictions developed in this study by testing borosilicate glass cylinders could be a conservative estimate in impact behavior of bushings made from C-120 porcelain.

The experimental testing presented in this work was developed to identify the combined impact of the air gun and the internal pressure inside the cylinders and potentially HV porcelain bushings. The internal pressure affects the resulting blast profile, fragmentation velocities, directions and sizes along with the flight dynamics of individual fragments. Internal pressure also affects the likelihood of cascading failure when an exploding cylinder is in close proximity to neighboring cylinders.

3.1 Materials and methods

For the ballistic testing, Corning 7740 borosilicate cylindrical glass cylinders were fabricated by Allen Scientific Glass in Boulder, Colorado. The cylinders had a diameter of 50.8 mm (2”), a wall thickness of 6.35 mm (¼”), and a height of 304.8 mm (12”). The cylinders were designed with a closed rounded top and a ball flange base, as shown in the schematic of Figure 3-2 and in Figure 3-3c.

3.1.1 Air gun testing on pressurized borosilicate glass cylinders

3.1.1.1 Test set-up

The glass cylinders were designed to fit inside a flange mounted on top of a pressure containment box, shown in Figure 3-2 and Figure 3-3. The pressure box allowed a standard air compressor to be attached and the cylinder pressurized under controlled conditions. Figure 3-3 shows the pressure containment box assembly. Figure 3-4 and Figure 3-5, provides both the top and side views of the full assembly. Two high-speed cameras were used throughout the air gun experiment (Figure 3-2): Phantom 5 (camera 1) and a Phantom 7 (camera 2) manufactured by Vision Research Inc. The Phantom 5 operated at 3703 frames per second at a resolution of 512 x 512 and the Phantom 7 at 15037 frames per second at a resolution of 512 x 216. For velocity tracking PCC 2.7 software was used.

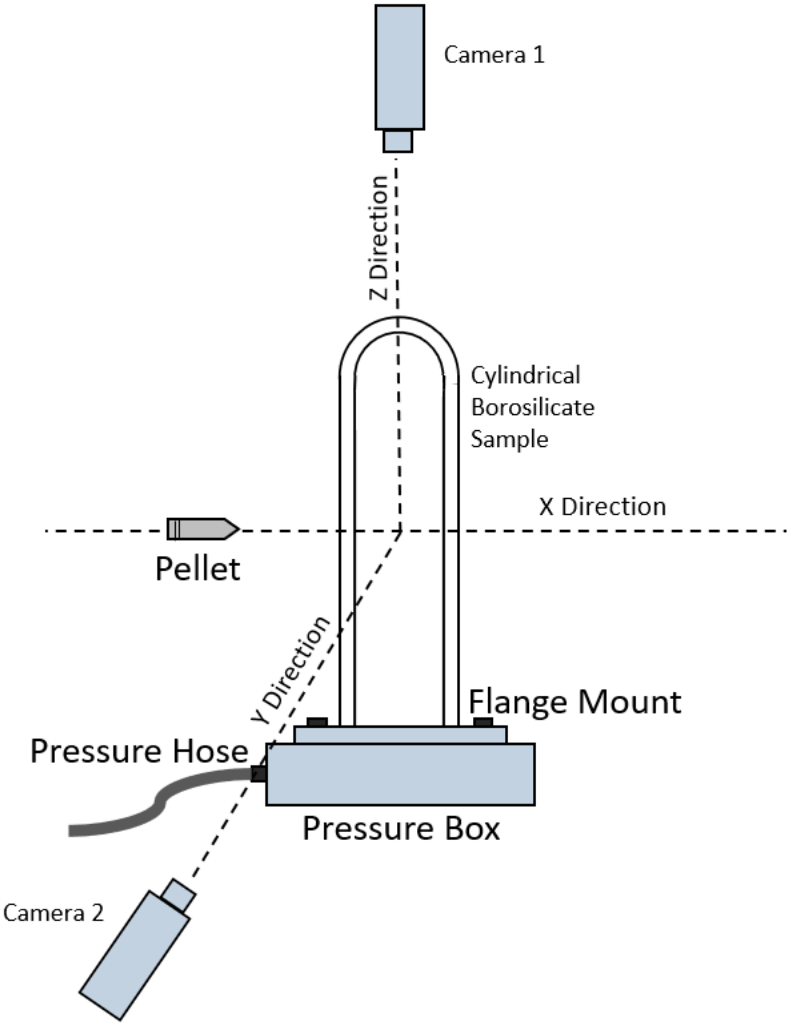

Figure 3-2: Schematic of ballistic testing layout with camera 1 located in the Z-direction and camera 2 located in the Y-direction.

a)

b)

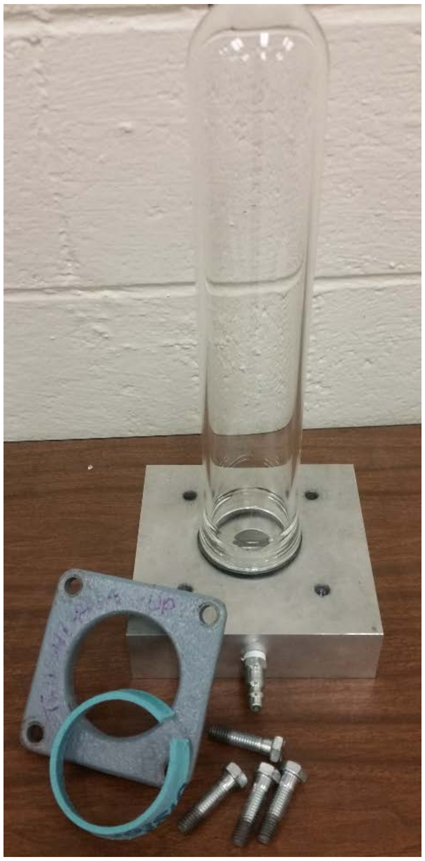

(c)

Figure 3-3: Pressure containment box prior to assembly.

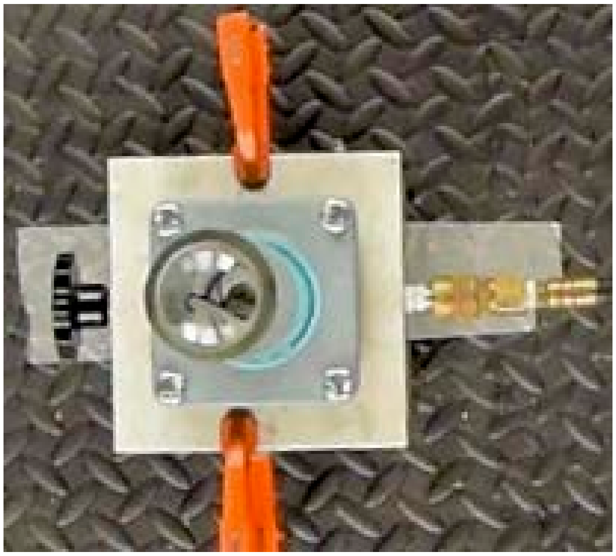

Figure 3-4: Top view of full set-up.

Figure 3-5: Side view of full set-up.

Figure 3-6a shows the complete ballistic testing set-up with the safety shielding, lighting, bullet catcher and cameras. An AirForce Condor^{TM} pre-charged pneumatic air gun with an onboard reservoir tank and a maximum recommended operating pressure of 20.7 MPa (3000 psi) of compressed air, was used to launch the projectiles (Figure 3-6b). The projectiles were H&N 5.6 mm (.22 caliber), 1.66 ± 0.02 g (25.62 grain) Rabbit Magnum II lead pellets. The muzzle velocity of each shot was recorded with a MagnetoSpeed Model V3 ballistic chronograph and was found to be 340 ± 1.84 m/s, giving an initial kinetic energy of the pellet at 95.3 ± 1.01 J.

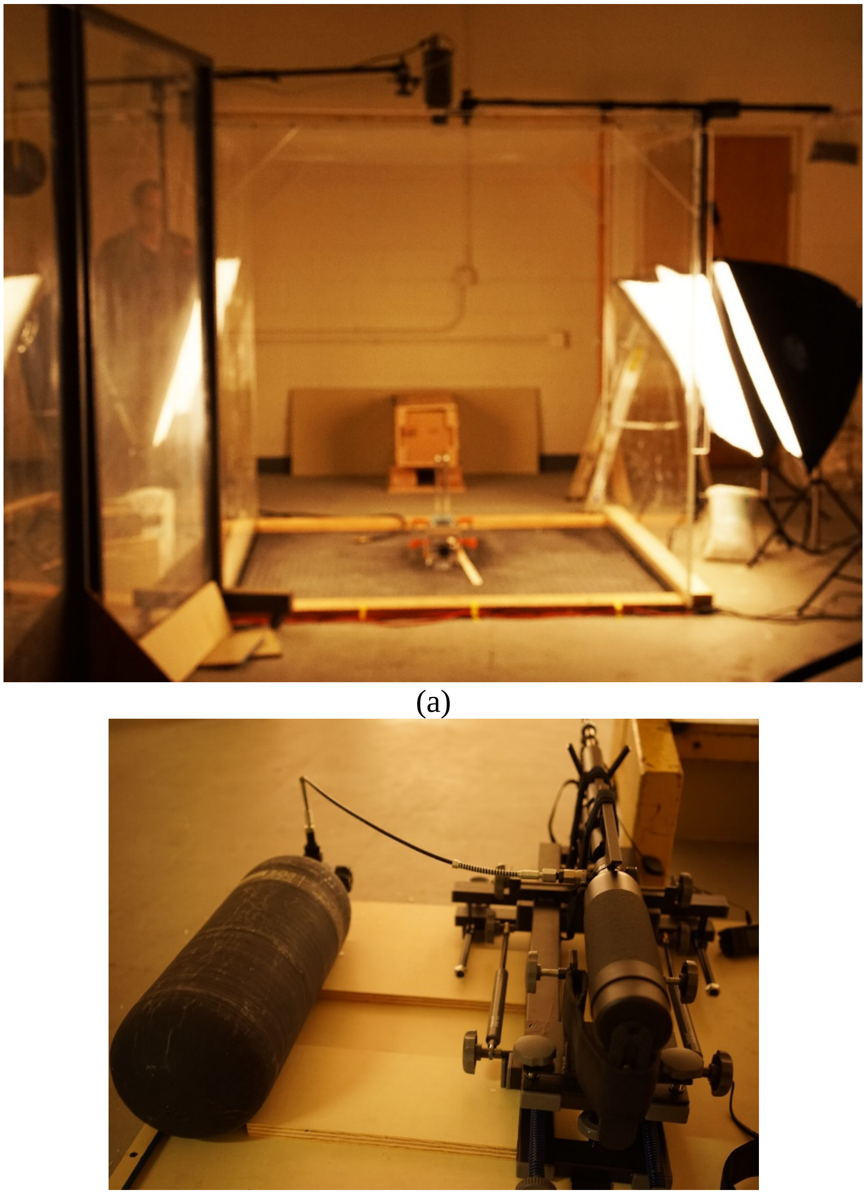

(a)

(b)

Figure 3-6: Testing set-up (a) safety containment and (b) air gun with reservoir tank.

The cylinders were tested at pressures of 0, 69, 207, 345, 448, 517, and 690 kPa (0, 10, 30, 50, 65, 75, and 100 psi). Two cylinders were tested at each pressure condition, except for one cylinder tested at 69, 517, and 690 kPa.

3.1.1.2 Velocity profiles

The overhead high-speed camera captured a radial profile of the resulting blast of the uncoated cylinders after impact. The images were analyzed to determine fragment profile velocities in relation to a 360-degree circle. Zero and 180-degrees were assigned as the locations of the pellet exit and entrance, respectively. Fragment velocities were plotted radially in the x-y plane. The radial distance from the centers of the graphs depicted the average magnitude of the tracked profile velocity in the x-y plane. The radial direction represented the position in degrees from the pellet exit point where the tracked fragment portions were located.

Profile velocities were obtained by tracking any portion of a fragment that could be measured, since most fragments were not fully resolvable. As many as 50 tracked fragment portions were followed for each test. Due to the set-up's measurement capabilities, the fragment velocity profiles were generated based on the x-y plane velocities seen in high-speed imagery, and not on the z-direction velocities. Based on limited visual observations, it was assumed that the x-y plane velocities are more significant than the z-direction velocities over the analyzed time interval of 0.2 seconds for the unpressurized cylinder and 0.1 seconds for the pressurized cylinder.

A profile velocity bar graph was generated for all pressures tested using an average of the top 10% of the measured profile velocities along with the maximum profile velocity for each test.

To examine symmetry of the blast profile, AutoCAD was used to trace out the fragment blast cloud in high-speed imagery and the cloud shape/profile was compared to a perfect circle. The blast profile examined the entire circular reference at 10-degree increments. Java was used to generate a symmetrical deviation plot comparing the blast profile to a perfect circle. A polar plot of this deviation was used to demonstrate areas where the blast had large deviations from symmetry. A bar graph was also generated based on the polar plot values.

3.1.1.3 Fragment size

All pre-tested cylinders and post-tested fragments were weighed to determine percent recovery. The percent recovery was computed by taking the original mass and subtracting it from the residual mass of the pieces collected. Mass histograms were generated for 0, 270, and 690 kPa tests. Pieces were not added to the data when they fell below a projected surface area size of roughly 0.3 cm^2 or a mass smaller than 0.17 g.

Recoverable pieces were spray painted and imaged using a 35 mm SONY mirrorless camera with a sensor size of 35.9 x 24 mm and a pixel size of 7260 x 4912. Images were outlined along the perimeter of each fragment in AutoCAD and their surface areas determined. A ruler was used in each image for proper scaling in the software. Larger pieces tended to display significant curvature. To account for this, multiple images were taken of consecutive surfaces along the curved fragment. Each image was traced, and the group of images summed up for a total surface area of the curved fragment. Figure 3-7 demonstrates the method used for measuring the surface area of a large curved fragment from the unpressurized test. A bar graph was used to show an average projected area of the top 10 largest pieces for each experimental hit along with the projected area of the largest piece recovered.

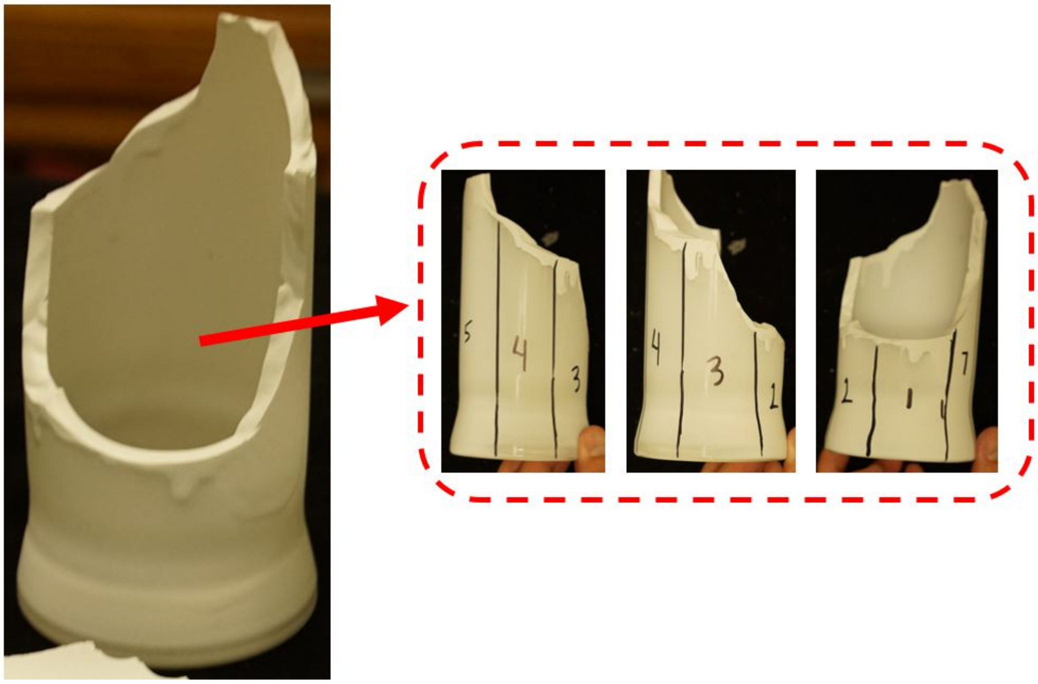

Figure 3-7: Method for surface area measurements of spray painted large curved fragments.

3.1.1.4 Fragment dynamics

The impact flash of the pellet for the pressurized and unpressurized cylinders marked the starting time point or initial frame. The ejection time of a fragment was determined to be the first measurable observation of a fully resolvable fragment. The Phantom 5 camera used to track fragments had a window frame of 22.86 cm x 22.86 cm (9 in x 9 in), which didn't allow tracking of fragments for the complete impact event. Some fragments tended to break apart as they hit the ground, causing a shape change that made them even less identifiable in comparison to fragments in the image. The limitation of this set-up precluded correlating actual fragments collected with the corresponding fragments seen in the window.

Because fragment mass could not be tracked experimentally, fragment volume was calculated by using an AutoCAD tracing of the projected surface area seen in the tracking software window and an assumed thickness equal to the cylinder wall thickness (6.35 mm). A majority of recovered fragments did show thickness to be equal to the wall thickness of the cylinder, therefore an assumption was made that the fragment thickness was constant. Mass, in turn, was calculated using the obtained volume of the fragment and an assumed borosilicate glass density of 2.23 g/cm^3. Initial velocities for corresponding ejection times were also measured for six fragment masses at both 0 and 207 kPa. This tracing method was conducted three times for each experiment to generate a confidence error in measurement, based on the observer's ability to track fragments in the software.

3.1.2 Air gun testing of neighbor effect

A set of four of the pressurized cylinders (Figure 3-8) were set up and pressurized under controlled conditions to 345 kPa (50 psi). The central cylinder impacted by the pellet was pressurized with a separate compressor from the remaining three cylinders. A total of 12 tests were run with 4 cylinders in each test. A Phantom VEO 710 high-speed camera was mounted above the cylinders for a radial view of the impact, following the set-up in Figure 3-2 (camera 1), and operated at 10,000 frames per second at a resolution of 512 x 256. The VEO 710 camera window only saw three of the four cylinders. A

Chronos 1.4 high-speed camera was set up as Camera 2 in Figure 3-2 to the side of the cylinders operating at 3,587 frames per second at a resolution of 800 x 480.

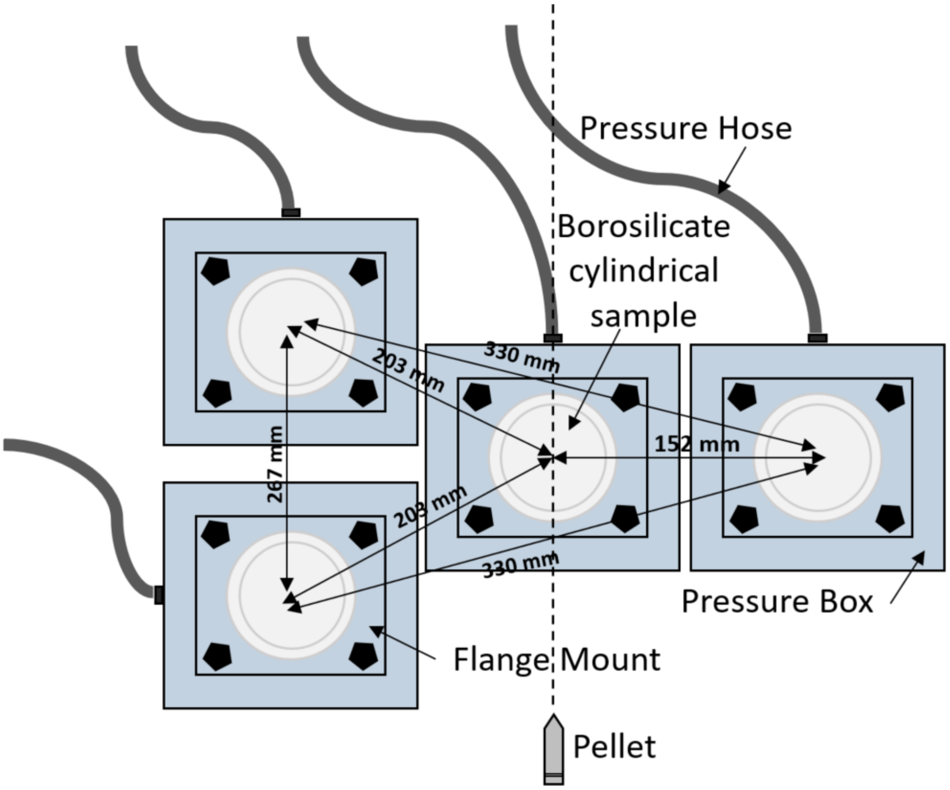

Figure 3-8: Top view of air gun ballistic test cylinder arrangement.

Probabilities were determined for the number of cylinders involved in a cascading reaction after the first cylinder was hit, for all 12 tests. This included the likelihood of zero, one, two or three cascading failures after the initial failure from the projectile impact. The first cylinder hit by the pellet was always involved and was not considered part of the number of cylinders involved in a cascading reactionary blast. Distances between cylinders causing cascading failures were also recorded and plotted on a bar graph. A scale factor was applied to the final results to correlate cylinder distances to bushing distances.

3.2 Results and discussion

3.2.1 Preliminary visual observations

In Figure 3-9, two sequences of visual images of cylinder blasts are presented for 0 and 690 kPa pressure. The top row shows the impact sequence for the 0 kPa cylinder at (a) 0 μs impact flash, (b) 67 μs, (c) as the pellet reached the far side at 399 μs, and at (d) 1596 μs. The bottom row represents the impact sequence for the 690 kPa cylinder at (e) 0 μs impact flash, (f) 66 μs, (g) after the pellet reached the far side at 399 μs, and (h) as the cylinder began to separate along its length at 1064 μs. The pellet direction was from left to right for both pressure tests.

The unpressurized cylinder formed a fine localized ejection cloud that can be seen in Figure 3-9d, as opposed to more spread-out cloud as shown in Figure 3-9h for 690 kPa. This was a highly expansive cloud that contained the gas (air), some potential water vapor from humidity in the compressor, and smaller glass particles. In Figure 3-9, the ejection traveled in the direction opposite to that of the pellet. Ejections in both directions similar to those seen in Figure 3-9d were also observed by Harold Edgerton in the well-known high-speed strobe pictures of bullets passing through various objects (31).

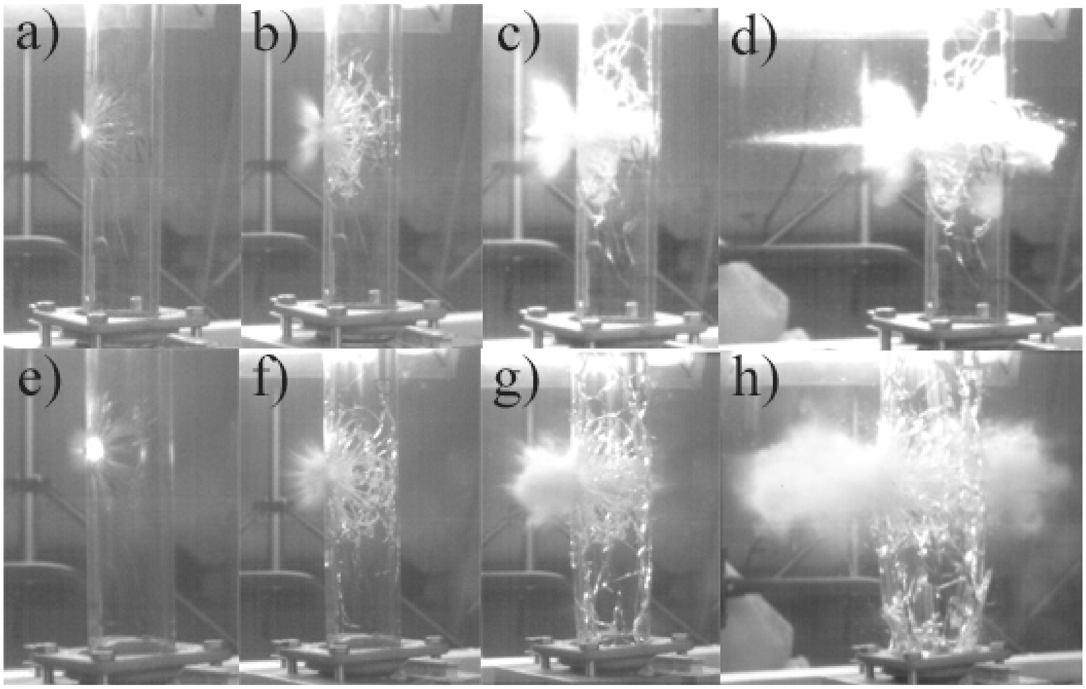

Figure 3-9: Impact sequences for the 0 kPa and 690 kPa pressure tests.

Failure modes of brittle materials under ballistic conditions have been extensively studied (32-37). Under dynamic loading, glass displays comminution, the formation of very small micron sized pieces (38). It was not readily apparent that comminution occurred in the high-speed imagery in Figure 3-9. However, the significant level of fine debris found inside of each pressurized hollow cylinder indirectly indicated that comminution occurred during the pressurized blasts of this study. According to Mebarki, et al. (27) cracks initiate and propagate along the perimeter of a pressurized metallic tube creating an “end cap” effect. An “end cap” refers to the fully intact breaking off of the rounded top portion of a closed end of a tube. Cracks can also branch out in various directions, creating many flatter fragments (27). The fragments in the unpressurized cylinders in our research followed the end cap generation mechanism, whereas the higher-pressure tests created more random and flatter fragments. This can be seen in Figure 3-9 in the level of cracks forming above and below the impact site.

Brittle materials under impact develop cone, radial, and ring cracking (34). Radial cracks initiate at the impact site and extend outwards. Ring cracks form concentrically around the impact site and move out through the radial cracks (35). In this research, the radial cracks were seen radiating in straight lines from the point of impact preceding the circular cracks in the high-speed imagery. Toshihiko et al. studied failure waves in water ice targets and demonstrated prominence in radial cracking as well (39). Cone cracks start at the surface as ring cracks and penetrate the thickness of the material. Cone cracks were not identified in our images; however, the ring and radial cracks were very prominent in all cylinders. Appendix B discusses further the common failure mechanisms of different material types.

3.2.2 Pressure effect on velocity profiles

All velocity profiles were examined for all the tested pressures. Velocity profiles are shown in Figure 3-10 for (a) 0 kPa, (b) 69 kPa, (c) 207 kPa, (d) 345 kPa, (e) 448 kPa, (f) 517 kPa, and (g) 690 kPa. Results are shown for only one experimental shot each, but the behavior was found to be repeatable between all tested cylinder pressures that had two shots tested. Based on the velocity profiles it was observed that the pressurized cylinders generated larger profile velocities as the pressure increased. It was also discovered that at higher pressures the fragmentation blast profile became more uniformly distributed radially around the cylinder, indicating symmetry. The profile velocities in Figure 3-10 do not demonstrate any time relationships; rather they show all measured fragment portions in direction and velocity magnitude only. All slow-moving and fast-moving tracked portions are displayed with no dependence on when they left the cylinder during the blast. The blast pattern of pressurized cylinders was more dependent on the pressurization than on the direction of the impacting pellet. Because the potential energy is much larger for a pressurized system, the incoming pellet primarily serves to release the potential energy by creating a pressure drop, as opposed to dictating blast behavior. Trends in Figure 3-11 indicate an increase in profile velocity as pressure increases.

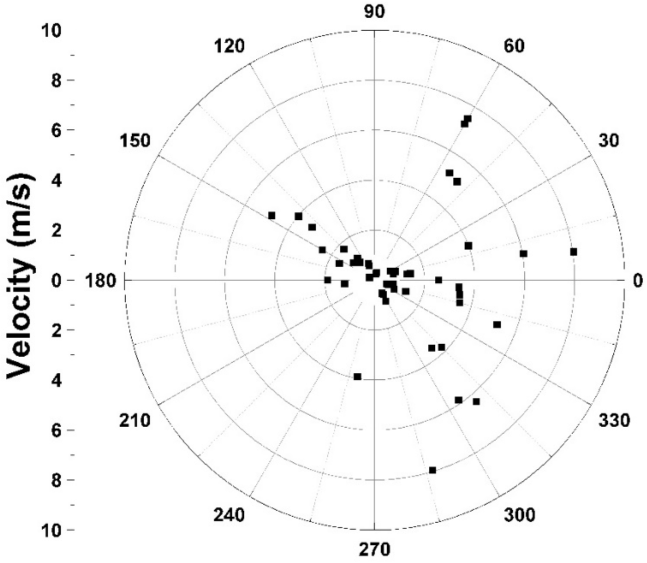

(a)

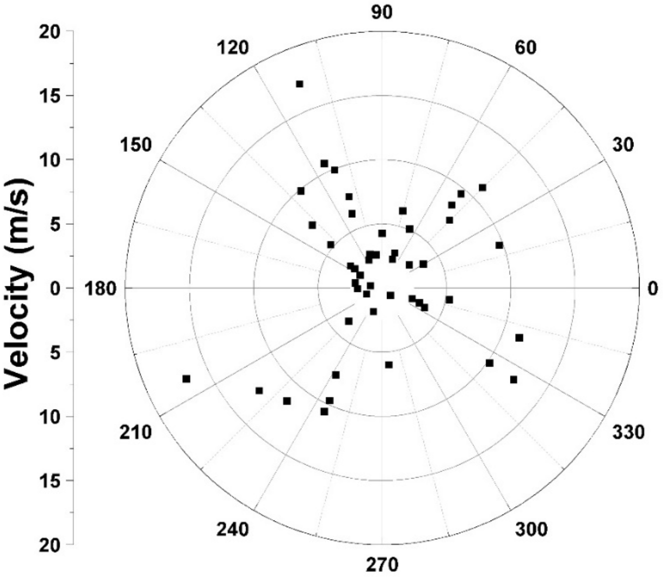
Velocity (m/s)
20
15
10
5
0
5
10
15
20
90
60
30
0
330
300
270
240
210
180
150
120

(b)

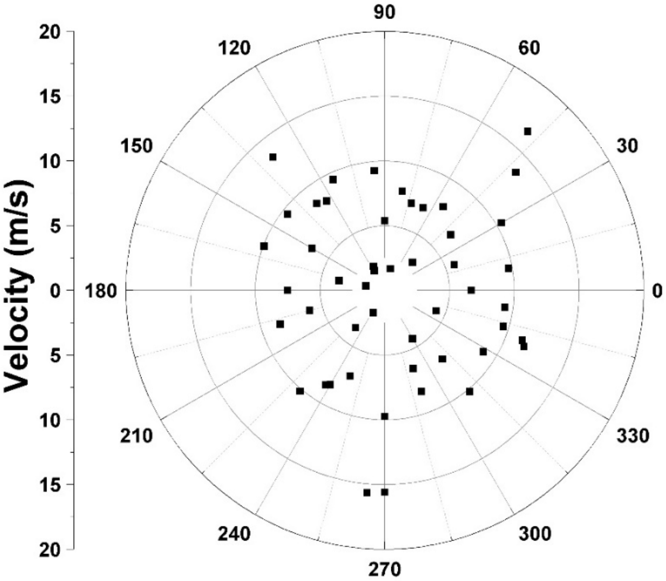
Velocity (m/s)
20
15
10
5
0
5
10
15
20
90
60
30
0
330
300
270
240
210
180
150
120

(c)

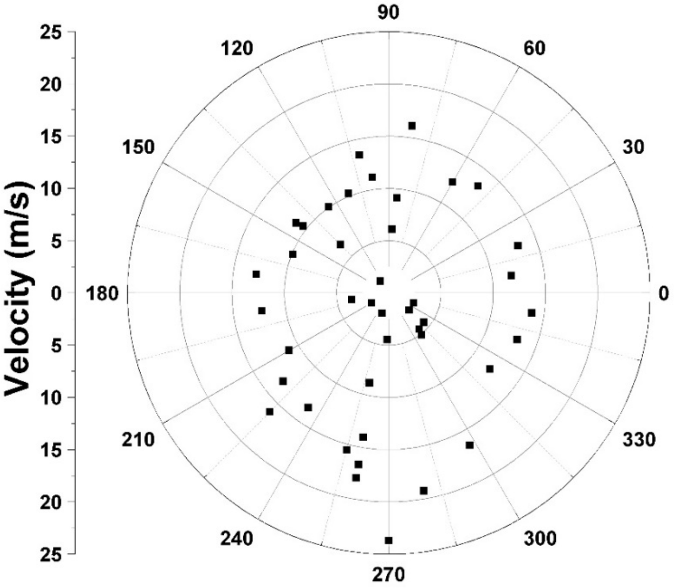
Velocity (m/s)
25
20
15
10
5
0
5
10
15
20
25
90
120
60
150
30
180
0
210
330
240
300
270

(d)

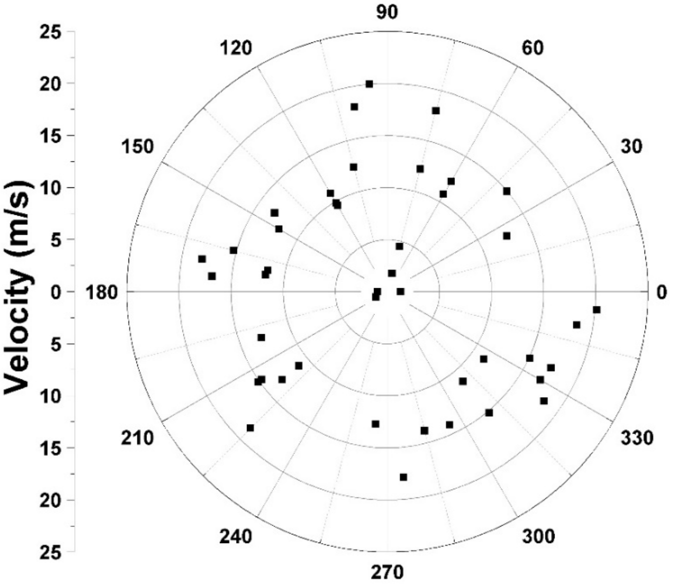
Velocity (m/s)
25
20
15
10
5
0
5
10
15
20
25
90
120
60
150
30
180
0
210
330
240
300
270

(e)

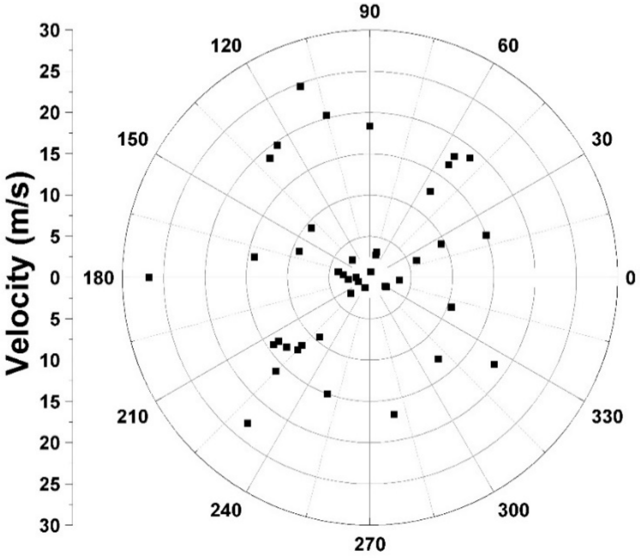

(f)

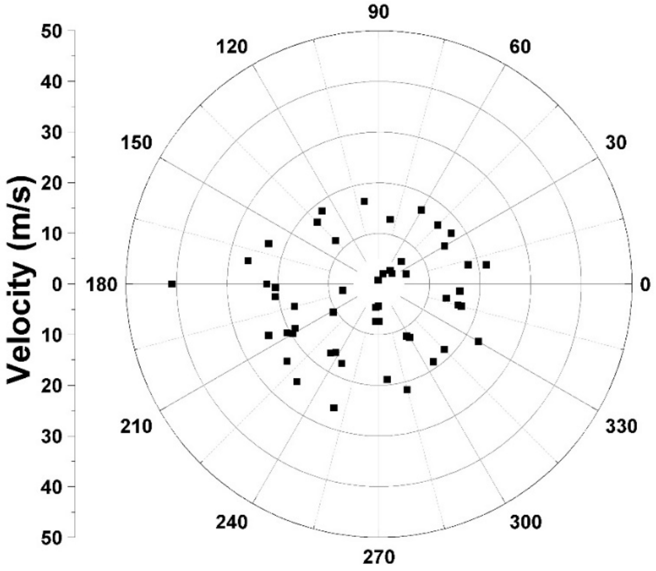

(g)

Figure 3-10: Velocity profiles of the fragments at a) 0, (b) 69, (c) 207, (d) 345, (e) 448, (f) 517 and (g) 690 kPa. Zero degrees is where the pellet exited the cylinder. Results for one experimental shot at each pressure are shown.

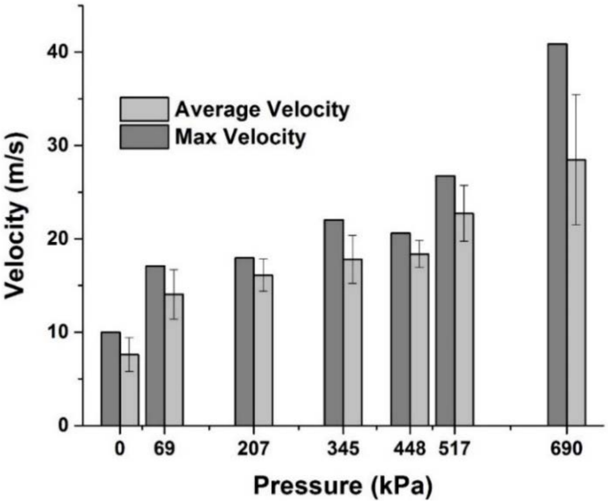

Figure 3-11: Profile velocity at tested pressures.

The blast symmetry was examined using Java to further validate the results seen in the velocity profiles shown in Figure 3-10. Deviation in the blast symmetry occurred in locations where the blast profile did not expand to form a perfect circle and is highest in directions where no fragments were found in the blast. Resulting deviations from symmetry are shown for all tested pressures in Figure 3-12, where the dashed lines represent pressurized cylinders and the solid lines represent the unpressurized cylinders. The lobes seen in Figure 3-12a show where the highest deviation from symmetry occurred. These areas contained no fragments. Repeat measurements demonstrated that the lobes were reproducible and were only present during unpressurized impact events. Average deviations, shown in Figure 3-13, were also determined for the total circular reference at 10-degree increments, with standard deviations represented for the pressures where two experimental shots were performed. It can be seen that symmetrical deviations occur predominantly in unpressurized cylinders.

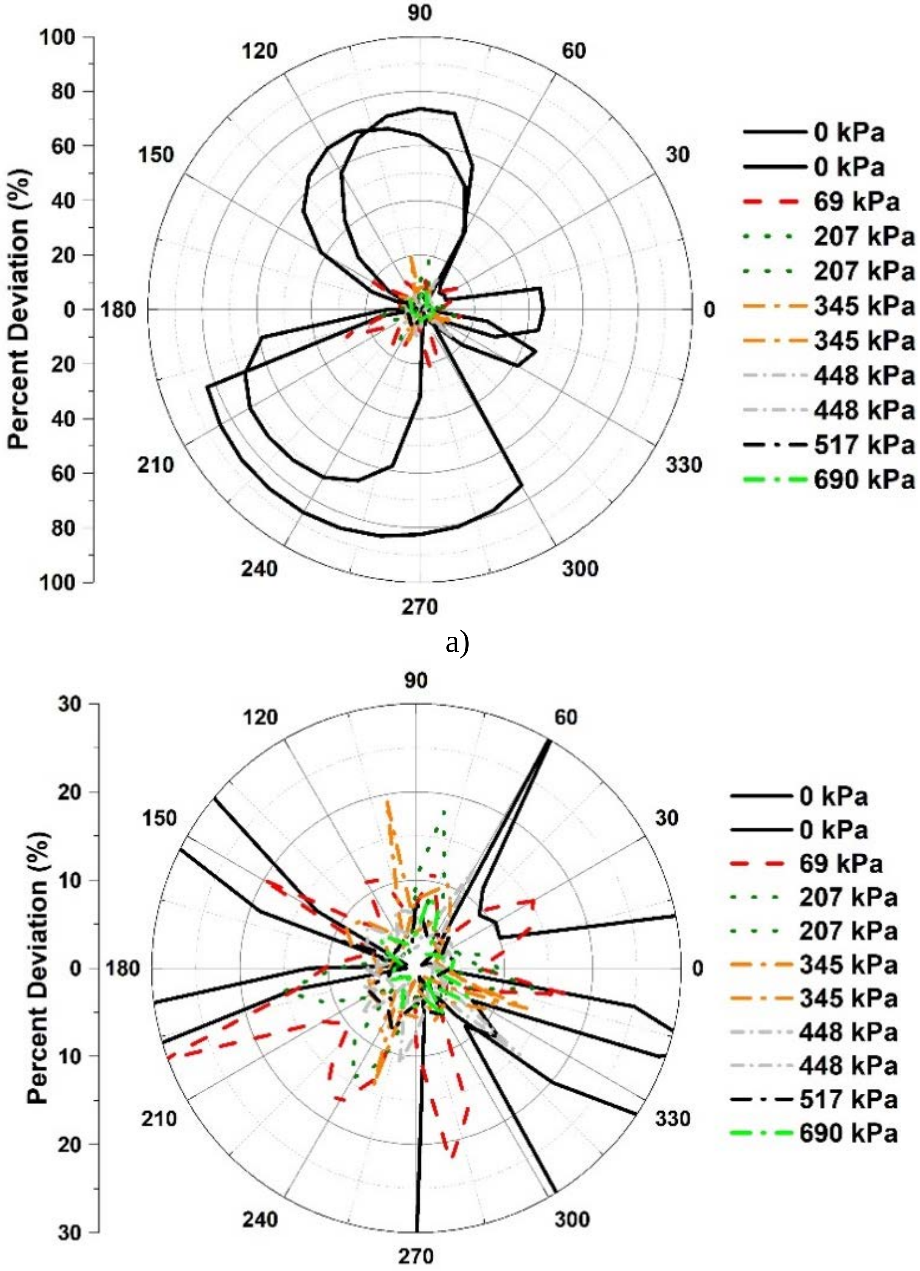

a)

b)

Figure 3-12: Polar plot of deviations occurring in symmetry of radial velocity during tested cylinder pressures a) in full-scale and b) zoomed in to show small deviations in the radial velocity.

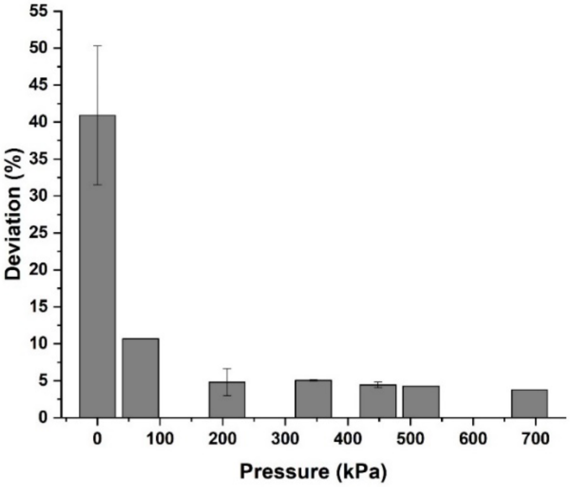

Figure 3-13: Average deviations in symmetry determined for the blast profiles at tested pressures.

3.2.3 Pressure effect on fragment size

Experimental research by Toshihiko et al. observed that smaller fragments occur in greater frequency than larger ones during material fragmentation (39). It was also observed in this study that a higher prevalence of smaller fragments was present in both the unpressurized and pressurized cylinders. Fragmentation of ductile metallic materials occur as cohesion is lost and small voids coalesce. Ductile materials stretch as they are pulled until the amount of voids combine to create a fracture large enough to rip the material apart (32). These ductile cracks can propagate further through the material before stresses at other flaws create more cracks (40, 41). Brittle materials, on the other hand, form microcracks that coalesce. Failure spreads through cracks that run in many directions (40). This microcracking behavior can result in many more fragments during the explosive blast.

In this study fragment sizes were strongly dependent on the type of material under impact (27), but also of the energies involved. Smaller loads were more closely associated with coarse fragment sizes. These smaller unpressurized loads did not contribute potential energy due to pressurization,

Figure 3-14 shows the visual observations of fragmentation for (a) the 0 kPa test at 8,773 µs, (b) the 270 kPa tests at 5,480 µs, and (c) the 690 kPa test at 3,059 µs. The pellet direction went from right to left in Figure 3-14. Visual observations in Figure 3-14a show less fragmentation for the unpressurized test. In fact, the top and bottom sections stayed mostly intact. The middle section was predominantly the only region that fragmented into smaller pieces. The pressurized test images in Figure 3-14b and Figure 3-14c show the whole cylinder being involved in fragmentation with no major pieces preserved. As pressure increased from 270 kPa to 690 kPa the fragments appeared to increase in quantity. It is difficult to determine if the size of the fragments differ significantly between the two pressurized tests using visual observations. In Figure 3-15, collected fragments were imaged for three different pressurized tests (a) 0 kPa, (b) 345 kPa, and (c) 690 kPa. The collected fragments help to confirm what is seen in Figure 3-14, that the coarser fragments are associated with the unpressurized tests. Figure 3-15c shows far less fragments collected, which was a result of recoverability.

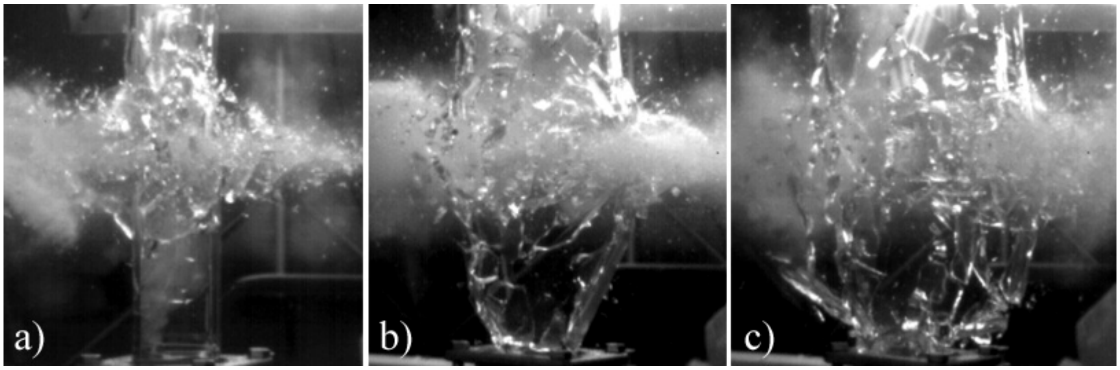

Figure 3-14: Fragmentation for tests at (a) 0, (b) 270 and (c) 690 kPa.

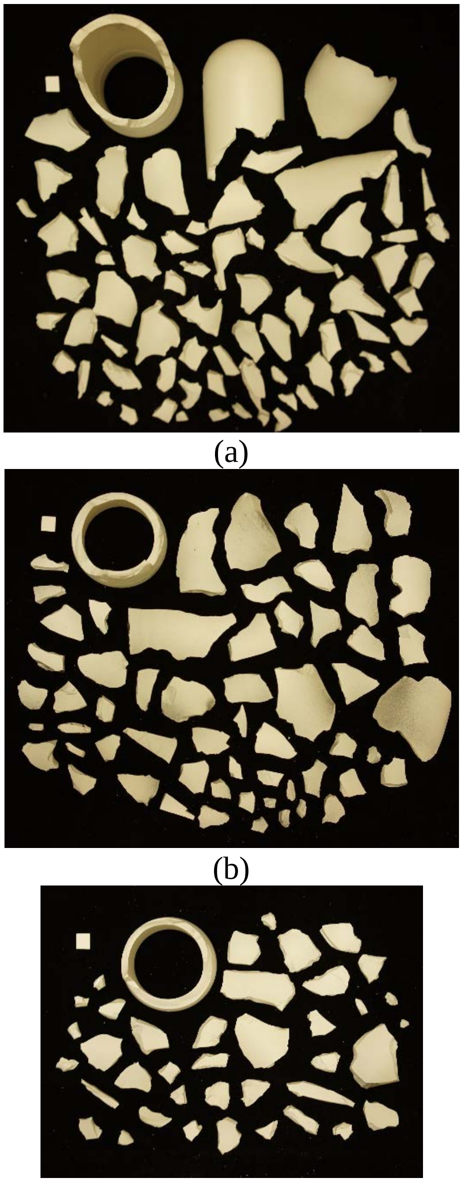

(a)

(b)

(c)

Figure 3-15: Fragment size of collected spray painted fragments (a) 0, (b) 345 and (c) 690 kPa.

Identifiable fragments were collected after each test was performed. The mass recovered was compared to the initial mass of each cylinder and expressed as percent recovery. The percent recovery of the fragments became more difficult as pressure increased. The smaller fragments travelled further and spread throughout the testing area.

In Figure 3-16, the linear relationship between pressure and the recoverability of the mass of the cylinder is shown. As pressure increased, the mass of fragments greater than the 0.3 cm^2 cutoff significantly decreased. At high pressures many more fragments were smaller than the 0.3 cm^2 collection limit.

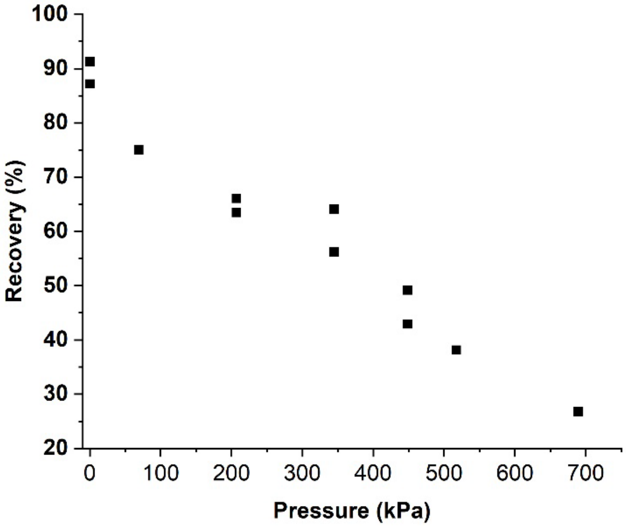

Figure 3-16: Percent recovery of fragments vs. pressure.

In Figure 3-17, the histogram for fragment mass at three pressures illustrates the visual results seen in Figure 3-14 and Figure 3-15. The number of fragments below 10 grams increased after a pressure of 207 kPa was reached. The unpressurized cylinder retained large fragments greater than 100 grams from the top, sides, and bottom of the cylinder. It should be noted that the results seen in the fragment mass histogram was affected by the percent recovery. Percent recovery was closest to 90% for the unpressurized test and reduced to 27% at 760 kPa. The histogram in Figure 3-17 does not consider the significant amount of unrecoverable mass in fragments.

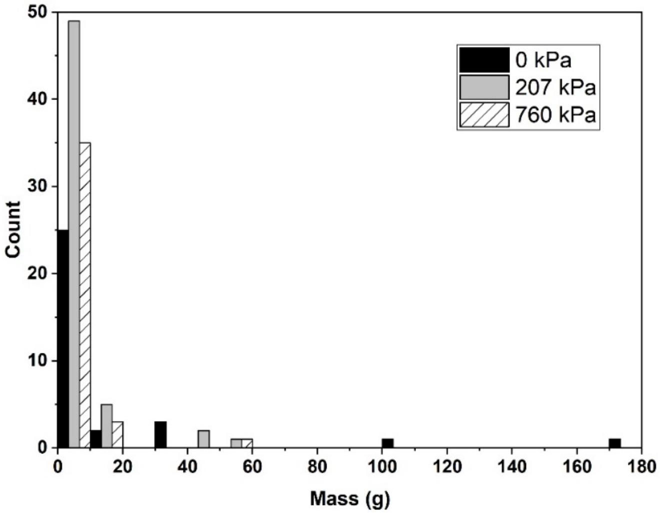

Figure 3-17: Histogram of collected fragments for 0, 207, and 690 kPa.

Recovered fragment size distributions are illustrated in Figure 3-18. Average projected areas were determined for the largest 10 pieces for each cylinder, to provide a basis for comparison and accounting for the difficulty in recoverability of fragments. Figure 3-18 shows decreasing average fragment size, as defined by the fragment area projected onto the x-y plane and decreasing maximum fragment size as pressure increases. It is interesting to note that the average size is decreasing, but only slightly compared to the maximum size found. After 207 kPa the change in fragment size became much smaller with the higher pressures.

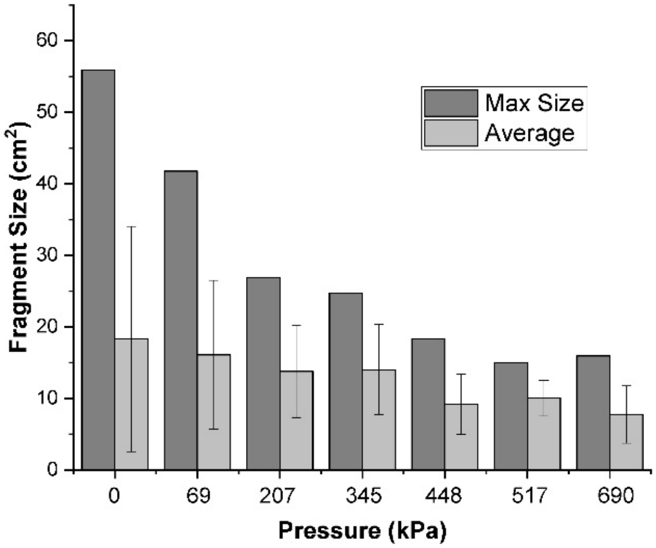

Figure 3-18: Fragment size versus pressure (kPa).

3.2.4 Fragment dynamics

3.2.4.1 Fragment velocities and ejection times

To estimate the range of impact by fragments after the explosive blast, predictions had to be made regarding the way the velocities of fragments were changing with time for the unpressurized and pressurized cylinders. In Figure 3-19, changes in fragment velocities with time and the masses of the fully resolvable fragments moving across the observation window are shown for tests at 0 and 207 kPa. The amount of data presented in Figure 3-19 provided no clear delineation regarding the effect of pressure on the fragment dynamics and the fragment mass.

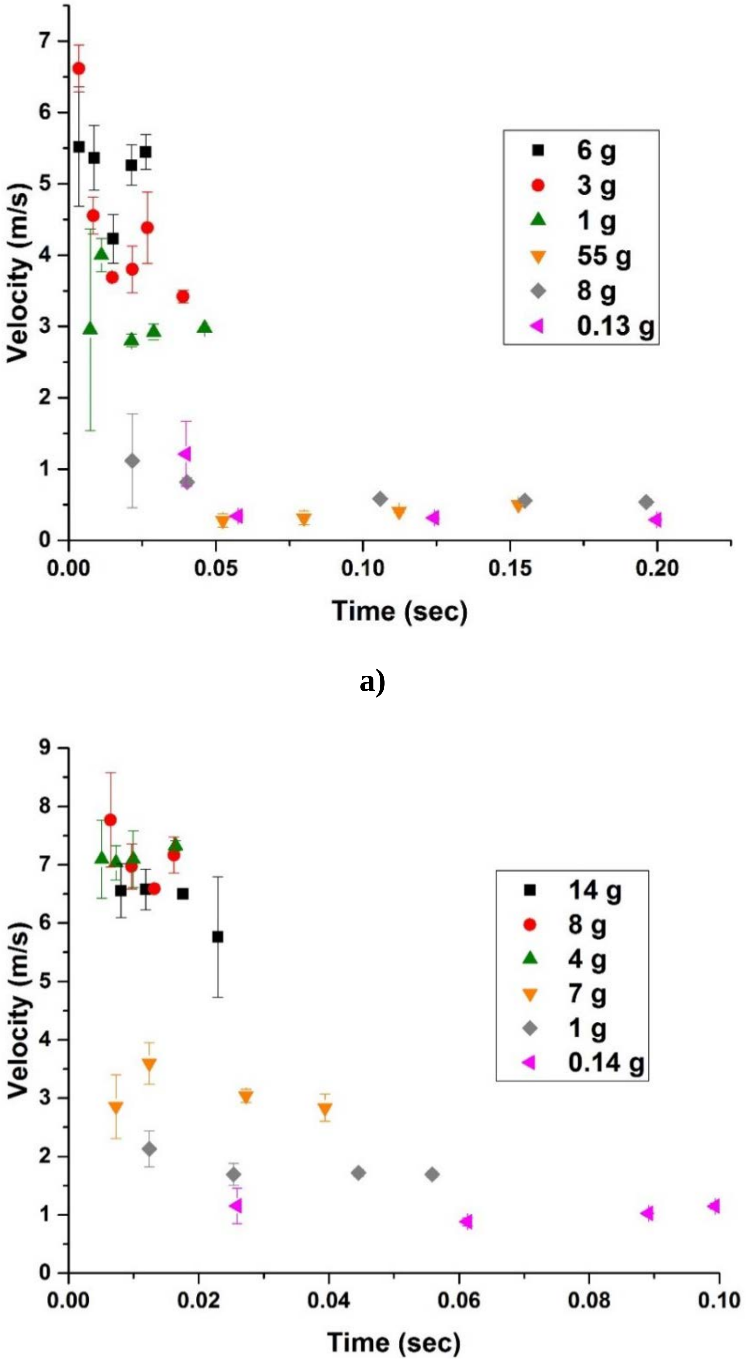

a)

b)

Figure 3-19: Fragment velocities and masses for a) 0 kPa and b) 207 kPa.

Fragments velocities appeared to slow down with time, with some exceptions, and the initial velocities seemed to be approximately 25% higher for the pressurized tests. To further examine the data in Figure 3-19 a portion of the figure was replotted in Figure 3-20 to show the initial velocities of the twelve fragments and their associated ejection times for the two pressure tests. Figure 3-19 and Figure 3-20 illustrate that the initial fragment velocities varied from 0.2 m/s to around 8 m/s. Further examination showed no definite mass relationship in the initial velocity and ejection time. Progression of the fragments was also analyzed in detail as a function of time and pressure in Section 3.2.4.2 to determine the range of impact of the fragments (see Figure 3-23).

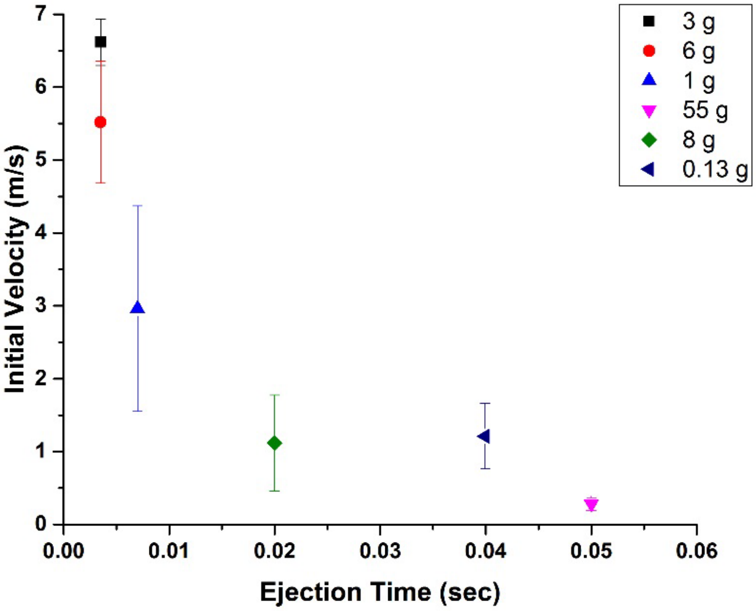

a)

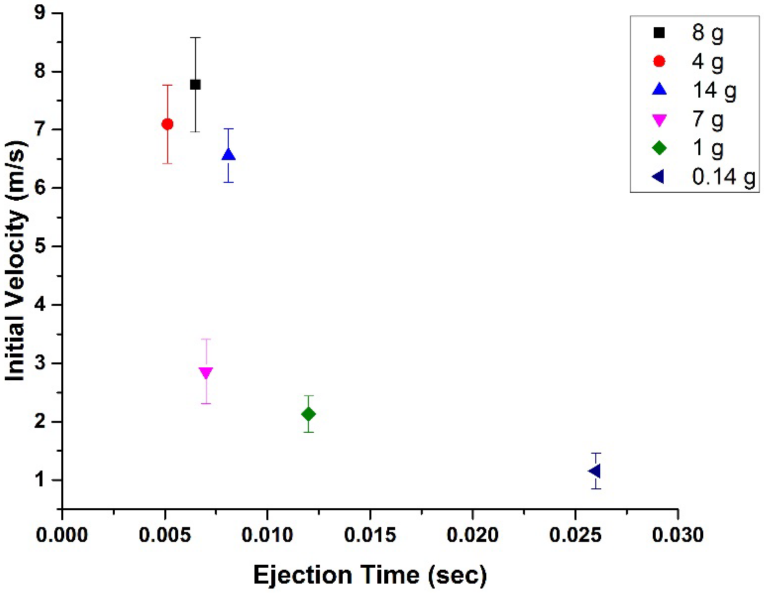

b)

Figure 3-20: Initial velocities versus ejection times for a) 0 kPa and b) 207 kPa.

All fragment velocities presented in Figure 3-19 and Figure 3-20 were determined visually using the tracking software. They were affected by similar errors, depending on the fragment velocity and mass. Slower moving fragments were easier to track and resulted in smaller error measurements. The largest measurement errors were incurred when tracking very fast-moving fragments. Since the ejection times were selected prior to the velocity measurements, the ejection times in Figure 3-19 and Figure 3-20 were not affected by user tracking errors.

Figure 3-19 is only able to show velocities for the time interval that the fragments remain in the camera's view. The faster-moving fragments were in view for very short time intervals, up to 50 msec in the unpressurized test and approximately 20 msec for the pressurized test. The slower-moving fragments remained in view for 200 msec in the unpressurized test and 100 msec in the pressurized test. Because the pressurized cylinder generated faster fragments, only four individual measurements of velocity were incurred over the given time interval, whereas five measurements were incurred for the fragments ejected from the unpressurized test.

The initial velocities shown in Figure 3-19 and Figure 3-20 were not always the peak velocities. For example, the initial velocity for the 7g fragment in Figure 3-19b was slightly lower than its peak velocity. For the other fragments, initial velocities were the maximum measured velocities of the fragments but still could be lower than the true peak velocities. The true peak velocities could have occurred before the fragments were identified in the tracking software.

Regarding potential relationships between peak velocities and fragment masses, numerical simulations and a Baker explosion model modified for 1 atmosphere external pressure have both shown that fragments from an idealized pressurized tank burst are first accelerated by the internal pressure and then decelerated with time (42). Peak velocities were essentially independent of the fragment mass. Similar conclusions can be drawn from the data shown in this research, for the fragment velocities where peak velocities could be determined. It is possible that the peak velocities were also affected by other factors such as air turbulence, discussed in the next section.

3.2.4.2 Estimation of impact range of airborne fragments

Since the fragment velocities in Figure 3-19 seemed to decrease with time, with some exceptions, an assumption was made that the decrease was caused by interactions of the flying fragments with air (the drag effect). A simplified Newtonian drag model was examined for air resistance to explain fragment dynamic behavior, using the force diagram shown in Figure 3-21. In general, an ejected fragment is subjected to three forces: F_P due to internal pressure of the cylinder, F_g due to gravity and F_D due to drag.

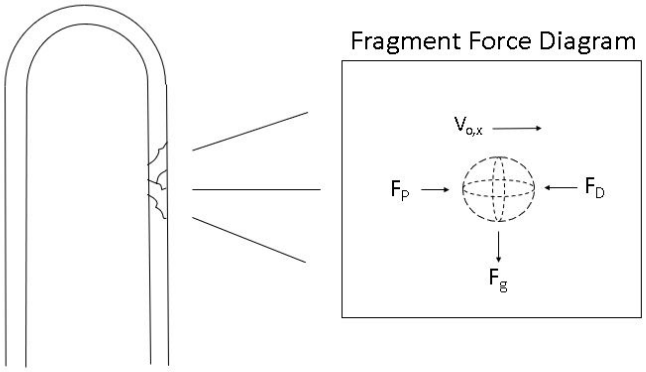

Figure 3-21: Fragment force diagram for air resistance of a flying fragment after ejection from cylinder.

Using Equations *(2)*- *(4)*, fragment velocities can be estimated as a function of time (14, 43). In Equation *(2)* the letter P is the pressure acting on the fragment during the blast and A is the area of the fragment where the pressure acts.

$$F_P = PA \tag{2}$$

$$F_g = mg \tag{3}$$

$$F_D = \frac{-C_D A_x \rho v^2}{2} \tag{4}$$

In Equation (3) the fragment mass is represented by m, and g is the acceleration due to gravity. In Equation (4) C_D is the drag coefficient, assumed to be 0.5 (43). The velocity in the x-y plane is v. The cross-sectional area perpendicular to the direction of motion is A_x and the density of air is ρ at the experiment location in Denver, Colorado at 25ºC.

The drag model was used with the assumptions that each fragment moves through the airspace and A_x was proportional to its mass. F_P was unknown due to factors such as frictional heating of the pellet and pressure dissipation at impact. It was assumed to be zero by the time velocity measurements were made. However, the pressure does affect the initial velocity. Since the fragment velocities in the x-y plane were the only measurable velocities, the F_g term was omitted. The air resistance on the fragment can then be represented by the following differential equation:

$$\frac{dv}{dt} = -\frac{C_D A_x \rho v^2}{2m} \tag{5}$$

After integration the solution was re-arranged to the following equation:

$$v = \frac{2mv_o}{C_D A_x v_o \rho t + 2m} \tag{6}$$

Nine fragments were considered with three different masses (0.1, 5, 55g) and three different velocities (1, 5, 10 m/s). The masses and velocities represented the ranges observed in the results in Figure 3-19. The 5g fragment represented the average mass of the fragments after eliminating the extremes (the smallest and largest fragments). The velocity of 5 m/s was approximately the middle of the range. Figure 3-22 shows the velocities of the idealized fragments obtained using Equation (6). Further assumptions are that the air is still, and fragments are moving uniformly without rotation. In a perfect scenario over a short time interval of 0.2 sec the fragments would behave as demonstrated by the simple Newtonian drag model in Figure 3-22.

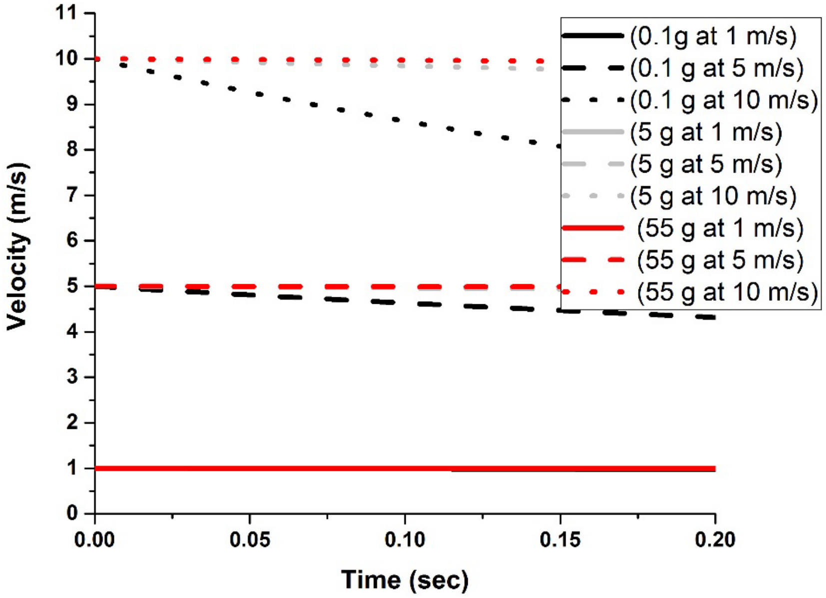

Figure 3-22: Predicted velocities of ejected fragments with time for nine combinations of mass and initial velocity.

After applying the drag model and examining Figure 3-19, the velocities versus time for each fragment was calculated independently and best exponential fits were applied. After extensive evaluations, the fragment dynamics were grouped into three predominant categories, based on observed trends: decreasing velocities, increasing velocities, and semi-stationary (fluctuating) velocities, with noticeable variability in each category. An experimental and numerical velocity set of fragments for both an unpressurized and a pressurized test in each category are shown in Figure 3-23.

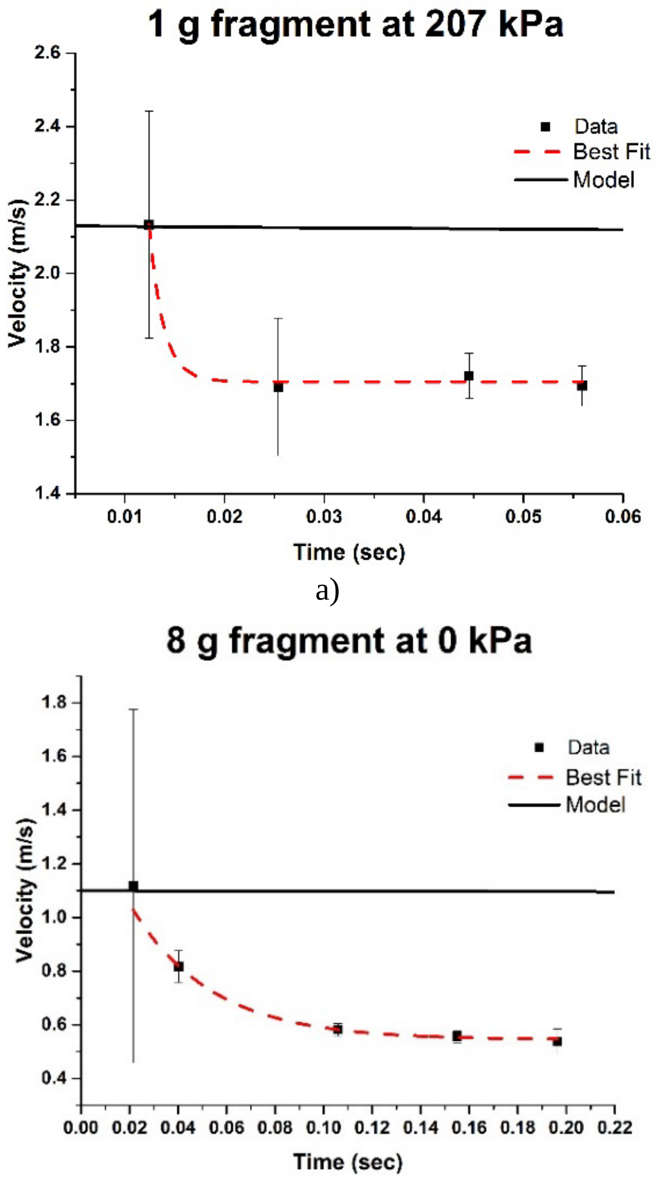
1 g fragment at 207 kPa
Velocity (m/s)
2.6
2.4
2.2
2.0
1.8
1.6
1.4
0.01
0.02
0.03
0.04
0.05
0.06
Time (sec)
Data
Best Fit
Model
8 g fragment at 0 kPa
Velocity (m/s)
1.8
1.6
1.4
1.2
1.0
0.8
0.6
0.4
0.00
0.02
0.04
0.06
0.08
0.10
0.12
0.14
0.16
0.18
0.20
0.22
Time (sec)
Data
Best Fit
Model

a)

b)

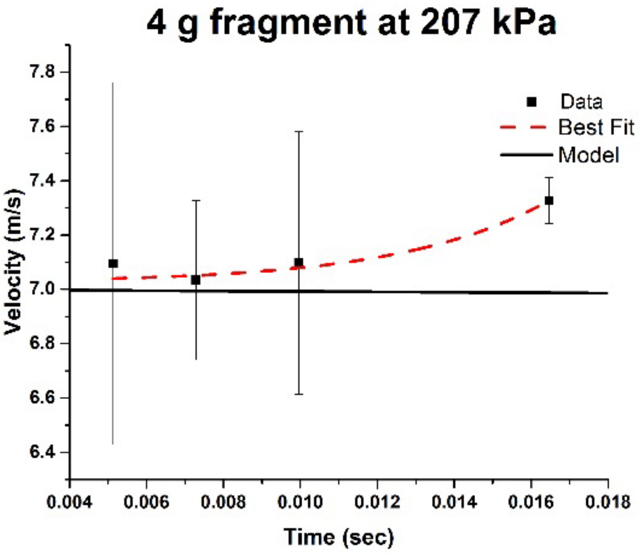
4 g fragment at 207 kPa
Velocity (m/s)
7.8
7.6
7.4
7.2
7.0
6.8
6.6
6.4
0.004
0.006
0.008
0.010
0.012
0.014
0.016
0.018
Time (sec)
Data
Best Fit
Model

c)

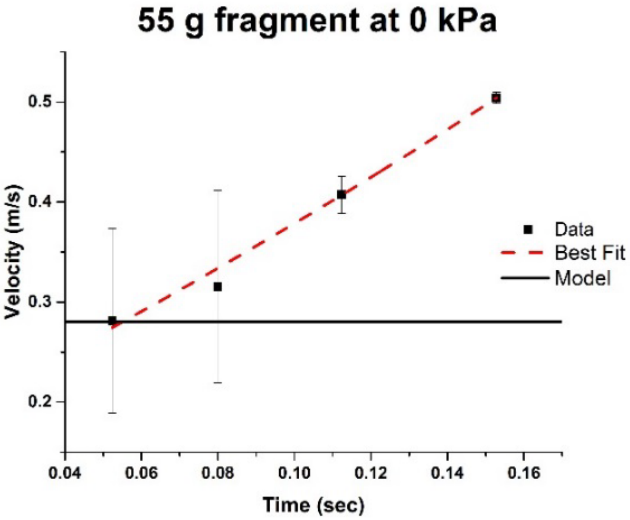
55 g fragment at 0 kPa
Velocity (m/s)
0.5
0.4
0.3
0.2
0.04
0.06
0.08
0.10
0.12
0.14
0.16
Time (sec)
Data
Best Fit
Model

d)

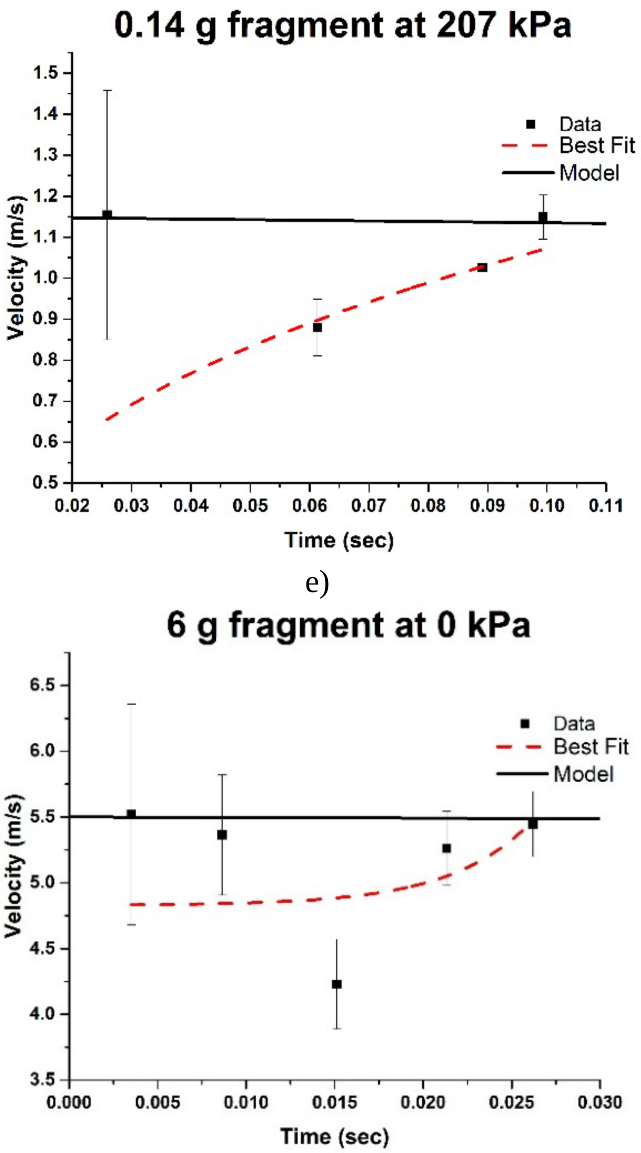

e)

f)

Figure 3-23: Experimental and calculated fragment velocities for three selected categories; a and b) decreasing velocities, c and d) increasing velocities, and e and f) semi-stationary velocities with best fits for the experimental data.

The best fits, shown in Table 3-1 followed an exponential fit function with the following equation:

$$v = v_o + Ae^{R_o t} \tag{7}$$

Fragment	v_0	A	R_o	R^2 Coefficient
14 g, 207 kPa	6.57	-0.00003	444.4	0.998
8 g, 207 kPa	6.57	65	-607.8	0.384
4 g, 207 kPa	7.02	0.004	262.4	0.989
7 g, 207 kPa	-430.9	434.5	-0.039	0.509
1 g, 207 kPa	1.705	2570	-700.6	0.944
0.14 g, 207 kPa	No convergence			
6 g, 0 kPa	4.82	0.002	219.6	0.329
3 g, 0 kPa	3.44	7.05	-226.9	0.958
1 g, 0 kPa	2.97	20.35	-297.5	0.567
55 g, 0 kPa	-0.97	1.14	1.68	0.999
8 g, 0 kPa	0.54	0.93	-30.42	0.996
0.13 g, 0 kPa	0.29	991.9	-174.9	0.676

Table 3-1: Best fit parameters for all fragments.

The velocities of approximately 50% of the fragments appeared to decrease over time. Of the 12 best fits, 6 displayed a decrease, 2 displayed an increase, and 4 demonstrated semi-stationary behavior. In the decreasing category, (Figure 3-23a and Figure 3-23b), 2 of the 6 fragments had a poor best fit curve. In the increasing category, (Figure 3-23c and Figure 3-23d), both exhibited good best fits. In the semi-stationary category, (Figure 3-23e and Figure 3-23f), 3 of the 4 fragments had poor fits and one didn’t converge. It was seen in Figure 3-23 that none of the plots demonstrated agreement with the simple Newtonian drag model in Figure 3-22.

The reason some fragments exhibited increasing trends in their velocities, as shown in Figure 3-23c and Figure 3-23d, could be accounted for by the possible explanations listed above and by the residual blast pressure after the impact. Since the drag model assumed zero pressure acting on the airborne fragments, the model underestimated the velocities of the fragments which were still accelerating before reaching their peak velocities. Clearly, the very simplistic version of the drag model did not explain the complex nature of fragment dynamics in the tests of this study. The model was only used to emphasize the complexity of the problem. It is doubtful that the model could be improved, even for the cases where velocities were gradually decreasing with time.

Due to the difficulties with the prediction of the velocities of the airborne fragments, no credible estimates could be made regarding their impact ranges. Our simplistic experimental model was not adequate to predict the fragment range. The sizes and velocities of fragments were inadequate to be easily tracked by the camera, correlated with the fragment mass collected, or fast enough to experience less effect from the explosion.

3.2.5 Cascading damage effect in borosilicate glass bushing models

Visual observations demonstrated that cascading (secondary, tertiary, etc.) failure occurred in nine of the twelve tests. In Figure 3-24, a cascading failure sequence is observed. The camera window could only see three of the four cylinders used in the testing. Figure 3-24a is the frame which the initial impact flash occurs. Figure 3-24b is the frame 600 μs after impact where the primary failure occurred due to the pellet impact on the cylinder. Figure 3-24c and Figure 3-24d were the secondary and tertiary failures that occurred 11,200 μs and 32,300 μs after impact. The arrows identify the pellet at impact and the failing cylinders.

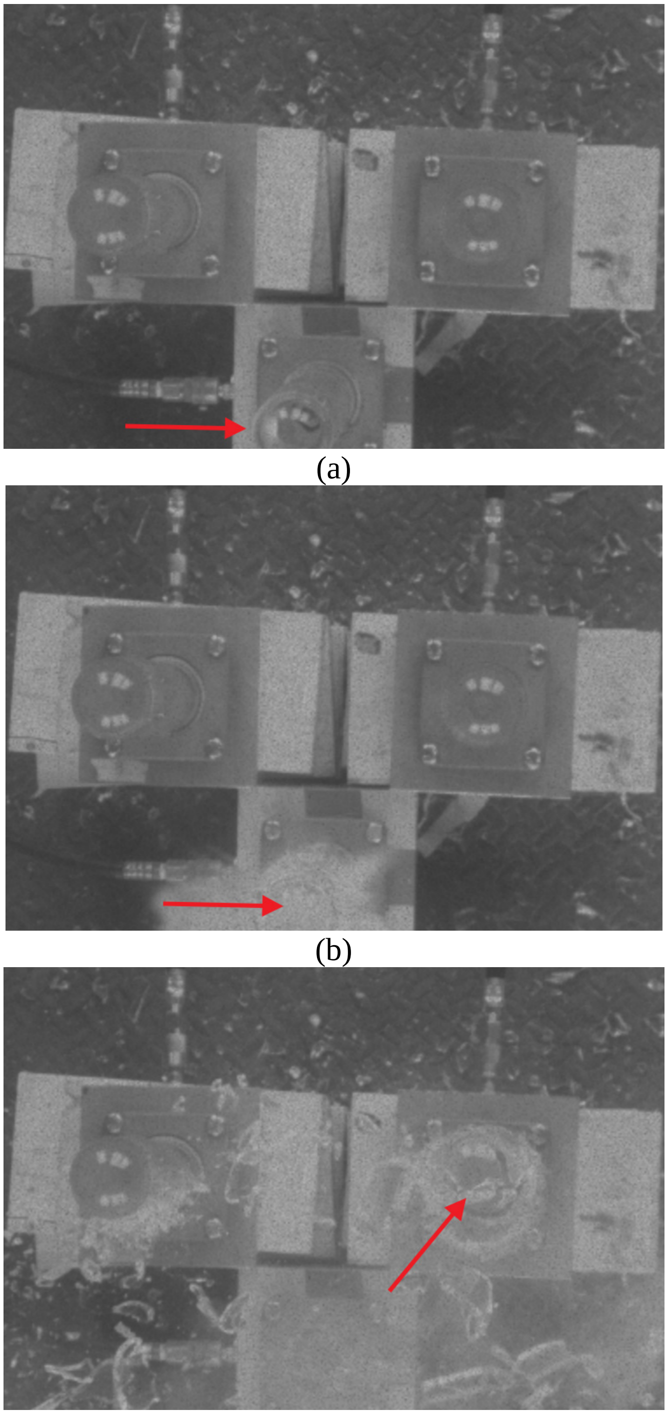

(a)

(b)

(c)

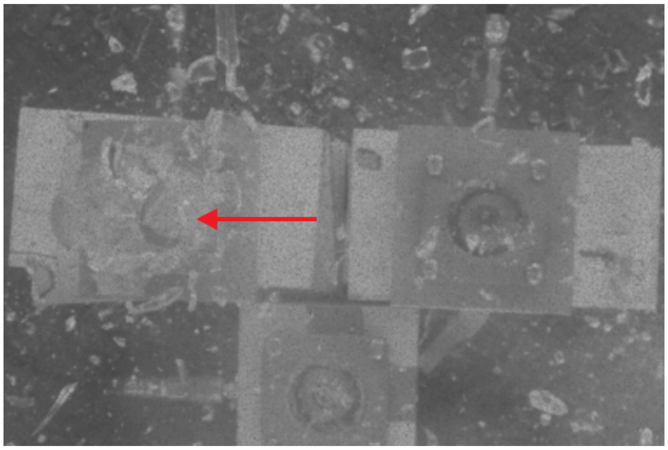

(d)

Figure 3-24: Visual observation of failure sequence at (a) impact flash, (b) primary reaction at 600 µs, (c) secondary reaction at 11,200 µs, and (d) tertiary reaction at 32,300 µs.

The configuration in this neighboring effect experiment was chosen to make sure that only the central cylinder was hit by the lead pellet. An assumption was made that the fragments from the cylinders would move symmetrically in the radial direction, so the probability of fragments impacting any of the cylinders was equal in the radial plane. The assumption of symmetry was based on the results from Section 3.2.2.

Probabilities were examined for the number of cylinders involved in a cascading reaction after the first cylinder was impacted. Figure 3-25 shows that a cylinder impacted by a lead pellet and pressurized at 345 kPa would have a 75% likelihood of fragmenting and destroying at least one more cylinder in the four-cylinder set-up in Figure 3-8. The likelihood that all cylinders would be destroyed is 17%, and the likelihood that none of the cylinders would be involved in a cascading reaction is 25% (considering that the first cylinder is always destroyed by the pellet and not included in the probability). These results show that the original assumption, that fragments from one cylinder could damage and destroy subsequent cylinders, was a valid hypothesis.

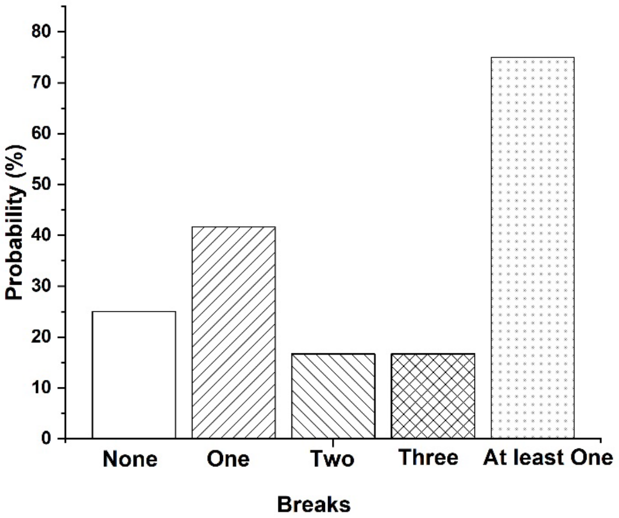

Figure 3-25: Probability of neighboring damage initiated by a single cylinder failure.

Proximity of neighboring cylinders to each other determined the likelihood of a cascading reaction. During this experiment the distances between two consecutive cascading cylinders was recorded. Figure 3-26 demonstrates that closer cylinders have a greater likelihood of being involved in a cascading reaction, than cylinders that are further apart.

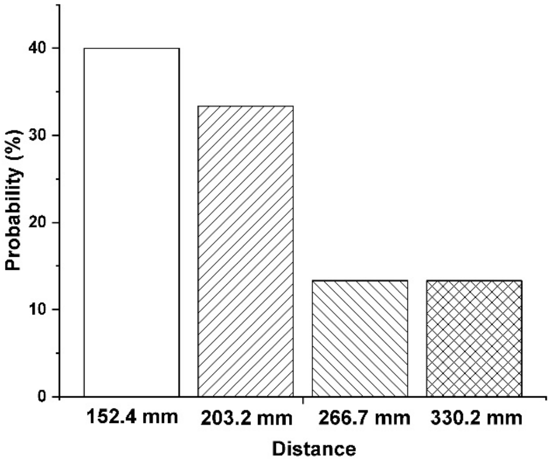

Figure 3-26: Probability of damage based on distance from center to center of cascading cylinder pairs.

To translate the observed statistical data from the borosilicate bushing models to actual bushings, it was assumed that bushings are vertically oriented just like the cylinders. Bushings are typically at an angle and obliquity during an impact increases the chance of deflection. It was also assumed that a lead pellet could be directly compared to a .308 caliber Winchester rifle cartridge and the borosilicate glass cylinders could be directly compared to a C-120 porcelain bushing. It was assumed that a scale factor could be used to linearly derive estimated bushing distances from the borosilicate cylinders tested. It is important to note that borosilicate glass is approximately three times less tough than C-120 porcelain (44). Therefore, this test could overestimate the likelihood of cascading failure for porcelain bushings.

The scale factor was derived based on the following relationship shown in Equation (8). $D_{Bushing}$ and D_{Sample} are the distances from center to center between two bushings and two borosilicate cylinders, respectively. The $\phi_{Bushing}$ and ϕ_{Sample} are the diameters of the bushing and borosilicate cylinder.

$$\frac{D_{Bushing}}{D_{sample}} = \frac{\emptyset_{Bushing}}{\emptyset_{sample}} \tag{8}$$

If a typical bushing is estimated to be 305 mm (12”) in diameter, and the diameter of the cylinders is 51 mm then the scale factor for this experiment would be 6. For cylinder distance ranges of 152 mm to 330 mm the bushing distances would be estimated using the scale factor as 912 mm to 1980 mm (3-6.5 ft). Using Figure 3-26, and the arrangement found in Figure 3-8, distances between bushings of 1980 mm would result in a probability of 13% that a cascading failure would result, and at a distance of 912 mm the probability increases to 40%. It is not uncommon to find bushings closely arranged on power transformers that could easily place them within those distance ranges of each other. The threat of a cascading reaction is too large to be ignored and the idea of fragmentation containment becomes critical for protecting the sustainability of the power grid during a high-velocity impact.

3.3 Summary

Pressurized borosilicate glass cylinders under impact from a .22 caliber lead pellet at 335 m/s (1100 ft/sec) were investigated. As pressure increased from 0 to 690 kPa the resulting fragment blast became fully symmetrical at about 207 kPa, whereas unpressurized cylinders displayed a directional fragment blast distribution after impact. It was found that fragment velocities increased with pressure and produced a greater quantity of smaller fragments. The ability to recover most fragments after an explosion significantly decreased with pressure; many fragments became harder to collect during testing. Fragments associated with end caps significantly reduce in prevalence and disappear entirely after an internal pressure of 270 kPa is reached.

No clear relationships were observed between fragment masses, their initial velocities, and ejection time for the unpressurized and pressurized tests. The impact range investigation turned out to be inconclusive due to a highly erratic nature of fragment dynamics. The velocities of airborne fragments rapidly decreased or increased with time irrespective of their masses, ejection times and testing conditions. The fragments did not follow a simple Newtonian drag model.

Pressurized borosilicate cylinders were tested in groups of four to elucidate the neighboring damage effect and to study cascading failure probabilities when a central cylinder was impacted with a lead pellet by an air gun. The cascading data was scaled to actual bushings positioned in a substation. The risk of cascading failures of multiple unprotected bushings in substations needs to be critically addressed, to avoid a single bushing failure which could initiate damage to an entire substation.

CHAPTER 4 NATURE'S VERSION OF IMPACT PROTECTION THROUGH ABALONE NACRE

When examining possible protection methodologies, the idea of looking at how nature has developed impact resistance over eons of time is a valuable one. This chapter will delve into the key elements involved in one of the most impact resistant gastropods, abalone. These key elements were chosen to help ascertain the types of elements available in nature for providing impact resistance. Section 4.1will cover the molecular "brick and mortar" arrangement that will be further pursued in this research in Sections 4.4.3 and 4.5.3, with the use of tiles and adhesives for drop weight impact protection. Section 4.2 will review the protein adhesive layer involved in this evolved gastropod, which ties into the choices and methodologies presented in the use of an elastomeric coating. The elastomeric coating is further discussed in Chapter 5 - Chapter 8.

The experiments presented in this chapter are listed here. Abalone was characterized to determine types of abalone shells which have the greatest impact resistant qualities. Tests were performed on abalone samples in different stages of hydration to determine the importance of the protein layer at low- and high-velocity impact. Drop weight test were performed to elucidate the combination of brick and mortar materials that were most impact resistant. Composites were built, tested, and compared against the National Institute of Justice (NIJ) standards, listed in Appendix B. The idea of building an abalone composite for use as an impact material is not feasible from a manufacturing and performance standpoint, but it is useful in examining structure and adhesive contributions to impact protection.

4.1 Abalone nacre “brick and mortar” tile structure

Nature has provided science with many examples of robust well-engineered impact resistant materials, an example being the red abalone (*Haliotis Rufescens*). Years of survival in the harshest environments and conditions has contributed to its biological development. Abalone sea shells exhibit a high level of strength and toughness and have been shown in nature to absorb heavy blows without breaking, due to a hierarchical arrangement of their “brick” layer with protein adhesive glue acting as “mortar” (45). The abalone is designed to be tough because predators are more likely to smash and break the shell as opposed to squishing or ripping apart the shell.

Nacre from seashells has attracted much attention for its enhanced mechanical properties, despite the structural weakness of its components (46). Nacre is the iridescent layer found inside the shell of mollusks, containing a rather simple structure, but providing exemplary mechanical properties applicable to high-velocity impact materials (47). Abalone sea shells are an excellent example of shells containing nacre and structural arrangements in the most optimal fashion. The weight distribution of nacre is 95% brittle aragonite (a crystalline form of calcium carbonate) and 5% organic material consisting of proteins, polysaccharides, and other organic molecules (47). The microscopic brittle aragonite is bonded by the thin layer of organic material that acts like a stretchy adhesive (48, 49). This brittle-ductile arrangement is similar to a ceramic “plywood” causing crack deflection and resistance of slippage, creating a tough biological material (50). The protein adhesive is strong enough to hold layers of the calcium carbonate tiles together, but weak enough to permit the layers to slide apart, absorbing impact energy (51).

The outer layer of the abalone shell is made of a hard calcite layer, seen in Figure 4-1, which is used to prevent penetration into the shell, but is prone to brittle failure. The inner nacreous layer is softer and tougher, which can dissipate more energy. If the brittle outer layer fails then the inner nacreous layer can function to preserve the shell by effectively dissipating the remaining energy (48) through deformation and fracture (52). The hard outside and softer inside is believed to be ideal for an armor system (48). Many effective human body armor systems are designed with hard outer material and softer inner material, or in the case of composites, a mixture of both material types, such as a soft resin with a tough fiber.

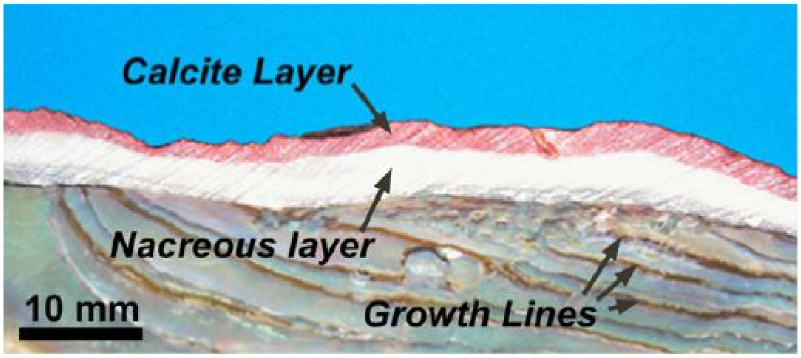

Figure 4-1: Abalone nacre macro-layer arrangement consisting of the hard outer prismatic calcite layer and soft inner nacreous layer. Reproduced from ref. (48).

The inside of the nacreous layer is comprised of brick tiles 0.5 µm thick surrounded by a thinner organic layer (53). Tiles are represented by hexagons in sequential layers with an overlap. The overlap between layers gives additional mechanical strength (49). Tiles have an approximate diameter of 10 µm. Figure 4-2 shows their hexagonal arrangement.

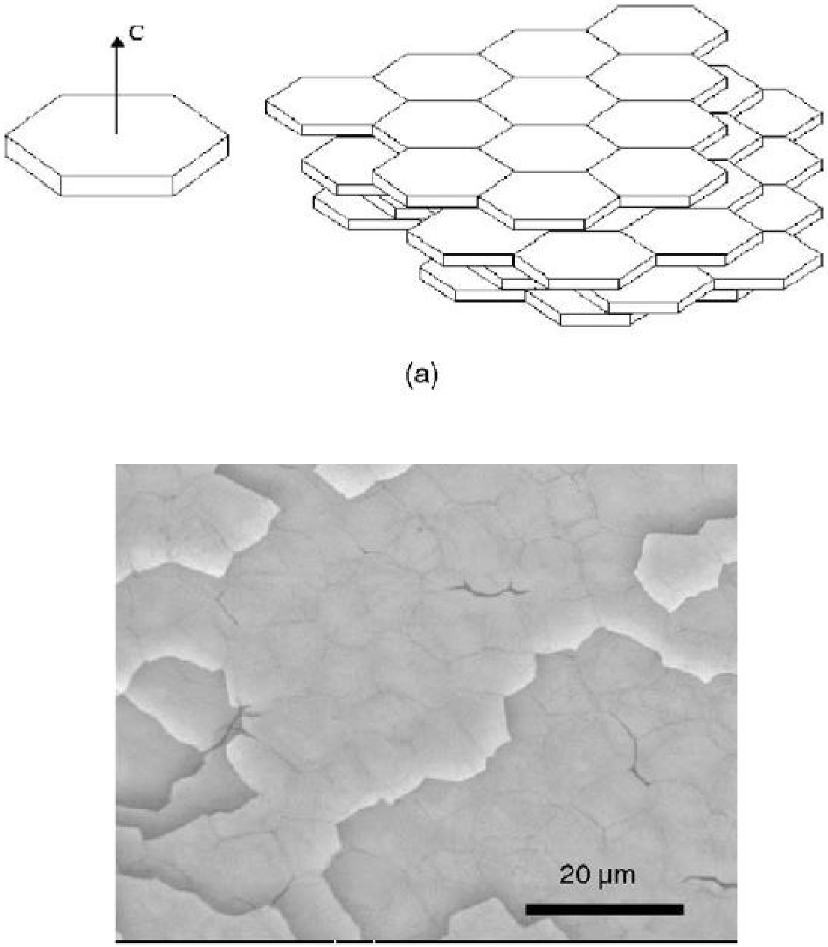

(a)

(b)

Figure 4-2: Depiction of abalone hexagonal tile arrangement a) schematic representation b) back scattered SEM image of hexagonal tiles on inner surface of shell. Reproduced from ref. (49).

Tile size appears to be independent of abalone shell size (age). No matter what the age of the shell is, the tiles have a consistent size. According to Lin and Meyers, shell lengths of 100 mm and 200 mm showed a consistent tile size of 0.5 µm thickness and 10 µm diameter (49).

Along with tile arrangement, an explanation is needed regarding the adhesive protein glue that is intertwined in the layers. The protein structure of the glue will be discussed in further detail in the following section.

4.2 Abalone nacre protein layer

There are over 30 functional proteins present in the abalone nacre (54). They vary in function from growing new layers of material, crystal organization, biomineralization, and molecular binding, but the protein responsible for impact resistance is Lustrin A (55). To understand how this protein layer contributes to impact protection, a review of the biochemical aspects of the Lustrin A protein will be performed in this section.

Lustrin A has been identified as a multi-domain protein in the thin organic “adhesive” layer between the aragonite tiles, responsible for impact resistance (49, 56). It is the first protein isolated from the nacreous material of the red abalone shell (55), and performs many functions. One function involves acting as a “molecular shock absorber” (57). The molecular shock absorbing qualities is due to the repetitive-domain sequence architecture: cysteine-rich and large glycine-serine residue rich domains.

The functional roles that Lustrin A plays can be determined based on how the protein is shaped (or folded). In Figure 4-3, the amino acid sequences for Lustrin A is shown for each individual domain of importance. Several repeat domains are present and are numbered C1-C10 and P1-P8 in Figure 4-3a and Figure 4-3b. The C domains are rich in cysteines (cys), and the P regions are rich in prolines (pro). The “GS” domain, shown in Figure 4-3a and Figure 4-3b, is called the glycine (gly)-serine (ser) rich domain. A number of other domains are included in the structure but are omitted in Figure 4-3; they don’t pertain to impact resistance. The deduced protein sequence, in Figure 4-3, identifies a highly modular protein structure with a large proportion of ser (16%), pro (14%), gly (13%) and cys (9%) (55). Individual amino acid structures, letters, and acronyms can be found in Appendix C.

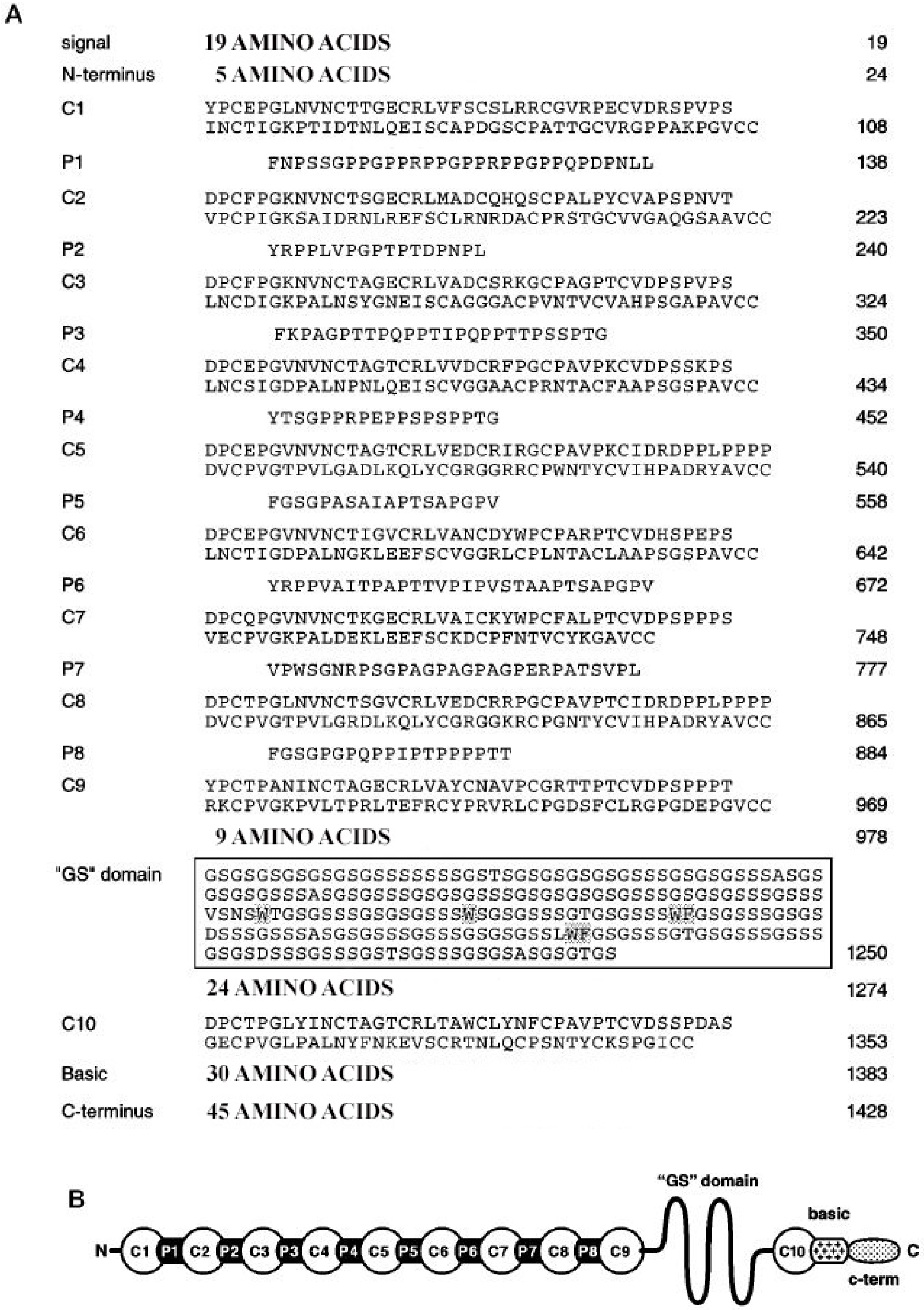

signal	**19 AMINO ACIDS**	19
N-terminus	**5 AMINO ACIDS**	24
C1	YPCEPGLNVNCTTGECRLVFSCSLRRCGVRPECVDRSPVPS INCTIGKPTIDTNLQEISCAPDGSCPATTGCVRGPPAKPGVCC	108
P1	FNPSSGPPGPPRPPGPPRPPGPPQPDPNLL	138
C2	DPCFPGKNVNCTSGECRLMADCQHQSCPALPYCVAPSPNVT VPCPIGKSAIDRNLREFSCLRNRDACPRSTGCVVGAQGSAAVCC	223
P2	YRPPLVPGPTPTDPNPL	240
C3	DPCFPGKNVNCTAGECRLVADCSRKGCPAGPTCVDPSPVPS LNCDIGKPALNSYGNEISCAGGGACPVNTVCVAHPSGAPAVCC	324
P3	FKPAGPTTPQPPTIPQPPTTPSSPTG	350
C4	DPCEPGVNVNCTAGTCRLVVDCRFPGCPAVPKCVDPSSKPS LNCSIGDPALNPNLQEISCVGGAACPRNTACFAAPSGSPAVCC	434
P4	YTSGPPRPEPPSPSPPTG	452
C5	DPCEPGVNVNCTAGTCRLVEDCRIRGCPAVPKCIDRDPPLPPPP DVCPVGTPVLGADLKQLYCGRGGRRCPWNTYCVIHPADRYAVCC	540
P5	FGSGPASAIAPTSAPGPV	558
C6	DPCEPGVNVNCTIGVCRLVANCDYWPCPARPTCVDHSPEPS LNCTIGDPALNGKLEEFSCVGGRLCPLNTACLAAPSGSPAVCC	642
P6	YRPPVAITPAPTTVPIPVSTAAPTSAPGPV	672
C7	DPCQPGVNVNCTKGECRLVAICKYWPCFALPTCVDPSPPPS VECPVGKPALDEKLEEFSCKDCPFNTVCYKGAVCC	748
P7	VPWSGNRPSGPAGPAGPAGPERPATSVPL	777
C8	DPCTPGLNVNCTSGVCRLVEDCRRPGCPAVPTCIDRDPPLPPPP DVCPVGTPVLGRDLKQLYCGRGGKRCPGNTYCVIHPADRYAVCC	865
P8	FGSGPGPQPPIPTPPPPTT	884
C9	YPCTPANINCTAGECRLVAYCNAVPCGRTTPTCVDPSPPPT RKCPVGKPVLTPRLTEFRCYPRVRLCPGDSFCLRGPGDEPGVCC	969
	9 AMINO ACIDS	978
"GS" domain	GSGSGSGSGSGSGSSSSSSSGSTSGSGSGSGSGSSSGSGSGSSSASGS GSGSGSSSASGSGSSSGSGSGSSSGSGSGSGSGSSSGSGSGSSSGSSS VSNSWTGSGSSSGSGSGSSSWSGSGSSSGTGSGSSSWFGSGSSSGSGS DSSSGSSSASGSGSSSGSSSGSGSGSSLWFGSGSSSGTGSGSSSGSSS GSGSDSSSGSSSGSTSGSSSGSGSASGSGTGS	1250
	24 AMINO ACIDS	1274
C10	DPCTPGLYINCTAGTCRLTAWCLYNFCPAVPTCVDSSPDAS GECPVGLPALNYFNKEVSCRTNLQCPSNTYCKSPGICC	1353
Basic	**30 AMINO ACIDS**	1383
C-terminus	**45 AMINO ACIDS**	1428

Figure 4-3: Lustrin A protein sequence: a) amino acid sequences of interest split out by domains and b) Lustrin A schematic of domain morphology. Reproduced from ref. (55).

Secondary structures can be ascertained by examination of the amino acids present in the different domains of Lustrin A. There are 10 cys rich repeats in Lustrin A. The high degree of sequence similarity in the ten C domains suggest they all undergo similar types of folding, while the prevalence of cys suggest a globular structure stabilized by disulfide bonding (55). Disulfide bonding is a covalent bond that occurs between the sulfur elements found in the cys amino acids. Pro is present in the cys-rich repeat domains, which is disruptive for alpha (α) helix and beta (β) sheet formation (55). The α-helix and β-sheet are common secondary structures that are present in many proteins. The α-helix is a common secondary structure for molecular binding functions (58). The β-sheets consist of strands connected laterally by at least two or three backbone hydrogen bonds, forming a pleated sheet in an extended conformation. Due to the extended backbone conformation, β-sheets resist stretching (59). A globular structure capable of stretching dominates the protein shape and is important for elastic response.

The gly-ser rich region is the largest single domain present in Lustrin A. It has repeating segments of gly-ser (GS) and gly-ser-ser-ser (GSSS). This domain consists of a significant prevalence of “β-turns.” These turns formed by the repeating segments, shown in Figure 4-4, result in a high degree of flexibility (55). The aromatic residues (phenylalanine, tyrosine and tryptophan) cause stacking behavior that forces phenyl ring (6 carbon atoms) alignment. This stacking behavior creates a forced loop in these regions. Phenyl rings have weak interactions, which allow the loops to behave like springs when a stretching force is applied (55).

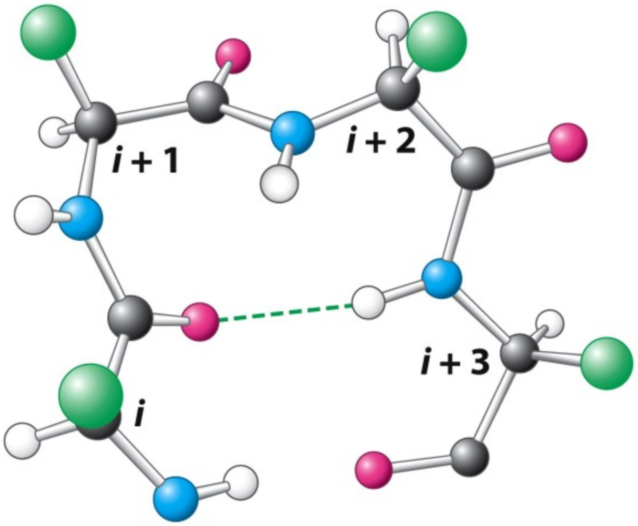

Figure 4-4: β-turn representation with the CO group of residue (i) hydrogen bonded to the NH group of residue (i+3). Reproduced from ref. (60).

A few amino acid interactions and protein secondary structures were just introduced. Lustrin A was shown to be a stretchy elastic protein that functions as a "shock absorber." The potential applications of this protein behavior may be studied in man-made materials and have garnered interest in the field of biomimetics.

4.3 Abalone biomimetics

Biomemetics is an emerging field in materials science and biology that attempts to utilize lessons learned from nature to design composite materials that can achieve certain material behaviors (53). The lessons from nacre are a source of inspiration for new materials and structures, such as biomimetic coatings, thin films, paper and other composite materials (50). Biomimetic materials attempt to mimic nacre in several ways: through material layout (lamination, brick and mortar arrangement, 5% organic versus 95% inorganic) and through the control of the interfacial properties between layers (50).

Artificial materials are often utilized because they can be synthesized with much stronger materials. The ratio of toughness to material size seen in nacre has been difficult to duplicate in synthetic materials (61).

Many efforts have been made to mimic nacre using inorganic tiles (clay), aluminum oxide (Al_2O_3), polymers such as polyvinyl alcohol (PVA), chitosan, and poly methyl methacrylate (PMMA) (62). The weaker inner layers mainly include the plastic resins, graphite, boron nitride, and porous ceramic layers (61). Other material types include alumina, zirconia, alumina/aluminum titanate, mullite/alumina, silicon carbide, silicon nitride, and silicon carbide/carbon (61). It was ascertained that materials that were too strong and too thick were a detriment to the toughness of the overall composite, due to a lack of crack divergence (61).

Sarikaya and Aksay produced a laminated structure of Al-B_4C, inspired by nacre, that was 5 times stronger than monolithic B_4C due to the utilization of a highly organized microstructure (63). By using the tiling layout in their composite to mimic nacre they were able to achieve better material properties. This same "brick and mortar" principle will be experimentally discussed in Section 4.5.3.

Thin films have been developed by Podsiadlo et al. and Walther et al. (64, 65) that demonstrate strong flexible behavior, using $Na^{\pm}$montmorillonite clay nanosheets (MTM) and both poly vinyl alcohol (PVA) and poly diallyldimethylammonium (PDDA) (50). PMMA tiles were created with multiple layers and columns mimicking the tile organization in nacre, shown in Figure 4-5 (50). These PMMA tiles were designed by relaxing the size scale requirements and using a millimeter scale versus the micrometer size seen in abalone (66).

The material closest to representing the impact response of nacre is alumina/PMMA developed by Munch et al. (67), Espinosa et al. (68), and Barthelat et al. (66). This material showed excellent toughness (3X abalone). The aluminum oxide is hard and brittle whereas the PMMA resembles the organic softer material, promoting sliding and stress release during impact (69). It maintained an 80% aluminum oxide and 20% PMMA ratio (as opposed to abalone's 95% inorganic and 5% organic ratio), with toughness being 300 times more than the constituent parts (66). While toughness was increased, the sliding mechanisms were not replicated successfully.

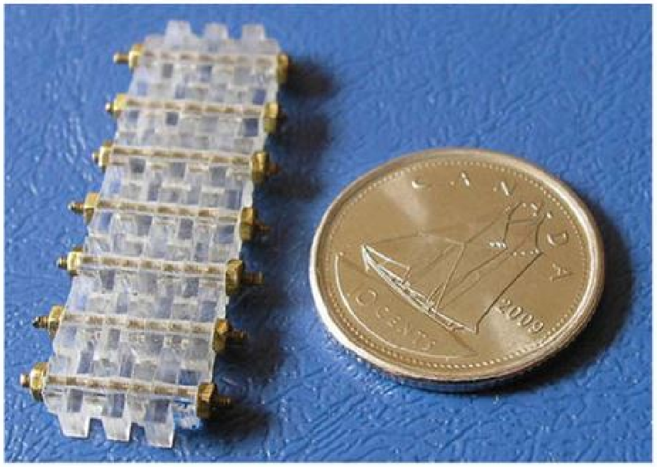

Figure 4-5: PMMA composite, mimicking nacre tile locking, after assembly. Reproduced from ref. (50).

The above examples have shown promise for impact resistant applications. This research utilized two of the major biomimetic concepts to study and investigate protection designs that could be implemented in fragmentation containment of brittle transformer bushings: the macro-structural tile arrangement and the adhesive "protein" glue.

4.4 Experimental materials and methods

4.4.1 Abalone characterization

Medium (2-3”) and large (4-7”) red and green unpolished abalone shells were purchased from the California Seashell company in bulk, in August 2015. Larger shells (7-10”) were borrowed from Monterey Abalone Company. An example of a loaner abalone shell is shown in Figure 4-6.

Figure 4-6: Loaner large red shell from Monterey Abalone Company.

The morphological surface conditions of an abalone shell were analyzed using a JEOL model JSM 5800 LV SEM with accelerating voltage of 10kV. Pieces of abalone shell were cut into 15 mm semi-squares. Before examination, each sample was fractured and mounted on SEM sample holders with double-stick carbon tape. Cross sectional samples were then coated with approximately 30 angstroms film of carbon using a Denton Vacuum, Inc. Desk II Cold Sputter Unit.

Surface areas of abalone shells were determined using photogrammetry and point cloud modeling. A SONY mirrorless SLR camera with sensor size 35.9 x 24 mm and pixel image size 7260 x 4912 with a 35 mm lens was used to capture images of each shell. Specimens were placed on black felt with two 200W bulbs hung 2 feet above the specimens. The camera settings used were f-stop = 7.1, shutter speed = 1/160 and ISO=800. Two scale bar rulers were used for each specimen for proper scaling in the modeling software. After images were captured Agisoft PhotoScan was used to generate the point cloud models. Agisoft PhotoScan performed error reduction, model building and surface area measurements. Figure 4-7 and Figure 4-8 show dense point cloud models of two respective green and red shells. After modeling and obtaining surface areas for each shell, growth pattern results were determined.

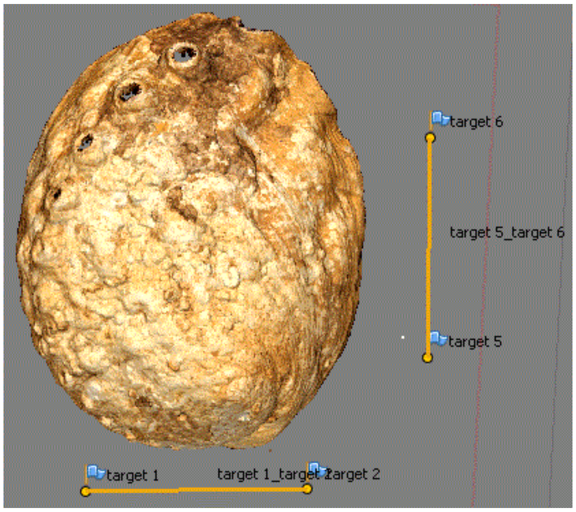

Figure 4-7: Photogrammetry dense point cloud model of large red shell with scale markers.

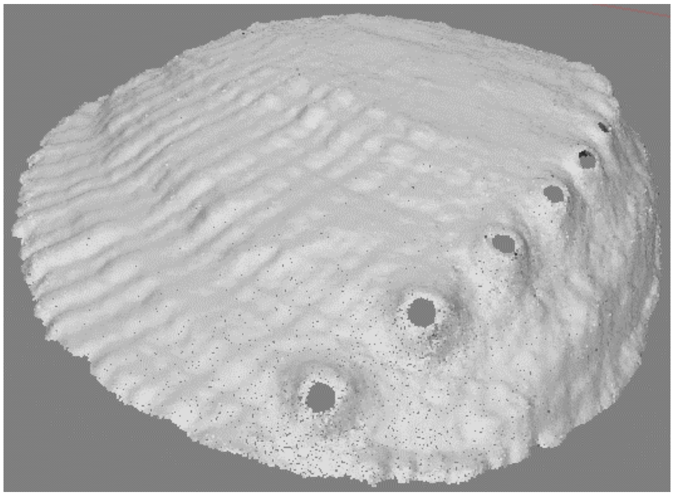

Figure 4-8: Photogrammetry dense point cloud greyscale model of small green shell.

To determine the density of each shell a modified procedure and equations were used from ASTM C127 (70), using the set-up in Figure 4-9. This method was chosen because the shells are considered a coarser arrangement in structure than a ceramic, requiring delineation of air voids. The final density value obtained is defined in the standard as the mass per unit volume of the impermeable portion of the sample.

Figure 4-9: Density determination set-up, USBR Geotech lab.

4.4.2 Abalone hydration

One aspect of the abalone that is discussed in the literature is the protein layer, which contributes to the impact resistance. In this section the importance of the protein layer is elucidated for low- and high-velocity impact using multiaxial and air gun tests. In dead and live abalone, the effect of hydration was studied.

For Multiaxial and Ballistic testing, saturated and oven-dried red abalone shells were purchased in bulk from California Seashell Company. Oven-dried samples were dried at 60°C for 96 hours prior to testing, and the saturated shells were soaked in distilled water for seven days prior to testing. Live red abalone shells were shipped directly from Monterey Abalone Company in California via overnight shipment on ice. The abalone remained sedated on ice until testing 36 hours after shipment. The live shells had their muscle removed from the shell immediately preceding testing.

Multiaxial impact testing was performed by Element labs in New Berlin, Wisconsin, using the falling dart method in accordance with ASTM D 3763 (71). For this method, a plunger with a steel rod was used. Force, time, and deflection was recorded using a load cell incorporated within the tip of the steel rod. The steel rod impacted all specimens at 3.3 m/s. From this data, the energy absorbed by the sample during the impact and through failure was determined. The energy at 50% of the peak force is considered the energy absorbed and was normalized by shell thickness in mm.

The ballistic air gun testing set-up shown in Figure 4-10, consisted of the same air gun and pellets discussed in Chapter 3.1.1.1. The target fixture, a custom-made wood frame with a cutaway to allow passage of the projectile mounted on top of a lab jack, shown in Figure 4-11, was used to hold the shells. It was located 0.76 m (2.5 ft) from the muzzle.

Figure 4-10: Abalone testing ballistic set-up.

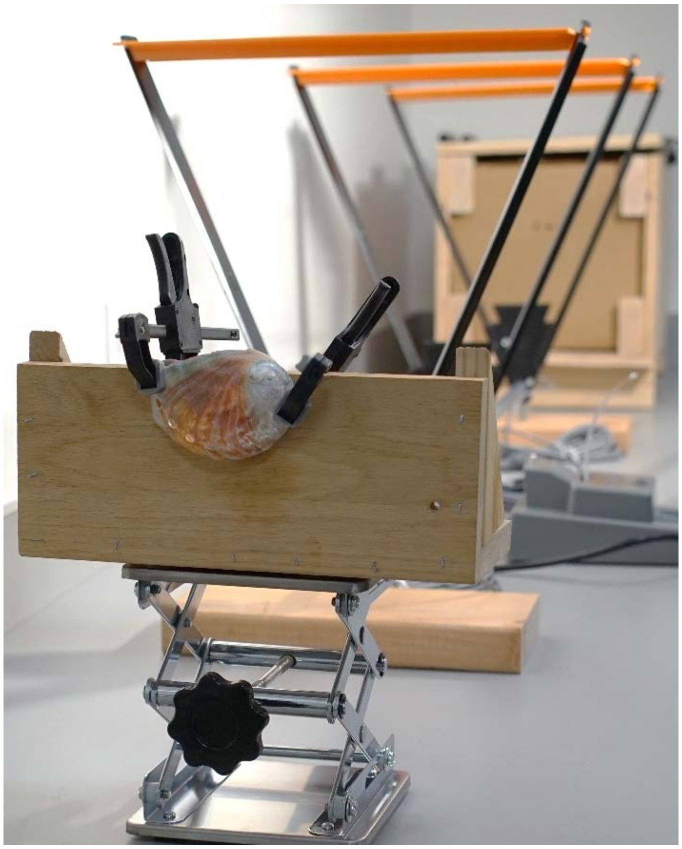

Figure 4-11: Abalone shell target fixture.

Downrange from the target fixture was an Oehler Model 35P ballistic chronograph located at 1.67 m (4.5 ft) from the muzzle of the air gun. This chronograph had three photodetectors at the base of three triangular gates. The gates are spaced with 0.61 m (2 ft) between each of the gates for a total length of 1.22 m (4 ft). The photodetectors detect the passage of the pellet through a gate as a slight drop in light. The chronograph was designed for use in sunlight, so supplemental lighting was provided by a light stand with two 300 W incandescent bulbs.

The final downrange structure was a bullet recovery box. This custom-made box was 0.72 m (2.37 ft) long and decelerated the projectile. Water-soaked paper was used in the box to slow down and stop the pellet. The mass of the lead pellet was recorded before and after testing.

Post-impact damage to the shells and pellets were examined using an Olympus BX51M optical microscope (OM). SEM images were taken of post-impacted shells using the same method presented in Section 4.4.1.

4.4.3 Brick and mortar structure

Square plate samples of borosilicate glass were fabricated by Allen Scientific Glass. Each sample had a measurement per side of 10.16 cm (4”) and a thickness of 0.635 cm (0.25”). Before drop weight testing, the samples were covered with different combinations of tiles and adhesives, according to the rubric presented in Table 4-1. Tiles were 0.32 cm (1/8”) thick and cut into three different sizes used for assembly: 2.5 x 2.5 cm, 5 x 5 cm, and 2.5 x 5 cm (1” x 1”, 2” x 2”, and 1” by 2”). The tiles were assembled according to the layout shown in Figure 4-12. A brittle and ductile material was chosen for this research: glass and PVC. The adhesives used to adhere the respective tile layers was Fibre Glast System 1000 Epoxy resin and GE Silicone 2+ caulk.

Protective Tile Material	Adhesive	Layering Scheme
PVC	Epoxy	1 layer 3 layer 5 layer
	Silicone	1 layer 3 layer 5 layer
	No Adhesive	1 layer 3 layer 5 layer
Glass	Epoxy	1 layer 3 layer 5 layer
	Silicone	1 layer 3 layer 5 layer
	No Adhesive	1 layer 3 layer 5 layer

Table 4-1: Sample testing rubric.

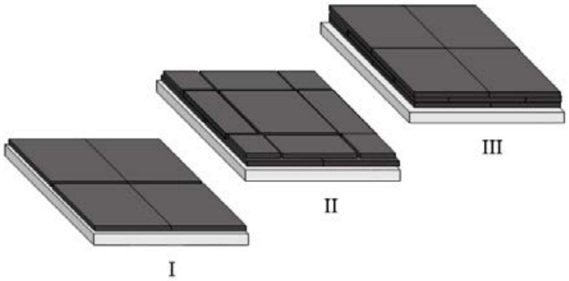

Figure 4-12: Tile layering scheme for drop weight testing. Repeat pattern.

A Gardner impact tester, catalog number TR 1120, was used to test each square plate sample following a modified ASTM D2794 (72), with a drop weight of 3.6 kg (7.9 lbs), and an indenter pin weight of 0.15 kg (0.33 lbs). All protected samples were tested to a maximum drop height of 1.02 m (40”) with the protected side facing the indenter pin. The potential energies (PE) tested ranged from 0.87 to 34.6 J. Figure 4-13 depicts the testing set-up for every protection method tested.

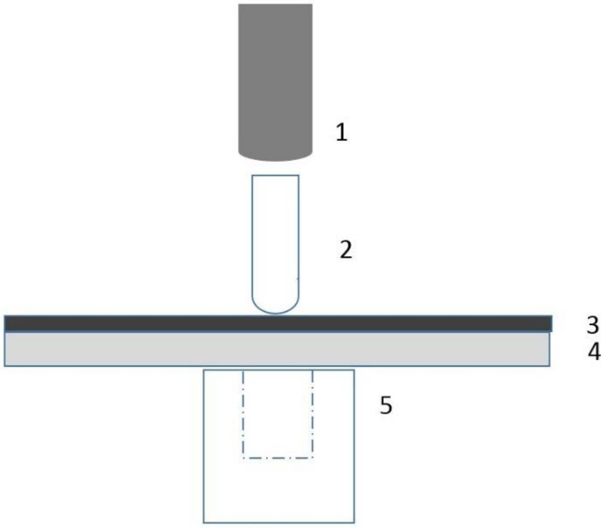

Figure 4-13: Drop weight testing set-up for the samples: 1) drop weight with accelerometer attached, 2) indenter pin, 3) protective material, 4) glass plate sample, and 5) cylindrical die.

To compare testing results, normalization by thickness was used. The total thickness for tile and adhesive (resin) samples is the protection material thickness, T, of the tile and the resin added together, using Equation (9).

$$T_{TOTAL} = T_{Tiles} + T_{resin} \tag{9}$$

The average no-failure energy was determined for each tile and adhesive combination at each thickness and compared. The average no-failure energy was found by taking the average of the impact energies from the first sample that broke and the un-broken sample immediately preceding the break.

4.4.4 Abalone composites

Abalone composites were constructed in this experiment. Abalone was purchased in bulk from the California Seashell Company. The composites used two different materials: similar sized pieces of red abalone broken by a hammer, and epoxy resin. The abalone pieces were obtained from the top portion of the shells and organized inside a clay 23 cm x 23 cm (9” x 9”) mold utilizing a four-layer brick and mortar stacking arrangement. Figure 4-14 demonstrates a basic two-layer stacking arrangement and shows the complexity imposed when dealing with non-uniform shapes. The matrix used in this composite was Fibre Glast System 1000 Epoxy, with a mixing ratio of 5:1 parts by volume of epoxy resin to hardener, according to the manufacturer’s instructions.

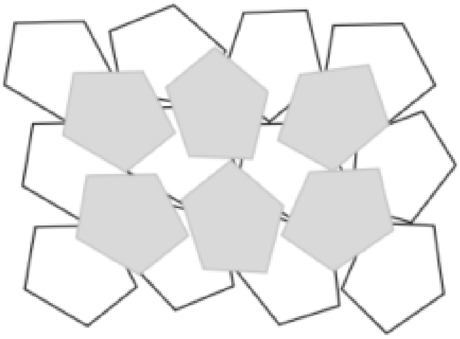

Figure 4-14: Representative stacking arrangement of abalone shell fragments.

Vacuum bagging was chosen as the manufacturing method of choice for the abalone composites, using a 1/8 HP GAST vacuum pump, model DOA-P704-AA, with a maximum pressure of 414 kPa (60 psi). The following steps were used during the manufacturing process: a clay mold was formed into a 23 cm x 23 cm square, fragments were arranged in a four-layer brick and mortar arrangement following Figure 4-14, epoxy was added slowly until it covered the top of all the fragments, a pink release fabric layer was placed on top, breather fabric was layered on top of the release fabric, a vacuum bag with an attached suction hose was sealed around the clay mold with sealant tape, and the composite was suctioned for 30 minutes until the breather fabric was saturated. Figure 4-15 shows some of the steps in process. After curing for 24 hours, the clay mold was peeled off and the surface of the composite was sanded to remove residue. The bottom right of Figure 4-15 shows the resulting 10 cm x 10 cm (4” x 4”) sample. Weight fraction of shells were determined for each sample by measuring the mass before and after the resin was added to the abalone fragments.

Figure 4-15: Vacuum bagging of abalone composites.

Oregon Ballistic Laboratories conducted ballistic limit testing on the composites. Each sample was tested in accordance with MIL-STD-662F (73) in an indoor range with the muzzle of the test barrel mounted 2.5 m (8 feet) away from the target. Samples were mounted as shown in Figure 4-16. A laser intervalometer, in conjunction with a time-based frequency counter, was positioned such that projectile velocity was measured 1.3 m (4 feet) from the target. A 2 grain (gr.) RCC and a 17gr. fragment stimulating projectile (FSP) was used, with powder weights ranging from 1.7 grams to 13.3 grams depending on the projectile velocity needed.

Figure 4-16: Oregon Ballistics test set-up for vacuum bagged abalone composite. Front view (left) and back view (right).

4.5 Experimental results and discussion

4.5.1 Abalone characterization

Experiments were performed to examine the tile microstructure inside the nacre and characterize optimal abalone types (red or green) for impact protection. Testing included scanning electron microscopy (SEM), growth pattern identification using photogrammetry and density characterization for different sizes of abalone.

SEM images of a red abalone shell confirmed what is discussed in Section 4.1. The 'brick and mortar' pattern is easily identifiable in Figure 4-17 of a) full side scan at 500µm, b) brick layering scheme at 10 µm, and c) hexagonal tile stacking at 10 µm.

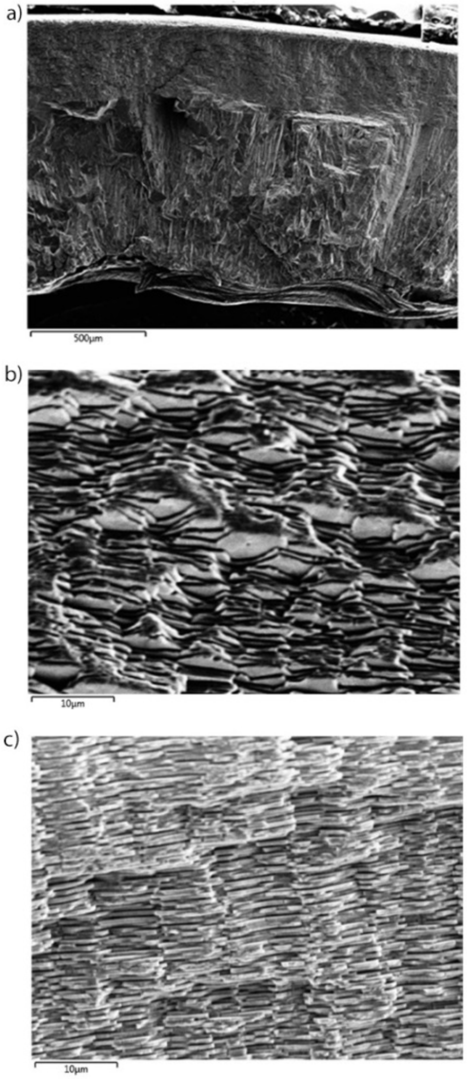

Figure 4-17: Scanning electron micrographs of abalone shell microstructure.

In Figure 4-18, both the green and red abalones show a linear growth pattern as they increase in mass. The green abalone showed a higher size increase as it aged. This conclusion was supported in the literature. The thickness of the mesolayers of the abalone were consistent with an annual pattern of growth arrest, which is similar to the examination of tree rings (49). Lapota et al. reported growth rates for both red and green abalone with seasonal variations: 36 mm/yr for red and 60 mm/yr for green (74). The reported growth rates are consistent with the mass versus surface area results in Figure 4-18, which indicates faster growth for green abalone.

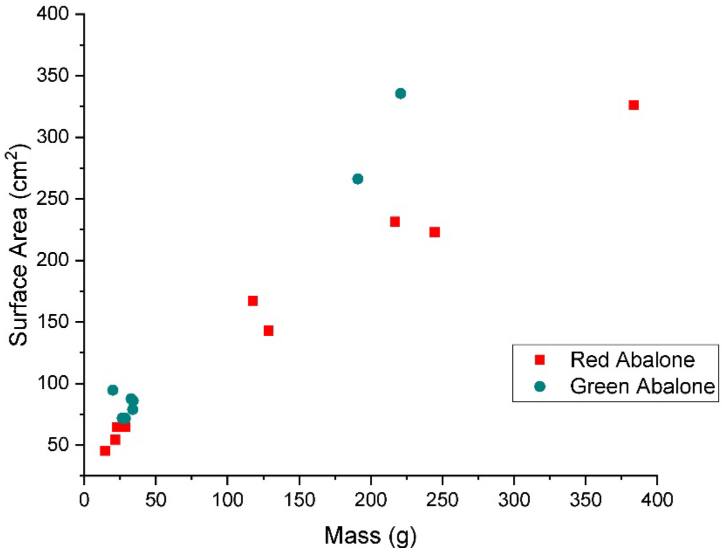

Figure 4-18: Growth pattern of red and green abalone.

The results shown in Figure 4-19 indicate that red abalone tends to maintain a fairly constant density as it ages, whereas the green abalone drops off significantly. The drop off would be indicated by a higher porosity of the shell. While the red abalone does start to decline in density initially it is a small relative decline as compared to the green abalone and eventually maintains a constant density. This is highly indicative of the reasons green abalone are not used for impact research in the literature, as compared to the red variety. Subsequent testing in this research uses only the red abalone shells.

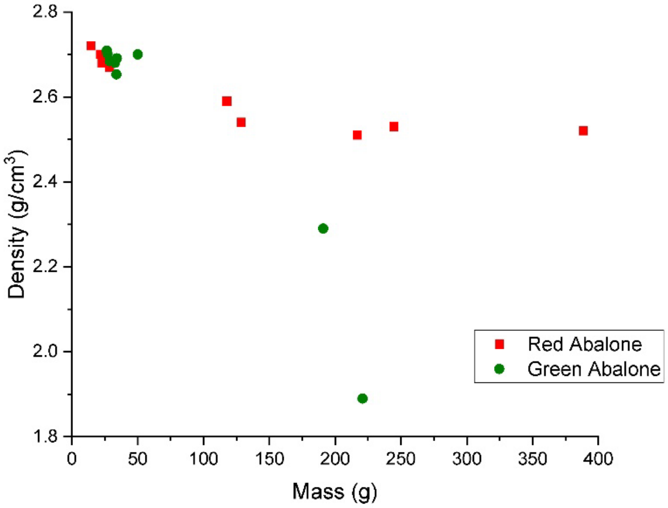

Figure 4-19: Density of red and green abalone.

4.5.2 Abalone hydration

Testing by Sun et al. demonstrated that dry nacre behaved like a monolithic ceramic and experienced brittle failure. The hydrated nacre, on the other hand, showed linear elastic behavior (50). While dry nacre exhibited brittle behavior, hydrated nacre exhibited soft rubbery ductile behavior and larger deformations before failure (48, 75).

In biological systems, proteins degrade once an organism dies. It was discussed in Section 4.2, that the Lustrin A protein plays a vital role in impact resistance. Between the ballistic air gun and the multiaxial falling dart test discussed in this section it is shown that the lower the strain rate, the more important a role hydration plays. At ballistic impact velocities hydration had little effect.

The multiaxial test impacted the shells at a fraction of the energy of the ballistic air gun tests. Results showed that oven-dried shells had an average energy at 50% of the peak force of 0.12 J ± 0.06 J and an average peak force of 360 N ± 20 N. Water-soaked shells had an average energy at 50% of the peak force of 0.39 J ± 0.14 J and an average peak force of 520 N ± 140 N. Live shells had an average energy at 50% of the peak force of 2.68 J ± 0.70 J and an average peak force of 1,900 N ± 310 N. After normalization for thickness of the shells a plot of the energy absorbed per unit thickness was assembled for all tested shells in their various states of hydration, shown in Figure 4-20. These results demonstrated that energy absorption increased as the hydration level went up. The live shells have the largest energy absorption before failure and as discussed earlier, this is due to the intact protein layer. The saturated shells showed an increase in energy absorption compared to oven-dried shells. Hydration helps increase the energy absorption capabilities of dead protein.

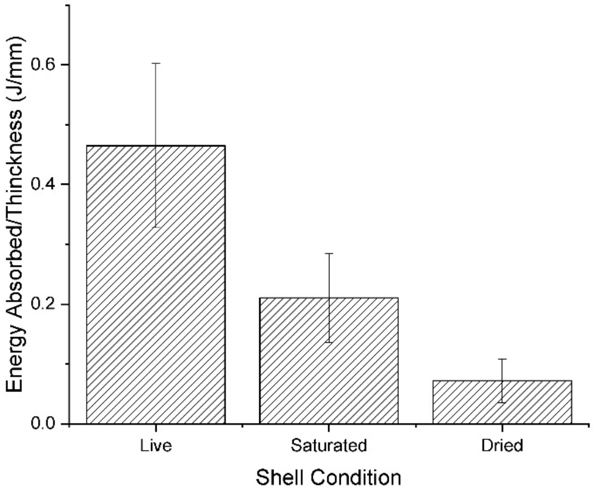

Figure 4-20: Abalone multiaxial impact test for various stages of hydration.

Ballistic air gun testing was performed on abalone in the same states of hydration as the multiaxial testing. The Energy absorbed (E_a), in Equation (10), was determined to be the change in kinetic energy of the pellet measured by the chronographs.

$$E_a = \frac{1}{2} m_f v_f^2 - \frac{1}{2} m_o v_o^2 \tag{10}$$

Where m_f and v_f represent the final mass and velocity of the pellet after exiting the abalone shell, and m_o and v_o represent the initial mass and velocity before entering the abalone shell.

Because the shells had different thicknesses, the kinetic energy was normalized per unit thickness in millimeters. It is demonstrated in Figure 4-21 that the change in kinetic energy between the live, hydrated, and dried shells was slightly elevated for the live shell. Under ballistic air gun velocities, the hydration level did not significantly influence the change in kinetic energy between the live and oven-dried shells.

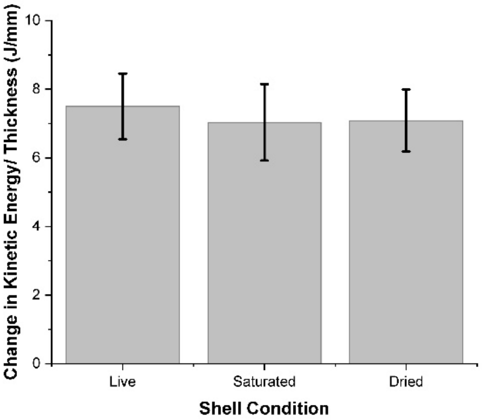

Figure 4-21: Kinetic energy dissipation of live, saturated and dried abalone shells.

Based on SEM images, shell failure and pellet deformation showed small differences between the live and dead abalone shells. In Figure 4-22, visual ballistic damage results of live versus dried abalone shells are shown: a) ballistic blowout model of live shell (with arrow representing the incoming pellet), b) interior view of live shell, c) exterior view of live shell, d) SEM view of live shell blowout at 1 mm, e) SEM view of live shell blowout at 500 µm, f) ballistic blowout model of dried shell (with arrow representing the incoming pellet), g) interior view of dried shell, h) exterior view of dried shell, i) SEM view of dried shell blowout at 1 mm, and j) SEM view of dried shell blowout at 250 µm. The differences in ballistic response between the live and dried shells were not readily apparent, except that the dried shell in Figure 4-22i shows more blow out along the interior of the shell as compared to the live shell in Figure 4-22d. Based on the visual imagery in Figure 4-22, the hydration response is minimal at air gun impact velocities.

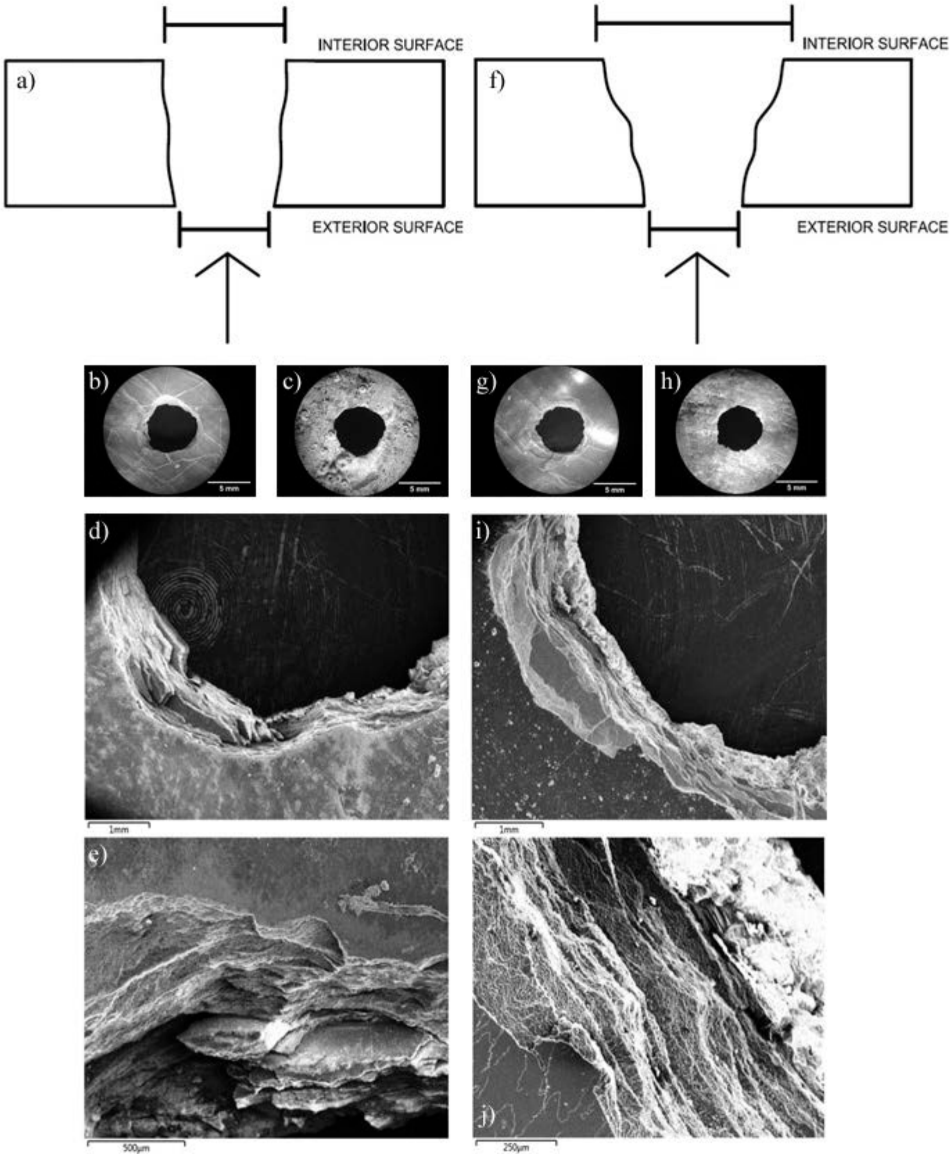

Figure 4-22: Visual ballistic damage results of post-impacted live versus dried abalone nacre shell.

Pellet responses, in Figure 4-23, show that the live abalone shell imparts the most damage to the pellet. The dried abalone shell is more brittle and easier to penetrate, so the pellet showed less deformation.

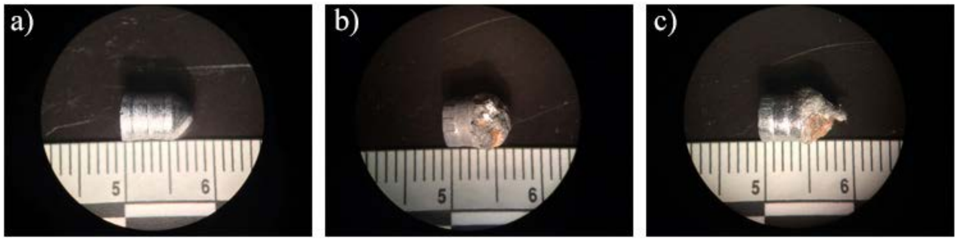

Figure 4-23: Pellet deformation responses: a) original undamaged (.22 caliber) 1.66 g pellet, b) live abalone impact and c) dried abalone impact.

The diameter of the holes left in the shells after impact was measured and a normalized plot of hole diameter per specimen thickness is shown in Figure 4-24. As the dead shell dries out the impacted hole diameter increased and produced more variability. The variability shown in Figure 4-24 is due to the inherent probabilistic behavior of brittle materials (76). Brittle materials tend to demonstrate a certain amount of randomness around failure (77, 78), especially in dynamic loading (79, 80). As a material moves from more ductile to more brittle, the variability increases.

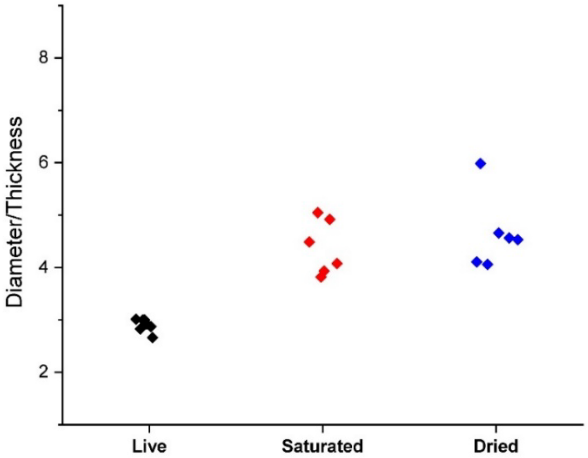

Figure 4-24: Normalized hole diameters after pellet penetration through live, saturated, and dried abalone shells.

More damage is imparted on the shell as it dries out, thus the hole diameters increase. The live shells have smaller hole diameters but essentially the same energy loss, which suggests that the energy absorption per fracture surface area is higher for the live shells. Some loss exists in fracture toughness of the shell after death when the larger fracture surfaces produce similar energy losses.

As the abalone dries out after death, the material takes on a more brittle ceramic quality. Although hydration helps, the protein vital to the elastic performance is no longer being renewed in the shell. Protein elasticity stops playing a role in the protective mechanism, but the brick and mortar microstructure is still intact. At ballistic air gun levels, the response of the shells in various states of hydration appears to be unaffected by the degradation of the protein. The next section experimentally examines the brick and mortar microstructure.

4.5.3 Brick and mortar structure

The living abalone animal is soft, and the transformer bushings are brittle. Thus, the goal of this section will discuss the brick and mortar microstructure arrangement on a base material of brittle glass. The brick and mortar arrangement are represented in this study using a combination of protective tile material and adhesive. Performance was examined based on the average no-failure energy (energy before failure) through drop weight testing.

Abalone nacre is suggested to be a model system for lightweight and high-impact composite design because of the micro structure, which creates a natural body armor

(81). Two critical aspects of the abalone that successfully contribute to impact resistance are the protein adhesive layer and the “brick and mortar” microstructure. In this section the combination of the two is evaluated by using the layering scheme found in Figure 4-12 using glass or PVC based tiles with Epoxy, Silicone or without adhesive for the mortar.

A brick arrangement of 50% overlap was chosen. It has been demonstrated by Gao that larger overlaps between tiles of at least 50% effectively provide energy dissipation during brick pull-out, which raises the toughness (82). Pro, et al. stated that an ideal microstructure will achieve toughness through perfectly overlapping stiff features that spread damage (83). The brick and mortar structures of nacre are responsible for their high toughness due to disparate material phases and overlapping stacking arrangements, which cause arrested crack propagation (84). Successful combinations of tile material and adhesive influence energy dissipation through rupture of the “brick” and adhesive interface (85).

In Figure 4-25, the results for the glass tiles demonstrate that the brittle glass “bricks” prefers a more ductile adhesive combination. The Combination with no adhesive performed the same as the combination with the brittle epoxy adhesive. In the latter two cases the energy dissipation mechanism only consisted of predominantly tile cracking. Tile sliding also dissipated energy for the condition without adhesive. The silicone performed the best because energy dissipation went towards the stretching and pulling of the ductile adhesive. This combination of brittle tile and ductile adhesive closely resembles what is seen in the abalone.

For the glass tile combinations, as the thickness increased in the tiles, the silicone adhesive increased the average no-failure energy significantly after 10 mm of combined tile and adhesive thickness. A failed sample for the silicone adhesive at five layers was not able to be determined using the range of impact energies allowed on the drop weight apparatus. Therefore, the average no-failure energy was set as the highest value possible on the drop weight for the sake of graphical visualization. Both the epoxy and no adhesive conditions increased at a slow and gradual rate with respect to thickness.

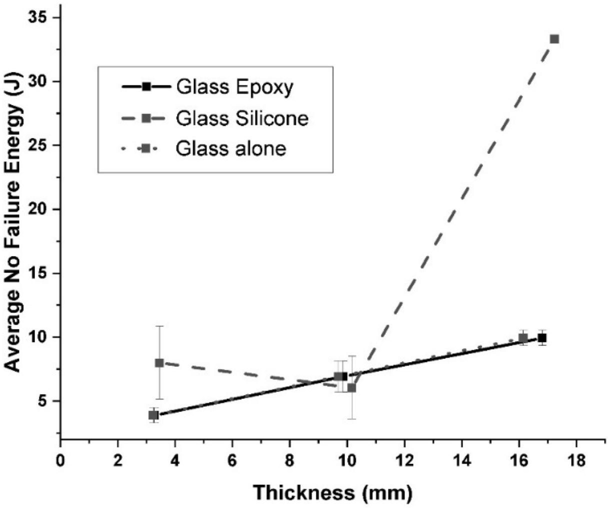

Figure 4-25: Critical energies of glass tiles with different adhesives.

In Figure 4-26, the ductile tiles were best paired with a brittle adhesive. In this scenario the ductile tiles are bending and elastically deforming, while the breaking and cracking occur at the epoxy interface. The PVC and epoxy performed the best. The PVC with the silicone and no adhesive seemed to interchange in their effectiveness at approximately 12 mm of combined tile and adhesive thickness. It is unclear why the 15 mm thick PVC without adhesive absorbed less energy than the 9 mm thick PVC without adhesive.

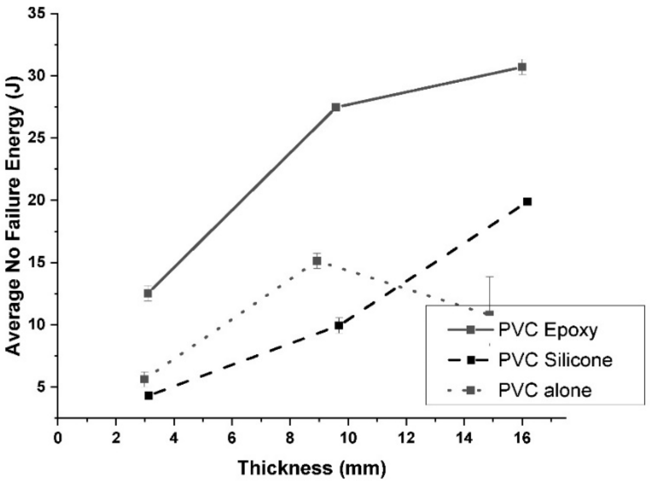

Figure 4-26: Critical energies of PVC tiles with different adhesives.

For “brick and mortar” arrangements it was discovered that a combination of a brittle and ductile constituents performed the best. For thinner layers the ductile tiles and brittle adhesive performed better. Once the layers reach a certain thickness (16 mm) the brittle tiles and ductile adhesive performed best. Modeling by Xie and Yao suggested the propagating direction of a crack ending at the interface could be controlled by the fracture strength of the brick and potentially the ductility of the mortar phase (86). But in this research, it became apparent that the thickness of the stacking arrangement could dictate performance.

Variability exists in our experimental drop weight results. The probabilistic nature of glass mentioned in Section 4.5.2, is a key factor in the scatter of the data. Pro et al. suggested that artificial versions of the abalone microscale displays variability in results because of defects, distributions in brick sizes and shape, and distributions in mortar properties from interface to interface (83). This could be caused by variable resin thicknesses, voids within the resin, and other anomalies.

For biomimetic applications, constituent materials can be used to utilize the “brick and mortar” structural arrangement with ductile tiles and a brittle adhesive for thinner samples or brittle tiles with ductile adhesive for thicker samples. Abalone cannot do this because of biomineralization, but man-made materials can utilize any combination necessary for the best performance.

4.5.4 Abalone composites

This section of our research will take the concepts discussed previously and utilize them by building a composite with abalone shells. The manufacturing method presented a unique process that addressed assumptions. The composites were tested for their ballistic limit and demonstrated the limitations behind using real shells instead of biomimetics.

Abalones have a composite “brick and mortar” layering scheme within their shells. To utilize their microscale structure at a macroscale level, several assumptions were made. The first assumption was that the thickness needed to be increased to achieve better impact resistance. To increase the thickness a macro-composite was designed using the same brick-like layering pattern with broken pieces of abalone shells. The second assumption was that an ordered brick layering pattern was necessary for the individual broken pieces as opposed to a random ordering. Larger pieces were assumed to be more advantageous, as this utilized the inherent structure of the individual pieces of shell.

With the curvature inherent in the shell it was difficult to have flat broken pieces. Therefore, when the curved pieces were stacked there was a larger amount of space between them. The curvature of the pieces made it difficult to obtain a large weight fraction of shells. The broken pieces had many different geometries, affecting how close they were in the arrangement of pieces.

The issue in creating tightly packed composites resulted in a maximum weight fraction of shells of 60% or less, as shown in Table 4-2. A typical composite performs better at higher volume fractions of fibers. The manufacturing difficulties with abalone composites make higher weight fractions difficult.

Composite	**Shot #**	**Wt % Shells**
E1A	1	56.8
E1B	2	56.8
E1C	3	56.8
E1D	4	56.8
E2A	5	57.5
E2B	6	57.5
E2C	7	57.5
E2D	8	57.5
E3A	9	55.7
E3C	10	55.7
E3D	11	55.7
E4D	12	59.7

Table 4-2: Weight fraction of shells for abalone composites.

Results for abalone composites show the ballistic limit (V50) of 1,329 m/s for a 2 gr. RCC projectile, which correlates to a KE of 114 J, as shown in Figure 4-27. In the 2 gr. RCC dataset, the open squares correlate with the samples that stopped the bullet from penetrating, and the V50 determination is based on the average of those two data points. The 17 gr. FSP bullets broke through every sample tested and the V50 could not be determined.

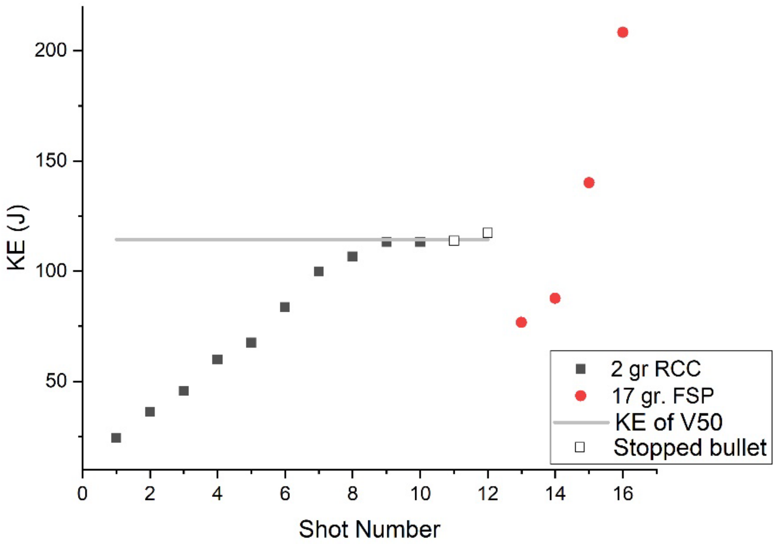

Figure 4-27: Ballistic limit kinetic energy results for abalone composites.

According to the results shown in Figure 4-27, the first NIJ classification category identified in Table B-2 of Appendix B was not reached. The mass of a 2 gr RCC bullet is not large enough to make the NIJ classification. These composites did not perform to standards to which most impact resistant materials are tested. Therefore, it was determined that pursuing abalone composites to utilize the inherent properties of the shell into a macroscale material was not feasible. It is best to remain with biomimetic concepts that mimic abalone.

4.6 Summary

Throughout this chapter various attributes of abalone were reviewed: the physical structure, protein layer, and biomimetic materials that mimic nacre. Several laboratory test results were also performed, identifying growth pattern characterizations, protein and hydration effects, brick and mortar micro-structure contributions and abalone composite design and performance.

Abalone characterization identified that red abalone is the most impact resistant variety because it maintained a constant density during biological growth, which explains why the literature shows results regarding impact protection of the red variety as opposed to the green variety. The protein layer found in abalone nacre was shown experimentally to be highly dependent on hydration. The protein layer predominantly protects the organism during low-velocity impacts. Ballistic tests with an air gun showed no major differences in abalone impact energy dissipation response at varying hydration levels; however, a decrease in hydration levels in the abalone showed less damage to the incoming lead pellet, an increase in the projectile hole diameters left on the shell, along with an increase in the amount of variability seen in post-impact analysis data.

The brick and mortar layering scheme found in abalone nacre demonstrated that a combination of brittle and ductile “bricks” and adhesive performed best for impact protection, as opposed to two brittle or two ductile combinations. The most optimum “brick and mortar” structural arrangement consist of using ductile tiles and a brittle adhesive for thinner samples up to 16 mm thick, and brittle tiles with a ductile adhesive for thicker samples.

Abalone composites were also experimentally designed and tested and did not perform according to NIJ classifications for the lowest energy class of materials, Class I. Theyare not recommended from a manufacturing standpoint for impact protection. It is apparent, through experimental testing, that the brick and mortar layering scheme and the protein elastic behavior is important for impact protection. The brick and mortar layering along with abalone composites are harder to implement on transformer bushings, therefore further research will not continue to examine these material options for impact protection. Instead, the research will examine an elastomeric coating that behaves similarly to the protein layer of abalone, in Chapter 5 - Chapter 8.

CHAPTER 5 CORRELATIVE DROP WEIGHT AND BALLISTIC TESTING OF AN ELASTOMERIC COATING

Polymeric coatings have been researched for use on porcelain bushings for contamination protection: room temperature vulcanizing (RTV) silicone rubber, greases, and petroleum jelly (87), but not for fragmentation mitigation. Such materials as RTV and ethylene vinyl acetate copolymer (EVA) have been examined for their performances under electrical load (87). Silicone rubber is also manufactured for use as a polymer bushing, not just as a coating. The surface of silicone rubber has excellent water repelling properties and can handle leakage current fairly well (88). Coatings for anti-fouling application have also been examined (89). While replacing porcelain bushings with composite counterparts is an option for many electrical utilities, there are many cases where it is not. The labor required to replace porcelain bushings currently in service is costly.

Polymer coatings have also been used for blast mitigation (90), but not on brittle glass materials. Research has been done on polyurea coatings for metal substrates (91-95) and polyurea coated ceramic tiles for impact resistance (96). Polyurea, which was a component of the coating used in this research, has been used in ballistic based applications due to its high toughness and glass transition temperature. The tough behavior is related to the strong intermolecular hydrogen bonds (97). High strain rate impacts can induce transitions of a rubbery polymer to a glassy state, but if the transition temperature remains below the ambient temperature then the polyurea can remain in its rubbery state; the hard- and soft- segment chain structures absorbs the impact energy (90, 94, 98). Polyurea's are formed from reactions of isocyanates with polyamines and have fast cure times making them relatively unaffected by temperature and humidity during application (91). In this chapter, a polymer coating was evaluated as a potential material option to contain fragments during the blast response seen in the bushing models under ballistic impact. It was assumed that if a polymeric coating was successful in containing fragments, then the risk associated with fragments damaging neighboring equipment or personnel could be potentially mitigated on full-scale bushings, in service.

The experimental testing methods presented in this chapter were developed to identify how the combined effect of the air gun and the internal pressure inside the cylinders resulted in a blast that could be absorbed by high-quality elastomeric coatings. Additional testing was performed using linear extrapolation from a non-instrumented drop weight approach to supplement the ballistic testing for a wider range of impact energies. A non-instrumented drop weight tester is simply a drop weight tester with no additional instrumentation (accelerometers, force sensors, velocity gates, etc.). The drop weight approach allowed for the implementation of a less expensive alternative to ballistic testing, could be done with a greater number of samples, and could be done in standard laboratory rooms as opposed to designated shooting areas. It allowed for material comparison and behavioral examination at smaller energies. However, high strain rates do change failure modes, which means direct comparisons cannot easily be made between static tests, high-strain rate tests at drop weight energies, and tests at ballistic energies.

5.1 Materials

Two types of glass samples were prepared for this research. For air gun and higher caliber ballistic testing, the same type of cylinders used in Chapter 3.1.1.1 were used. The cylinders were coated on the outside with a Line-X XS-100 coating. For the drop weight testing, square plate samples described in Chapter 4.4.3 were used. The square glass samples were coated with the same coating as the cylinders.

The coatings were applied at Line-X of Boulder, in Colorado. The coating was sprayed on using a Fusion Air-Purge gun with a Graco round mix chamber (AR4242) with a 1 mm (0.042 in) impingement port and an extension tip with orifice diameter of 1.52 mm (0.06 in). The spray technique was applied at 18.6 MPa (2700 psi) at 347 Kelvin (165 degrees Fahrenheit). The coating is a proprietary polyurethane/polyurea elastomeric coating with a flexibility of 91.2% at room temperature (99).

5.2 Testing set-up and methods

5.2.1 Air gun ballistic testing

The glass cylinders were set-up as described in Chapter 3.1.1.1. Two cylinders at each coating thickness of 1.43 mm (45 mil), 2.29 mm (90 mil), 3.05 mm (120 mil) and 6.10 mm (240 mil) were tested at a pressure of 207 kPa. The coated cylinders were weighed before and after testing to obtain a percentage of mass loss due to impact. The full assembly of a coated cylinder is shown in Figure 5-1a, with a more detailed image of the set-up along the base in Figure 5-1b. Figure 5-1c shows the bottom of the cylinder assembly before it is set on top of the pressure containment box. Scatter plots and best fits were generated for fragment confinement.

(a)

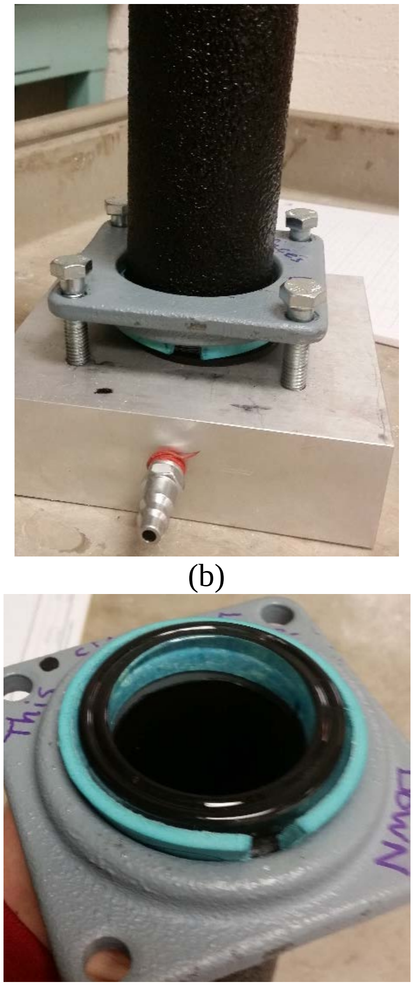

(b)

(c)

Figure 5-1: Set-up of coated cylinders.

5.2.2 Non-instrumented drop weight testing for linear extrapolations

Testing pressurized cylinders is time consuming and expensive. A simpler test method was developed using a drop weight on flat plates with an applied coating on the top surface. This method controlled the impact energy but was capped out at lower energies compared to the air gun tests. By using the drop weight tester, it could be determined at which energy levels the glass plates did not break under certain coating thicknesses.

The same impact tester that was used in Chapter 4.4.3, was used for this experiment. Six uncoated flat plate samples were impacted with a 0.907 kg (2 lbs) drop weight at a height range of 0.051 to 0.127 m (2” to 5”) to determine the breaking energy of the flat glass plates alone. The coated samples at 1.43, 2.29, 3.05 and 6.10 mm coating thickness were tested with drop weights of 1.814 kg (4 lbs) and 4.536 kg (10 lbs). All coated samples were tested at drop heights between 0.254 m (10”) and 1.016 m (40”) with the coated side facing the indenter. The potential energies for all tests ranged from 0.45 to 45.2 J.

All coated samples were weighed before and after drop weight testing to obtain their percentage mass loss. Any debris on the sample was removed prior to measuring the mass loss. Scatter plots and best fits were generated of the drop weight raw data and broken out into two parts: fragment confinement and the energy before failure occurs, also called the no-failure energy.

5.2.3 Ballistic testing at higher impact energies

Six additional 3 mm coated cylinders, using the same set-up as Section 5.2.1, were tested at Oregon Ballistic Laboratories, in Salem Oregon. All six cylinders were pressurized to 207 kPa (30 psi). Infrared velocity light screens, in conjunction with a time-based frequency counter, was used to measure projectile velocity. Different gun and bullet combinations, listed in Table 5-1, were used to ascertain coating efficiency at higher kinetic energy levels. All cylinders were weighed before and after testing to obtain a percentage mass loss due to impact.

Cartridge/Projectile	Muzzle Velocity (m/s)	Projectile Mass (g)	Kinetic Energy (J)
.22 Long rifle caliber, lead	360	2.6	168
Fragment simulating projectile (FSP)	610	1.1	205
.45 ACP* caliber, Speer total metal jacket (TMJ)	235	15	414
9x19 mm Luger, IMI‡ full metal jacket (FMJ)	372	7.5	519
9x19 mm Luger, full metal jacket (FMJ)	430	8.0	740
.40 Smith & Wesson (S&W) RHTǂ Speer	495	7.5	919

*Auto Colt Pistol (ACP), ‡Israel Military Industries (IMI), ǂ Reduced Hazard Training (RHT)

Table 5-1: Cartridges and projectiles used in coated borosilicate cylinder testing.

A scatter plot and best fit power curve was generated for mass loss of the cylinders. The scatter plot included data from the six cylinders tested at higher impact energies and two .22 caliber air gun test results from Section 5.3.1.

5.3 Results and discussion

5.3.1 Coating effectiveness for air gun impacted cylinders

The behavior of brittle HV bushings under combined pressure and high-velocity impact is of major concern for the integrity of the power grid. One mitigation strategy could be an elastomeric coating applied to the surface of the bushings, to prevent ejection of fragments into the surrounding area. Observations of the tested coated cylinders, modeling bushings, showed significant crack networks inside their walls. However, the fragments were still held together by the coating. The exception was a partial side rupture of a cylinder coated with a thickness of 1.43 mm (Figure 5-2). The majority of the fragments remained adhered to the coating despite the side rupture.

Figure 5-2: Side rupture of 1.43 mm thick coated cylinder.

For the thicker coated cylinders, a fine white powder was present inside the cylinders instead of much larger glass fragments. The mass loss was small in all tests (less than 4%), as shown in Figure 5-3, and was primarily the result of small pieces of glass and powder that were sloughed off the cylinders. It was observed that the smaller thicknesses of 1.43 mm and 2.29 mm were not as effective at keeping the pellet entrance and exit holes small. The smaller thicknesses showed significantly more damage, with the 1.43 mm thick cylinder being the worst (Figure 5-2), while keeping the cylinder fragments contained. When examining the percent mass loss versus coating thickness for the coated cylinders, an exponential fit was used (Figure 5-3). The equations used for the fit and the best fit parameters are shown in Table 5-2.

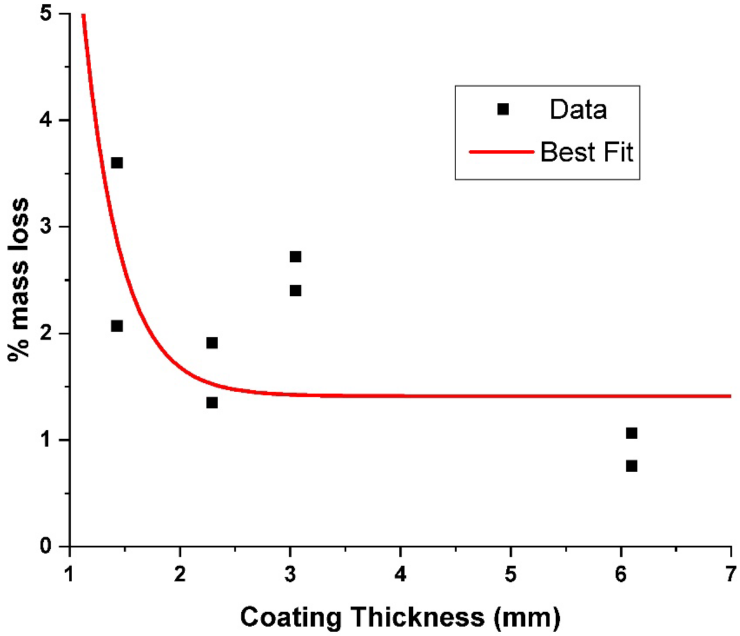

Figure 5-3: Measured mass loss at 95J for all coating thicknesses on glass cylinders.

BEST FIT OPTIONS for MASS LOSS of COATED CYLINDERS
Exponential $y = y_0 + Ae^{\frac{x_0-x}{t}}$
y_o 1.411 A 112.36 x_0 -0.044 t 0.339 R^2 0.998

Table 5-2: Best fit parameters for the data in Figure 5-3.

Based on the R^2 values, the exponential approximation was a good fit. The exponential fit becomes horizontally asymptotic at a mass loss of 1.41% at around 3.2 mm of coating thickness. This horizontal asymptote is a limitation of the fit. Experimentally, there is likely a thickness threshold in which no mass loss would occur. The fit also showed large increases in mass loss for thicknesses less than 1.25 mm of coating thickness. This was not experimentally tested, because obtaining very thin coating layers is not feasible.

If a criterion of 1.5% mass loss is assumed, then the exponential fit predicted that a coating thickness of about 2.35 mm is sufficient. Experimentally, confinement of between 1.35- 1.91% occurred at a thickness of 2.3 mm. Mass loss of between 0.75 – 1.06% was achieved for the 6.10 mm cylinder. For the purposes of our research, an optimal coating thickness of 3 mm was chosen, where the fit became horizontally asymptotic. Further testing at higher impact energy levels using a 3 mm thick coating on borosilicate cylinders is discussed in Section 5.3.3.

5.3.2 Mass loss examination of non-instrumented drop weight testing of borosilicate glass plates

Air gun tests resulted in significant damage to the glass cylinders underneath the coating and a no-failure energy was unable to be determined experimentally. Drop weight testing at lower impact velocities on flat plate samples was utilized to obtain the no-failure energies. In this section drop weight testing results are compared to air gun testing results. Key differences between the drop weight test and the air gun tests are: size, mass, velocity, and geometry of the projectile, geometry of the sample, pressure versus no pressure, and potentially others. Therefore, one test could either overestimate or underestimate mass loss and the no-failure energy as compared to the other type of test.

Figure 5-4 shows the mass loss for drop weight samples at varying energies for different coating thicknesses. Best fits were determined for each individual thickness, shown in Table 5-3. In Figure 5-4a, both the no-failure energy data sets and the failed data sets are shown. The no-failure energy data points are shown at 0% mass loss. Figure 5-4b examines the data except for the no-failure energy data and the data obtained from the 6.10 mm thick coating. The drop weight delivered up to 45J of impact energy and the 6.10 mm samples broke at higher energies than the other thicknesses. The range in Figure 5-4a was too small to obtain a best fit for the 6.10 mm coating. Two overlapping points are shown in Figure 5-4a for two uncoated samples which did not fail. Catastrophic failures of four other uncoated samples resulted in 100% mass losses, which are not included in Figure 5-4.

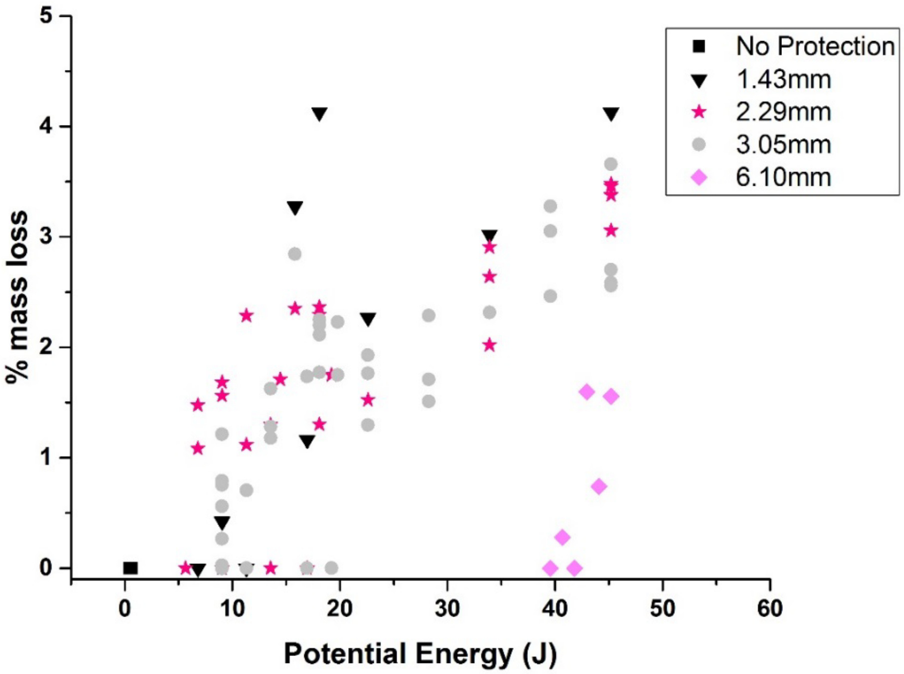

(a)

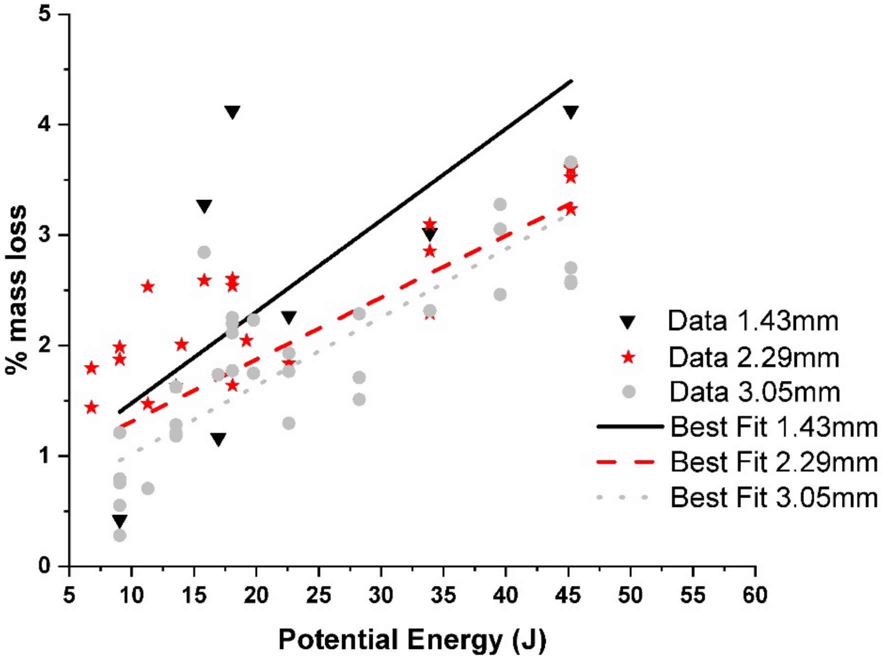

(b)

Figure 5-4: Mass loss as a function of coating thickness; (a) all data, (b) damaged samples.

BEST FITS for DROP WEIGHT SAMPLES		
Linear $y = mx + B$		
1.43 mm Thickness	*2.29 mm* Thickness	*3.05 mm* Thickness
m 0.083 *B 0.650* R^2 *0.851*	*m 0.053* *B 0.900* R^2 *0.969*	*m 0.061* *B 0.400* R^2 *0.927*

Table 5-3: Best fit parameters for the data in Figure 5-4.

Using the best fit values from Table 5-3, the mass loss for fragment confinement was extrapolated out to 95J and was found to be 8.5%, 5.9% and 6.2% for coating thicknesses of 1.43 mm, 2.29 mm and 3.05 mm, respectively. Examining the data in Figure 5-3 for the air gun test at those same thicknesses, an average percent mass loss of 2.8%, 1.6% and 2.6% was calculated. Based on the fragment confinement from the two tests, the drop weight approach overestimated the mass loss by 3 times, 3.7 times and 2.4

times for the same thicknesses. An average overestimate for the drop weight tests for all three thicknesses was calculated to be 3 times.

The drop weight tests also allowed examination of no-failure energy. The impact energies for the samples with zero percent mass loss in Figure 5-4a for the four coating thicknesses were identified. The average no-failure energy samples that did not break for each thickness was determined by averaging the first point's breakage and the zero percent mass loss data point before breakage occurred. The upper limit no-failure energy was identified for each coating thickness as the highest drop weight impact energy measured where a sample did not break.

If no-failure energy data from the drop weight tests (Figure 5-4a and Figure 5-5) is extrapolated out to 95J, shown in the air gun experiment, the coating thickness needed to prevent failure would be 15.36 mm using the average energy and 14.05 mm using the upper limit energy. Assuming the overestimate of the drop weight test of 3 times can be applied to no-failure energy when using the average and upper limit energies, then the coating thickness would be 5.12 mm and 4.68 mm. Considering that the air gun tests show crack networks present at 6.10 mm, these estimates are slightly below the actual observations.

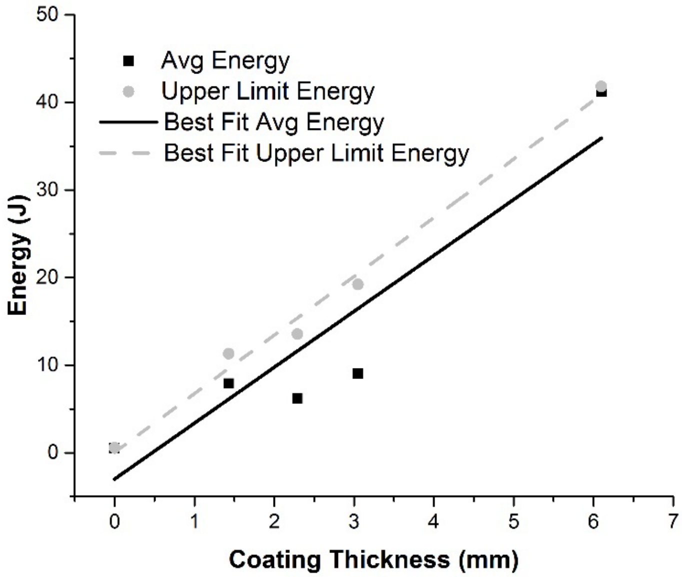

Figure 5-5: Average and upper limit energies for the drop weight samples as a function of coating thickness.

BEST FIT for NO-FAILURE of COATED DROP WEIGHT SAMPLES	
Linear $y = mx + B$	
Average Energy	Upper Limit Energy
m 6.382 B -3.000 R^2 0.914	m 6.692 B 0.065 R^2 0.987

Table 5-4: Best fit parameters for the data in Figure 5-5.

5.3.3 Refinement of fragment confinement predictions using higher caliber impact energies.

Higher energy weapons were used in this study to determine if the coatings would continue to contain fragments under higher energy impact situations as compared to previous air gun tests in Section 5.3.1. It was observed that the coated borosilicate glass cylinders had significant crack networks inside their walls, but the fragments were held together by the coating. The cylinders tested with the 9x19 mm Luger 8 g FMJ and .40 S&W 7.5 g RHT Speer broke at the mounting point. In these two scenarios, the issue was with the mounting of the cylinder. The stress during impact concentrated at the base and was large enough to break the cylinder off. Despite this issue, the fragments of the borosilicate cylinder itself remained adhered to the coating. Figure 5-6 shows how the coated cylinders tended to behave under high-velocity impact.

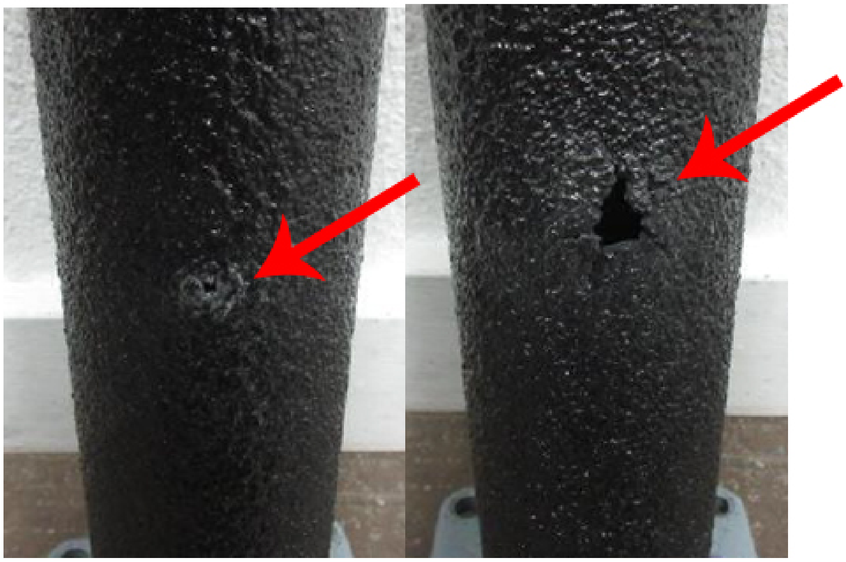

Figure 5-6: Images of post impact response from the 9x19 mm IMI FMJ test demonstrating fragmentation containment for coated cylinders: (left) bullet exit (right) bullet entrance.

Mass loss was used as a measure of the tendency of the coated cylinder to lose fragments into its surroundings. The mass loss was small in all tests (less than 4.5%), as shown in Figure 5-7. For the scenarios where the cylinders broke off at the mounting point, the broken fragments along the base were included in the measured mass after impact, to remove the effect of the failure at the mounting point.

Previous tests with coated cylinders under air gun impact and the drop weight tests assumed a linear relationship between impact energy and fragment confinement. It can be observed by examining the actual energy versus mass loss relationships in Figure 5-7, that the assumed linear relationship is not a correct approximation. Based on linear assumptions, the percent mass loss of the borosilicate cylinders at 800 J of kinetic energy should be approximately 16%. In this research, impact energies of 919, 740, and 554 J, recorded mass losses of less than 4.5%. Therefore, the coating confines fragments better than originally predicted, at a thickness of 3 mm.

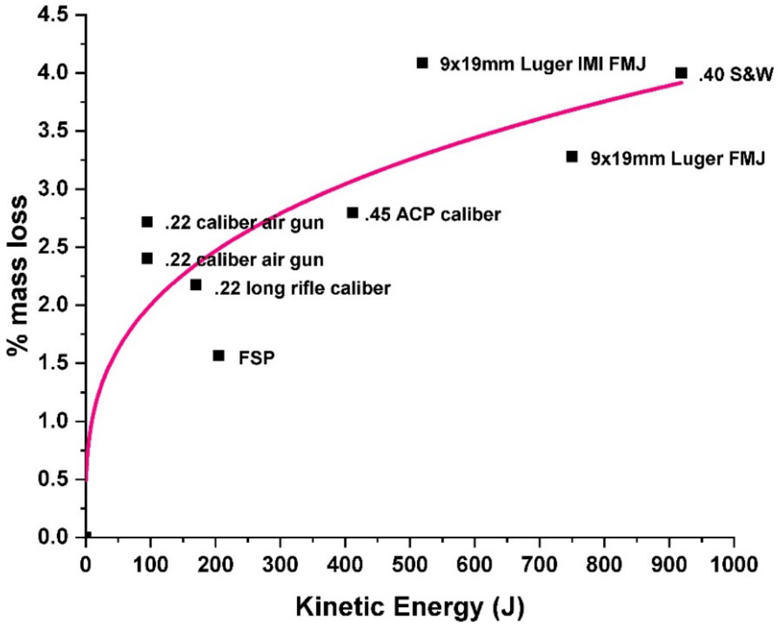

Figure 5-7: Measured mass loss for borosilicate cylinders at different bullet kinetic energies for 3.05 mm thick coating with a best fit power curve.

A possible power function relationship between mass loss and kinetic energy could be suggested, as shown in Figure 5-7 by the best fit. The fit is represented by Equation (11), with the values of a and b equal to 0.49 and 0.3, respectively.

$$y = a(1 + x)^b \qquad (11)$$

The best fit achieved an R^2 value of 0.75, which might not represent a strong fit, but was the best fit based on the data available. The variability in the data can be explained by factors involving micro-flaws inside the borosilicate glass cylinders, location of impact, slight differences in coating thickness and others. Despite the variability, the mass loss stayed within 4.5% for the 95 - 919 J kinetic energy range shown in the test results.

5.4 Summary

Elastomeric coatings were investigated for their fragment confinement and potential no-failure energy capabilities on pressurized and impacted glass cylinders and flat glass drop weight samples. Several major observations were made regarding the coating effect. First, the drop weight testing was found to be a complementary technique for the ballistic testing of the coated glass cylinders with the drop weight damage predictions overestimating the air gun approach by a factor of about 3. Mass losses were much higher from the coated drop weight samples than from the coated air gun impacted and pressurized cylinders.

Second, the coatings changed the failure characteristic and fragment dynamics drastically by protecting the cylinders from the initial impacts, minimizing mass loses of the impacted glass, and greatly affecting the fragment confinement, depending on the thickness of the coatings and testing methods.

Coated borosilicate cylinders under impact energies higher than that of an air gun (95 J) were shown to contain fragments with a mass loss of much less than what was predicted in the linear extrapolations from drop weight testing. The efficiency of fragment containment by the coating and the mass loss of the coated cylinders were shown to follow a power function relationship with impact energies, as opposed to the originally assumed linear relationship. At impact energies up to 919 J, coated borosilicate cylinders exhibited a mass loss of less than 4.5%, whereas predictions from the linear extrapolations of the mass loss with 800 J energy estimated a 16% mass loss.

CHAPTER 6 INSTRUMENTED DROP WEIGHT TESTING OF COATED BOROSILICATE GLASS PLATES

In Chapter 5, an elastomeric coating protected pressurized borosilicate glass cylinders against ballistic impact and flat glass plates against drop weight impact. It was postulated that the same coatings could protect full-scale porcelain HV transformer bushings against high powered rifle bullets. The air gun and rifle impact testing on the cylinders was correlated with drop weight testing at lower projectile energies. Despite the significant successes of the research presented in Chapter 5, the effectiveness of the coating in the protection of brittle materials against impact was not determined. This chapter will explore further the coating effectiveness and performance using a drop weight approach with the addition of instrumentation via an accelerometer.

In the literature, impact behavior of materials has been studied using instrumented drop weight, drop ball, and non-instrumented drop weight testing to determine the response to impact of concrete (100, 101), glass (102, 103), helmets (104, 105), windshields (106-108), composites (109-111), and many others to name a few. Tempelmann et. al. looked at a new method using a modified instrumented drop weight to examine the behavior of portable consumer-based electronic equipment (112), such as liquid crystal displays (LCD)s, cell phones and printed circuit boards (PCB)s (113-116). It has been shown that instrumented drop weight testing could be a useful and complimentary technique for understanding impact behavior of many structures and materials. In Chapter 5, non-instrumented drop weight testing was shown to give basic feasibility information and allow a generalized evaluation of a protection scheme for further testing. By enhancing the drop weight method to an instrumented version, impact parameters, coating thickness effects, and an overall effectiveness of coated samples compared to uncoated samples could be determined.

6.1 Materials

For the drop weight testing, square plate samples described in Chapter 4.4.3 were used. The square glass samples were coated with the same coating as the plates in Chapter 5.1.

6.2 Testing set-up and method

6.2.1 Visual examination of instrumented drop weight samples

After the impact, the damage morphology was examined using an optical microscope discussed in Chapter 4.4.2 and an SEM using the same method presented in Chapter 4.4.1.

6.2.2 Instrumented drop weight testing using an accelerometer

Initial drop weight testing in Chapter 5.2.2 implemented standard drop weight testing without instrumentation. Mass loss was the evaluation criteria that could be utilized for those tests. The capabilities of the drop weight tester was further enhanced to do more extensive evaluations. Mass loss, the criteria used previously, is fairly limited in comparability between samples.

The same impact tester that was used in Chapter 4.4.3, was used for this experiment, with drop weight measurements of 0.9 and 3.6 kg (2 and 7.9 lbs). Uncoated samples were tested using the 0.9 kg drop weight to a maximum height of 0.08 m (3”). All coated samples of five different coating thicknesses 0, 1.32, 2.33, 3.11, and 5.64 mm (0, 52, 92, 122, and 222 mils) were tested using the 3.6 kg drop weight to a maximum drop height of 0.76 m (30”). The sample’s protected side faced the indenter pin. The drop weight impacted the indenter pin, of mass 0.15 kg (0.33 lbs), which transferred the impact to the sample. The potential energies (PE) tested ranged from 0.19 to 0.38 J for the unprotected samples and 4.3 to 28 J for the protected samples.

To obtain acceleration data, an EVAL-ADXL001-500Z accelerometer was attached to the drop weight, shown in Figure 6-1. A Polyethylene Terephthalate Glycol (PETG) mounting bracket was 3-D printed to fit the slotted opening on the drop weight tester. The PETG was used to provide a rigid mounting location for the vibration dampener and accelerometer. The vibration dampener, made of styrene butadiene rubber (SBR), was attached to the mounting bracket. The vibration dampener prevented high frequency harmonics created by the weight from interfering with the accelerometer reading. Accelerometer readings were obtained using a RIGOL DS1054Z oscilloscope. The output range of the accelerometer was 0-5 Volts with 5 Volts corresponding to 4903.33m/s^2 (500g). The sensitivity of the accelerometer was 3.3 mV/g and was used to convert the signal from volts to m/s^2, with the understanding that 1 g is equal to 9.81

m/s^2. The oscilloscope recorded at a rate of 1,000,000 samples/second. An accelerometer offset was subtracted from the raw dataset to make sure the accelerometer voltage reading prior to impact correlated with 0 g.

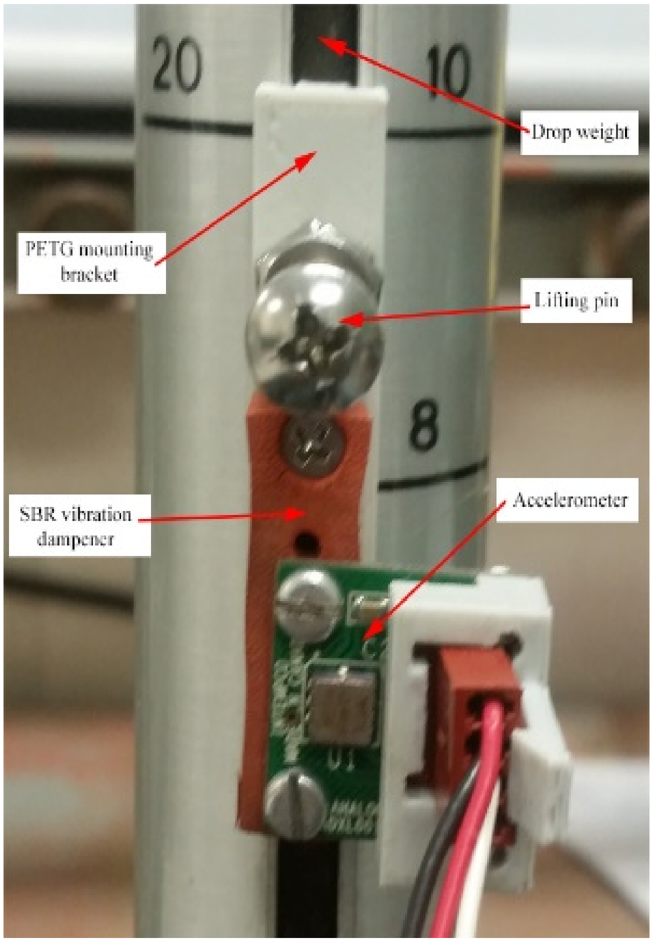

Figure 6-1: Accelerometer mounting details.

6.2.2.1 Accelerometer data filtering

Many vibrations/oscillations appeared in the raw data due to the natural frequency of the drop weight impactor and the indenter pin, which represented "ringing" in the system (117). Vibrations in the system occurred due to flexural vibrations of the sample (117), which was unable to be clamped in this set-up. The high frequencies in the data were removed with a smoothing filter. However, filtering can inadvertently remove high frequency components that are representative of damage phenomena happening to the material (110). The raw deceleration data was put through a lowpass 10th order Butterworth filter in MATLAB and set to remove frequencies greater than a cutoff frequency of 1800 Hz. The Butterworth filter frequency response is shown in Figure 6-2.

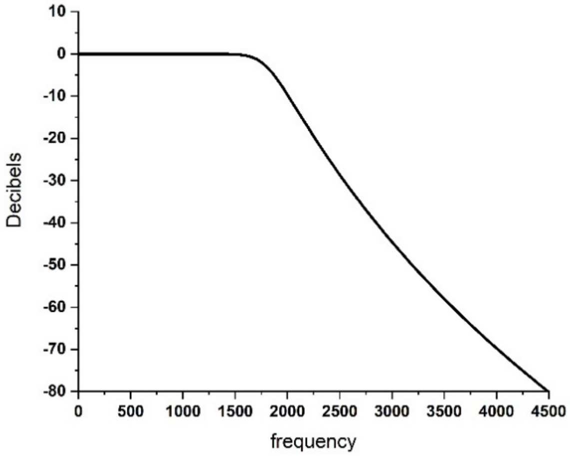

Figure 6-2: 10th order Butterworth 1800 Hz low pass filter bode magnitude plot

The cutoff frequency was selected based on the manufacturer's data sheet for the accelerometer, which indicated that the frequency response begins to decay at approximately 2 kHz (118). The smoothing function was generated in the raw acceleration data to remove the high frequency vibrations as demonstrated in Figure 6-3.

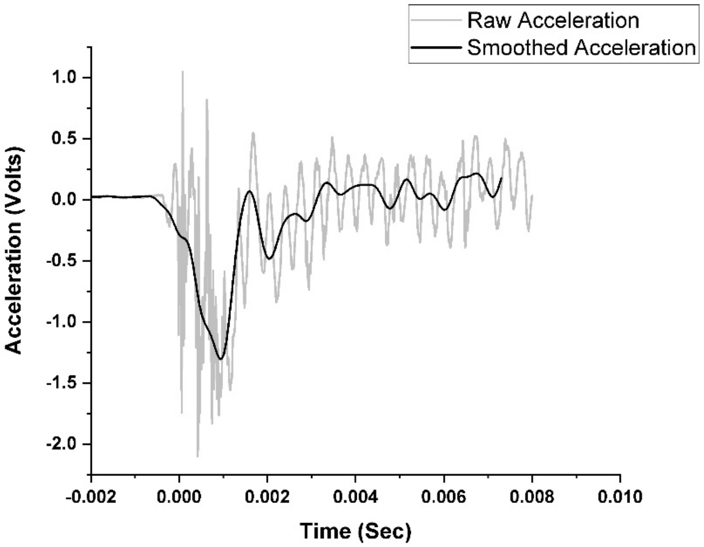

Figure 6-3: Smoothed vs. noisy raw acceleration data for 3.11 mm coated sample at 15.6 J of impact energy.

6.2.2.2 Numerical integration

After a filtered acceleration dataset was generated, single and double numerical integration was performed during data analysis. Three numerical integration methods were examined: Riemann Summation, Trapezoidal Rule, and Simpson's Method. Mathematically the three numerical integration methods followed Equations (12) - (14) (119), using acceleration from the measured accelerometer data, $a(t)$.

Riemann Summation followed the relationship shown in Equation (12):

$$\int_a^b \boldsymbol{a(t)dt} = \frac{\boldsymbol{b-a}}{\boldsymbol{n}}[\boldsymbol{a(t_1)} + \boldsymbol{a(t_2)} + \cdots + \boldsymbol{a(t_n)}] \tag{12}$$

The Trapezoidal Rule followed Equation (13*)*:

$$\int_a^b \boldsymbol{a(t)dt} = \frac{\boldsymbol{b-a}}{\boldsymbol{2n}}[\boldsymbol{a(t_0)} + \boldsymbol{2a(t_1)} + \cdots + \boldsymbol{2a(t_{n-1})} + \boldsymbol{a(t_n)}] \tag{13}$$

The Simpson's Method followed Equation (14):

$$\int_a^b a(t)dt = \frac{b-a}{3n}[a(t_0) + 4a(t_1) + 2a(t_2) + 4a(t_3) + \cdots + 2a(t_{n-2}) + 4a(t_{n-1}) + a(t_n)] \tag{14}$$

The three integration methods were plotted in Figure 6-4. During integration the step size, Δt (or dt), was equal to the time step of 0.01 msec. It is shown in Figure 6-4 that the small step size produced similar integration results in all three methods. The least accurate method, the Riemann Summation, was chosen as the integration method of choice, because it required the least amount of computing power.

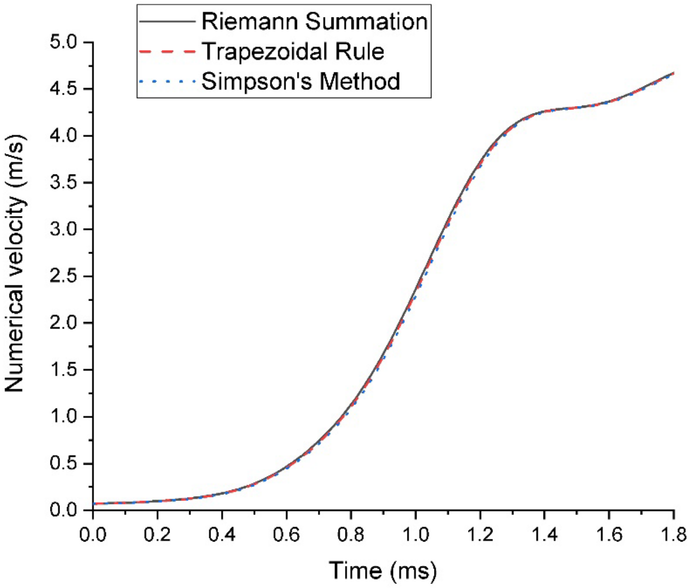

Figure 6-4: Numerical method comparison for a single accelerometer data set.

6.2.2.3 Collected impact data

For accelerometer data analysis, methods adapted from the literature (117, 120, 121) were used. The contact force was computed using Equation (15), where M_T is the mass of the combined drop weight (m_1) and indenter pin (m_2), and $a(t)$ is the deceleration from the measured accelerometer data.

$$F(t) = M_T a(t) \tag{15}$$

To determine the impact velocity of the combined drop weight and pin, several assumptions were made. These assumptions were as follows: the potential energy (PE) of the drop weight was converted fully to kinetic energy (KE) just before hitting the indenter pin, there were no losses in energy due to friction from the drop weight moving down the impact tester rails, the indenter pin was initially at rest, the collision between the drop weight and the indenter pin was perfectly inelastic (they stuck together at impact), there was no rebound between the drop weight and indenter pin during the impact event, the rigid two body system was closed and isolated, and no air drag or friction was acting on the system (which is valid at speeds less than 10 m/s (112) for a compact drop weight). The accelerometer recorded the combined mass of m_1 and m_2 in the deceleration reading during the impact, when the drop weight contacted the indenter pin.

In an inelastic collision, momentum is conserved but energy is not. Therefore, the momentum just before impact with the drop weight mass is equal to the momentum after impact with the combined mass. The velocity of the drop weight and pin during impact with the sample (V_0), was derived from the below momentum relationships (Equations (16)- (18)). V_0' is the velocity of the drop weight at impact with the indenter pin. The value of h is the drop weight initial height and g is acceleration due to gravity.

$$\frac{1}{2} m_1 {V_0'}^2 = m_1 g h \tag{16}$$

$$m_1 V_0' = m_T V_0 \tag{17}$$

$$V_o = \frac{m_1}{M_T} \sqrt{2gh} \tag{18}$$

The drop weight impactor velocity function, $V(t)$, can be computed using Equation (19), obtained from ASTM D7136 (117).

$$V(t) = V_o + gt - \int a(t)dt \tag{19}$$

The displacement function, $\delta(t)$, of the drop weight was determined by Equation (20). The energy transferred (Equation (21) (120)) to the sample during the impact is the work done by the contact force during the impactor displacement. The impulse (Equation (22)) can also be determined from the drop weight testing.

$$\delta(t) = \int V(t)dt \tag{20}$$

$$E_{transfered} = \int F(t)d\delta \tag{21}$$

$$I = \int F(t)dt \tag{22}$$

For equations (19)- (22), the limits of integration was carried out when the combined drop weight and indenter pin first make contact with the sample, to the time the contact force returns to zero; for thicker coatings, the contact force reaches a minimum without returning to zero.

6.3 Results and discussion

6.3.1 Visual results of sample failure behavior

6.3.1.1 Impact damage to glass samples on their bottom side

The glass samples fractured on the underside with a predominant radial type of pattern, irrespective of the coating thickness or impact energy. Ring cracks and comminution occurred at the impact site and are visible in both images shown in Figure 6-5. The radial and ring cracks support other experimental observations stating that brittle materials under impact tend to crack and fail via radial cracks, which extend outwards from the impact site through ring cracks (35). This research methodology could not identify which cracks were leading or trailing propagators, just the visual post-impact presence of various cracks. Figure 6-5a and Figure 6-5b illustrates the differences of two representative failure modes exhibited by all fractured samples: spalling or no spalling, respectively. Spalling occurs in brittle materials stronger in compression than tension, under dynamic loading when shock waves induce large tensions inside a solid (32, 33).

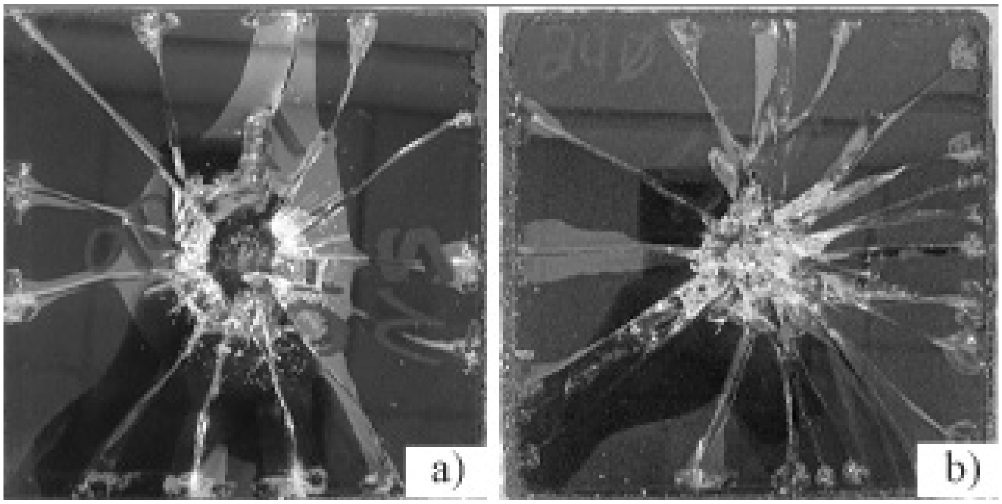

Figure 6-5: Coated sample failure modes: (a) radial cracking with significant spalling for 2.33 mm thick sample impacted at 19.9 J and (b) radial cracking with reduced spalling for 5.64 mm thick sample impacted at 23.4 J.

Because all fractured samples followed the cracking behavior seen in Figure 6-5, the number of cracks were estimated and plotted for each thickness, as shown in Figure 6-6, to elucidate differences in radial cracking behavior. The samples with the thinnest coatings produced the highest number of cracks at lower impact energies. For the thicker coatings, the scatter in the number of cracks is too large to be able to draw firm conclusions.

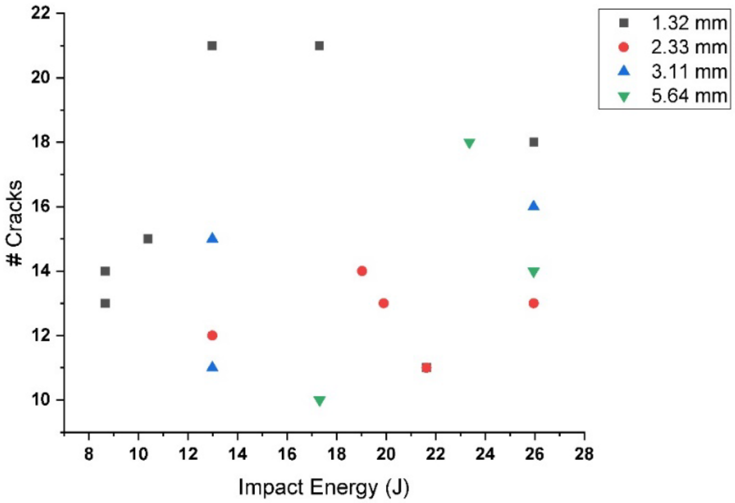

Figure 6-6: Number of cracks for all failed samples.

6.3.1.2 Impact damage to coated sides of samples

The optical images in Figure 6-7 show typical damage in impacted specimens on their coated sides for each coating thickness and four impact energies. For the sample with the thinnest coating a large amount of permanent deformation to the coating caused by the impactor can be seen in Figure 6-7a. The deformation zone was characterized by extensive tearing and crushing of the surface. The damage zone has a circular shape with a diameter of about 15 mm. The damage is especially extensive in a small concentric compression zone of about 5 mm which is considerably smaller than the indenter pin diameter (15.75 mm). Within the compression zone radial cracking of the coating and the permanent damage done by the impactor was observed. In Figure 6-7b, the damage pattern exhibits a circular shape with a diameter of about 9 mm. For the impacted surface in Figure 6-7c, the extent of damage was considerably less severe than in the previous two cases, shown in Figure 6-7a and Figure 6-7b. No observable damage zone was noticeable in Figure 6-7d, despite the higher impact energy delivered.

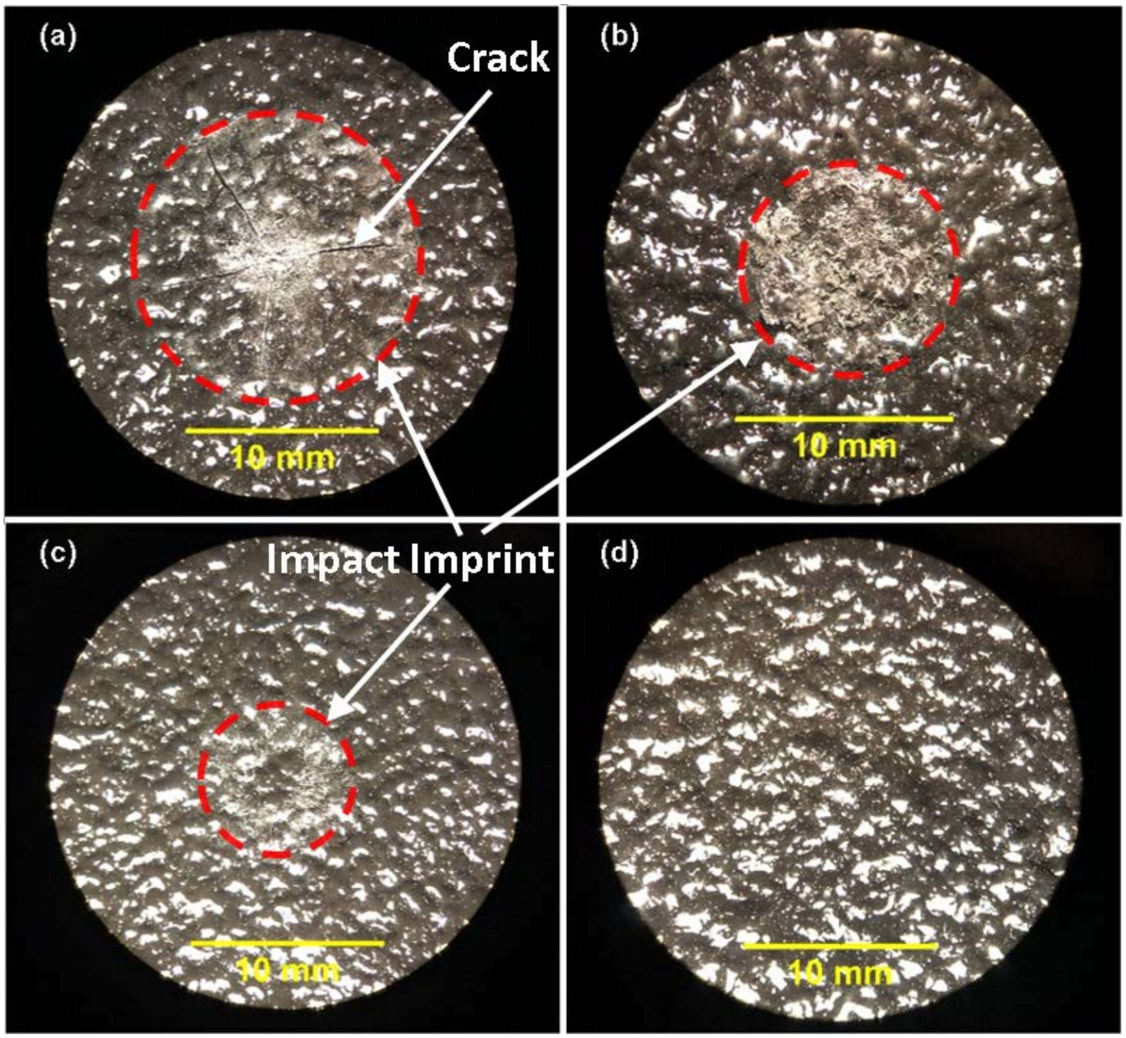

Figure 6-7: Optical images of typical damage to the coatings on the impacted side of the specimens with (a) 1.32 mm at 17.3J, (b) 2.33 mm at 18.6J, (c) 3.11 mm at 16.4 J and (d) 5.64 mm at 26 J of coating.

The coating damage for the 3.11 mm thick sample was further examined at higher magnification using SEM. Figure 6-8a is a schematic representation of the coating cross-section with the impactor location. The SEM image in Figure 6-8b shows the distinctive "bubbly" morphology of non-impacted coating. SEM images in Figure 6-8c and Figure 6-8d reveal micro-details of the permanent damage caused by the impactor. The main characteristic was that the "bubbly" surface showed significant radial stretching-bands in the impact area. Figure 6-8c and Figure 6-8d show tearing of the surface at higher magnification, which was not visible in Figure 6-7c.

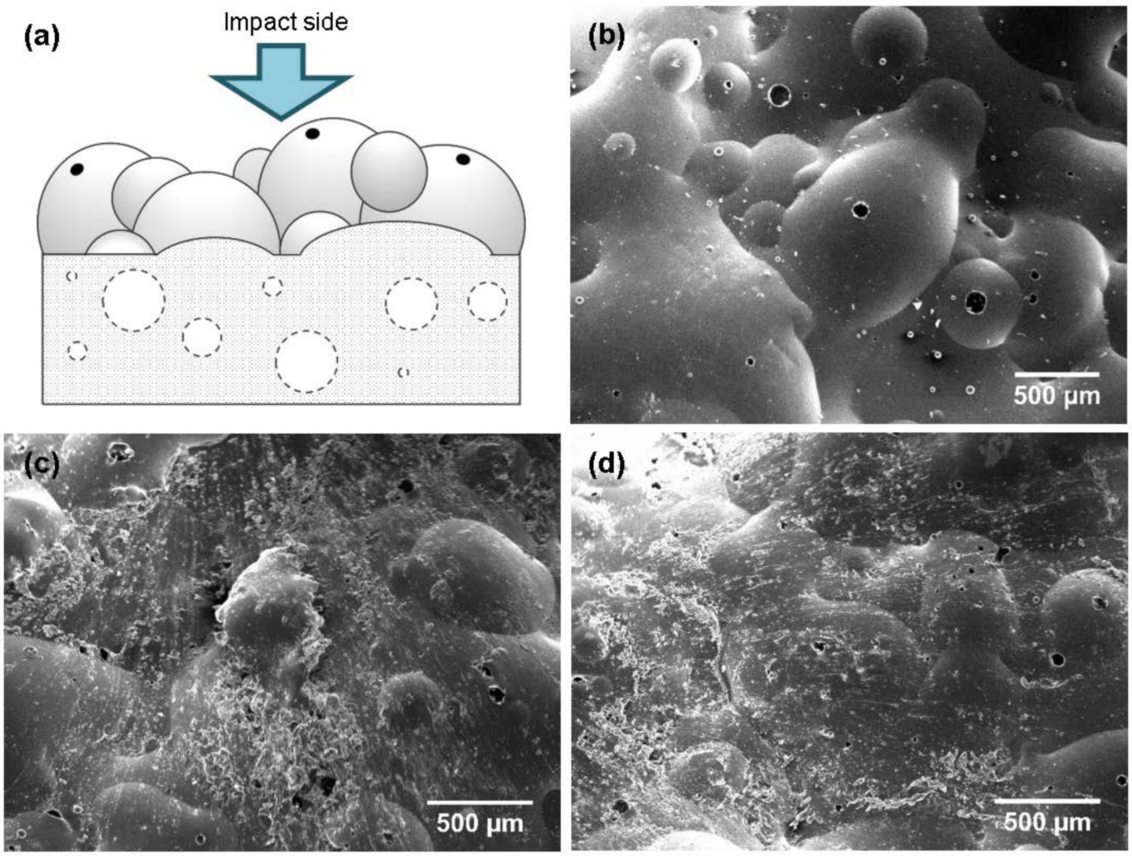

Figure 6-8: 3.11 mm thick coating sample: (a) Schematic of the coating cross section and impactor location with internal voids represented by dashed circles, (b) SEM image of non-impacted surface, (c) and (d) damage modes on the impact area, i.e. crushing, tearing and radial stretching marks.

6.3.2 Analysis of accelerometer responses as a function of coating thickness

6.3.2.1 Time history plots for unfractured samples

Impact parameters, defined as the maxima in the contact force (i.e. deceleration), impactor velocity, maximum displacement, maximum energy transferred to the sample, time to maximum contact force, duration of the impact and the impulse were determined from the time histories (Figure 6-9, Figure 6-10 and Figure 6-11) and are tabulated in Appendix F.

In Figure 6-9, Figure 6-10 and Figure 6-11 only one representative plot is shown for an uncoated, a 1.32 mm coated, and a 5.64 mm coated sample. All impacted samples behaved in similar manners, with a few exceptions. The set-up used in this testing did not allow the samples to be clamped. It was observed in the time history graphs that the maximum contact force, the zero velocity point, the maximum impactor displacement, and the maximum energy transferred to the sample all typically occurred approximately simultaneously, like what is shown in Figure 6-9 and Figure 6-10. Some of the time history plots had maximum contact forces that preceded the other three quantities, as seen in Figure 6-11, probably due to the viscoelastic nature of the coating dominating the deformation of the sample.

The uncoated sample in Figure 6-9 exhibited a clear parabolic contact force curve without any bumps before and after the maximum contact force, behavior indicative of an elastic response. The time history plots for the coated samples in Figure 6-10 and Figure 6-11 display a large bump in the contact force as it moves towards its maximum. This appears to be specific to the coating and is likely related to the material behavior as it deformed during impact. This behavior was seen for all samples at all energies. Some variability existed, and additional bumps occasionally occurred before the maximum was reached.

Impact duration can be compared in the time history plots with samples that were tested at the same impact energies. The impact duration is the amount of time that occurred from the beginning of the impact to the end. The thicker sample, in Figure 6-11, has a more spread-out force time curve as compared to the thinner sample in Figure 6-10.

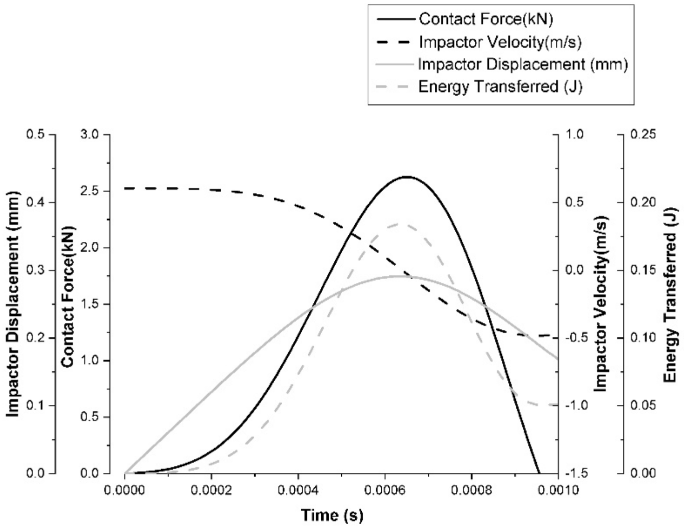

Figure 6-9: Time history plot for uncoated sample at 0.19 J of impact energy.

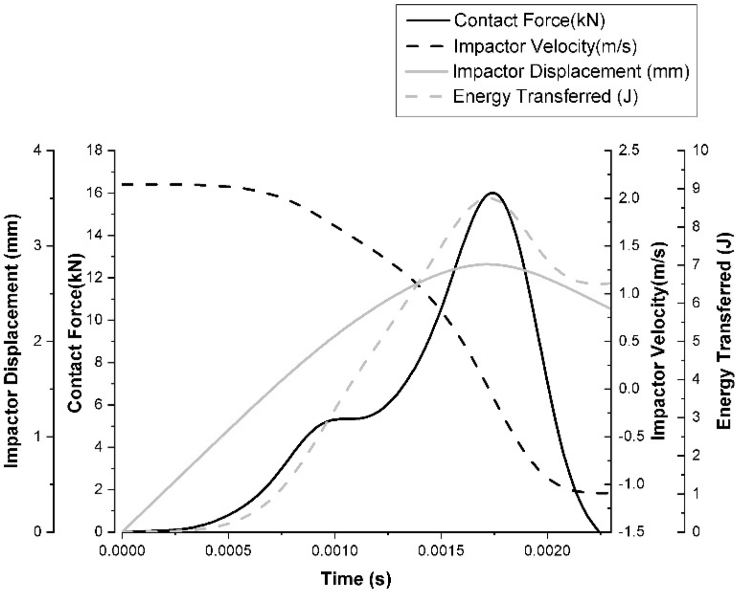

Figure 6-10: Time history plots for 1.32 mm coating at 8.65 J of impact energy.

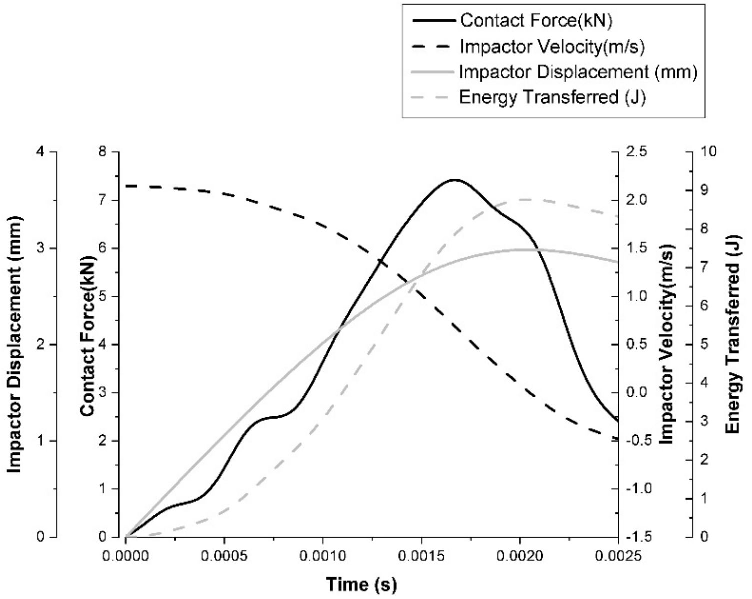

Figure 6-11: Time history plots for 5.68 mm coating at 8.65 J of impact energy.

Impactor velocity

Impactor velocities are shown in Figure 6-9, Figure 6-10 and Figure 6-11. Impactor velocity represents the sample velocity and was derived from the deceleration data using Equations (18) and (19). Examination of time history plots showed that the drop weight rebound velocities of the coated samples were always less than the original impact velocity. The rebound velocity of the drop weight is considered the negative portion of the velocity curve after passing zero. Rebound to nearly the same velocity would suggest that little energy was transferred and the collision was entirely elastic (122). The thicker coating in Figure 6-11 produced a smaller rebound compared to the thinner coating at the same impact energy in Figure 6-10. The thicker coating takes more energy away from the rebound, as shown by the larger transferred energy at 0.0025s in Figure 6-11. The uncoated samples, on the other hand, demonstrated a rebound velocity that was shown to be approximately the same as the initial velocity, which suggest impact collisions that are elastic in nature. In one of the uncoated impact tests that was performed the impactor velocity showed an energy gain in the rebound, which is not physically possible. User error was likely, during that specific impact test.

6.3.2.2 Impact energy effect on tested samples

Deceleration and contact force

Equation (15) demonstrates that the contact force is directly related to the maximum deceleration. The contact force is associated with the resistance exerted by the sample during the impact event. Samples that did not fail demonstrated an increasing relationship between maximum contact force and impact energy, shown in Figure 6-12. Samples that failed demonstrated that the maximum contact force dropped significantly compared to samples that did not break.

In Figure 6-11, the general trend is that thinner coatings produce larger contact forces compared to the thicker coatings, with some variability due to scatter in the data. This behavior in maximum contact force was observed by Metz, who concluded that softer surfaces result in a smaller impact force (and smaller deceleration) as the surface slows down the impact (122). In Figure 6-11, the contact force is spread over a longer time than in Figure 6-10. Scatter in the results is observed in Figure 6-12. The scatter is due to the inherent probabilistic nature of brittle materials (76), demonstrating a certain amount of randomness around failure (77, 78). The randomness around failure is especially prominent in dynamic impact (79, 80). The absence of a crystalline structure and presence of micro-flaws for materials like glass presents difficulty in evaluation of failure behavior (78). Other brittle materials, such as porcelain, are crystalline (123); making them more deterministic in their failure results (78). Because this research used borosilicate glass plates, evaluation of impact behavior generated significant scatter.

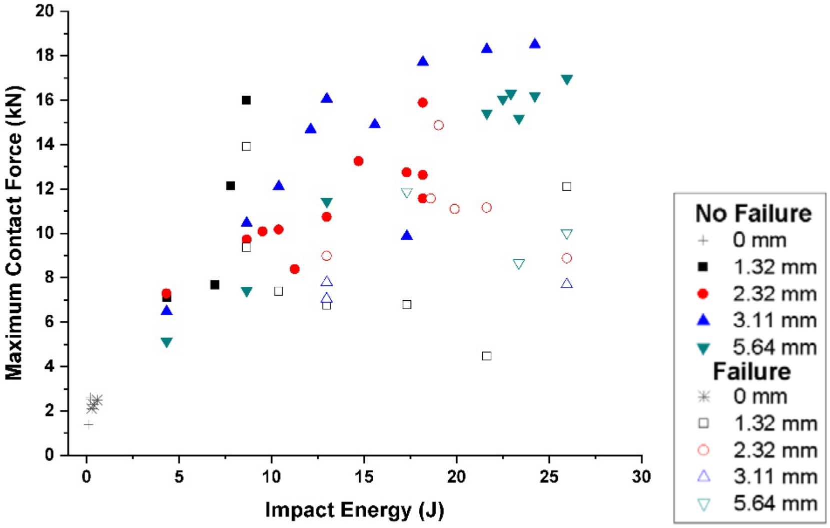

Figure 6-12: Maximum contact force with respect to thickness and impact energy for all tested samples.

Impactor displacement

Impactor displacement was derived from the impactor velocity using Equation (20). The normalized displacement (displacement per unit coating thickness), for all coated samples that did not fail as a function of impact energy is shown in Figure 6-13. It appears that the normalized displacements increase with impact energy for a given coating thickness, roughly following an s-shaped response. Normalized displacements are seen to decrease with increasing coating thickness. The dashed line in Figure 6-13 represents the normalized value where the coating thickness and impactor displacement are equal. Values above and below the dashed line represent displacement dominated by bending of the glass plate and coating deformation, respectively.

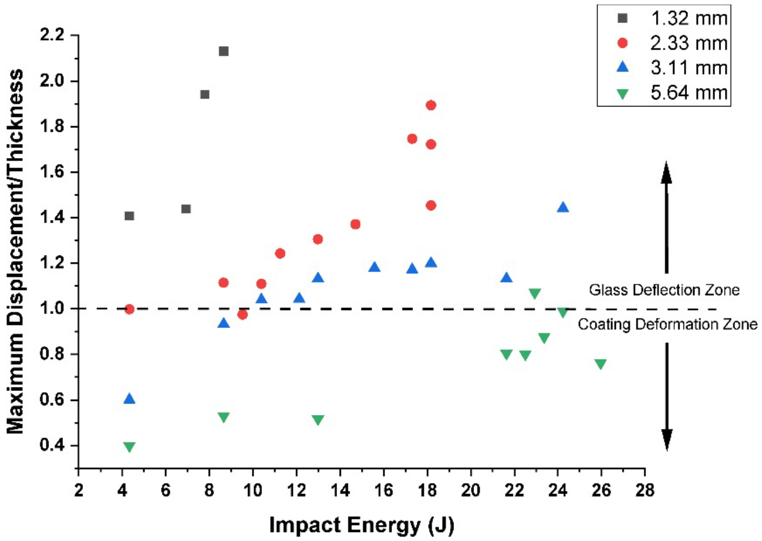

Figure 6-13: Maximum normalized displacement vs. impact energy for un-failed samples.

Average normalized maximum displacements, listed in Table 6-1, were calculated for all the samples that did not fail for each thickness. The average normalized values decreased as the coating thickness increased. Thicker coatings create a buffer that reduces the amount of bending the glass plate endures during impact.

Thickness (mm)	**Avg. Normalized Maximum Displacement (mm)**
1.32 ± 0.18	1.73 ± 0.36
2.33 ± 0.15	1.36 ± 0.32
3.11 ± 0.46	1.09 ± 0.22
5.64 ± 0.14	0.75 ± 0.23

Table 6-1: Average normalized maximum displacements.

Impact duration

The duration of impact is the time interval that occurs while there is resistance acting on the impactor from the sample until the contact force goes to zero, or to a minimum. The time to maximum contact force was also examined. This is the time from the beginning of the impact until the maximum contact force is applied to the sample. Both the impact duration and time to maximum contact force were found by taking the average of all the sample results for each thickness. According to Figure 6-14 the time to maximum contact force and the total duration of impact appear to be constant irrespective of thickness, which was noted in studies by Elavenil and Knight (100). The scatter in the data in Figure 6-14 makes it difficult to decipher if the time duration and the time to maximum contact force are constant or slightly increasing. The uncoated sample, however, exhibited a different type of failure; duration times and times to maximum contact force were much less than the values for all coating thicknesses. This suggests that even a coating thickness of 1.32 mm produces a significant improvement in the sample impact duration and time to maximum contact force. Longer duration times reduced the shock to the underlying material and allowed substantial increases in impact energy before failure.

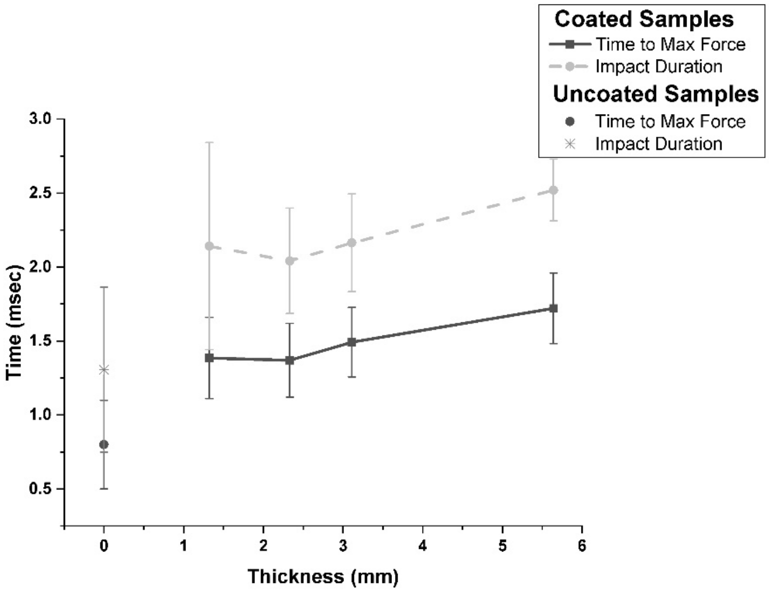

Figure 6-14: Impact duration and time to maximum contact force with respect to coating thickness.

Transferred energy

Transferred energy is considered the energy present in the sample as a result of the impact event. Transferred energy, a function of time from Equation (21), increases from the moment of impact to its maximum and then decreases as the sample recovers elastically, or viscoelastically, for coated samples. The value at the maximum is termed the maximum transferred energy and is listed in Appendix F.

Appendix F shows that the maximum transferred energy is, in most cases, a little less than the impact energy delivered. This difference is due to losses from friction in the sample, micro-damage that occurs within the glass sample during loading, and energy lost due to molecular movement and stretching of the polymer network in the coating. Since the collision between the drop weight, pin and sample is considered perfectly inelastic, as discussed previously, energy loss is to be expected. Research by Sutherland and Guedes Soares suggested that the energy transferred is linear until higher impact energies above 50 J are reached (124).

Figure 6-15a shows that for un-failed samples, the maximum energy transferred to the sample increases linearly as impact energy increases, in agreement with Sutherland and Guedes Soares (124). Higher energy impacts were beyond the scope of the drop weight apparatus. The increase in maximum transferred energy is greater for thick coatings than for thin coatings. When the maximum energy transferred is normalized by the coating thickness, (Figure 6-15b); samples with the thinnest coating have the largest specific maximum energy transferred and progressively decrease as the coating thickness increases. These trends are maintained for samples that did not fail, but with increased scatter in the data. This behavior supports a study by Naik et al. on composites, which identified that thickness has a direct effect on the energy transferred under drop weight testing (121).

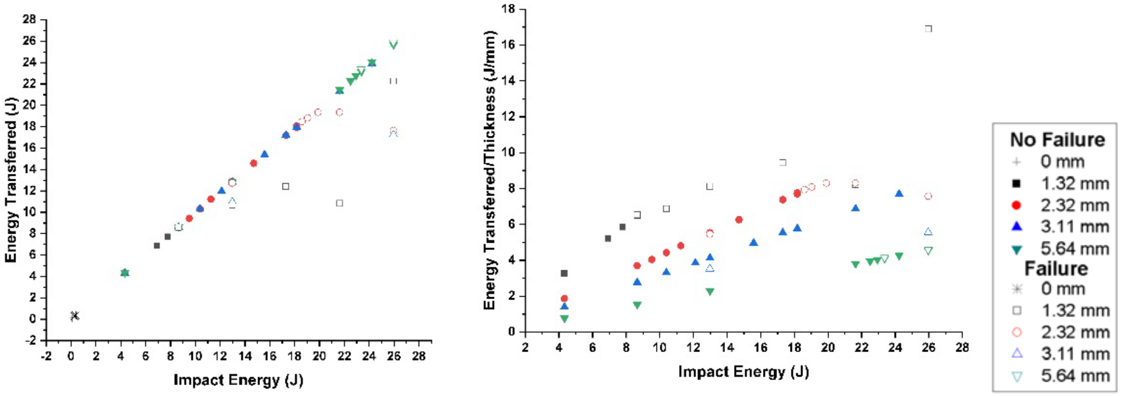

Figure 6-15: Maximum energy transferred, and specific energy transferred with respect to coating thickness and impact energy for all tested samples.

Impulse

Impulse relates the average contact force experienced by the sample over the impact duration. The impact duration was determined to be potentially constant irrespective of the coating thickness, shown in Figure 6-14. Therefore, the dominant factor controlling the impulse is the contact force experienced by the sample, which was shown to increase with increasing impact energy in Figure 6-12. In Figure 6-16, the impulse demonstrates an increasing relationship with impact energy for samples that did not fail. Samples that fail offer less resistance to the drop weight and experience less contact force, resulting in lower impulse values.

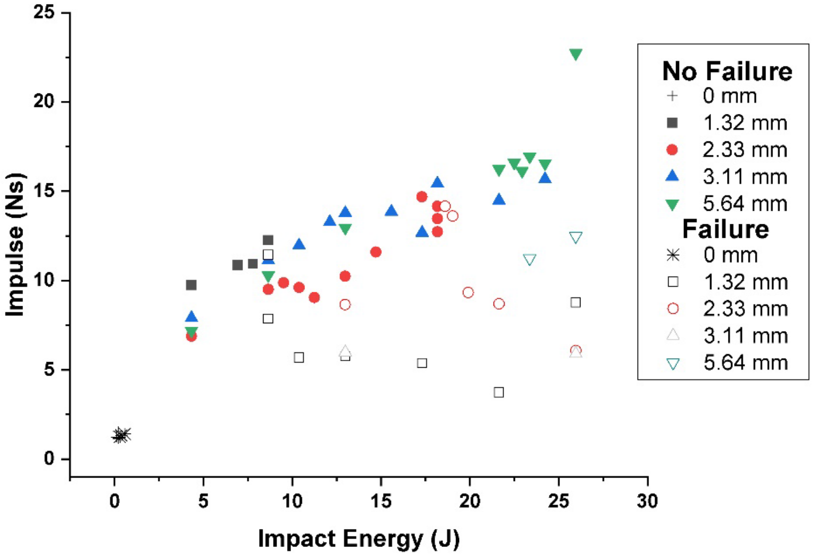

Figure 6-16: Relationship between impulse and impact energy.

6.3.3 Critical impact parameters at failure

Certain impact parameters at failure could stabilize irrespective of coating thickness. Impact energy, maximum contact force, and impulse were examined further at the point of transition from no failure to failure. If the transition point of no failure to failure becomes constant, this would suggest that the glass was under a critical state of stress at the point of failure. Then, the critical point (critical impact energy, critical contact force, and critical impulse) could be determined for other coating thicknesses. This critical impact parameter method could be utilized for many types of coatings or materials, allowing for comparison in performance.

Critical impact parameters for impact energy, maximum contact force, and impulse were examined further, as listed in Table 6-2a - Table 6-2c. Critical impact parameters are values at which failure was assumed to occur. Several different approaches could be taken to determine the critical parameters at failure. The parameters could be determined from either their maximum values just before failure or the maximum/minimum values just after the failure of the specimens. They could be determined from a single data point before and another single point after failure. Then the values could be averaged. Considering the effect of scatter, they could be estimated from three or five, or even more individual data points taken before and the same number of points after failure, and then averaged. In this research they were estimated from (1) the average of single data points before and after failure, and (2) the average from three data points before and three points after failure. More than three data points before and after failure were not considered due to the limited number of failed samples.

It is important to mention that for the critical maximum contact force and impulse estimates, the highest values before and the highest values after failure were considered. For the critical impact energy estimates, the individual or three highest values were taken before failure; the individual and lowest three estimates were considered after failure. The difference in the approaches for the critical maximum contact force and impulse and the critical impact energy at failure was justified by the facts that the energy estimates were determined from the applied impact energy, which is an independent variable. On the other hand, the maximum contact force and impulse estimates were determined from the response of the samples.

Critical impact parameters for impact energy, maximum contact force and impulse are listed in Table 6-2a - Table 6-2c and shown in Figure 6-17a - Figure 6-17c. The values listed in Table 6-2 were determined from the single highest and three highest un-failed samples, the three highest (or lowest for impact energy) values for the failed samples, and the averages of the failed and un-failed datasets. For Figure 6-17a - Figure 6-17c, only the average of the three highest and three lowest/highest datasets are plotted. All subsequent analysis used the average of the three highest and three lowest/highest datasets.

	Impact Energy for Un-failed Samples		Impact Energy for Failed Samples		Average Impact Energy from Un-Failed and Failed Samples	
Thickness (mm)	**Single Highest Value**	**Three Highest Values**	**Single Lowest Value**	**Three Lowest Values**	**Single Highest & Lowest Value**	**Three Highest & Lowest Values**
0.00 ± 0.00	0.19	0.19 ± 0.00	0.29	0.42 ± 0.15	0.24 ± 0.07	0.30 ± 0.15
1.32 ± 0.18	8.65	7.79 ± 0.87	10.38	9.23 ± 1.00	9.52 ± 1.22	8.51 ± 1.15
2.33 ± 0.15	18.18	18.18 ± 0.00	19.04	16.87 ± 3.38	18.61 ± 0.61	17.52 ± 2.25
3.11 ± 0.46	24.23	21.35 ± 3.04	25.96	17.31 ± 7.50	25.10 ± 1.22	19.33 ± 5.57
5.64 ± 0.14	25.96	24.52 ± 1.32	25.96	22.21 ± 4.44	25.96 ± 0.00	23.37 ± 3.19

(a)

	Maximum Contact Force for Un-failed Samples		Maximum Contact Force for Failed Samples		Average Maximum Contact Force from Un-Failed and Failed Samples	
Thickness (mm)	**Single Highest Value**	**Three Highest Values**	**Single Highest Value**	**Three Highest Values**	**Single Highest Value**	**Three Highest Values**
0.00 ± 0.00	2.63	2.59 ± 0.07	2.49	2.29 ± 0.20	2.56 ± 0.09	2.44 ± 0.21
1.32 ± 0.18	16.01	11.94 ± 4.16	13.91	11.80 ± 2.28	14.96 ± 1.48	11.87 ± 4.73
2.33 ± 0.15	15.88	13.96 ± 1.68	14.87	12.53 ± 2.03	15.37 ± 0.72	13.25 ± 2.68
3.11 ± 0.46	18.51	18.17 ± 0.41	7.80	7.52 ± 0.41	13.15 ± 7.57	12.85 ± 0.75
5.64 ± 0.14	16.97	16.49 ± 0.42	11.88	10.19 ± 1.62	14.43 ± 3.60	13.34 ± 2.14

(b)

	Impulse for Un-failed Samples		Impulse for Failed Samples		Average Impulse from Un-Failed and Failed Samples	
Thickness (mm)	**Single Highest Value**	**Three Highest Values**	**Single Highest Value**	**Three Highest Values**	**Single Highest Value**	**Three Highest Values**
0.00 ± 0.00	1.55	1.32 ± 0.20	1.42	1.33 ± 0.09	1.48 ± 0.09	1.33 ± 0.14
1.32 ± 0.18	12.26	11.39 ± 0.78	11.45	9.36 ± 1.86	11.85 ± 0.57	10.36 ± 1.68
2.33 ± 0.15	14.69	14.10 ± 0.62	14.15	12.36 ± 2.64	14.42 ± 0.38	13.23 ± 1.96
3.11 ± 0.46	15.68	15.20 ± 0.63	6.85	6.24 ± 0.53	11.27 ± 6.24	10.72 ± 4.93
5.64 ± 0.14	22.73	18.76 ± 3.45	12.49	11.68 ± 0.70	17.61 ± 7.24	15.22 ± 4.47

(c)

Table 6-2: Critical impact parameter method for (a) impact energy (J), (b) maximum contact force (kN), and (c) impulse (Ns).

After closer examination of the critical impact parameters in Table 6-2, it was shown that the critical impact energies increase with thickness. This means that more energy can be applied to the samples before failure initiates, with increasing thickness. However, the energy values do not stabilize (become constant or level off in a plateau) with the increasing coating thickness, as shown in Figure 6-17a. On the other hand, both the critical maximum contact force and critical impulse values at the onset of sample failure appear to stabilize with the thickness. This indicates that there is a critical maximum contact force and a critical impulse where the samples begin to fracture; the samples reach a critical state of stress. To better illustrate this effect, the critical maximum contact force and impulse are shown in Figure 6-17b and Figure 6-17c. What is surprising is that the critical maximum contact force and the critical impulse values stabilize even at small coating thicknesses, making the coatings very effective in protecting against impact.

Studies by Kim and Kang showed a non-linear behavior between impulse and thickness (125). Our studies identify non-linear behavior with significant scatter. It is possible that the thickness range tested is too narrow to see any significant change in the critical maximum contact force or critical impulse with respect to thickness. It is assumed in this work that the critical maximum contact force and critical impulse begins to plateau, for the thickness range tested.

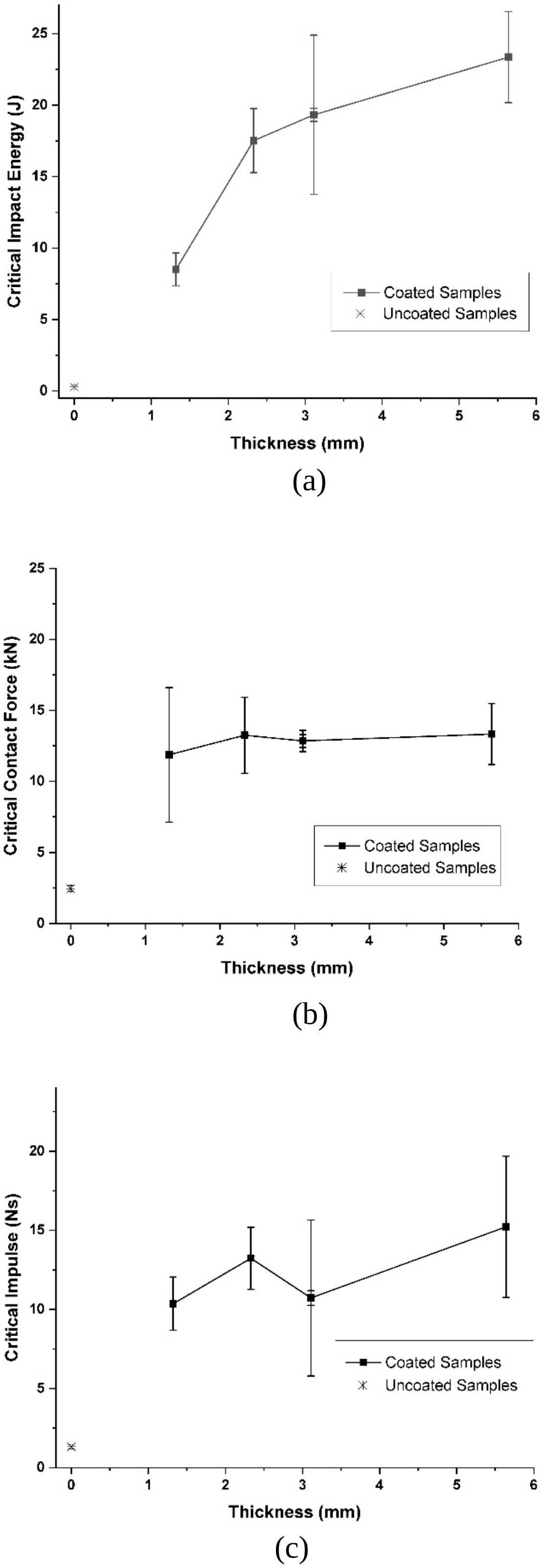

Figure 6-17: Critical parameters at failure with respect to coating thickness.

Table 6-3 demonstrates further analysis, which resulted in a coating effectiveness estimate. For coated samples of any thickness tested in this research an average critical maximum contact force over all thicknesses that may initiate failure was determined to be approximately 12.8 kN, which corresponds to a critical deceleration of approximately 3,413 m/s^2. The average critical impulse was determined to be approximately 12.4 Ns. To determine the effectiveness of a protective coating, the average critical value for maximum contact force and impulse for the coated samples was compared to uncoated samples, by dividing the coated by the uncoated critical values. The coated critical value was obtained by averaging the critical values for all coating thicknesses. The average critical maximum contact force appears to give the most conservative effectiveness of about 5.25; the average critical impulse resulted in a coating effectiveness of 9.31. Approximately this equates to an overall coating effectiveness of about 7.28. The fact that the coating effectiveness determined from the average critical impulse is significantly higher than from the average critical maximum contact force could be attributed to the fact that impulse is related to the distribution of force over the impact time interval. The maximum contact force is only concerned with the magnitude of the force, not how the force is delivered over time. Because impulse is more akin to an average force it gives a more conservative estimate of effectiveness. The maximum contact force may be the most important critical value to consider when comparing protections; it is the most aggressive estimation. It is easier to protect brittle samples from an impulse for a given duration of time, rather than a maximum contact force.

Average Critical Parameters	**Values for Coated Samples**	**Value for Uncoated Samples**	**Coating Effectiveness**	**Overall Coating Effectiveness**
Maximum Contact Force (kN)	12.82 ± 3.65	2.44 ± 0.21	5.25 ± 1.56	7.28 ± 3.24
Impulse (Ns)	12.38 ± 3.89	1.33 ± 0.14	9.31 ± 3.08	

Table 6-3: Average critical impact parameters and coating effectiveness.

6.4 Summary

This research has shown that borosilicate glass plates and most likely other brittle materials can be successfully protected in drop weight testing by a small amount of elastomeric coating if the impact parameters, such as: the maximum contact force, impulse, and applied impact energy are below their critical values. Above their critical thresholds, the samples failed, and their failure modes were affected by the coating thickness. The coating on failed samples contained a vast majority of fragments. For the uncoated samples the critical parameters at failures were much lower and the samples failed by shattering. It was noticed that the coated samples behaved more like nonlinear materials, whereas the uncoated samples responded elastically to impact. For the uncoated samples clean parabolic maximum contact force vs. time history plots were observed. On the other hand, the plots for the coated samples exhibited additional local irregularities caused by the coating and were not smooth.

The borosilicate glass samples produced significant scatter in their impact parameter results due to the inherent probabilistic behavior of failure in non-crystalline brittle materials. It was also observed that the critical impact energy increased as coating thickness increased, whereas the critical maximum contact force and the critical impulse appeared to stabilize for the smallest coating thickness (1.3 mm) and then stayed almost constant with small variations for the coating thicknesses up to 5.6 mm.

To initiate failure of the glass samples protected by the coating, the average critical maximum contact force was determined to be approximately 12.8 kN, which corresponded to a critical deceleration of approximately 3,413 m/s^2. The average critical impulse was established to be approximately 12.4 Ns. These three critical parameters at failure of the coated samples were subsequently compared with their values for uncoated samples to determine the coating effectiveness. The average critical maximum contact force provided a more conservative coating effectiveness of about 5.25, whereas the average critical impulse resulted in a less conservative coating effectiveness estimate of about of 9.31. Consequently, the overall coating effectives for all the glass samples tested in the drop weight experiments was determined to be approximately 7.28.

CHAPTER 7 FINITE ELEMENT MODELING OF INSTRUMENTED DROP WEIGHT TESTING OF COATED BOROSILICATE GLASS PLATES

Finite Element Methods (FEM) is a method for a numerical solution of field problems, where a larger structure is divided into many elements that are connected at nodes. Each element is associated with field quantities that are described by polynomials (126, 127). The arrangement of elements is called a mesh. FEM implements advanced mathematical models that are expressed through a system of partial differential equations in space and time (128). The systems of equations are solved for the unknown field quantities at each node, element by element, in a piecewise fashion (126). Generating a solution by FEM involves several key steps:

- Pre-processing: A pre-processor, like TrueGrid, is used to define geometry, material properties, loads, and boundary conditions. Mathematical models are chosen to best describe the type of dynamics each material will experience. A fluid and a brittle glass would require very different material models to describe their behavior, as an example.
- Processing: Software, such as LS-DYNA, generates structural matrices that describe the behavior of each element at each timestep and interconnects each element to its neighbor into a large solution matrix; it solves structural equations to determine material behavior at each node.

- Post-processing: The solution of many structural variables are tabulated or graphically displayed via a post-processor, like LS-PrePost. An analyst can pick and choose what variables are of interest and graphically represent them.

Finite Element Modeling can often provide useful verification of experimental results, risk assessment, or generate expected outcomes for situations that cannot be experimentally tested. If a given problem is modeled correctly, analyses can provide greater understanding of predicted material response, failure, and load distribution behavior (129).

7.1 Processing

7.1.1 TrueGrid

TrueGrid is a pre-processing mesh generating tool (130). By using a specified geometry in the program, TrueGrid generates a mesh for all the elements in a structure. The TrueGrid mesh generator uses 3-D blocks with indices according to the i,j,k coordinate system to generate surfaces, and curves, shown in Figure 7-1 (128, 130).

The first step used in TrueGrid to generate a final model mesh involves assigning a block to each material part with a specified size/dimension in the x,y,z coordinate plane. For a cylinder, as demonstrated in Figure 7-1, the central and corner indices are removed from the block. Figure 7-1b shows how the block looks once the specified indices have been removed. To obtain the correct cylindrical shape, cylindrical surface definitions are applied and visualized. The edges are moved towards the 45-degree intersections where they can be mapped to the cylindrical surface, seen in the bottom right corner of Figure 7-1c. A final cylinder generation with a complete mesh is the result (Figure 7-1d). These steps were followed for each part. The plate used in the model did not need surfaces that displayed curvature so only the step shown in Figure 7-1a was necessary.

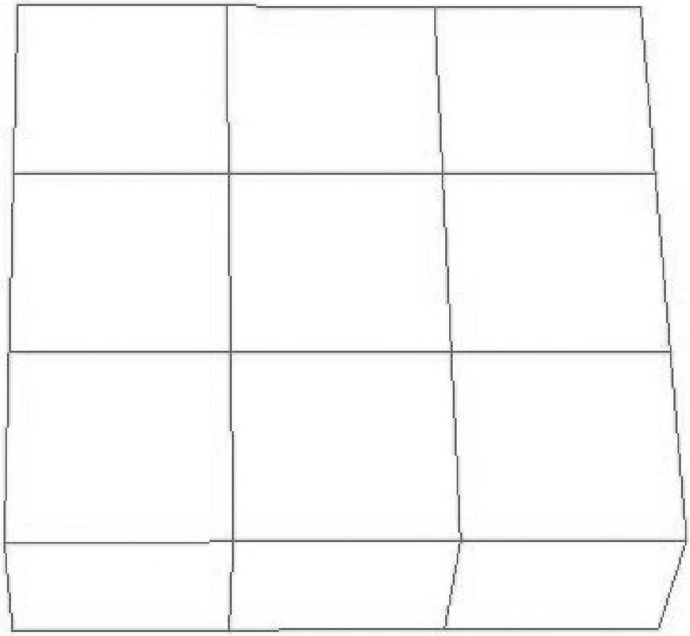

(a)

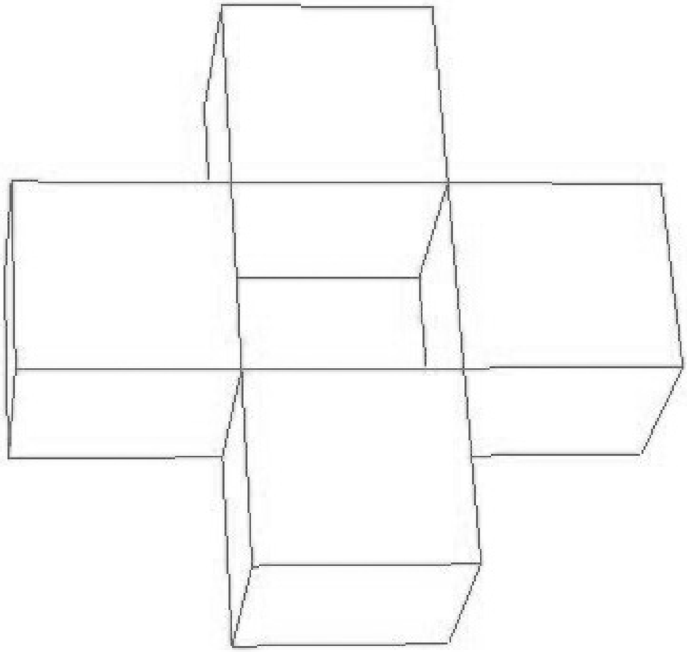

(b)

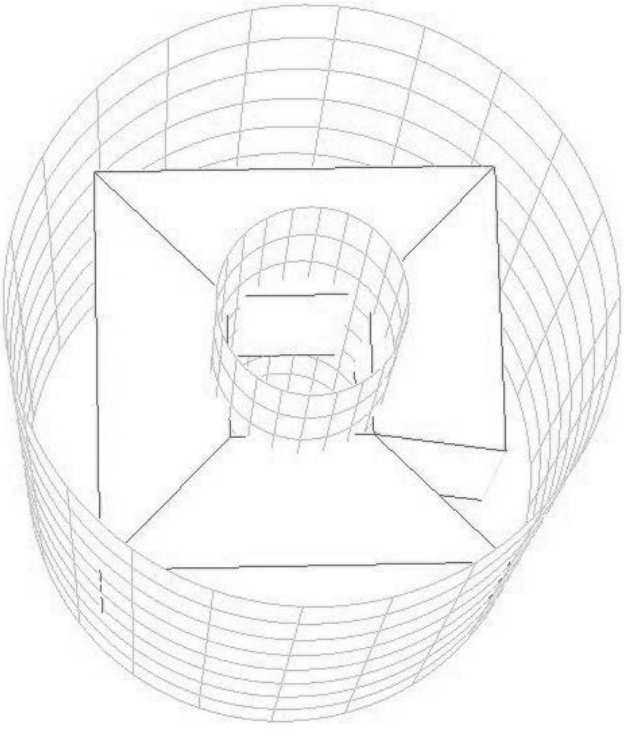

(c)

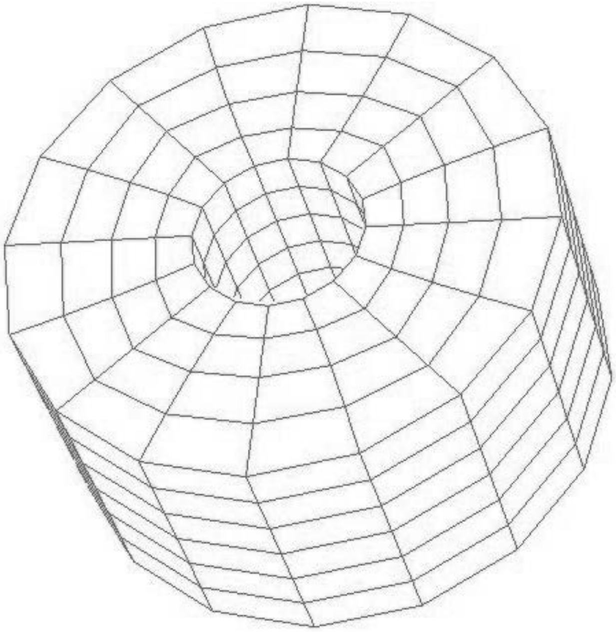

(d)

Figure 7-1: TrueGrid mesh generation steps: (a) initial block, (b) deletion of center and corner indices, (c) cylindrical surface definition and corner shifting, and (d) final meshed cylindrical die.

After generating the final model mesh, as shown in Figure 7-2, TrueGrid produces an output file that can be exported into LS-DYNA. The output file contains all the respective elements, nodes, loads, boundary conditions, connectivity, and material properties (130). A final ¼ model is shown in Figure 7-2.

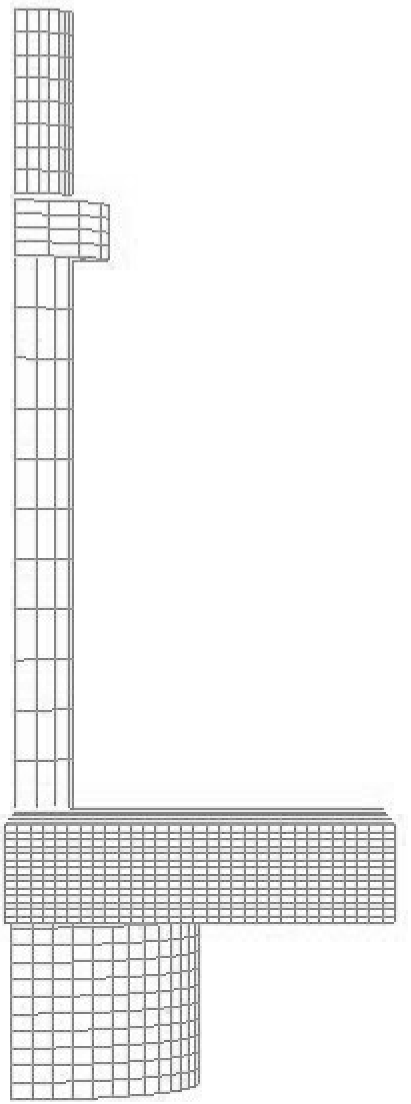

Figure 7-2: Final model mesh generation in TrueGrid.

7.1.2 LS-DYNA

LS-DYNA is a finite element solver that analyzes static and dynamic response in structures. It is particularly good at dealing with large deformations and high-velocity impact loading (131). The solution method predominantly used by LS-DYNA is the explicit solution mode. Both 2-D and 3-D element generation is used for solution methods; 3-D element generation was used in this research. Practical examples of simulations that have been performed by LS-DYNA include: simple gravitational loading of beams and plates, ballistic impacts, vehicle crashes, airbag deployment, seatbelts, rocket launches, earthquakes on dams, and many others (128, 129, 131, 132).

LS-PrePost is the post-processing portion of the LS-DYNA software that deals with the final analysis of the results. It is in the post-processor that stresses, strains, displacements, velocities, accelerations, forces, and other quantities can be examined for the duration of the simulation.

7.1.3 Finite element formulation

Analytical solutions tend to be restricted to regular geometries and simple boundary conditions. Problems faced by engineers often cannot be solved analytically because of the disproportionate amount of effort or mathematical complexities that are present. FEM can provide a numerical solution to a mathematically difficult problem by reducing the number of degrees of freedom of the system to a finite number (called discretization) (132). The derivation of the finite element formulation resulting in the system of second order ordinary differential equations with constant coefficients for time t is represented by Equation (23) (128, 133), where M, C, and K, are the mass, damping, and tangent stiffness matrices, respectively.

$$M\Delta\ddot{u}(t) + C\Delta\dot{u}(t) + K\Delta u(t) = \Delta R(t) \tag{23}$$

The vector $u(t)$ represents the relative displacements at the nodes of the elements. The velocities and accelerations are represented by the vectors $\dot{u}(t)$ and $\ddot{u}(t)$, respectively. The forcing vector $R(t)$ contains external forces. The nomenclature that will be used in Section 7.1.4 substitutes u^t for $\Delta u(t)$ and R^t for $\Delta R(t)$.

7.1.4 Explicit method

There are two common approaches used in solving Equation (23) with respect to time: explicit and implicit approximations. For dynamic loads, like the drop weight impact in our research, explicit analysis is needed when the variation of displacement with time is so rapid that inertial effects cannot be ignored. Time dependence is very important in dynamic loading because of the calculation of inertial forces at each time step (128). Only the explicit method will be discussed in this work.

As a solution is pursued, the change in displacement (velocity) at each time step, Δt, is expressed in Equation (24). The variable u is the displacement, $\dot{u}$ is the velocity, and time is t.

$$\dot{u}(t) = \frac{\partial u}{\partial t} = \left\{\frac{-u^{t-\Delta t} + u^{t+\Delta t}}{2\Delta t}\right\} \tag{24}$$

The acceleration, $\ddot{u}$, at each time step is demonstrated by the following relationship:

$$\ddot{u}(t) = \frac{\partial^2 u}{\partial t^2} = \left\{\frac{u^{t+\Delta t} - 2u^t + u^{t-\Delta t}}{\Delta t^2}\right\} \tag{25}$$

Equations (24) and (25) can be substituted into Equation (23). The result is shown in Equation (26). The solution of the unknown displacement $u^{t+\Delta t}$, at each timestep for each node is then calculated from the equilibrium values at time t and the previous time, $t - \Delta t$ (128). R, K, M, and C are mentioned in Section 7.1.3.

$$u^{t+\Delta t} = \frac{R^t - \left(K - \frac{2}{\Delta t^2} M\right) u^t - \left(\frac{1}{\Delta t^2} M - \frac{1}{2\Delta t} C\right) u^{t-\Delta t}}{\left(\frac{1}{\Delta t^2} M + \frac{1}{2\Delta t} C\right)} \tag{26}$$

7.2 Model generation

For model generation each part was dealt with separately. There were five separate parts in the model: steel drop weight, steel cylindrical die, steel indenter pin, square glass plate, and polymer coating layer. Each part is defined in the input data according to the material type that best represented their failure behavior. The model was reduced to one quarter the size of the full model with symmetry conditions assigned to every part. This allowed for a reduction in the run time cost involved in simulating the drop weight impact numerically.

Contacts

To prevent nodes from merging into each other a penalty-based surface to surface contact was used, which allows sliding and no penetration from one surface to another. To define contact between two surfaces, LS-DYNA assigns a master and slave to the contact surfaces that are touching. Figure 7-3 shows the representation of the master and slave contact surface for the cylindrical die and the glass plate. The only two parts that did not have contacts assigned were the coating layer and the glass plate. These two layers are bonded together experimentally and were allowed to merge in the model.

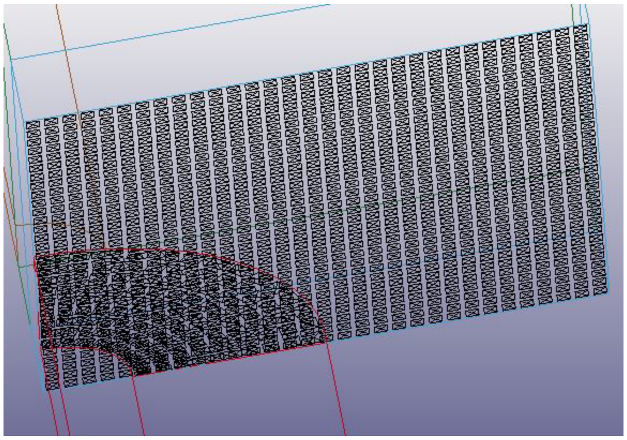

Figure 7-3: LS-DYNA graphical representation of master and slave contact surface for the cylindrical die and glass plate.

Element formulation

Every element used in this model was a fully integrated solid element. Fully integrated solid elements have 8-nodes and 6 integration points, as demonstrated in Figure 7-4. Fully integrated elements require longer run times. It was decided to do the fully integrated element formulation because the results were closer to the experimental values. Fully integrated elements can create instability in high-impact simulations and a few instances of the thinner coatings at higher drop weight impact energies created a negative volume error, to be discussed further in Section 7.3.3. In those cases, the element formulation was changed to a constant stress solid element with one-point integration and hourglass control was set to the Flanagan-Belytschko stiffness form.

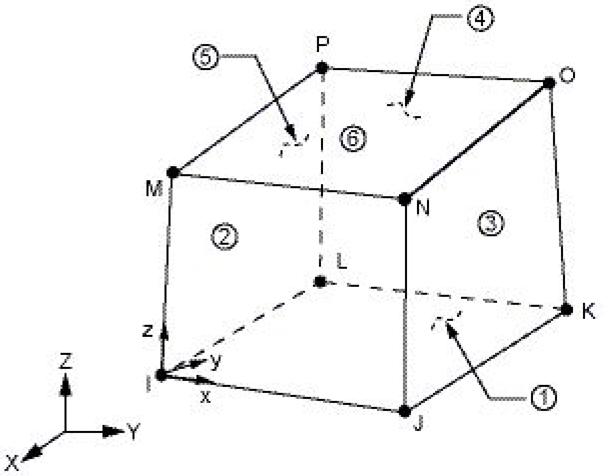

Figure 7-4: Representation of a fully integrated 8-noded solid element. Reproduced from ref. (134).

Mesh

A hexagonal mesh type was used in this model. In LS-DYNA the mesh size controls the timestep of the simulated run. Smaller meshes slow down run time. For this model the element mesh size ranged from 5.37 mm^3 to 20.74 mm^3 (smallest side being 1.02 mm and the largest side being 6.93 mm).

7.2.1 Drop weight, indenter pin and cylindrical die

The drop weight, indenter pin and cylindrical die are three separate parts in this model. However, they use the same material type. The material type chosen to represent these three parts was *MAT_001 (MAT_ELASTIC). This material type is an isotropic elastic material that can be used on solid elements (135).

The geometry for the drop weight, indenter pin, and the cylindrical die is specified in Table 7-1. It is important to note that the drop weight height dimension used in this model is not the same as the experimental drop weight height dimension.

Therefore, the mass density used in the input file was adjusted to make sure the actual experimental drop weight mass was reflected in the model, assuming the same density per unit volume listed in Table 7-2.

Part	Height	Diameter (OD)	Diameter (ID)
Drop Weight	25.40 mm	15.75 mm	----
Indenter Pin	83.82 mm	15.75 mm	15.75 mm
Cylindrical Die	25.40 mm	50.80 mm	15.88 mm

Table 7-1: Drop weight, indenter pin and cylindrical die model geometry.

The material properties follow the stated values in the literature for standard carbon steel (136, 137) and are listed in Table 7-2.

Material Property	Metric
Density	7.84 g/cm^3
Young's Modulus, E	200 GPa
Poisson's Ratio	0.3

Table 7-2: Drop weight, indenter pin and cylindrical die material properties.

Boundary conditions are important for setting allowable movement in an FEM model. If the parts can move freely with no specified boundary conditions, the model could become nonsensical; parts can move anywhere they want with no correlation to reality. The drop weight and indenter pin were bound in such a way that only movement in the y-direction (up and down) was allowed. The cylindrical die was set so that no movement was allowed in any direction.

The drop weight was given an applied velocity using the INITIAL_VELOCITY command. Velocities were selected based on the drop height assumed in the test run. Velocities were chosen ranging from 1.58 m/s to 3.87 m/s.

7.2.2 Glass plate

The glass plate in this model used the material *MAT_024 (MAT_PIECEWISE_LINEAR_ELASTIC). This material type is an isotropic elastic material that could be used on any type of element (beam, shell, solid) (135). The boundary conditions were set to allow movement in the y-direction only.

The geometry for the glass plate was set to match the same experimental plate geometry used in Chapter 4.4.3 of 10.16 mm x 10.16 mm x 0.635 mm. The material properties used for the glass plate follow the stated values for 7740 corning borosilicate glass (138, 139) and are listed in Table 7-3.

Material Property	Metric
Density	2.23 g/cm^3
Young’s Modulus, E	64 GPa
Poisson’s Ratio	0.2
Yield Stress	70 MPa

Table 7-3: Glass plate material properties.

Borosilicate glass is a brittle material with no plastic region in its stress-strain curve, shown in Figure 7-5. The yield stress becomes the same as the ultimate tensile stress. The yield stress varies between 30 to 100 MPa (140). In this case, 70MPa is assumed as the yield stress value.

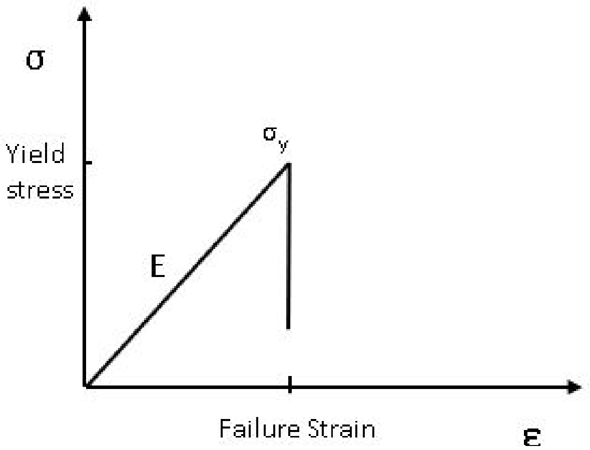

Figure 7-5: Representative stress vs. strain curve for glass. Reproduced from ref. (140).

7.2.3 Polymer coating layer

The polymer coating in this model used the same material *MAT_024 (MAT_PIECEWISE_LINEAR_ELASTIC) that was used for the glass, however the input parameters were different. A tangent modulus was specified for the polymer, whereas it was not for the glass. The geometry of the polymer only differed from the glass geometry by the thickness specified, because the width and the length were the same as the glass. The thicknesses used in the model were 1.32 mm, 2.33 mm, 3.11 mm, and 5.64 mm. The boundary conditions used for the polymer coating layer were the same as the glass plate, only allowing movement in the y-direction.

The material properties of the polymer coating required experimental testing, discussed further in Chapter 7.4. Table 7-4 lists the material properties used in the model along with the source for the information.

Material Property	**Metric**	**Source**
Density	1.08 g/cm^3	(141)
Young's Modulus, E	141 MPa	Chapter 7.4
Poisson's Ratio	0.4	(142)
Yield Stress	10.7 MPa	Chapter 7.4
Tangent Modulus	6.7 MPa	Chapter 7.4

Table 7-4: Polymer coating material properties.

7.3 Checks and issues

7.3.1 Convergence study check

To ensure that the proper mesh size was selected, which balanced run time and the value of the final result, a convergence study was performed. The mesh was increased until the convergence plot for the maximum contact force, shown in Figure 7-6, leveled off in value. Where the plot leveled off indicated a good safe number of nodes that would not result in an inaccurate answer. This convergence in the plot indicates the least amount of run time required. The convergence study was done on a 6.35 mm thick coated model at a drop weight impact energy of 12.98 J.

The logarithm of the degrees of freedom (DoF) was plotted on the x-axis and was used to represent the number of nodes present in the model. To find the DoF the number of nodes were multiplied by the number of axes used. A 3-D program assumes three axes per node. A medium mesh was selected for the model, with a total number of 18,485 nodes.

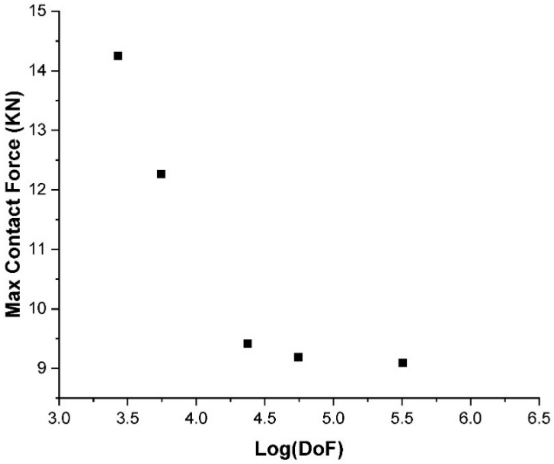

Figure 7-6: Mesh convergence test.

7.3.2 Hourglass control check

Hourglass modes are nonphysical, zero-energy modes of deformation that produce zero strain and no stress. Hourglass modes occur only in under-integrated solid, shell, and thick shell elements (143). This model used the stiffness-based hourglass control (type 4) algorithm.

In some cases, a fully integrated element produced instability, mentioned in Section 7.2. Therefore, hourglass control was set. To verify that hourglass control was working properly, plots were run using a matsum command in LS-PrePost and the internal hourglass energy were checked for each part. Figure 7-7 demonstrates an hourglass check for the coating material part for a simulation with 1.32 mm coating thickness and 17.3 J of impact energy. It can be identified that some hourglass energy occurred during the impact at about 13% of the internal energy. Because the hourglass data differed significantly from the fully integrated data, further data analysis did not include results from simulations that required hourglass control.

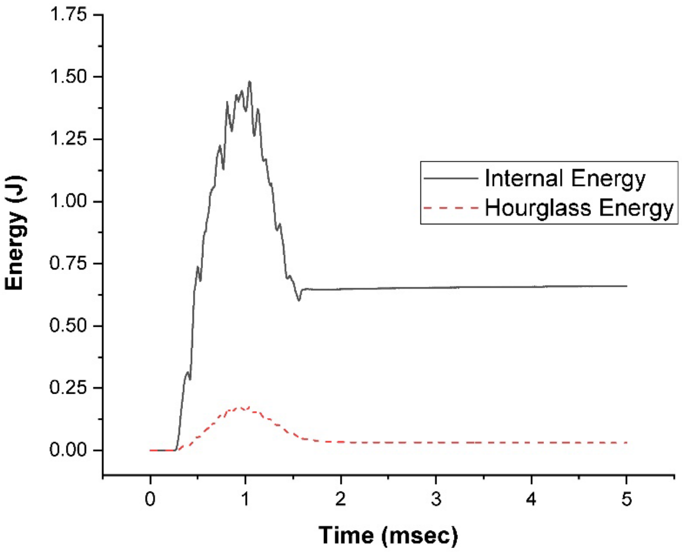

Figure 7-7: Hourglass energy check.

7.3.3 Issues

While running a simulation several issues can occur. Two that were encountered during this work were negative volume and added mass. Both issues will distort the final result and create an inaccurate model.

Negative volume occurs when an element becomes distorted in such a way that the volume of the element becomes nonsensical. LS-DYNA stops all simulations once negative volume occurs. High-velocity impact can induce large deformations in an element producing the negative volumes that were seen. For this model, the only way to successfully fix negative volume was by using hourglass control and dropping from fully integrated elements to one-point integration. Negative volume with hourglass correction was used for the 1.32 mm thick coating at impact energies above 12.98 J and for the 2.33 mm thick coating at impact energies above 17.3 J. As mentioned previously in Section

7.3.2, hourglass control results differed significantly from the fully integrated elements, so it was decided not to include the results with the final analysis.

Another issue that arose was from added mass. This is also called mass scaling. Adding mass occurs when the timestep drops below the timestep allocated in the program. During simulation, mass is added to an element to increase its density, which reduces the speed of sound and increases the timestep needed to solve the simulation. Adding mass introduces error in a simulation in an effort to increase the run time (140). This was corrected by reducing the allowable timestep. For all simulations, it was verified that no mass was added to the model.

7.4 Experimental testing for polymer properties

FEM can be used to provide physical insight into the impact behavior of the coated glass samples. However, FEM requires a material constitutive model as an input; the tensile modulus (Young's modulus), tangent modulus and yield stress of the coating were parameters required by the FEM input.

Sheets of 3 mm thick elastomeric coating used in Chapter 5 were provided by Line-X of Boulder for tensile testing. The sheets were cut into four type I dogbone samples, shown in Figure 7-8, with a width of 11 mm and a gauge length of 67 mm. A United STM-50KN Testing Machine (United Calibration Corp., CA) with a United TVI113993 1000 lbf load cell was used to perform the tensile testing following ASTM D638 (144) at a strain rate of 8.5 mm/sec (20 in/min). Figure 7-9 shows a representative stress strain curve from one of the tensile tests.

Figure 7-8: Elastomeric coating dogbone sample.

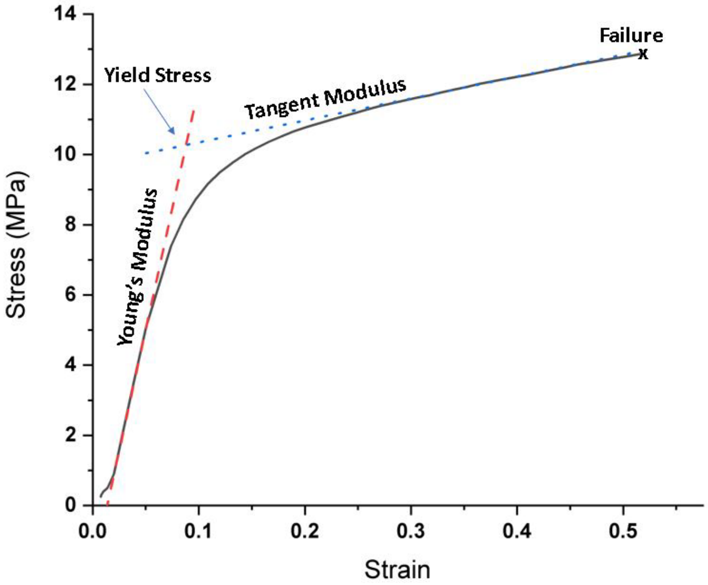

Figure 7-9: Stress vs. strain curve for elastomeric coating sample.

The results from tensile testing for the elastomeric coating used in this research identified that the strain was 52%, which is less than the value cited in the literature of 91.2% for Line-X XS-100 (99). The discrepancy could be explained by the choice to use the load cell rather than an extensometer to measure strain. The crosshead extension from the load cell includes the strain occurring in the grips, around the larger dogbone head area, and the strain in the gauge length; an extensometer would only measure the true strain inside the gauge length.

The Modulus of Elasticity was found to be 141 ± 11 MPa, the yield stress was 10.7 ± 0.8 MPa and the tangent modulus was 6.7 ± 0.5 MPa. It is important to note that the actual tangent modulus may have registered as a lower value if an extensometer was used, instead of the load cell.

7.5 FEM model results and discussion

7.5.1 Numerical method

After each simulation was run, the y-acceleration values located for a specified node on the front face of the drop weight were exported to an excel file. The output file was analyzed using the same MATLAB program and method described in Chapter 6.2.2. The only difference was that the Butterworth filter used on the FEM data was a 4th order instead of a 10th order filter. The reason for the change to a 4th order filter had to do with the ability of MATLAB to read the noisy dataset from the FEM acceleration. The vibration dampener, discussed in Chapter 6.2.2, experimentally reduced the high frequency harmonics created by the drop weight and indenter pin impact. Numerically, the vibration dampener was not modeled. Therefore, the FEM dataset had significantly more high frequency noise.

7.5.2 Time history plots

Experimental results from Chapter 6.3.2 were compared to FEM simulations to verify trends. The impact parameters were determined from the force time histories in the same way as the experimental results. The impact parameters are listed in Appendix G.

FEM results in Figure 7-10, Figure 7-11 and Figure 7-12 demonstrated time force histories with the same trends as experimental results from Figure 6-9, Figure 6-10, and Figure 6-11, with a few differences. The similarities and differences between the experimental and numerical time histories from the above mentioned six figures are listed in the following bulleted list.

1. The experimental time history plots for the coated samples displayed large bumps in the contact force as it moved towards its maximum. Numerically this was the case for the thickest coating only.
2. For the uncoated sample it was seen both experimentally and numerically that the contact force displayed an elastic behavioral response by returning to zero. However, the contact force maximum was approximately twice as large numerically (5.25 kN) as it was experimentally (2.5 kN). Experimentally, this may have been due to flaws introduced to the glass surface because of handling.
3. For the thin coatings, the contact force maximum was about the same, numerically and experimentally. Both showed a marked increase over the uncoated samples, respectively. For the thickest coating the contact force maximum was less numerically than experimentally.
4. The contact force for the thickest coating did not return to zero in the experimental results. For the FEM results the contact force returned to zero.
5. It was observed in the time history plots for the experimental and numerical uncoated sample, that the maximum contact force, the zero-velocity point, the maximum impactor displacement, and the maximum energy transferred to the

sample all occurred approximately simultaneously. For the coated samples, the contact force maximum preceded the other three quantities numerically. Experimentally, the contact force maximum only preceded the other three quantities for the thickest coating.

6. The displacement for the uncoated and coated samples did not return to zero in the numerical results, which matched the experimental results.
7. The impact duration shows similar trends for the experimental and numerical results: the thicker sample has a more spread-out time duration than the thinner sample.
8. The drop weight rebound velocities of the coated samples were always less than the original impact velocity, both experimentally and numerically.
9. Experimentally, the thicker coating produced a smaller rebound compared to the thinner coating at the same impact energy. Numerically, the thicker and thinner coating demonstrated similar changes in rebound velocity.
10. The uncoated sample showed the rebound velocity was approximately equal to the impact velocity, both numerically and experimentally. This suggest an elastic collision.
11. Experimentally, the thicker coating took more energy away from the rebound, as shown by the larger transferred energy that occurred at the end of the impact. Numerically, the transferred energies were the same for the thin and thick coating.

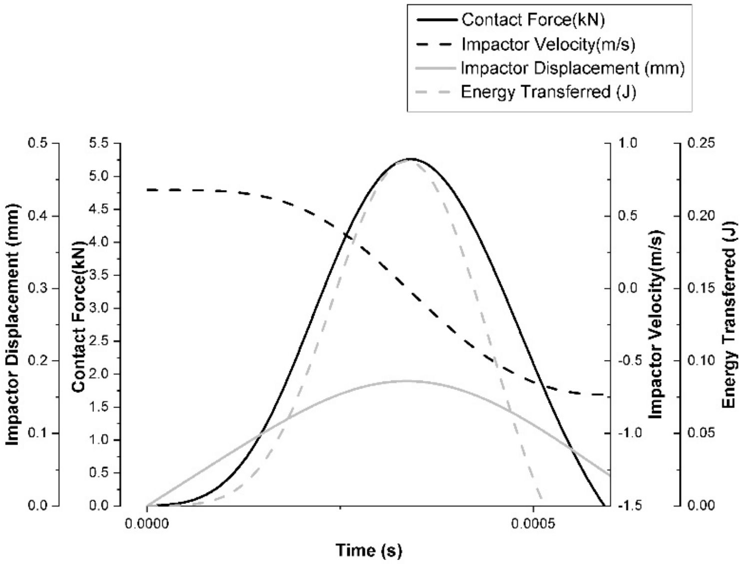

Figure 7-10: Time history plot for FEM simulation of uncoated sample at 0.23 J of impact energy.

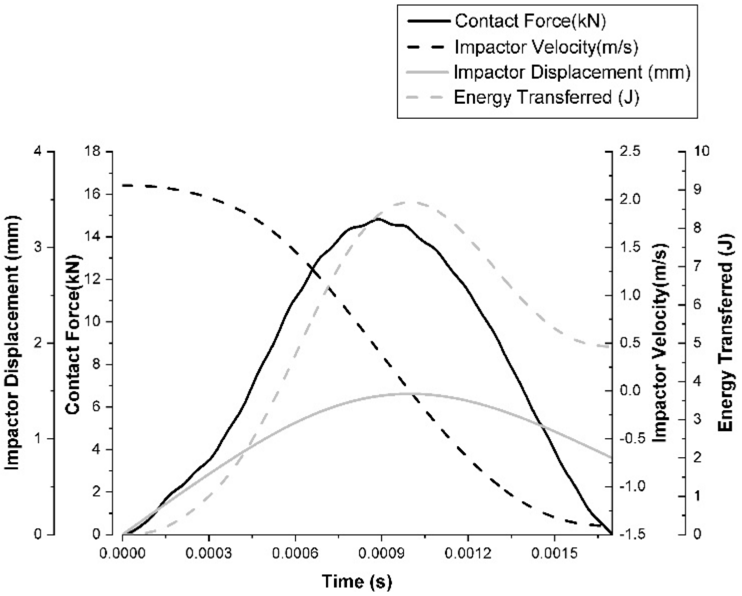

Figure 7-11: Time history plot for FEM simulation of 1.33 mm coating at 8.6 J of impact energy.

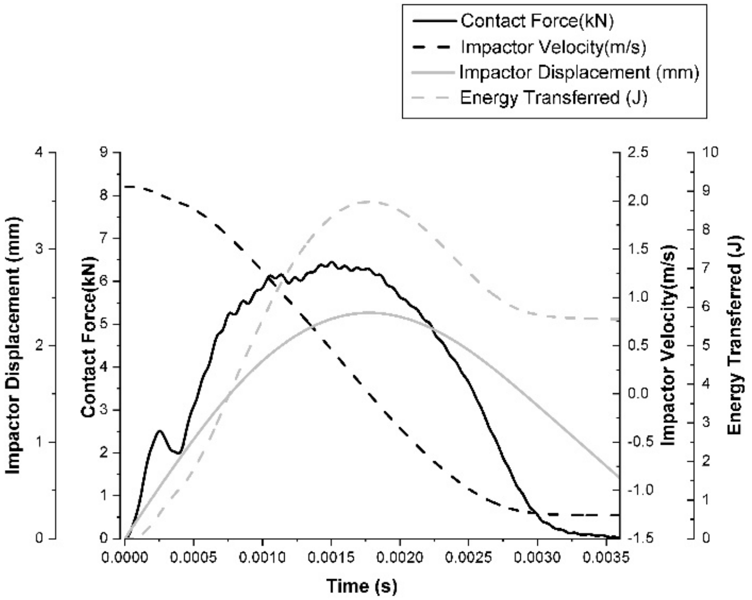

Figure 7-12: Time history plot for FEM simulation of 5.64 mm coating at 8.6 J of impact energy.

7.5.3 Maximum contact force and impulse comparisons

Contact force

Experimental and numerical results for the maximum contact force (Figure 7-13) show different values but demonstrate similar trends in behavior. Uncoated samples in Figure 7-13a showed an increasing trend, however it is uncertain if the increasing trend was linear or non-linear. In Figure 7-13b, experimental coated samples that did not fail demonstrated an increasing relationship between maximum contact force and impact energy. Numerical results further demonstrated that the increasing trends were non-linear. Samples with thinner coatings experienced the largest maximum contact force, which was evident both experimentally and numerically.

It is important to note that the error present in the uncoated and coated numerical results stems from error that is present in the entire model as opposed to the physical properties of the polymer layer. This was determined based on the error present in the uncoated sample (Figure 7-13a), when no polymer was present. Possible sources for the error in the model could be: impact between the drop weight and the indenter pin, the material type used for the glass, the Butterworth filter applied to the acceleration readings, or any number of other factors not discussed.

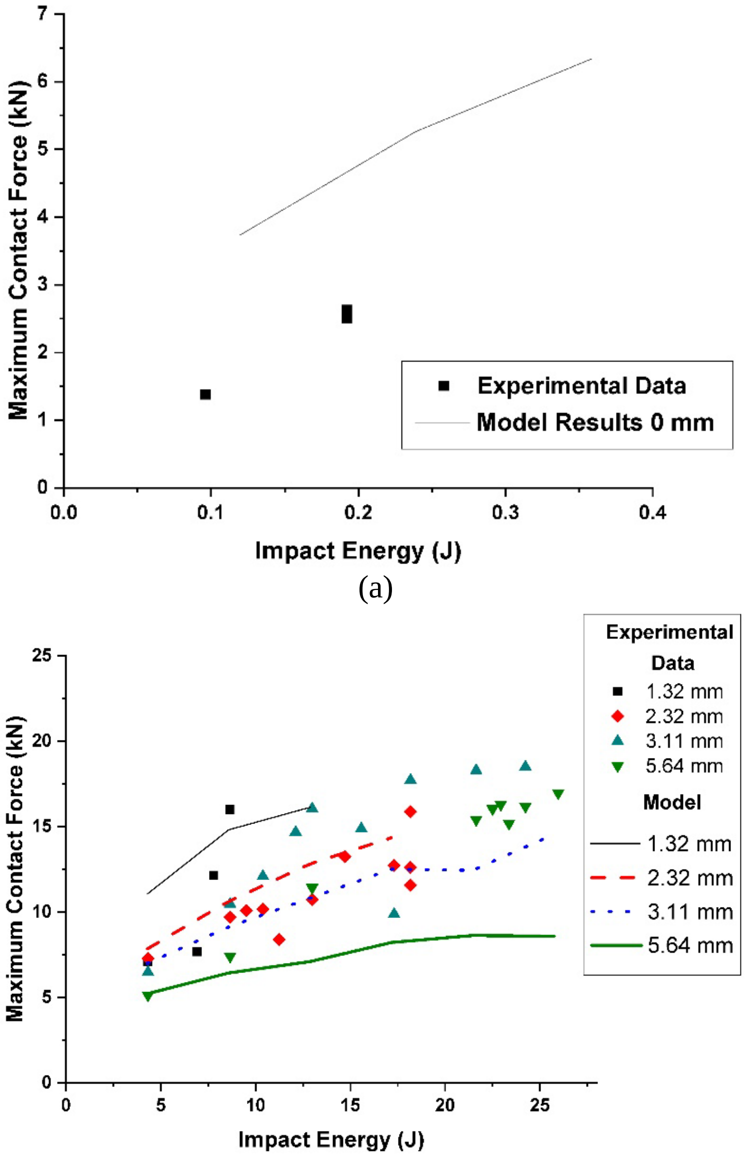

(a)

(b)

Figure 7-13: Maximum force (a) uncoated samples and (b) coated samples.

Impactor displacement

The normalized displacements (displacement per unit coating thickness), for all un-failed coated experimental results and numerical results as a function of impact energy are shown in Figure 7-14. Numerical and experimental results showed the same trends, that normalized displacements decrease with impact energy for a given coating thickness. Experimentally, a rough s-shaped response was observed, but numerically it followed a more linear response.   In Chapter 6.3.2.2, it was described that the dashed line seen Figure 7-14 represented the normalized value where the coating thickness and impactor displacement were equal. Values above the dashed line represented displacement dominated by bending of the glass plate; values below the dashed line represented displacements dominated by coating deformation. Numerically, the coating deformation zone is more prominent, except for the thinnest samples at higher impact energies; experimentally this was not the case. Only the thickest coating showed coating deformation predominant in the normalized impactor displacement.

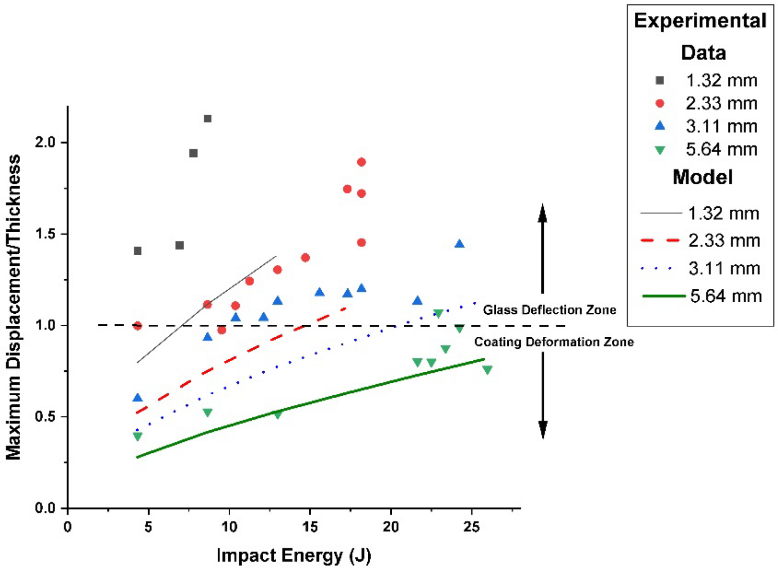

Figure 7-14: Numerical and experimental normalized maximum displacements.

Impact Duration

The scatter in the experimental data in Figure 7-15 made it difficult to decipher if the time duration and the time to maximum contact force were constant or slightly increasing. Numerical results further clarified that the trend was increasing with thickness. The numerical and experimental values for the time to maximum contact force matched up better than the values for impact duration. The numerical results do not support the initial experimental assumptions from Chapter 6.3.2.2 and research by Elavenil and Knight, that claim that the time to maximum contact force and the total duration of impact appear to be constant irrespective of thickness (100).

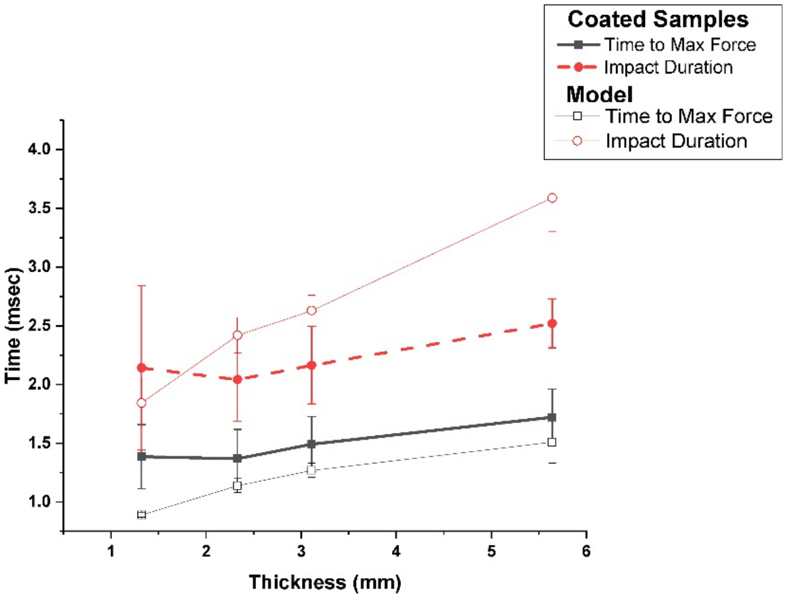

Figure 7-15: Numerical and experimental results for impact duration and time to maximum contact force.

Impulse

Numerical and experimental results agreed in Figure 7-16 that impulse demonstrated an increasing relationship with respect to impact energy. It is difficult to ascertain any type of trend in the experimental uncoated samples (Figure 7-16a); numerically the increasing trend was demonstrated.

The numerical and experimental trends were rather surprising for impulse. Numerically, it was shown that the impact duration with respect to thickness was increasing as opposed to constant, as was assumed experimentally Chapter 6.3.2.2. Contact force was also shown to be affected by coating thickness. Therefore, it was surprising to see that the contact force and impact duration components of impulse appeared to be negating each other. Impulse is numerically shown to be unaffected by coating thickness.

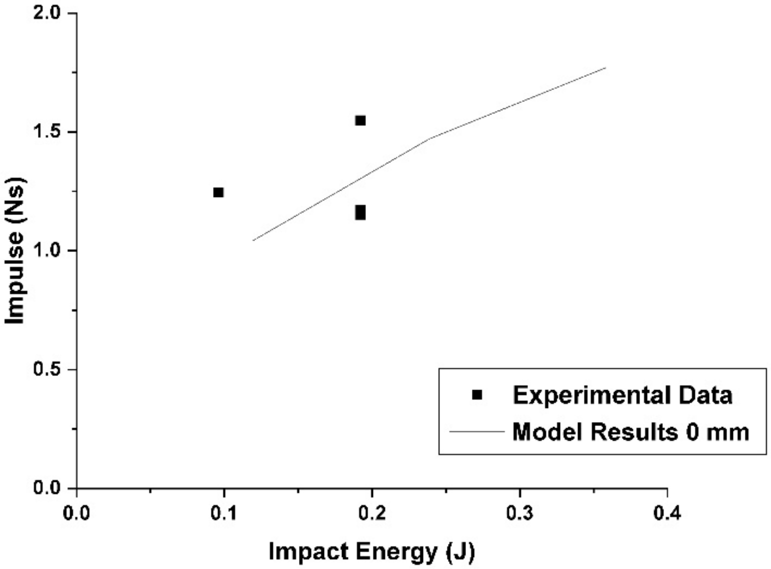

(a)

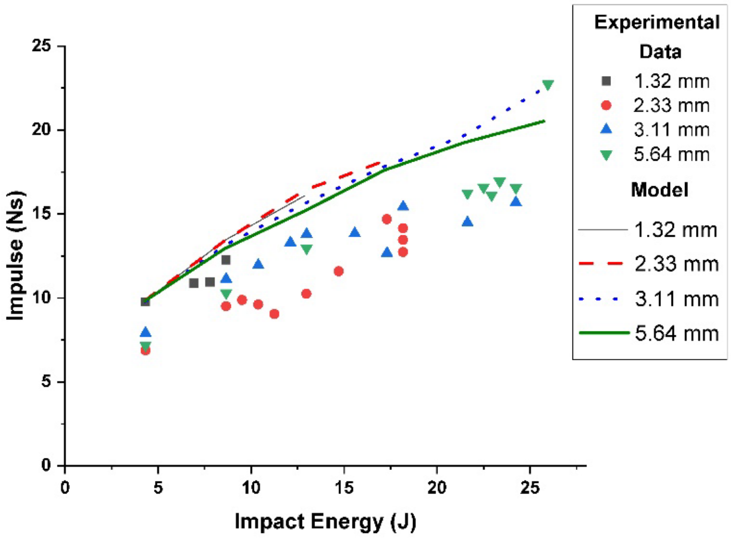

(b)

Figure 7-16: Impulse (a) coated samples and (b) uncoated samples.

7.6 Summary

The numerical results from FEM agreed with the experimental results from Chapter 6, with a few exceptions. Some differences were present in the time force histories for uncoated, 1.33 mm, and 5.64 mm coated samples. The differences consisted of: curve shapes, contact force behavior, and transferred energy behavior.

General trends in experimental impact parameter results (contact force, displacements, impulse) matched numerical results, while the actual values were slightly different. The exception was the impact duration and time to maximum contact force. Experimental results assumed constant behavior irrespective of coating thickness. However, it was shown numerically that the coating thickness had an increasing effect on the impact times.

The goal of FEM was to provide useful verification of experimental results or further clarification of the types of trends seen in the data. In this case, differences in the types of increasing trends (i.e. non-linear or linear) were seen, which were hard to decipher in experimental results. Contact force was experimentally determined to be increasing with respect to impact energy. Numerical results further elucidated that the increasing trends were non-linear and began to level off. Impulse was experimentally shown to be increasing as well, but the numerical results were able to further clarify the trend was non-linear and results were unaffected by coating thickness.

If needed, the simulated drop weight testing could be extrapolated further past the capabilities of the experimental drop weight tester. The FEM simulations of the drop weight were useful for further clarification of trends and behaviors when the probabilistic nature of experimentally tested specimens created too much scatter to make firm conclusions.

CHAPTER 8 FULL-SCALE TESTING OF TRANSFORMER BUSHINGS

This research evaluated a spray applied coating that could be used to protect existing bushings from explosive fragmentation. This chapter describes the first ever application of an elastomeric coating on a full-scale pressurized transformer bushing for protection against mechanical damage during high-velocity impact. It also provides a validation of the modeling work performed on pressurized uncoated borosilicate cylinders in Chapter 3. Linear and power fit predictions of percent mass loss for full-scale bushings subjected to rifle bullet impact from Chapter 5, were verified through full-scale bushing tests with 3 mm of coating thickness under an impact energy of 3.1 kJ.

8.1 Materials and methods

For full-scale impact tests, four transformer bushings were supplied from various Bureau of Reclamation facilities. Two LAPP 115kV bushings and two Hunan Gaoqiang Electrical Ceramic and Appliance Co.(HNGQ) bushings were tested. One of each type of bushing was coated and one was not. Figure 8-1 shows the uncoated bushings and Figure 8-2 shows the coated bushings used in this research. The LAPP bushings were 1118 mm (44”) tall with a diameter ranging from 178 mm to 305 mm (7” to 12”). The HNGQ bushings were 737 mm (29“) tall with a diameter ranging from 229 mm to 356 mm (9” to 14”). All bushings were a minimum of 19 mm (0.75”) thick, with the exception of the HNGQ bushings, with a minimum thickness of 25 mm (1”). The thickness varied as the bushing petticoat profile changed. The elastomeric coating was applied using the same method described in Chapter 5.1. A coating thickness of 3 mm was chosen based on the exponential fit method used in Chapter 5.3.1.

(a)

(b)

Figure 8-1: Two types of bushings used in this research. (a) bolt-mount and (b) rod-mount.

(a)

(b)

Figure 8-2: Pre-test condition of coated bushings (a) bolt-mount and (b) rod-mount.

Two high-speed cameras were used to photograph and record the pressurized transformer bushing impact events: a Chronos 1.4 and a Phantom VEO 710. The Chronos 1.4 high-speed camera recorded at 3,587 frames per second at a resolution of 800 x 480. The Phantom VEO 710 high-speed camera operated at 16,000 frames per second and a resolution of 512 x 256.

The four bushings were pressurized to 345 kPa (50psi) with an air compressor. The pressure inlet port entered through the top plate of all pressurized bushings. The LAPP bushings were mounted simply with bolts and gaskets to create a seal and were not under compression. The HNGQ bushings were mounted using a rod under compression and gaskets to create a seal. Figure 8-3 shows the two different mounting styles used for the bushings. The pressure and temperature were monitored during the test and remained stable and consistent. The bushings were impacted with a .308 Winchester rifle cartridge using a Steyr SSG rifle at an impact velocity of 750 m/s, and a bullet mass of 10.9 g, yielding a kinetic energy of 3.1 kJ at impact.

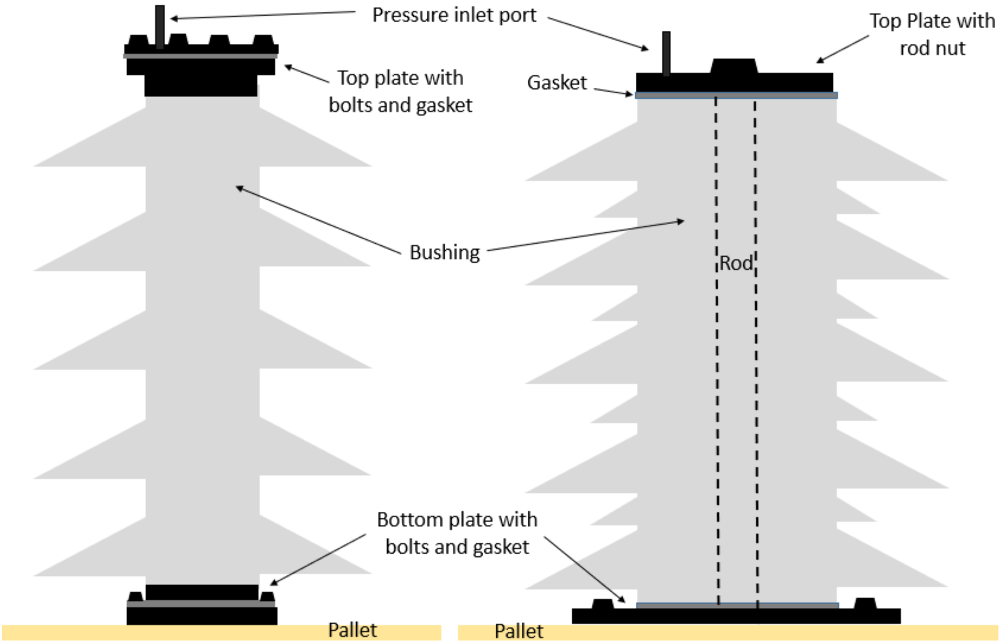

Figure 8-3: Bushing mounting style for bolt-mount (left) and rod-mount (right).

During post-impact data collection each fragment was marked in the field; the distance and angular location was determined along with the fragment mass. The bullet entrance was set to an angular location of 0° and the bullet exit at 180°. A polar plot was generated to identify the fragment location for all fragments larger than 70 g. A histogram of fragment masses collected along with a scatter plot of the mass versus distance was plotted. The bushings were weighed before and after to determine a percentage of mass loss and were visually examined to determine the extent of damage. Because of the expense associated with full-scale testing of transformer bushings, repeatability of the results was not carried out in this study.

8.2 Results and discussion

8.2.1 Impact characteristics of uncoated bushings

Visual examination of the blasts for the uncoated bushings demonstrated a strong dependence on the bushing mounting style. Figure 8-4 shows the blast response for the bolt-mounted uncoated bushing at (a) impact and after (b) 115,042 µs. The bolt-mounted bushing's top portion was ejected upwards as the pressure escaped; the bushing was not under compression. The escaping energy was more localized, and the entire bushing did not shatter. The rod-mounted bushing blast response (a) at impact and (b) after 40,125 µs is shown in Figure 8-5. The escaping pressure was forced radially throughout the bushing, shattering the entire structure, because the bushing was under compression. Visually it appeared that the fragments did not travel as far for the rod-mounted set-up, due to the explosive reaction contributing kinetic energy to fragments originating from the entire length of the bushing, as opposed to just the central portion.

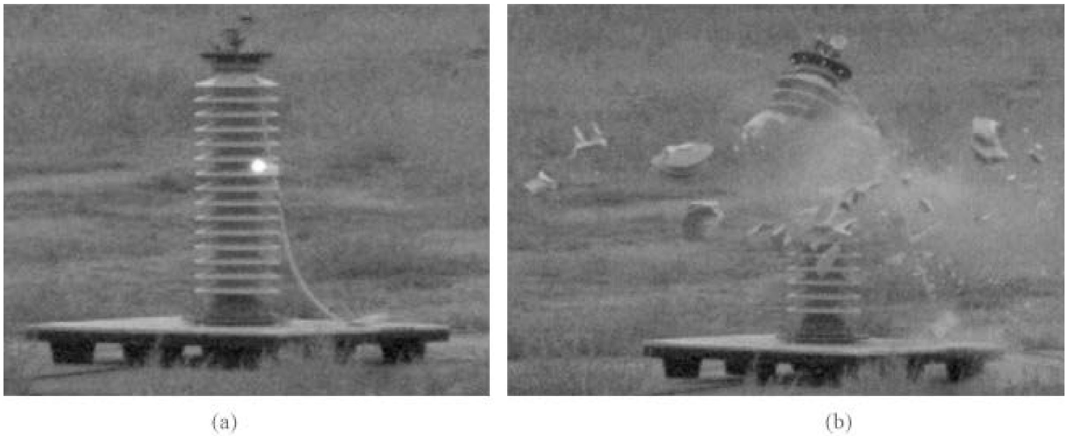

(a) (b)

Figure 8-4: High-speed images of the bolt-mounted uncoated bushing impact event.

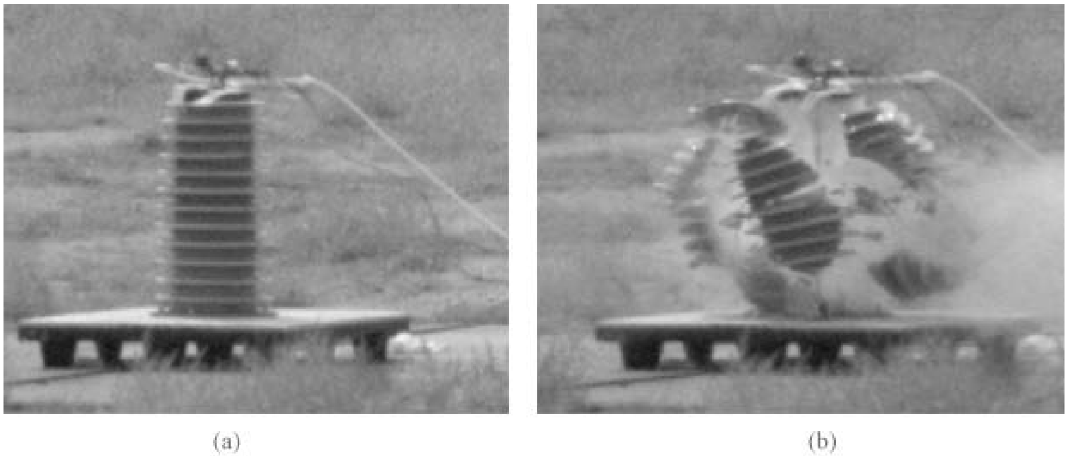
(a) (b)

Figure 8-5: High-speed images of the rod-mounted uncoated bushing impact event.

Fragment distributions, shown in Figure 8-6, identified where all the fragments rested on the ground. The bolt-mounted fragments did not travel as far for the rod-mounted bushing, which supported visual examinations. In the bolt-mounted set-up, an observed fragment maximum distance was about 12 m. The maximum fragment distance for the rod-mounted set-up was approximately 8 m. The bolt-mounted set-up showed less symmetrical fragment distribution; previous testing in Chapter 3 indicated otherwise. While there are fragments appearing in a 360° circle around the bushing (identifying the presence of symmetry), the farthest travelled fragments appeared to follow directional behavior. The rod-mounted bushing follows fully symmetric behavior, with less directional dependence; demonstrated by testing results on borosilicate glass models under pressure in Chapter 3.

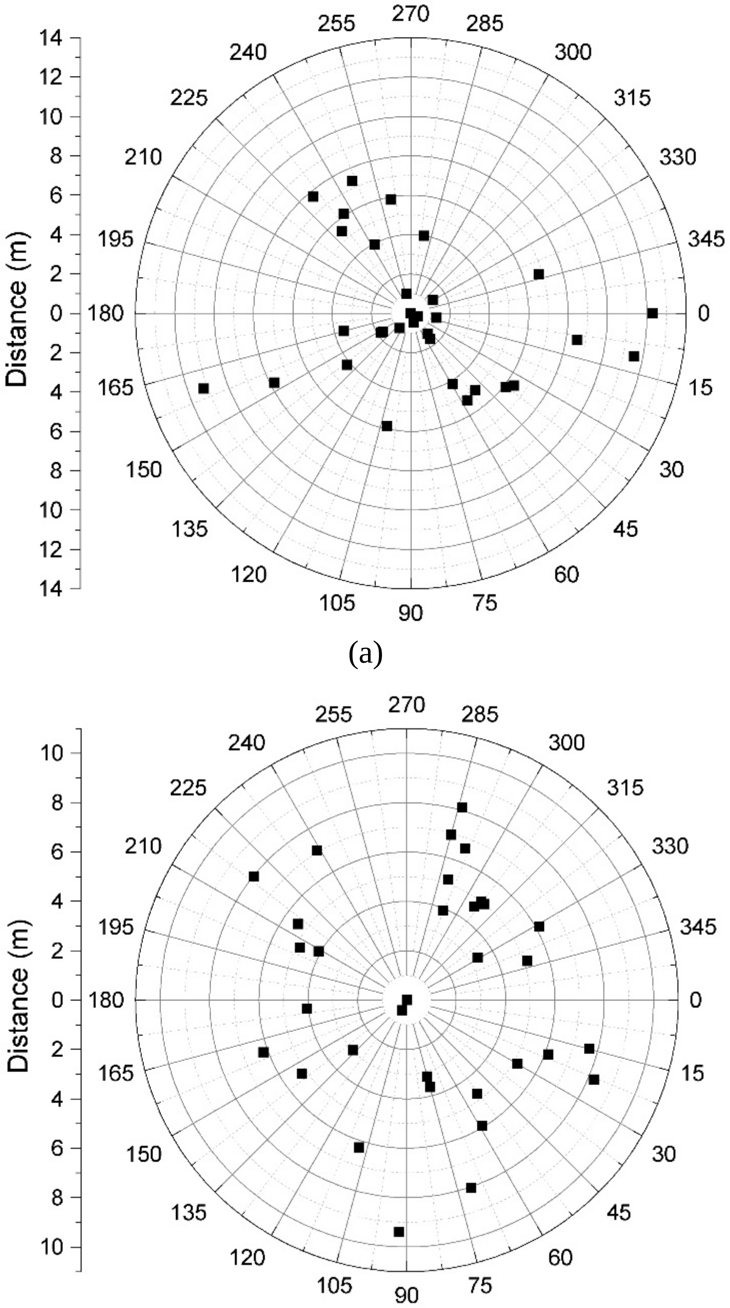

(a)

(b)

Figure 8-6: Fragmentation distribution for (a) bolt-mounted bushing and (b) rod-mounted bushing.

Mass distribution of the fragments in Figure 8-7 identified that fragmentation mass and distributions are not just affected by pressure; they are affected by the type of mounting used on the bushing. Under no compression, the bushing broke up into smaller fragments and produced the largest fragment. The largest fragment was the top portion and was ejected upwards as shown in Figure 8-4. Figure 8-8 shows the top and bottom portions that remained intact for the bolt-mounted bushing.

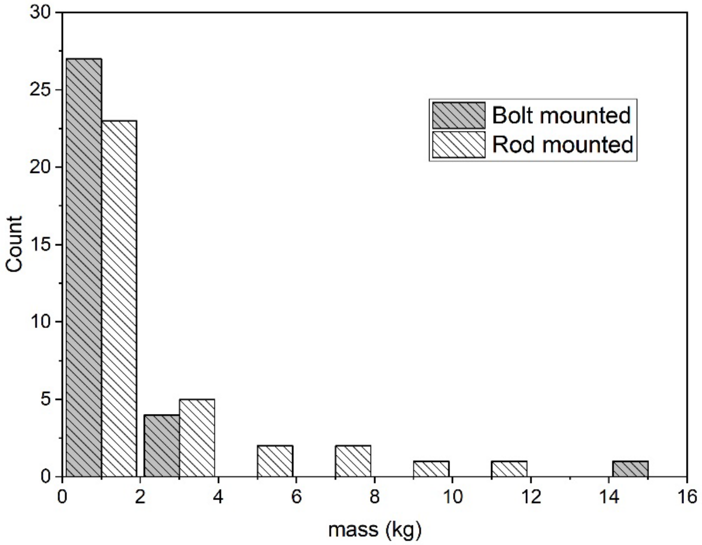

Figure 8-7: Fragment masses collected for the pressurized bushings.

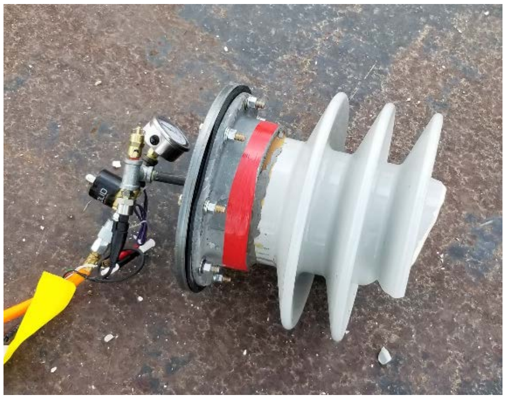

(a)

(b)

Figure 8-8 Pictures of (a) top and (b) bottom intact portions from bolt-mounted bushing.

To determine if fragment mass played a role in the distance the fragment travelled during the explosion of uncoated pressurized bushings, the mass vs. distance was plotted. In the bolt-mounted set-up, the smaller fragments travelled the farthest, in Figure 8-9. For the rod-mounted bushings, the fragment masses tended to be consistent in their distances travelled. The majority of the rod-mounted fragment masses fell within a 4 m range and were larger in mass than the ones seen in the bolt-mounted set-up.

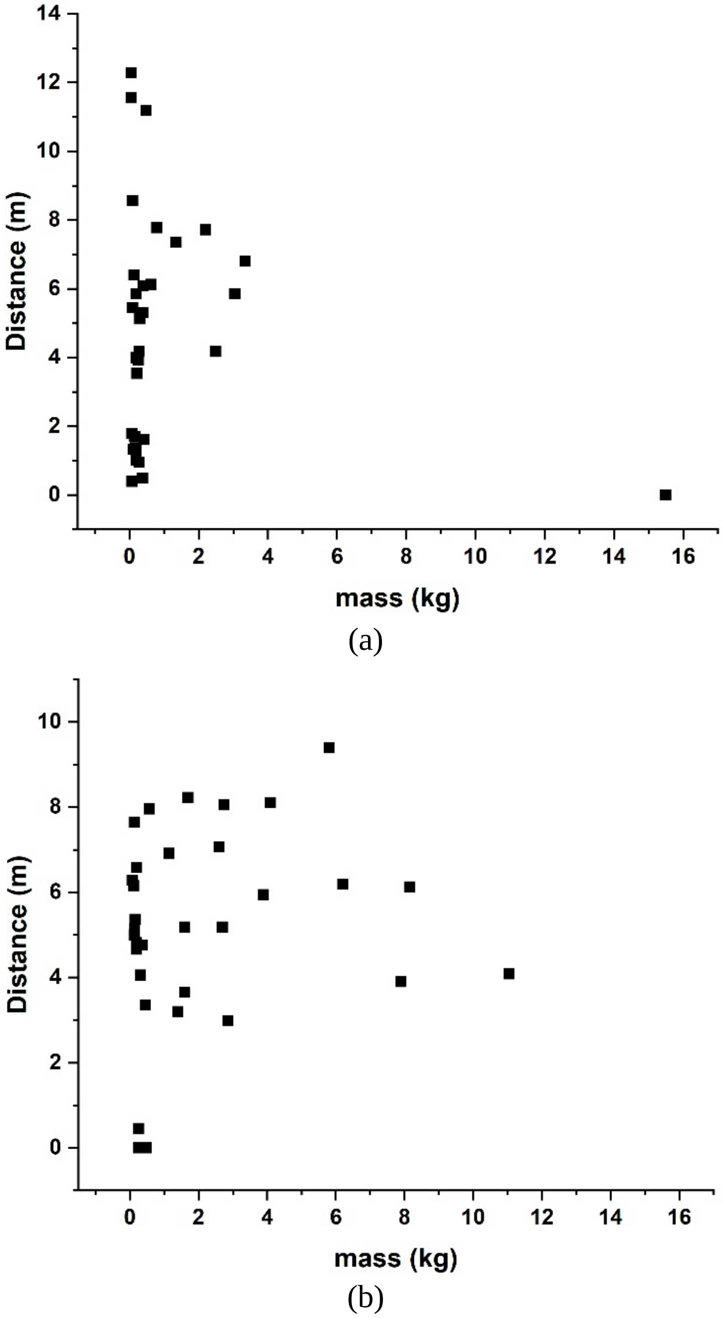

Figure 8-9: Mass vs. distance of fragments for (a) bolt-mounted bushing and (b) rod-mounted bushing.

8.2.2 Impact characteristics of coated bushings

Coated bushings changed the mode of failure in comparison with the uncoated bushings. The coating created a type of failure that would mimic the leak-before-break

(LBB) concept seen in metallic pressure vessels (26). The coating allowed the pressure to escape when the bullet perforated the bushing, preventing the explosive behavior seen in the uncoated bushings. Figure 8-10 shows the high-speed imagery of the bolt-mounted bushing: (a) at impact, (b) after 23,000 μs, (c) after 210,062 μs and (d) after 337,688 μs. It is shown in Figure 8-10b that the escaping pressure forced the top half of the bushing upwards, which severed the bushing into top and bottom halves. Figure 8-10c displays how extensive the upwards force was on the bushing; the 122.5 kg (270 lbs) bushing assembly (including the bushing, pallet, and hardware) was lifted off the ground. Despite the severing of the bolt-mounted bushing and the upwards force that lifted the entire assembly, Figure 8-10d identifies that the coating kept the bushing halves confined by stretching and pulling the halves back together.

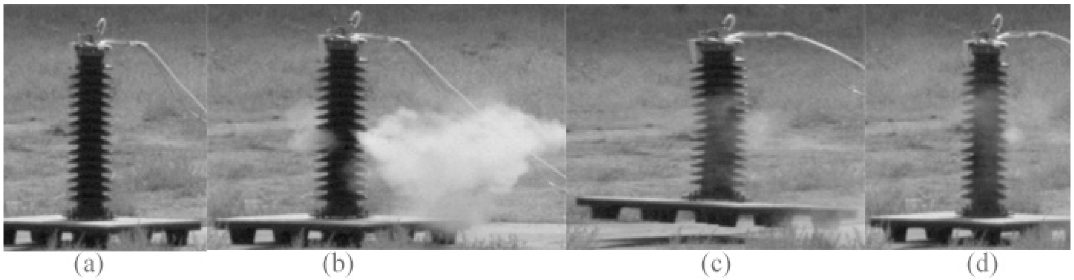

Figure 8-10: High-speed imagery of bolt-mounted coated bushing response.

Figure 8-11 illustrates where the split occurred in the bolt-mounted bushing without evidence of additional cracks. The bushing experienced one major crack around the entire circumference, which severed the bushing, with some small fragments spalling off into the inside of the bushing. The bullet impact zone was unidentifiable in Figure 8-11a because of the severing of the two halves along with the twisting and stretching of the coating.

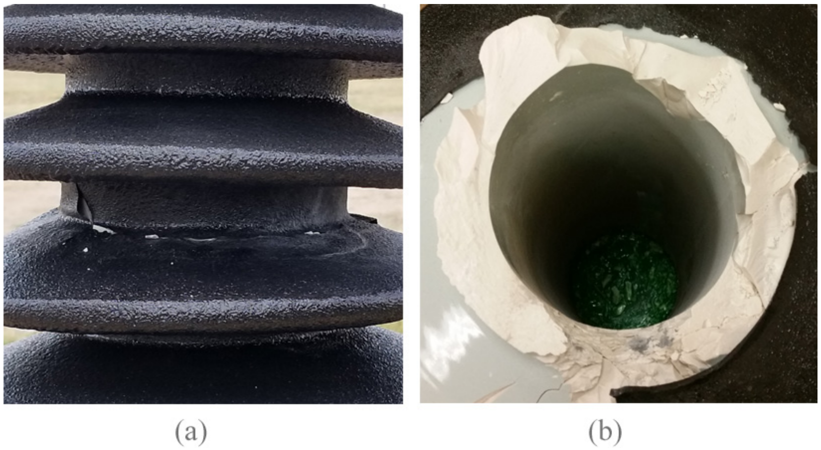
(a) (b)

Figure 8-11: Damage of bolt-mounted and coated bushing (a) on outside petticoat and (b) inside the bushing.

Figure 8-12 showed the rod-mounted bushing impact sequence: (a) at impact and (b) after 4,000 µs. A single crack formed inside the bushing which caused pressure to escape, as seen in Figure 8-12b and was identified by the arrow in Figure 8-13b. The bullet impact zone showed perforation of the coating along with some fragments of the porcelain along the outer surface of the petticoat in Figure 8-13a. The bullet did not pass through and was unrecoverable. For the rod-mounted set-up, a 3 mm thick coating arrested the bullet.

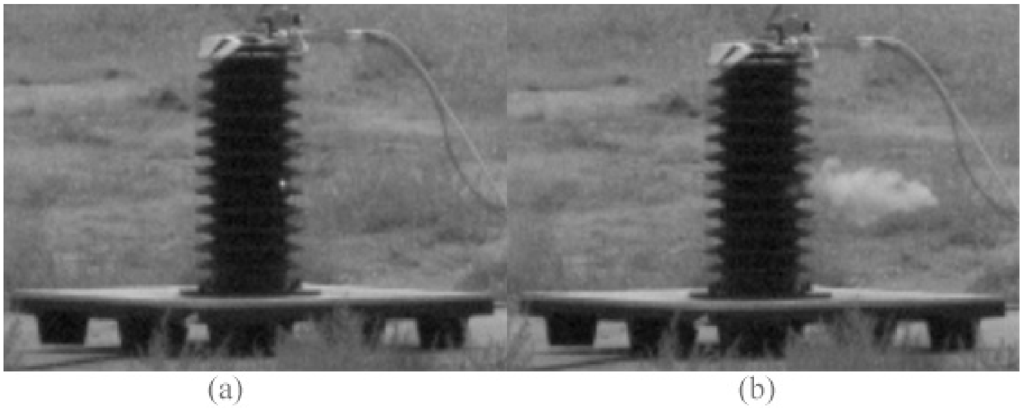
(a) (b)

Figure 8-12: High-speed imagery of rod-mounted and coated bushing responses.

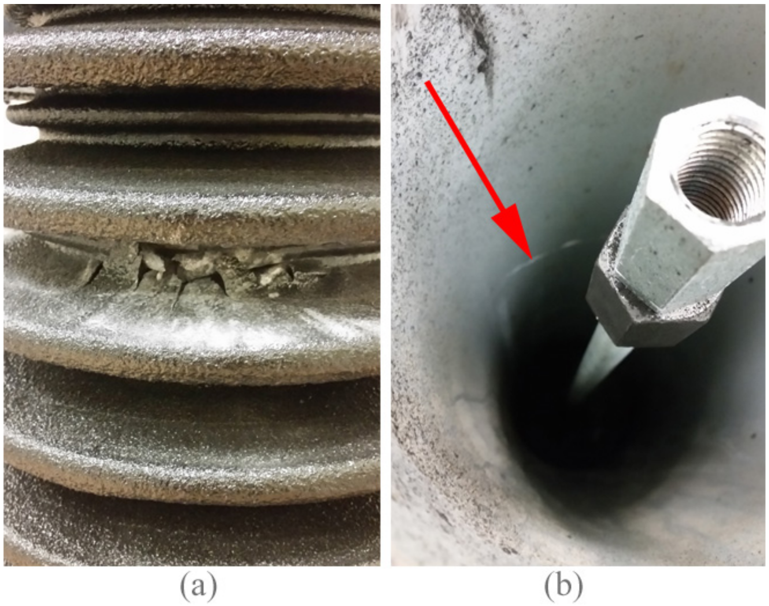
(a) (b)

Figure 8-13: Damage of rod-mounted and coated bushing (a) on outside of petticoat and (b) inside the bushing.

8.2.3 Comparison of coating efficiency from full-scale testing with previous estimates in Chapter 5.

Despite the fact that the high-velocity impact testing was performed on uncoated and coated small-scale glass cylinders in Chapter 3 and Chapter 5 as opposed to full-size transformer bushings, useful experimental observations were made. Estimates were generated based on two different test methods to gain a perspective regarding the ability of an elastomeric coating to confine fragments and prevent failure for borosilicate glass and C-120 porcelain bushings in high-velocity impact scenarios. The most important prediction made in this research was that full-scale bushings could be protected by elastomeric coatings under high energy rifle impact if sufficient coating thickness is applied.

8.2.3.1 Linear extrapolation estimates for full-scale bushings

After examination of the linear extrapolations in Chapter 5.3.2, it was estimated at which impact energies borosilicate glass would not fail under a certain coating thickness and the percent mass loss that would occur at a designated rifle impact energy. When linear extrapolation was performed, the maximum energies delivered was 45J for the drop weight apparatus. Energies delivered by conventional rifles are much higher. A .308 Winchester caliber delivers approximately 3.1 kJ of energy. The best fits from Figure 5-5 and Table 5-4 were extrapolated to the thickness required, at which no failure would occur, for an impact energy of 3.1 kJ. Under 3.1 kJ of impact energy a coating thickness of 162 mm (6.4”) was estimated to prevent failure of the borosilicate glass when the average no-failure energy was used and a thickness of 154 mm (6.1”) when the upper limit no-failure energy was used. A 3x overestimate was assumed when converting the extrapolation from drop weight to ballistic energies, as was described in Chapter 5.3.2.

The difference in the material properties for the borosilicate glass tested in this study versus C-120 porcelain used in actual bushings was taken into account. This allowed estimates to be made regarding the coating thicknesses needed to prevent bushing failure and potential mass losses. This conversion could be done by comparing the fracture toughness, K_{Ic}, of borosilicate glass and C-120 porcelain. Borosilicate glass has a fracture toughness of 0.75 MPa-$m^{1/2}$ (30) whereas the fracture toughness of C-120 porcelain is 2.0 MPa-$m^{1/2}$ (145). The ratio between the two indicates that C-120 is tougher by approximately 3 times. To prevent porcelain bushing failure at a delivered energy of 3.1 kJ, a coating thickness of 54 mm (2.1”) would be needed when the average no-failure energy is used, or 51 mm (2.0”) when the upper limit no-failure energy was used.

Bushings can be up to several meters in length and up to a half meter in diameter depending on its voltage class. They have an outer petticoat profile to increase leakage distance that varied in spacing from approximately 50 – 150 mm (146). A 51 – 54 mm coating is comparable in size to the surface characteristics of the bushings. It was estimated that the percent mass loss that would occur at 3.1 kJ of impact energy for a C-120 porcelain bushing would have been 21% using 3 mm instead of the predicted 51- 54 mm of coating thickness.

The prediction of coating thickness was determined based on low energy impact on borosilicate glass plates, performed by drop weight experiments. The extrapolations were based on the quasi-static fracture properties of both materials (29, 30), which could be very different under ballistic conditions. Since the dynamic fracture properties of porcelain and borosilicate glass are not known at present, their static properties were used in the extrapolations. This could be a source of error. Another source of error could be that the linear extrapolation does not correctly model the behavior. However, one study presented a potential linear relationship between a depth of penetration quantity and the projectile energy (147). It should be emphasized that the specimen geometry and projectile shape effects were not discussed in detail in this work, which could introduce additional errors to the predictions of the critical coating thickness.

8.2.3.2 Power fit estimates for full-scale bushings

After examination of the power fit determined by higher caliber energy testing on coated pressurized borosilicate cylinders in Chapter 5.3.3, it was estimated where the coating could sufficiently confine fragments to a mass loss of 1%. The thickness of the coating required to prevent failure was not examined in the higher caliber energy research and cannot be predicted using this method. The maximum energies delivered in the power fit research was 919 J for the .40 caliber S&W. The best fits from Figure 5-7 and Equation (11) were extrapolated to energy levels of 3.1 kJ used in full-scale testing. It was shown that a mass loss of 5.5% was predicted to occur on a coated pressurized borosilicate cylinder at 3.1 kJ of delivered impact energy.

Extrapolating the results from a borosilicate cylinder to a C-120 porcelain bushing followed the description introduced in the previous section. By assuming that the ratio between C-120 porcelain and borosilicate glass is 3x, the mass loss predicted for a C-120 porcelain bushing would be estimated at 1.82% when the delivered kinetic energy is 3.1 kJ.

8.2.3.3 Actual results for full-scale testing in comparison to previous estimates

In both mounting set-ups, the coating performed much better than predicted in Chapter 5. Under pressure of 345 kPa and 3.1 kJ of impact energy, the 3 mm coatings contained fragmentation and arrested extensive crack network formation in a bolt-mounted set-up. The coating arrested a bullet when the mounting set-up was changed to a rod-mounted one. The bolt-mounted bushing failed with a mass loss of 1.46%. In the full-scale tests the coating protection was well predicted by the power fit at 1.82% for the bolt-mounted bushing. The rod-mounted bushing cracked and released pressure but did not fail, with a mass loss unmeasurably less than 0.1%. The power fit estimates could not be used for the rod-mounted bushing.

It was estimated previously with linear extrapolations that a coating thickness to prevent failure would have to be 51 – 54 mm at a delivered kinetic energy of 3.1 kJ. The coating thickness of 3 mm used in these tests was significantly less than estimated by the linear extrapolation method.

8.3 Summary

The research on the coated borosilicate pressurized cylinders and drop weight glass plates was further extended in this section to full-scale testing of transformer bushings, with and without a 3 mm thick coating and at an impact energy of 3.1 kJ. For uncoated transformer bushings, observations were made regarding the fragmentation behavior for two different mounting types, the bolt and rod-mounted set-ups. The bolt-mounted bushing exhibited smaller fragments traveling further in a less symmetrical distribution, whereas the rod-mounted bushing demonstrated a more even distribution of middle-sized fragments.

Coated bushings showed fragmentation mass loss of approximately 1.46% for the bolt-mounted bushing and less than 0.1% for the rod-mounted bushing. These test results demonstrated that the original predictions of 21% mass loss for a 3 mm thick coating, using the linear extrapolation method in Chapter 5.3.2 were a significant overestimate.

The power fit extrapolations in Chapter 5.3.3 predicted a mass loss of 1.82% for a 3 mm thick coating at 3.1 kJ of kinetic energy, which was close. The power fit is a good method for estimating mass loss.

The original linear extrapolations predicted that a coating thickness of approximately 52 mm would be required to prevent initiation of failure via cracking at a 3.1 kJ impact energy. However, the results obtained in this study found that a 3 mm thick coating at a 3.1 kJ bullet impact energy protected the rod-mounted bushing from explosive failure. It minimized the crack network formation and contained fragments.

CHAPTER 9 SUMMARY DISCUSSION AND CONCLUDING REMARKS

The research in this dissertation has evaluated viable protection methods which could be applied to brittle porcelain transformer bushings subjected to high-velocity impact. In Figure 9-1, a summary diagram of the research is shown, including: materials considered as possible solutions to protect a bushing, geometries that were tested, experimental and numerical approaches that were used, types of impact tests performed, and a list of the most important observations and recommendations.

Testing of impact protection concepts on a full-scale bushing without initial exploratory study would be costly. A transformer bushing can cost tens of thousands of dollars. Bushings also have complicated profile geometries, which can affect testing results. Therefore, less expensive simplified geometries could be tested first in a preliminary study to obtain an understanding of the feasibility, viability and applicability of the protection concept. Subsequently, the research could proceed to the testing of real full-scale bushings under impact.

Listed below are the suggested testing steps developed in this research, which could be used when evaluating a new impact protection concept on a bushing:

1) Choose a simplified relatively inexpensive models to represent the full-size bushing.
2) Test selected materials for impact protection using drop weight methods on plates of a representative material closely matching the bushing.

3) Test simplified models of the bushings and selected protections with an air gun.
4) Move to higher caliber weapons to test the protection concepts on simplified models.
5) Test full-scale bushings with the selected protections, if possible.

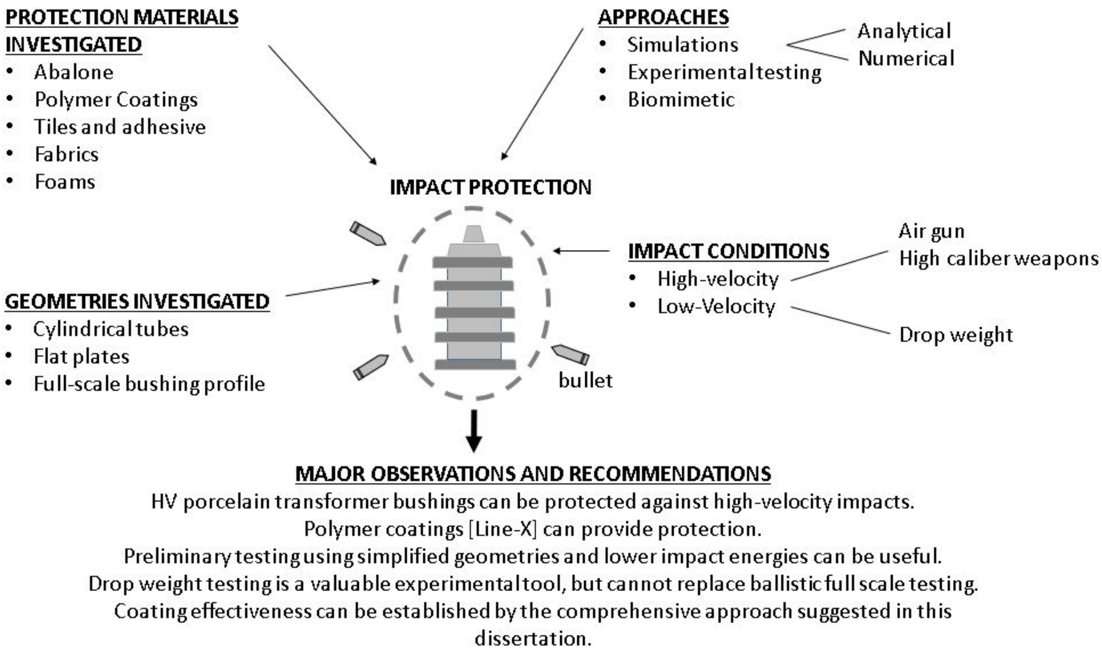

Figure 9-1: Summary diagram.

9.1 Unprotected bushing models

In this research, a borosilicate glass cylinder was chosen to represent the transformer bushing, as described in Chapter 3. A less expensive material was selected with similar properties to the C-120 porcelain commonly used in transformer bushings. Borosilicate glass and C-120 porcelain have similar density, a stiffness range for porcelain that is 1–2 times stiffer than glass, and a strength 2 times greater for glass (29, 30). The cost of a borosilicate cylinder was approximately $250 per sample. The idea of testing C-120 porcelain cylinders was also considered; however, the cost approached several thousand dollars per sample.

The first step in testing unprotected borosilicate cylinders was to simulate the response of a transformer bushing during a high-velocity impact. The most important observation from the testing revealed that the fragment blast of pressurized borosilicate glass cylinders under impact from a .22 caliber lead pellet at 335 m/s became fully symmetrical above 207 kPa of internal pressure. The unpressurized cylinders displayed a directional fragment blast distribution after impact. If it is assumed that the cylinder model closely represents an actual bushing, then the symmetrical distribution of fragments could imply that personnel or structures inside the explosion radius are at risk. If a transformer bushing was unpressurized (out of service or in storage), the fragmentation behavior would be dominated by the bullet trajectory, posing less risk.

Another important finding for the unprotected borosilicate models was that the pressurization creates an increase in fragment velocity and quantity (Chapter 3). Fragments associated with end cap generation (tops and large fragments that tended to move slowly) were not present after an internal pressure of 270 kPa was reached. Generally, in metallic pressurized cylinders, end cap generation is prominent (27); however, this research showed that for borosilicate cylinders end cap generation does not occur once a certain level of pressurization is reached. The whole cylindrical sample was involved in the explosion, rather than just the middle section. The same behavior could be expected in the case of full-scale bushings subject to impact.

Another observation was that ejected fragment dynamics for the cylinders were not predictable. The highly turbulent nature of the explosion made estimates of fragment dynamics difficult. The fragments did not follow any pre-defined Newtonian model. Airborne fragment velocities rapidly decreased or increased with time, with no clear relationship, irrespective of their masses, ejection times and testing conditions. It was postulated that the effect of air turbulence from the explosion on fragment dynamics was dependent on material type (27). Turbulence would have more of an effect on fragments that are lighter and smaller, as was the case with the borosilicate fragments. Larger heavier fragments from a transformer bushing should be less affected by air turbulence. Therefore, a major limitation from testing borosilicate cylinders was an inability to predict the fragment dynamics and impact range of full-scale bushings.

Observation of neighboring borosilicate cylinders during impact demonstrated that cascading failure of cylinders in close proximity could occur when a central cylinder is impacted by a .22 lead pellet with an air gun. Statistical testing showed that a 75% likelihood existed for a cascading reaction of at least one additional cylinder in twelve tests. The statistical tests would not have been financially possible to run, if more expensive cylinders or bushings had to be used; considering that 48 cylinders were used in the cascading experiments.

It was concluded in Chapter 3 that the pressurization of borosilicate cylinders and their impaction with an air gun pellet was a useful exploratory impact test for this research. It provided approximations for how a full-scale bushing might behave and was significantly less expensive than the alternatives.

9.2 Natural solutions for impact protection

Tackling the protection of brittle transformer bushings required “out of the box” thinking, and nature was the first place to look for new ideas. The abalone is a highly evolved impact resistant gastropod that uses brittle constituent materials in a brick stacking arrangement, along with a protein adhesive layer to resist impact (45, 48, 49). Multiaxial impact testing of abalone shells performed in this study (Chapter 4) showed that the properties of the protein layer are highly dependent on hydration and protect the organism during low-velocity impact. Ballistic tests with an air gun indicated no major difference in the kinetic energy dissipation of the lead pellets with respect to hydration level. However, as hydration levels decreased: damage on lead pellets at ballistic impacts using an air gun was lessened, projectile hole diameters on the shell increased, and the amount of variability seen in post-impact analysis increased.

The elastic response of the adhesive layers was affected by whether the abalone was dead or alive; protein degrades after death; therefore, dead abalone had no significant elastic response. It was subsequently concluded that a manmade material that could closely duplicate the elastic response of the abalone protein layer should be used in this research. The protein layer in the abalone provided insight that an elastomeric coating could potentially be a novel impact protection material for bushings. As a result, Line-X XS-100 was chosen as the protective coating of choice, due to ease of application, product availability, and potential ballistic protection properties.

Another aspect of abalone impact protection that was studied was the brick and mortar layering geometry (Chapter 4). This was done in two ways: (1) manmade tile and adhesive combinations on flat glass plates and (2) abalone composites. The brick and mortar testing showed that a combination of brittle and ductile “bricks” and adhesive performed best for impact protection in drop weight tests, as opposed to two brittle or two ductile combinations. The optimum “brick and mortar” structural arrangement consisted of ductile tiles and a brittle adhesive for thinner samples and brittle tiles with a ductile adhesive for thicker samples. A brittle-ductile arrangement causes crack deflection as in plywood, creating a tougher material (50). Abalone itself only uses a brittle tile and ductile adhesive, so manmade materials were necessary to demonstrate the ductile tile and brittle adhesive combination.

Abalone composites were also studied in Chapter 4 to identify if expanding the microscale of the tile and protein layer would work on a larger scale. The abalone composites did not perform according to NIJ classifications for Class I materials and were not recommended from a manufacturing standpoint for impact protection. It was determined through this research that the feasibility of applying a tile and adhesive based protection mechanism on a geometrically complicated structure, like transformer bushings, was not do-able. The profile shape of the transformer bushing would not be maintainable. Therefore, further research with the tiles and composites were not pursued in this study.

9.3 Elastomeric coating protection at low- and high-velocity impact

The experimental and numerical methods, presented in Chapter 5 - Chapter 8, were used to explore how an explosive blast from a combined effect of high-velocity impact and internal pressure applied to a bushing could be absorbed by an elastomeric coating. Polymeric coatings have been investigated for use on porcelain bushings for many applications (87, 89), none of which involved fragmentation mitigation. Blast mitigation of polyurea based polymeric coatings have been studied in depth for other material applications (90); with specific studies involving ceramic tiles (96) and metal substrates (91, 92, 94, 95). The high toughness of polyurea based polymeric coatings is highly effective for energy absorbing applications.

Implementing a drop weight testing approach provided a less expensive alternative to ballistic testing involving a greater number of samples and could be accomplished under laboratory conditions rather than in designated shooting areas. Drop weight testing was also performed at lower impact energies, providing results for impact energies before the tested samples failed, which could not be easily accomplished by ballistic testing. The cost of the borosilicate cylindrical tubes used in the ballistic testing (Chapter 3 and Chapter 5), whereas the cost of the flat borosilicate plates used for drop weight testing (Chapter 4 – Chapter 6) was only $25/sample. However, the major drawback to the drop weight testing was that pressurized samples could not be used, flat plate geometries were required, and only low-velocity impact could be delivered to the samples. Therefore, high strain rate effects could not be investigated, making direct comparisons difficult between static tests, drop weight tests, and tests at ballistic energies (41).

Low- and high-velocity impact testing showed that an elastomeric coating successfully confined fragments on pressurized borosilicate cylinders and flat glass plates

(Chapter 5). The impact energy limits of the testing were 95J – 919J for the ballistic test and 45J for the drop weight test. Most importantly, it was shown that the drop weight tests on the glass plates protected by the coating overestimated the mass loss of cylindrical samples subjected to air gun pellets, by approximately three times, using a linear fit to the data. Higher caliber ballistic tests on 3 mm coated cylinders also revealed that the percent mass loss versus impact energy relation was better represented by a power law fit, as opposed to a linear fit, which was initially assumed (Chapter 5).

The ballistic and drop weight tests in Chapter 5 were subsequently used in combination to make predictions regarding the percent mass loss for the full-scale bushings protected by a coating subjected to impact energies of a rifle bullet. Following the approaches from the ballistic and drop weight tests, the initial predictions for the bushings protected by a coating were overestimated. It was predicted, assuming the linear fit for mass loss vs. impact energy, that approximately 52 mm of coating on a porcelain bushing would be required to prevent its failure from rifle impact (Chapter 8.2.3.1). This initial prediction was subsequently corrected by full-scale testing of the bushings in Chapter 8. It turned out that significantly less coating (approximately 3 mm) could drastically reduce the rifle bullet effect on the bushings.

In addition to an elastomeric coating, aromatic thermosetting co-polyester (ATSP) foams and basalt and Kevlar fabrics bonded with epoxy to borosilicate glass cylinders were subjected to air gun pellet impacts (148, 149). The foams and the fabrics bonded with epoxy did not confine fragments adequately as compared with the elastomeric coating, therefore the fabric and foam testing were not reported in this study.

9.4 Coating effectiveness in low-velocity impact

Overall, the drop weight testing in Chapter 5 was found to be a complementary and useful testing technique; allowing for the testing of many samples under impact at a lower cost. The drop weight testing was further enhanced (Chapter 6 and Chapter 7) using an instrumented technique to examine behavioral properties of the coating in a more fundamental way. This testing was done experimentally using an instrumented drop weight tester with an attached accelerometer (Chapter 6) and numerically (Chapter 7) using FEM. Overall, the FEM provided a useful comparison to the experimental results and showed logical trends.

The instrumented drop weight testing provided results in the form of impact parameters (maximum contact force, deceleration, impulse, applied impact energy and transferred energy) instead of percent mass loss. It was shown that borosilicate glass plates can be successfully protected in drop weight testing by a relatively thin elastomeric coating if the impact parameters are below their critical values. Above these critical thresholds, the samples failed, and their failure modes were affected by the coating thickness. Coated samples behaved more like nonlinear materials, whereas the uncoated samples responded elastically. Numerical simulations demonstrated the same behavior.

One issue with drop weight testing of borosilicate glass plates is that they produced significant scatter in their impact parameter results, due to the inherent probabilistic behavior of failure of non-crystalline brittle materials (77, 78) . Some trends were easy to identify; FEM simulations helped to elucidate trend behavior when experimental results could not.

The experimental and numerical results exhibited similarities and differences in their time history plots. The uncoated samples displayed elastic responses in the parabolic maximum contact force vs. time history plots, both experimentally and numerically. Coated samples exhibited local irregularities caused by the coating. However, the numerical simulations only showed local irregularities in the thickest coated sample.

The experimental and numerical results demonstrated certain trends. The thinner coatings produced larger maximum contact forces compared to thicker coatings. The thicker coatings caused the normalized maximum impactor displacement to decrease compared to thinner coatings. The maximum contact force and impulse exhibited non-linear increasing behavior with respect to impact energy for the samples which did not fail, irrespective of coating thickness. Impulse was found to be relatively unaffected by coating thickness.

The critical impact energies determined at the onset of specimen failure in the instrumented drop weight tests were measured as a function of coating thickness (Chapter 6). The energies increased as coating thickness increased, whereas the critical maximum contact force and the critical impulse appeared to stabilize for the smallest coating thickness (1.3 mm) and stayed constant, with small variations, for coating thicknesses up to 5.6 mm. To initiate failure of the coated glass samples, the average critical maximum contact force was determined to be approximately 12.8 kN, which corresponded to a critical deceleration of approximately 3,413 m/s^2. The average critical impulse was established to be approximately 12.4 Ns.

In the instrumented drop weight testing a small thickness of protective coating changed the failure from one that resembled brittle failure for the uncoated glass samples to more ductile failure when the sample were coated, which was an important observation. The elastomeric coating used in this research demonstrated a mode of failure that differed from other coatings or materials, such as fabrics, displaying different types of patterns in critical impact parameters (149). In addition to the elastomeric coating, basalt and Kevlar fabrics placed on borosilicate glass samples were subjected to instrumented drop weight testing. The fabrics were bonded with brittle (epoxy) and ductile (Silicone) adhesives. Since the samples protected by the fabrics did not perform as well as the samples protected by the coating, the fabric testing was not reported in this study.

Assumptions can be made for all coating types that the critical impact parameters will behave in three different ways, as shown schematically in Figure 9-2, affecting the effectiveness of a coating in protecting a structure against impact. Coating effectiveness can be estimated from the ratio of a critical impact parameter of interest (maximum contact force or impulse) of protected samples vs. unprotected samples. The overall coating effectiveness for the glass samples protected by the coating was determined to be approximately 7.28 times that of uncoated samples (Table 6-3 of Chapter 6).

Coating usefulness (Figure 9-2) is determined by how quickly a coating can achieve effectiveness as the coating thickness is increased. A useful effective coating system, which is being demonstrated by the elastomeric coating in this research (Figure 6-17), shows a dramatic increase in protection performance at small coating thicknesses.

An ineffective coating for impact protection would require a large thickness, which is not possible with many coating types, to reach a less than ideal performance in impact protection. A coating in the middle range may reach satisfactory effectiveness but also require greater thickness. A high protection performance with a minimally coated specimen is the ideal case; this type of performance was clearly demonstrated for the Line-X XS-100 coating in instrumented drop weight testing of uncoated and coated borosilicate glass plates (Chapter 6).

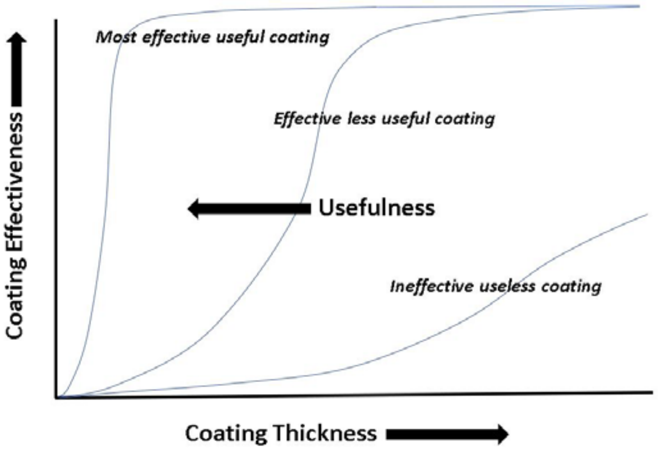

Figure 9-2: Schematic representation of coating effectiveness and usefulness.

9.5 Full-scale testing

Full-scale testing of transformer bushings was the culmination of this research (Chapter 8). Two types of porcelain bushings as supplied or coated with 3 mm of Line-X XS-100 were subjected to high-velocity impact created by a .308 Winchester rifle cartridge at 3.1 kJ. The uncoated bolt-mounted bushing exhibited smaller fragments after impact, which travelled the farthest in a less symmetrical distribution. The uncoated rod-mounted bushing demonstrated a more even distribution of middle-sized fragments. The effect of a 3 mm thick coating on the failure of the bushings was dramatic. With a mass loss of 1.46%, the bolt-mounted bushing split in the middle, but was held together by the coating. With a mass loss immeasurably less than 0.1%, the rod-mounted bushing experienced a single crack and released pressure but otherwise remained fully intact.

The original predictions of 21% mass loss for a 3 mm thick coating using the linear extrapolation method in Chapter 5 were a significant overestimate compared to the actual bushing mass loss of 1.46%. The power fit extrapolations from the higher caliber ballistic testing in Chapter 5.2.3, on the other hand, predicted a mass loss of 1.82% for a 3 mm thick coating at 3.1 kJ of impact energy. It was therefore determined that the predictions used to determine mass loss of a transformer bushing for a given coating thickness would follow a power fit instead of a linear fit; another important fundamental discovery of this study

9.6 Final observations and recommendations

It can be stated that this comprehensive research summarized in Figure 9-1, identified the risks associated with pressurized transformer bushings impacted by high-velocity projectiles. Various protection concepts were studied, and a protective elastomeric coating produced by Line-X was found to be an excellent mitigating solution. Testing methods were used and compared to each other resulting in a significant number of new fundamental discoveries, practical observations, and critical recommendations, which will have potential implications for national security and be useful for federal agencies and utilities. Most importantly, all primary and secondary objectives of this research, listed in Chapter 1.2, have been fully satisfied. It can be concluded from Figure 9-1, that:

- HV porcelain transformer bushings can be protected against high-velocity impacts.
- Polymer coatings [Line-X XS-100] can provide the protection.
- Preliminary testing using simplified geometries and lower impact energies can be useful.
- Drop weight testing is a valuable experimental tool but cannot replace ballistic full-scale testing.
- Coating effectiveness can be established by the comprehensive approach suggested in this dissertation.

It is important to add that this research has been limited to transformer bushings, but the approaches and ideas developed to protect the bushings against high-velocity impacts could be used to explore protections of other brittle structures against impact situations. Many potential applications of brittle structures have military and civilian applications. More specifically, the behavior of brittle materials under impact could apply to some applications, such as: cementitious military armors, bunkers and walls, fall protection for cell phones and other electronics with glass screens, windshield damage by moving objects, advances in impact resistant helmets, impact protection from space debris, and ceramic roof tile protection from hail impacts.

9.7 Future testing recommendations

It is recommended that Line-X coatings be further studied for use on transformer bushings in-service. To further examine this coating, the following is suggested:

- The Line-X XS-310 and XS-350 coatings be tested using the methods in this dissertation.
- The coating needs to be optimized for in-service conditions.
- The electrical properties need to be examined to ensure electrical interference is not an issue.
- Higher energies should be examined using explosives inside the bushing, to simulate the electrical ionization energy present during a high-velocity impact to the conductor.
- Accelerated weathering tests should be performed on Line-X coated coupon samples to determine long term durability (i.e. UV, salt-fog, fire retardance, electrical breakdown resistance, etc.).

REFERENCES

1. Parformak PW. Physical security of the U.S. power grid: High voltage transformer substations. Print. Congressional Research Service; 2014.
2. Physical vulnerability of electrical systems to natural disasters and sabotage. Print. Washington DC: GPO: Office of Technology Assessment; 1990. Report No.: OTA-E-453.
3. High-impact, low-frequency event risk to the North American bulk power system. Print. North American Electric Reliability Corporation; 2010.
4. Pagliery J. Sniper attack on California power grid may have been 'an insider,' DHS says [Web]. CNN Money; 2015 [Available from: https://money.cnn.com/2015/10/16/technology/sniper-power-grid/].
5. Anderson C. Principles, function and concepts for compliant mechanically reactive armor elements [master's thesis]. Provo, UT: Brigham Young University; 2007.
6. Clough E. Large-displacement lightweight armor [master's thesis]. San Luis Obispo, CA: California Polytechnic State University; 2013.
7. ABB Launches substation physical security and resiliency initiative. T&D World Magazine [Internet]. December 1, 2015.
8. Security guideline for the electricity sector: Physical security. North American Electric Reliability Corporation; 2004.
9. Terrorism and the electric power delivery system. Committee on enhancing the robustness and resilience of future electrical transmission and distribution in the United States to terrorist attack. Washington, DC: The National Academic Press; 2012.
10. Power substation guides [Web]. Electrical Engineering Portal; [23 June 2015].
11. Statement of reasons concerning the making of a final determination with respect to the dumping of certain liquid dielectric transformers originating in or exported from the Republic of Korea decision. Print. Ottawa, Canada: Canada Border Services Agency; 2012.
12. Lusk B. Blast protection for power transformers. Blast and ballistic final report. Lexington, KY: National Institute for Hometown Security; 2012.
13. Transformers [Internet]. [Accessed: 20 June 2015]. Wikipedia. Available from: https://en.wikipedia.org/wiki/Transformer.
14. Halliday D, Resnick R, Walker J. Fundamentals of physics. 8th ed. New York, NY: Wiley & Sons.; 2007.
15. IEEE Standard C57.12.10-2010, "Standard Requirements for Liquid-Immersed Power Transformers". New York, NY: IEEE Power & Energy Society; 2011.
16. Jonsson L, Johannson R. High-voltage bushings- 100 years of technical advancement. Sweden: ABB; 2010. p. 32-4.
17. Mitchell K. Transformers. [Accessed: 9 September 2015]. University of Sydney. School of Electrical Engineering. Available from: sydney.edu.au/engineering/electrical/courses/power/plant/transformers.xml.

18. McGrail T. Transformer truth or dare: How to make decisions on the health and reliability of transformers [Web]. Electric Energy Online; [Accessed: 20 June 2015].
19. Ellis KP. Bushing selection- making the right choice: Trench Limited.
20. Hiel B. Design, production and evaluation of the reliability of bushings. HSP Hochspannungsgeräte GmbH & Trench Bushing Group; 2013.
21. Partial discharge [Internet]. [Accessed: September 15, 2015]. Wikipedia. Available from: https://en.wikipedia.org/wiki/Partial_discharge.
22. Keshwani S, Mataray M. RIP (resin impregnated paper) bushing for EHV class power transformer. IJPTT. 2014;4(2):19-22.
23. Ellis K. Bushings for power transformers: A handbook for power engineers: AuthorHouse; 2011. 116 p.
24. Bushing (electrical) [Internet]. [Accessed: August 20, 2015]. Wikipedia. Available from: https://en.wikipedia.org/wiki/Bushing_(electrical).
25. Pirovano A. UHV and HVDC transformers bushings, analysis of temperature rise tests results and definition of a simplified methodology for the calculation and prediction of the thermal behavior. Alstom grid, Milan: Politechnico Di Milano; 2012-2013.
26. Chang JB. Operational guidelines for spaceflight pressure vessels. El Segundo, CA: Space Launch Operations: The Aerospace Corporation; 2005. Report No.: ATR-2005(5128)-1.
27. Mebarki A, Mercier F, Nguyen QB, Saada RA. Structural fragments and explosions in industrial facilities. Part I: Probabilistic description of the source terms. J Loss Prev Process Ind. 2009;22(4):408-16.
28. Gill P. Electrical power equipment maintaince and testing. 2nd ed. Boca Raton, FL: CRC Press; 2008.
29. Springer handbook of condensed matter and materials data. 1st ed. Martienssen W, Warlimount H, editors. Germany: Springer; 2005. 1121 p.
30. Ceramics and glasses. ASM Handbook. 4. USA: ASM International; 1991. p. 1217.
31. Harold "Doc" Edgerton. Iconic Images. [Web]. Massachusetts Institute of Technology; 2010 [Available from: http://edgerton-digital-collections.org/galleries/iconic.
32. Rosenberg Z, Dekel E. Terminal ballistics. New York: Springer; 2012.
33. Carlucci DE, Jacobson SS. Ballistics: theory and design of guns and ammunition. 2nd ed. Boca Raton, FL: CRC Press; 2014.
34. Compton BG, Gamble EA, Zok FW. Failure initiation during impact of metal spheres onto ceramic targets. Int J Impact Eng. 2013;55:11-23.
35. Henderson S, Fahrenholtz W, Hilmas GE. High-velocity impact resistance of ZrB2-SiC: American Ceramic Society; 2007. 3-10 p.
36. Yamada M, Sekine K, Kumazawa T, Tanabe Y. Relationship between the cone crack and fracture mode in ceramics under high-velocity-projectile impact. J Ceram Soc Jpn. 2010;118(1382):903-8.

37. Woodward RL, Gooch WA, O'Donnell RG, Perciballi WJ, Baxter BJ, Pattie SD. A study of fragmentation in the ballistic impact of ceramics. Int J Impact Eng. 1994;15(5):605-18.
38. Bell W. Multi-length scale modeling of the high-pressure, large-strain, high-strain-rate response of soda-lime glass [dissertation]. Clemson, SC: Clemson University; 2011.
39. Kadono T, Arakawa M. Crack propagation in thin glass plates caused by high velocity impact. Phys Rev E. 2002;65(035107):1-4.
40. Hogan JD, Farbaniec L, Daphalapurkar N, Ramesh KT. On compressive brittle fragmentation. J Am Ceram Soc. 2016;99(6):2159-69.
41. Forquin P. Brittle materials at high-loading rates: an open area of research. Philos Trans Royal Soc A: Mathematical, Physical and Engineering Sciences. 2017;375(2085):20160436.
42. Manning TA, Lawrence SL, editors. Physics-based fragment acceleration modeling for Ppessurized tank burst risk assessments. Probablistic Safety Assessment and Management Conference (PSAM 12); 2014; Honolulu, HI.
43. Crowe CT, Roberson JA, Elger DF. Engineering fluid mechanics. 7th ed. New York, NY: Wiley and Sons; 2001.
44. Henderson CN, DeFrance CS, Predecki P, McCloskey TV, Truitt E, Hoffman J, et al. Ballistic fragmentation confinement of coated brittle transformer bushing models. Int J Impact Eng. 2018;122:363-73.
45. Uncovering the secrets of abalone body armor [Web]. Univeristy of California San Diego. Jacobs School of Engineering; [cited: 01 July 2015].
46. M. Sarikaya, K. E. Gunnison, Yasrebi M, Aksay IA. Mechanical property-microstructural relationships in abalone shell. Mat Res Soc Symp Proc 1989;174:109-18.
47. Dastjerdi AK, Rabiei R, Barthelat F. The weak interfaces within tough natural composites: Experiments on three types of nacre. J Mech Behav Biomed Mater. 2013;19:50-60.
48. Barthelat F, Tang H, Zavattieri PD, Li CM, Espinosa HD. On the mechanics of mother-of-pearl: A key feature in the material hierarchical structure. J Mech Phys Solids. 2007;55(2):306-37.
49. Lin A, Meyers MA. Growth and structure in abalone shell. Mat Sci Eng A-Struct. 2005;390(1-2):27-41.
50. Sun J, Bhushan B. Hierarchical structure and mechanical properties of nacre: a review. RSC Adv. 2012;2(20):7617-32.
51. Lloyd R. Abalone armor: Toughest stuff theoretically possible [Web]. Livescience; 2004 [Accessed: 6 Sep 2015].
52. Qi HJ, Bruet BJF, Palmer JS, Ortiz C, Boyce MC. Micromechanics and macromechanics of the tensile deformation of nacre. In: Holzapfel GA, Ogden RW, editors. Mechanics of Biological Tissue. Berlin, Heidelberg: Springer; 2006. p. 189-203.

53. Menig R, Meyers MH, Meyers MA, Vecchio KS. Quasi-static and dynamic mechanical response of Haliotis rufescens (abalone) shells. Acta Mater. 2000;48(9):2383-98.
54. Welsh J. Seashells get their strength from interlocking 'bricks' [Web]. Livescience; 2011 [Accessed: 20 Jun 2015].
55. Shen XY, Belcher AM, Hansma PK, Stucky GD, Morse DE. Molecular cloning and characterization of Lustrin A, a matrix protein from shell and pearl nacre of Haliotis Rufescens. J Biol Chem. 1997;272(51):32472-81.
56. Treccani L, Mann K, Heinemann F, Fritz M. Perlwapin, an abalone nacre protein with three four-disulfide core (whey acidic protein) domains, inhibits the growth of calcium carbonate crystals. Biophys J. 2006;91(7):2601-8.
57. Smith BL, Schaffer TE, Viani M, Thompson JB, Frederick NA, Kindt J, et al. Molecular mechanistic origin of the toughness of natural adhesives, fibres and composites. Nature. 1999;399(6738):761-3.
58. Alpha Helix [Internet}. [Accessed: January 13, 2016]. Wikipedia. Available from: https://en.wikipedia.org/wiki/Alpha_helix.
59. Beta Sheet [Internet]. [Accessed: January 13, 2016]. Wikipedia. Available from: https://en.wikipedia.org/wiki/Beta_sheet.
60. Berg J, Tymoczko J, Stryer L. Biochemistry. 7th ed. New York, NY: W.H. Freeman and Company; 2012.
61. Wang J, Cheng Q, Tang Z. Layered nanocomposites inspired by the structure and mechanical properties of nacre. Chem Soc Rev. 2012;41(3):1111-29.
62. Hu X, Xu Z, Gao C. Multifunctional, supramolecular, continuous artificial nacre fibres. Sci Rep. 2012;2.
63. Sarikaya M, Aksay IA. Nacre of abalone shell: a natural multifunctional nanolaminated ceramic-polymer composite material. In: Kubiak, Jacek Z., Kloc, Malgorzata, editors. Results and Problems in Cell Differentiation. 19: Springer; 1992. p. 1-26.
64. Podsiadlo P, Kaushik AK, Arruda EM, Waas AM, Shim BS, Xu J, et al. Ultrastrong and stiff layered polymer nanocomposites. Science. 2007;318(5847):80-3.
65. Walther A, Bjurhager I, Malho J-M, Pere J, Ruokolainen J, Berglund LA, et al. Large-area, lightweight and thick biomimetic composites with superior material properties via fast, economic, and green pathways. Nano Lett. 2010;10(8):2742-8.
66. Barthelat F, Zhu D. A novel biomimetic material duplicating the structure and mechanics of natural nacre. J Mater Res. 2011;26(10):1203-15.
67. Barthelat F. Nacre from mollusk shells: a model for high-performance structural materials. Bioinspir Biomim. 2010;5(3).
68. Espinosa HD, Rim JE, Barthelat F, Buehler MJ. Merger of structure and material in nacre and bone - Perspectives on de novo biomimetic materials. Prog Mater Sci. 2009;54(8):1059-100.
69. Lessons learned from the abalone shell [Web]. Cath Science; Dec 12, 2011 [Accessed: Jan. 13, 2016].

70. ASTM Standard C127-15, "Standard Test Method for Relative Density (Specific Gravity) and Absorption of Coarse Aggregate". West Conshohocken, PA: ASTM International; 2015.
71. ASTM Standard D3763-06, "Standard Test Method for High Speed Puncture Properties of Plastics Using Load and Displacement Sensors". West Conshohocken, PA: ASTM International; 2006.
72. ASTM Standard D2794-93, "Standard Test Method for Resistance of Organic Coatings to the Effects of Rapid Deformation (Impact)". West Conshohocken, PA: ASTM International; 2010.
73. Military Standard MIL-STD-662F: "V50 Ballistic Test for Armor". Rev F: DoD; 18 Dec 1997.
74. Lapota D, Rosen G, Chock J, Liu CH. Red and green abalone seed growout for reseeding activities off Point Loma, California. J Shellfish Res. 2000;19(1):431-8.
75. Barthelat F, Espinosa. H. Tensile testing of abalone nacre minature specimens using microscopy and speckle correlation. SEM Annual Conference and Exposition on Experimental and Applied Mechanics; June 10-12, 2002; Milwaukee, WI.
76. Hild F, Forquin P, Denoual C, Brajer X. Probabilistic-deterministic transition involved in a fragmentationprocess of brittle materials: application to a high performance concrete. Lat Am J Solids Stru. 2005;2(1):41-56.
77. JeongH J, Adib-Ramezani H, Pluvinage G. Tensile strength of the brittle materials, probabilistic or deterministic approach? Strength of Mater. 2006;38(1):72-83.
78. Griffith AA, Taylor GI. The phenomena of rupture and flow in solids. Philos Trans Royal Soc A: Containing Papers of a Mathematical or Physical Character. 1921;221(582-593):163-98.
79. Cheong YS, Salman AD, Hounslow MJ. Effect of impact angle and velocity on the fragment size distribution of glass spheres. Powder Technol. 2003;138(2):189-200.
80. Cho SH, Ogata Y, Kaneko K. Strain-rate dependency of the dynamic tensile strength of rock. Int J Rock Mech Min Sci. 2003;40(5):763-77.
81. Wu K, Zheng Z, Zhang S, He L, Yao H, Gong X, et al. Interfacial strength-controlled energy dissipation mechanism and optimization in impact-resistant nacreous structure. Mater Design. 2019;163:107532.
82. Gao H. Application of fracture mechanics concepts to hierarchical biomechanics of bone and bone-like materials. Int J Fract. 2006;138:101-37.
83. Pro JW, Lim RK, Petzold LR, Utz M, Begley MR. The impact of stochastic microstructures on the macroscopic fracture properties of brick and mortar composites. Extreme Mech Lett. 2015;5:1-9.
84. Egan P, Sinko R, LeDuc PR, Keten S. The role of mechanics in biological and bio-inspired systems. Nat Commun. 2015;6.
85. Begley MR, Philips NR, Compton BG, Wilbrink DV, Ritchie RO, Utz M. Micromechanical models to guide the development of synthetic ‘brick and mortar’ composites. J Mech Phys Solids 2012;60(8):1545-60.

86. Xie Z, Yao H. Crack deflection and flaw tolerance in "brick-and-mortar" structured composites. Int J Appl Mech. 2014;06(02):1450017.
87. Gorur RS, Cherney E, Tourreil Cd, Dumora D, Harmon R, Hervig H, et al. Protective coatings for improving contamination performance of outdoor high voltage ceramic insulators. IEEE Trans Power Delivery. 1995;10(2):924-33.
88. Pradeep MA, Vasudev N, Reddy PV, Khastgir D. Effect of ATH content on electrical and aging properties of EVA and silicone rubber blends for high voltage insulator compound. J Appl Polym Sci. 2007;104(6):3505-16.
89. Bowen S, Hyunil K, Wonseok C, Jung Hyun K. Characterization of a functional coating film synthesized on the ceramic substrate for electrical insulator application according to coating method. Trans Electr Electron Mater. 2017;18(3):148-50.
90. Iqbal N, Tripathi M, Parthasarathy S, Kumar D, Roy PK. Polyurea coatings for enhanced blast-mitigation: a review. RSC Adv. 2016;6(111):109706-17.
91. Roland C, Fragiadakis D, Gamache RM, Casalini R. Factors influencing the ballistic impact resistance of elastomer-coated metal substrates. Philos Mag. 2013;93:468-77.
92. Barsoum GS, Dudt PJ. The fascinating behaviors of ordinary materials under dynamic conditions. AMMTIAC Q. 2010;4:11-4.
93. Xue Z, Hutchinson JW. Neck development in metal/elastomer bilayers under dynamic stretchings. International Journal of Solids and Structures - INT J SOLIDS STRUCT. 2008;45:3769-78.
94. Grujicic M, Pandurangan B, He T, A. Cheeseman B, Yen C-F, L. Randow C. Computational investigation of impact energy absorption capability of polyurea coatings via deformation-induced glass transition. Mater Sci Eng, A. 2010;527:7741-51.
95. Roland C, Fragiadakis D, Gamache RM. Elastomer–steel laminate armor. Compos Struct. 2010;92:1059-64.
96. Samiee A, Isaacs J, Nemat-Nasser S. Ballistic performance of polyurea-coated armor grade ceramic tiles. Proceedings of SPIE - The International Society for Optical Engineering. 2010;7644.
97. Born L, Hespe H. On the physical crosslinking of amine-extended polyurethane urea elastomers: A crystallographic analysis of bis-urea from diphenyl methane-4-isocyanate and 1,4-butane diamine. Colloid Polym Sci. 1985;263:335-41.
98. Roland CM. Viscoelastic behavior of rubbery materials: Oxford University Press; 2011.
99. XS-100. Standard Line-X [Internet]. Line-X. March 2017. Available from: https://www.linexfortworthtexas.com/product-list.
100. Elavenil S, Knight GS. Impact response of plates under drop weight impact testing. DIU J Sci Technol. 2012;7(1).
101. Banthia N, Mindess S, Bentur A, Pigeon M. Impact testing of concrete using a drop-weight impact machine. Exp Mech. 1989;29(1):63-9.

102. Chaparala S, Xue L, Yu D, Park S. Dynamics behavior of flat glass panels under impact conditions: Experiments and numerical modeling. J Soc Inf Disp. 2015;23(3):97-106.
103. Daryadel SS, Mantena PR, Kim K, Stoddard D, Rajendran AM. Dynamic response of glass under low-velocity impact and high strain-rate SHPB compression loading. J Non-Cryst Solids. 2016;432:432-9.
104. Zahid B, Chen X. Development of a helmet test rig for continuously textile reinforced riot helmets. Int J Text Sci. 2013;2(1).
105. Rush GA, Prabhu R, Rush GA, Williams LN, Horstemeyer MF. Modified drop tower impact tests for American football helmets. J Vis Exp. 2017(120):e53929.
106. Gao W, Wang R, Chen S, Zang M. An intrinsic cohesive zone approach for impact failure of windshield laminated glass subjected to a pedestrian headform. International Journal of Impact Engineering. 2019;126:147-59.
107. Yu G, Zheng Y, Feng B, Liu B, Meng K, Yang X, et al. Computation modeling of laminated crack glass windshields subjected to headform impact. Computers & Structures. 2017;193:139-54.
108. Li Y, Xiong D, Wang L, Feng B, Xu J. Dynamic mechanical behavior and pedestrian safety characteristics of toughened laminated windshield. Composites Part B: Engineering. 2019;163:740-51.
109. Abrate S. Impact on composite structures. Cambridge, MA: Cambridge University Press; 1998.
110. Aymerich F, Marcialis P, Meili S, Priolo P. An instrumented drop-weight machine for low velocity impact testing. Transactions on the Built Environment 22: WIT Press; 1996.
111. Winkel JD, Adams DF. Instrumented drop weight impact testing of cross-ply and fabric composites. Composites. 1985;16(4):268-78.
112. Tempelman E, Dwaikat MMS, Spitás C. Experimental and Analytical Study of Free-Fall Drop Impact Testing of Portable Products. Exp Mech. 2012;52(9):1385-95.
113. Kwon S, Lee BY, Park SH. Investigation of the failure of a liquid crystal display panel under mechanical shock. Proc Inst Mech Eng Pt C J Mechan Eng Sci. 2007;221(11):1475-82.
114. Zhou CY, Yu TX, Lee RSW. Drop/impact tests and analysis of typical portable electronic devices. Int J Mech Sci. 2008;50(5):905-17.
115. Lim CT, Ang CW, Tan LB, Seah SKW, Wong EH, editors. Drop impact survey of portable electronic products. 53rd Electronic Components and Technology Conference; 27-30 May 2003; New Orleans, LA: IEEE.
116. Goyal S, Buratynski EK. Methods for realistic drop-testing. Int J Microcircuits Electron Packag. 2000;23:1063-674.
117. ASTM Standard D7136/D7136M-15, "Standard Test Method for Measuring the Damage Resistance of a Fiber-Reinforced Polymer Matrix Composite to a Drop-Weight Impact" Event. West Conshohocken, PA: ASTM International; 2015.
118. High performance, wide bandwidth accelerometer ADXL001 product data sheet. Analog Devices; 2010.

119. Anton H. Calculus: A new horizon. 6th ed. New York, NY: Wiley and Sons 1999.
120. Naik NK, Joglekar MN, Arya H, V.Borade S, Ramakrishna KN. Impact and compression after impact characteristics of plain weave fabric composites: effect of plate thickness. Adv Compos Mater. 2003;12(4):261-80.
121. Naik NK, Borade SV, Arya H, Sailendra M, Prabhu SV. Experimental studies on impact behaviour of woven fabric composites: Effect of impact parameters. J Reinf Plast Compos. 2002;21(15):1347-62.
122. Metz B. Impact and drop testing with ICP® force sensors. Sound Vib. 2007;41:18-20.
123. Shackelford JF. Introduction to materials science for engineers. 7th ed. Upper Saddle River, NJ: Pearson Prentice Hall; 2009.
124. Sutherland L, Guedes Soares C. Impact tests on woven-roving E-glass/polyester laminates. 1999;59:1553-67.
125. Kim J, Kang K. An analysis of impact force in plain-weave glass/epoxy composite plates subjected to transverse impact. Compos Sci Technol. 2001;61:135-43.
126. Rullkoetter P. FInite element methods [Lecture notes}. University of Denver; September 14, 2015.
127. Ramaeker K. Numerical modeling of corrosion and cathodic protection for Reclamation water storage and conveyance infrastructure. Denver, CO: Bureau of Reclamation. Technical Services Center; 2017. Report No.: ST-2017-1720-01.
128. Nguyen L, Salamon J. Guide for analysis of concrete dam structures using finite element methods. Denver, CO: Bureau of Reclamation. Technical Services Center; 2018. Report No.: DSO-2018-09.
129. Mills-Bria B. State-of-practice for the nonlinear analys is of concrctc dams at the Bureau of Reclamation. Denver, CO: Bureau of Reclamation. Technical services Center; 2006.
130. Rainsberger R. TrueGrid user's manual- A guide and a reference. Volume 1: Introduction, graphical user interface, and parts: XYZ Scientific Applications, Inc.; 2014.
131. LS-DYNA theory manual [Internet]. Livermore, CA: Livermore Software Technology Corporation; 2006.
132. Felippa C. Advanced finite element methods. Boulder, CO: University of Colorado Boulder; 2013.
133. Bathe KJ. Finite element procedures in engineering analysis. Englewood Cliffs, NJ: Prentice-Hall, Inc.; 1982.
134. SOLID164: Explicit 3-D structural solid [Internet]. LSDYNA; [Accessed: June 2019]. Available from: https://www.sharcnet.ca/Software/Fluent14/help/ans_elem/Hlp_E_SOLID164.html#aDbxSnf5tlm.
135. LS-DYNA keyword user's manual: Volume II. Livermore, CA: Livermore SoftwareTechnology Corporation.

136. Carbon steel handbook. Palo Alto, CA: Electric Power Research Institute; 2007. 172 p.
137. Materials data book. UK: Cambridge University Engineering Department; 2003.
138. Basic engineering data. Boulder, CO: Allen Scientific Glass.
139. Properties of Pyrex, Pyrexplus and low actinic Pyrex code 7740 glasses [Internet]. Corning. Available from: http://www.azom.com/article.aspx?ArticleID=4765.
140. Gandhi S. Simulation of crack pattern on borosilicate glass cylinder under pellet impact [master's thesis]. Houghton, MI: Michigan Technological University; 2017.
141. Line-X solutions guide: Product line XS-100 EU Polyurea/polyurethane hybrid [Internet]. Line-X
142. Bodin CK. Energy storage and dissipation in polyurea composites [master's thesis]. Cambridge, MA: Massachusetts Institute of Technology; 2013.
143. Hourglass [Internet]. LS-DYNA Support; [Accessed: May 2019]. Available from: www.dynasupport.com.
144. ASTM Standard D638-14, "Standard Test Method for Tensile Properties of Plastics". West Conshohocken, PA: ASTM International; 2014.
145. Carlström E, Carlsson R, Tjernlund A-K, Johannesson B. Some fracture properties of alumina-containing electrical porcelains. In: Bradt RC, Evans AG, Hasselman DPH, Lange FF, editors. Fracture mechanics of ceramics volume 8: Microstructure, methods, design, and fatigue. Boston, MA: Springer; 1986. p. 137-42.
146. Few B. Personal communication. [email] September 19, 2018. Bureau of Reclamation.
147. Savio SG, Madhu V. Effect of tile thickness and projectile velocity on the ballistic performance of boron carbide against 12.7 mm AP. Procedia Eng. 2017;173:286-92.
148. Bakir M, Henderson CN, Meyer JL, Oh J, Miljkovic N, Kumosa M, et al. Effects of environmental aging on physical properties of aromatic thermosetting copolyester matrix neat and nanocomposite foams. Polymer Degradation and Stability. 2018;147:49-56.
149. Henderson CN, Kumosa M. Internal reports. . Bureau of Reclamation and NSF I/UCRC Novel High Voltage/High Temperature Materials and Structures; 2015-2018.
150. NIJ Standard 0108.01, "Ballistic Resistant Protective Materials". National Institute of Justice; September 1985.
151. Chinella JF, Pothier B, Wells MGH. Processing, mechanical properties, and ballistic impact effects of austempered ductile iron. Army Research Laboratory; 1998. Report No.: ARL-TR-1741.
152. Under the hood: The physics of projectile ballistics [Web]. [Accessed: 2 October 2015]. Available from: http://panoptesv.com/RPGs/Equipment/Weapons/Projectile_physics.php.

153. Wadley Research Group. Ballistic impact mechanisms of materials [Web]. Univeristy of Virginia. Department of Material Science and Engineering; [Accessed: October 2015].
154. Bouzid S, Nyoungue A, Azari Z, Bouaouadja N, Pluvinage G. Fracture criterion for glass under impact loading. Int J Impact Eng. 2001;25(9):831-45.
155. Astrom BT. Manufacturing of polymer composites. New York, NY: Chapman & Hall; 1997.
156. Thomas S, Joseph K, Malhotra SK, Goda K, Sreekala MS. Polymer composites. Singapore: Wiley; 2012.
157. Chung D, Deborah L. Composite materials: Science and applications. New York: Springer; 2010.
158. Song C. Low velocity impact testing and computed tomography damage evaluation of layered textile composite [master's thesis]. Iowa City, IA: University of Iowa; 2014.
159. Strong BA. Fundamentals of composites manufacturing materials, methods, and applications. 2nd ed. Dearborn, MI: Society of Manufacturing Engineers; 2008.

APPENDIX A ACRONYMS

2-D	Two dimensional
3-D	Three dimensional
ACP	Auto Colt Pistol
Al_2O_3	Aluminum oxide
$Al\text{-}B_4C$	Aluminum boron carbide
AP	Armor piercing
ASTM	American Society for Testing and Materials
ATSP	Aromatic thermosetting co-polyester
CA	California
CAD	Computer aided design
C	Celsius
cm	Centimeter
cys	Cysteine
DoF	Degrees of freedom
EVA	Ethylene vinyl acetate copolymer
FEM	Finite element methods
FMJ	Full metal jacket
FSP	Fragment stimulating projectile
ft	Feet
g	gram

g	Acceleration due to gravity
GE	General Electric
gly	Glycine
GPa	Gigapascals
gr.	Grain
GS	gly-ser
GSSS	gly-ser-ser-ser
H&N	Haendler & Natermann
HNGQ	Hunan Gaoqiang Electrical Ceramic and Appliance Company
HV	High-Voltage
Hz	Hertz
IEEE	Institute of Electrical and Electronics Engineers
IMI	Israel Military Industries
in	Inch
I/UCRC	Industry/university cooperative research center
J	Joule
KE	Kinetic energy
kg	Kilograms
kHz	Kilohertz
kJ	Kilojoule
kN	Kilonewton
kPa	Kilopascal

kV	Kilovolts
LBB	Leak-before-break
lbf	Pound force
lbs	Pounds
LCD	Liquid crystal display
LR	Long rifle
m	Meter
Mag	Magnum
min	Minute
µm	Micrometer
µs	Microsecond
mm	Millimeter
msec	Millisecond
MPa	Megapascals
MTM	Na±montmorillonite
mV	Millivolt
N	Newton
NERC	North American Reliability Organization
NIJ	National Institute of Justice
Ns	Newton seconds
NSF	National Science Foundation
OIP	Oil impregnated paper

OM	Optical microscope
OTA	Office of Technology
oz	Ounce
PCB	Printed circuit board
PCC	Phantom camera control
PD	Partial discharge
PDDA	Poly diallyldimethylammonium
PE	Potential energy
PETG	Polyethylene terephthalate glycol
PMMA	poly methyl methacrylate
pro	Proline
psi	Pounds per square inch
PVA	Polyvinyl alcohol
PVC	Polyvinyl chloride
RCC	Right circular cylinder
RHT	Reduced hazard training
RIP	Resin impregnated paper
RTV	Room temperature vulcanizing
s	Second
S&W	Smith & Wesson
SBR	Styrene butadiene rubber
sec	Second

SEM	Scanning electron microscopy
ser	Serine
SP	Soft point
sq.	Square
SRI	Silicone rubber insulator
SSG	Scharfschützengewehr
SSLE	Security, Safety and Law Enforcement
TMJ	Total metal jacket
V50	Ballistic limit
W	Watt
Wt	Weight
yr	Year

APPENDIX B BALLISTICS TERMINOLOGY

Interior, exterior, and terminal ballistics

The study of ballistics can be broken down into three basic areas: interior, exterior and terminal ballistics. Interior ballistics deals primarily with interactions and mechanisms that take place while the projectile is located inside the gun. This includes such mechanisms as propellant ignition, pressurization in the gun chamber, initial motion of the projectile, shape and design of projectiles, rotational dynamics, motion of the projectile as it exits the barrel, muzzle effects, and various other aspects involving the initial stages of a ballistic event (33). Exterior ballistics takes place during the period of time after the projectile has left the gun until it impacts the target. This covers a wide range of topics involving projectile dynamics: spin and rotational motion, projectile motion, atmospheric effects on motion, and other factors that modify the dynamics of motion of the bullet between the source and target (33).

Terminal ballistics is the study of ballistics involving the time period after the projectile strikes the target. Terminal ballistics involves penetration and perforation mechanics, fragmentation effects, shock wave theory, compression, tension, pressure effects, wound theory, material design and failure mechanisms, energy dispersion and transfer, target types, and many other topics relating to material impact (33). Terminal ballistics is the field that applies best to this research. This research is only concerned with effects and mechanisms after the projectile has reached the target, therefore interior and exterior ballistics are not applicable.

Target classification

When dealing with terminal ballistics, one aspect of key importance is the target. Target materials can be classified into types based on behaviors relating to target thickness and penetration effects: semi-infinite, thick, intermediate thickness, and thin. The boundaries of a semi-infinite target have no influence on penetration, a thick target is one where the boundary influences penetration after the projectile is some distance into the target, an intermediate thickness target is one where boundaries influence throughout the impact, and a thin target is one where stress or deformation gradients are negligible throughout the thickness (33). Experiments with semi-infinite types of targets focus more on physics of penetration rather than armor designs. An example would be penetration into the surface of the earth to reach an underground bunker. The thickness of intermediate targets are deep enough to stop a projectile without damaging the target's back surface. Intermediate targets are relevant for armor designs because they more closely resemble interactions between target and projectile. Thin targets are perforated by the projectile and are relevant through the damage they can induce on the projectile (32), such as brittle materials. Thin targets are the primary focus of this research.

Velocity regimes and kinetic energy

Incoming velocity determines the type of impact scenario that will be observed, and are categorized as: low-velocity impact, high-velocity (or ordinance velocity) impact, and hypervelocity impact. This research will only deal with low- and high-velocity impact scenarios. Hypervelocity involves scenarios such as: fast-moving space debris impacting aerospace vehicles or meteor impact into planetary surfaces.

Low-velocity impact involves velocities less than 250 m/s, and penetration is very much coupled with the overall structural dynamics of the target. As the velocities increase into the high-velocity ranges (500-2000 m/s), the behavior of the target material dominates. In this case the impact zone also begins to increase to about 2-3 projectile diameters from the center of impact. Above velocities of about 2000 m/s, the pressures become such that the impact effects can be modeled using fluids. Hypervelocity occurs after 2,000 m/s. At about 12,000 m/s impacts involve large energy transfer effects that vaporization of the materials is the result (33).

Regime	Impact Velocity (m/s)
Low-velocity	< 250
High-velocity	500 – 2,000
Hypervelocity	2,000 – 12,000 > 12,000

Table B-1: Velocity regime characterization.

National Institute of Justice classification

Ballistics can be classified into levels of protection identified by the National Institute of Justice (NIJ) standards required for testing of materials (150). Shown in Table B-2 are the classification levels identifying: type of projectile, speed of projectile, type of weapon and associated kinetic energies. In the literature, a material can be classified by its ballistic level from the NIJ standards. This classification is only important if ballistic testing related to a performance standard or comparisons on a material of interest are made. NIJ standard comparisons are commonly practiced in industry for demonstrating performance levels of a protection scheme. Our research utilized these standards during the testing of abalone composites.

NIJ Class	Caliber	Mass (g)	Bullet Velocity (m/s)	Kinetic Energy (J)
I	.22 LR	2.6	320	133
	.38 SP	10.2	250	318
IIA	9 mm Luger	8	332	441
	.357 Mag	10.2	381	740
II	9 mm Luger	8	385	593
	.357 Mag	10.2	425	921
IIIA	9 mm	8	426	726
	.44 Mag	15.5	426	1407
III	.388 FMJ	9.7	838	3406
IV	30.06 AP	10.8	868	4069

Table B-2: Kinetic energy for NIJ classifications.

The mass and velocity of the bullet in each class determine the kinetic energy delivered by the projectile to the target. Kinetic energy (KE) is defined, where m is the mass and v is the velocity, as:

$$KE = \frac{1}{2}mv^2 \tag{27}$$

In Table B-2, the projectiles can be delivered at different velocities based on the type of gun used. Different guns will deliver different ranges of kinetic energy to the projectile. Discussed throughout this research, the target and subsequent protection mechanisms have different effects on how kinetic energy is mediated. The difference in kinetic energy delivered by a weapon in class I versus class IV can be seen. The target would need significantly more stopping energy for an armor piercing bullet from class IV as opposed to a .22 bullet from class I.

Target impact failure mechanisms

The idea behind ballistic defeat is not a difficult one, but the mechanisms are. A projectile is stopped when its kinetic energy is consumed by a target. Either large forces or large deflections and contact times must arise during ballistic defeat to stop a projectile (6). Forces give rise to stresses in the projectile and the target that can be classified into types of failure mechanisms to explain energy dissipation. When a projectile hits a steel plate, different scenarios happen based on the velocity of the projectile, angle of impact, and the mechanical properties of the target and projectile. The first scenario could be the shattering or break-up of the projectile. The second scenario could involve projectile deflection in a different direction. The third scenario could involve penetration or perforation of the projectile into the steel target. The scenarios could also be combined (5). The most common failure mechanisms are shown in Figure B-1.

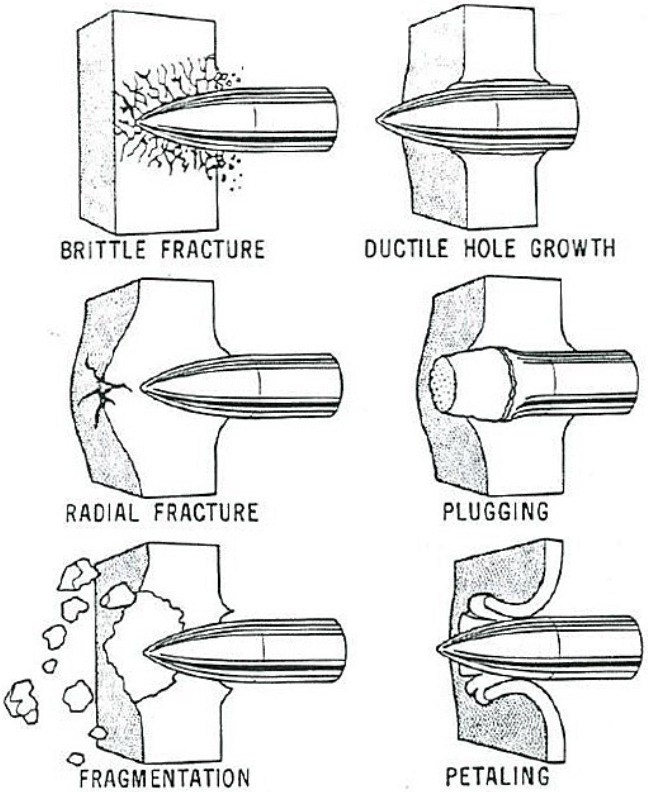

Figure B-1: Common impact failure modes. Reproduced from ref. (151).

Metals

Metals are considered ductile materials within the confines of this research. Most metals stretch and elongate before breaking. Some metals are less ductile than others, but generally follow stress strain curve behavior associated with more ductile materials (123). Ductile metals defeat a projectile through plastic deformation and have a high tolerance to multiple impacts within a small area (6). In metals, petaling and ductile hole growth are typically observed. Petaling, shown in Figure B-1, is caused by high radial and circumferential tensile stresses. As the material pushes ahead of the projectile, large plastic deformation occurs, which leads to a star shaped pattern of petals. Hinging happens at the base of the petals and the petals bend out of the way as the projectile exits

(6, 151). As the target material begins to rupture, stress can concentrate along the cracks that begin to form and the stress will release by elongating the cracks instead of the bulk material, resulting in the petal formation (152).

Ductile hole growth happens typically in thicker targets. When the projectile pushes forward, the material displaces by spreading out in a conical fashion resulting in an enlargement of the projectile path (151). Figure B-1 shows the metal bends around the projectile as it pushes through. If the material doesn't displace then projectile defeat occurs.

Plugging is also present in thicker materials that are ductile. Plugging occurs when the impact velocity is close to the ballistic limit of the target (33). A crater forms as a result of plastic flow, which is needed to accommodate the volume of the projectile; a "plug" is pushed out of the target material (153).

Ductile metals, as opposed to brittle ceramics, fail under tension or shear. Fracture of the ductile material occurs as it loses cohesion in its interior and small voids coalesce. Ductile materials stretch until the amount of voids combine to create a fracture large enough to rip apart the material (32).

Ceramics and glasses

Ceramics and glasses are classified as brittle materials. Ceramics demonstrate variability in failure that make testing difficult. The variability is due to the inherent probabilistic behavior of brittle materials. These materials demonstrate a certain amount of randomness around failure (77, 78), especially in dynamic loading (79, 80). The absence of a crystal network and presence of microflaws for materials like glass, presents difficulty in evaluation of failure behavior (78). Other brittle materials, such as porcelain and ceramic, do have crystal networks (123). The crystal networks are more deterministic in failure results (78). Dynamic fracture of brittle materials leads to a failure of the whole material and not simply fracture at a localized defect (154). Brittle materials form microcracks that coalesce and spread damage through cracks in many directions (32).

Spalling is a unique failure mode, indicated as fragmentation in Figure B-1. It takes place under dynamic situations when shock waves induce large tensions inside a solid. If the additive amplitude of these shocks waves are big enough, the material will fail via spalling (32). Spalling is more common in materials stronger in compression than tension (33), such as seen in ceramics, glasses and concrete. Within ceramics, the modes of failure during impact includes: cone cracking (identified as brittle fracture in Figure B-1), radial cracking and intergranular or transgranular microcracking (34). Radial cracks, shown in Figure B-1 and Figure B-2, initiate at the impact site and extend outwards through the ring cracks (35). Cone cracks start at the surface as ring cracks and penetrate into the substrate when a critical impact load is exceeded. Cone cracking, also thought of as microcrack spreading, serves as an efficient dissipation mechanism. The extensive cracking has an added benefit of creating a high-energy spall of ceramic particles that also serve to erode the projectile (6). Figure B-2 shows schematics of radial, cone and ring cracks.

The high hardness of ceramics allow for a larger capacity to deform and erode impacting projectiles, reducing the energy that must be dissipated elsewhere within a protective system (34). A major issue with ceramics is that, when ceramics fail, they can no longer offer protection.

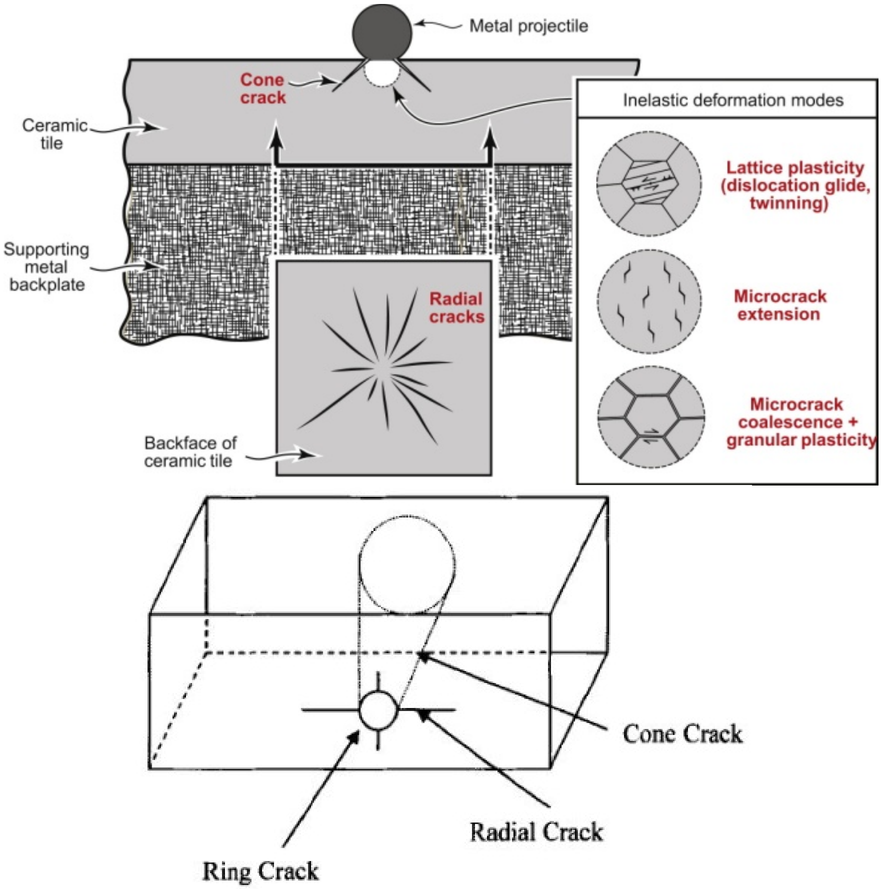

Figure B-2: Schematics of brittle ceramic impact modes of failure. Reproduced from refs (34, 35)..

Polymers

Polymer materials can display both ductile or brittle failure mechanisms depending on the type of polymer, impact loading, strain rate sensitivity and temperature (6). Polymers can soften at higher temperatures or become harder at lower temperatures. Polymers dissipate impact energy through rearrangements occurring within the polymer chains, breaking of bonds and brittle fracture (6).

Polymers can be broken into two distinctive types: thermosets and thermoplastics. Thermosets experience chemical cross-linking. Thermosets can't be reshaped or reformed after cross-linking occurs (123, 155, 156). Due to crosslinking, thermosets tend to be harder and more brittle. Thermoplastic polymers, on the other hand, are soft and pliable. They do not experience cross-linking and tend to behave in a more ductile, stretchy fashion and can be reshaped if heated (123, 156).

Composites

Composites are defined as a combination of materials with two or more distinctive components(123). The components are chemically and physically different. The materials work together to create unique properties that the separate components could not achieve individually (157).

Composites fail via modes such as matrix cracking, delamination, fiber breaking and fiber buckling (33, 158). Matrix cracking occurs parallel to the fibers due to tension, compression, or shear; delamination is produced by interlaminar stresses. Fiber breakage occurs in tension and fiber buckling occurs in compression (158). Fiber breakage or buckling is the final step during failure in the impact process (158).

When cracks form in an area and spread out, they encounter boundary regions that divert the crack onto different paths or stop it altogether. This creates a longer path length for the microcracks to follow. Delamination within the material promotes energy dissipation by forcing the fibers to elongate and stretch (33). Composite materials can absorb energy without breaking. This property depends on the ability of the matrix to quickly diffuse the energy of impact, and the ability of the matrix and fibers to withstand the accumulation of energy at a given point (159). The matrix material in a composite can diffuse the energy by essentially converting it to other forms, such as heat or motion through stretching, sliding, and rotating (159).

Composite materials have advanced properties compared to traditional materials, but their mechanical behavior lacks predictability (158). Reliability and performance can be difficult to ascertain for composite materials, making industry players less than enthusiastic about incorporation.

APPENDIX C AMINO ACIDS. REPRODUCED FROM REF. (60).

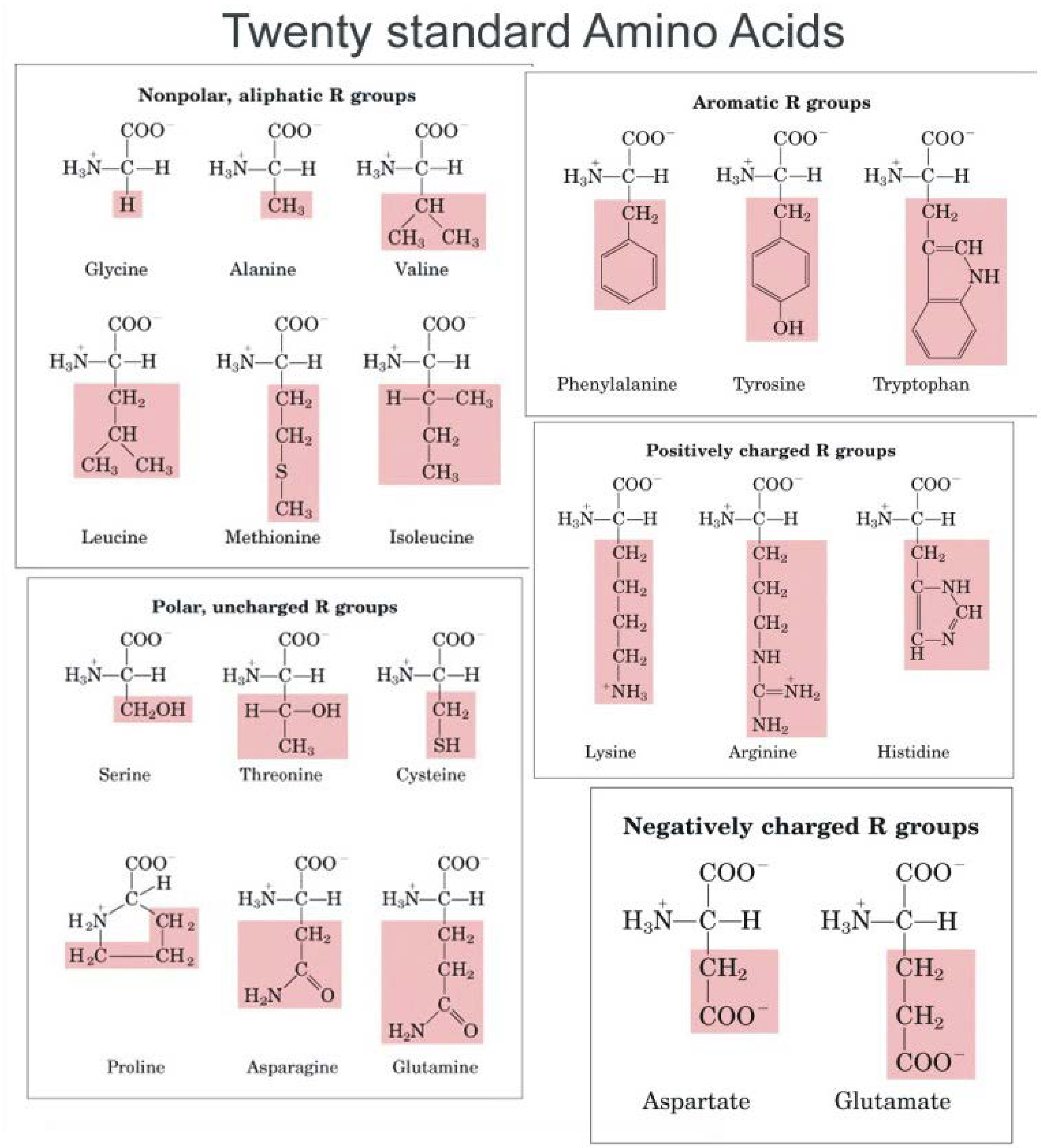

Amino Acid	Acronym	Letter
Alanine	ala	A
Arginine	arg	R
Asparagine	asn	N
Aspartic acid	asp	D
Cysteine	cys	C
Glutamic acid	glu	E
Glutamine	gln	Q
Glycine	gly	G
Histidine	his	H
Isoleucine	ile	I
Leucine	leu	L
Lysine	lys	K
Methionine	met	M
Phenylalanine	phe	F
Proline	pro	P
Serine	ser	S
Threonine	thr	T
Tryptophan	trp	W
Tyrosine	tyr	Y
Valine	val	V

Table C-1: Amino acid acronyms and letters.

APPENDIX D “BRICK AND MORTAR” DROP WEIGHT DATA

PVC tiles with epoxy

Sample Thickness (mm)	Impact Energy (J)	Did the glass break?
3.1 ± 0.11	1.73	N
	4.33	N
	8.65	N
	11.68	N
	12.11	N
	12.98	Y
	13.84	Y
	15.57	Y
	17.30	Y
	21.63	Y
	25.96	Y
	30.28	Y
	33.74	Y
9.6 ± 0.16	1.73	N
	4.33	N
	8.65	N
	12.98	N
	17.30	N
	21.63	N
	25.96	N
	25.96	N
	25.96	N
	26.82	N
	27.26	N
	27.69	Y
	28.12	Y
	28.55	Y
	30.28	Y
	30.28	Y
	33.74	Y
16.0 ± 0.19	4.33	N
	8.65	N
	12.98	N
	21.63	N
	25.96	N
	30.28	N
	31.15	Y
	31.15	N
	32.01	N
	32.88	N
	32.88	Y
	32.88	N
	32.88	N
	32.88	N
	32.88	N
	33.31	Y

PVC tiles with silicone

Sample Thickness (mm)	Impact Energy (J)	Did the glass break?
3.1 ± 0.13	1.73	N
	3.46	N
	3.89	N
	4.33	N
	4.33	Y
	5.19	Y
	6.92	Y
	8.65	N
	9.52	Y
	11.25	Y
	12.98	Y
	17.30	N
	21.63	Y
	25.96	Y
	33.74	Y
9.7 ± 0.15	1.73	N
	4.33	N
	8.65	N
	8.65	N
	9.52	N
	10.38	Y
	11.25	N
	11.25	Y
	12.11	Y
	12.11	Y
	12.98	Y
	17.30	Y
	21.63	Y
	25.96	Y
	30.28	Y
	33.74	Y
16.2 ± 0.13	1.73	N
	4.33	N
	8.65	N
	12.98	N
	17.30	N
	19.04	N
	19.90	N
	19.90	N
	19.90	Y
	20.77	N
	20.77	Y
	21.63	Y
	21.63	Y
	25.96	Y
	30.28	Y
	33.31	Y

PVC tiles with no adhesive

Sample Thickness (mm)	Impact Energy (J)	Did the glass break?
3.0 ± 0.05	1.73	N
	4.33	N
	5.19	N
	5.19	N
	6.06	Y
	6.06	N
	6.06	Y
	6.92	N
	7.79	Y
	8.65	Y
	10.38	Y
	12.98	Y
	25.96	Y
	33.74	Y
8.9 ± 0.14	4.33	N
	8.65	N
	12.98	N
	14.71	N
	15.57	Y
	15.57	N
	15.57	N
	16.44	Y
	17.30	N
	18.17	Y
	19.90	Y
	21.63	Y
	25.96	Y
	30.28	Y
14.9 ± 0.23	1.73	N
	4.33	N
	8.65	N
	12.98	Y
	17.30	N
	18.17	N
	19.04	N
	19.90	N
	20.33	N
	20.77	Y
	21.20	Y
	21.63	N
	23.36	N
	30.28	Y

Glass tiles with epoxy

Sample Thickness (mm)	Impact Energy (J)	Did the glass break?
3.3 ± 0.11	0.87	N
	1.73	N
	1.73	N
	2.60	N
	3.46	N
	4.33	Y
	4.33	Y
	8.65	Y
	12.98	Y
	17.30	Y
9.9 ± 0.16	0.87	N
	1.73	N
	1.73	N
	2.60	N
	4.33	N
	6.06	N
	7.79	Y
	8.65	Y
	12.98	Y
	17.30	Y
16.8 ± 0.38	1.73	N
	4.33	N
	8.65	N
	9.52	N
	10.38	Y
	12.98	Y
	17.30	Y
	25.96	Y
	34.61	Y

Glass tiles with silicone

Sample Thickness (mm)	Impact Energy (J)	Did the glass break?
3.5 ± 0.13	1.73	N
	4.33	N
	7.79	Y
	8.65	N
	11.25	Y
	12.98	Y
	17.30	Y
	25.96	Y
	33.74	Y
10.2 ± 0.18	4.33	N
	6.06	N
	6.92	N
	7.79	N
	8.65	Y
	12.98	Y
	17.30	Y
17.2 ± 0.32	1.73	N
	4.33	N
	8.65	N
	12.98	N
	12.98	N
	17.30	N
	25.96	N
	33.31	N
	33.31	N
	33.31	N

Glass tiles with no adhesive

Sample Thickness (mm)	Impact Energy (J)	Did the glass break?
3.2 ± 0.01	0.87	N
	1.73	N
	1.73	N
	2.60	N
	3.46	N
	4.33	Y
	4.33	Y
	8.65	Y
	12.98	Y
	17.30	Y
9.7 ± 0.04	0.87	N
	1.73	N
	1.73	N
	4.33	N
	6.06	N
	7.79	Y
	8.65	Y
	12.98	Y
	17.30	Y
16.1 ± 0.07	1.73	N
	4.33	N
	8.65	N
	9.52	N
	10.38	Y
	12.98	Y
	17.30	Y
	25.96	Y
	34.61	Y

APPENDIX E NON-INSTRUMENTED DROP WEIGHT DATA

Line-X

Sample Thickness (mm)	Impact Energy (J)	% Mass Loss	Did the glass break?
1.43	6.78	0.00	N
	9.04	0.42	Y
	11.30	0.00	N
	15.82	3.28	Y
	16.95	1.16	Y
	18.08	4.13	Y
	22.60	2.27	Y
	33.91	3.02	Y
	45.21	4.13	Y
2.29	5.60	0.00	N
	6.78	1.48	Y
	6.78	1.08	Y
	9.04	0.00	N
	9.04	1.68	Y
	9.04	1.56	Y
	11.30	1.12	Y
	11.30	2.29	Y
	13.56	0.00	N
	13.56	1.30	Y
	14.01	1.71	Y
	15.82	2.35	Y
	18.08	1.30	Y
	18.08	2.36	Y
	18.08	2.29	Y
	19.21	1.75	Y
	22.60	1.52	Y
	33.91	2.91	Y
	33.91	2.02	Y
	33.91	2.64	Y
	45.21	3.06	Y
	45.21	3.48	Y
	45.21	3.38	Y
	45.21	3.46	Y
3.05	4.52	0.00	N
	9.04	0.75	Y
	9.04	0.79	Y
	9.04	0.00	N
	9.04	1.21	Y
	9.04	0.55	Y
	9.04	0.28	Y
	11.30	0.70	Y
	11.30	0.00	N
	13.56	1.62	Y
	13.56	1.18	Y
	13.56	1.21	Y
	13.56	1.28	Y
	15.82	2.84	Y
	16.95	1.74	Y
	16.95	0.00	N
	16.95	0.00	N
	18.08	2.20	Y
	18.08	1.77	Y
	18.08	2.20	Y
	18.08	2.11	Y
	18.08	2.25	Y
	18.08	1.77	Y
	19.21	0.00	N
	19.78	2.23	Y
	19.78	1.75	Y

	22.60	1.76	Y
	22.60	1.93	Y
	22.60	1.30	Y
	28.26	2.29	Y
	28.26	1.71	Y
	28.26	1.51	Y
	33.91	2.31	Y
	39.56	3.28	Y
	39.56	3.05	Y
	39.56	2.46	Y
	45.21	3.66	Y
	45.21	2.70	Y
	45.21	2.56	Y
	45.21	2.58	Y
6.10	39.56	0.00	N
	40.69	0.28	Y
	41.82	0.00	N
	42.95	1.60	Y
	44.08	0.74	Y
	45.21	1.56	Y

APPENDIX F INSTRUMENTED DROP WEIGHT DATA

Coating Thickness (mm)	Impact Energy (J)	Max Contact Force, F_m (kN)	Max Accel., a_m (m/s^2)	Max displ., δ_m (mm)	Time to Max Force, t_{max}	Duration of impact, Δt (msec)	Max Energy Transferred (J)	Impulse (Ns)	Did the glass break?
0.00	0.10	1.38	1315	0.30	1.4	2.6	0.10	1.24	N
	0.19	2.63	2502	0.29	0.7	0.96	0.18	1.15	N
	0.19	2.62	2498	0.28	0.6	0.95	0.18	1.17	N
	0.19	2.51	2389	0.28	0.8	1.2	0.19	1.55	N
	0.29	2.10	2000	0.34	0.6	1.2	0.28	1.25	Y
	0.38	2.28	2172	0.48	0.7	1.2	0.37	1.34	Y
	0.58	2.49	2375	0.66	0.7	1.2	0.56	1.42	Y
1.32	4.33	7.13	1901	1.85	1.6	3.9	4.32	9.75	N
	6.92	7.68	2049	1.89	1.4	2.9	6.88	10.87	N
	7.79	12.15	3239	2.56	1.7	2.2	7.73	10.95	N
	8.65	16.01	4268	2.81	1.7	2.3	8.57	12.26	N
	8.65	13.91	3709	2.46	1.5	2.0	8.55	11.45	Y
	8.65	9.37	2499	3.62	1.2	1.9	8.61	7.86	Y
	10.38	7.40	1973	9.54	1.6	2.0	9.07	5.68	Y
	12.98	6.77	1806	9.01	1.0	1.5	10.69	5.76	Y
	17.30	6.78	1809	16.03	1.2	1.5	12.43	5.37	Y
	21.64	4.45	1192	5.1	1.0	1.7	10.84	3.74	Y
	25.96	12.11	3230	11.95	1.3	1.7	22.26	8.78	Y
2.33	4.33	7.30	1945	2.32	1.8	2.5	4.33	6.88	N
	8.65	9.72	2591	2.60	1.5	2.1	8.59	9.51	N
	9.52	10.09	2690	2.27	1.1	1.9	9.43	9.87	N
	10.39	10.17	2713	2.58	1.4	1.8	10.29	9.61	N
	11.25	8.39	2238	2.90	1.5	1.9	11.21	9.05	N
	12.98	10.74	2396	3.04	1.3	1.9	12.89	10.24	N
	12.98	8.99	2863	3.30	1.2	1.9	12.73	8.65	Y
	14.71	13.25	3533	3.19	1.3	2.0	14.58	11.59	N
	17.31	12.74	3398	4.07	1.9	2.3	17.19	14.69	N
	18.18	15.88	4235	3.39	1.2	1.9	17.94	13.46	N
	18.18	12.63	3367	4.01	1.6	2.4	18.03	12.73	N
	18.18	11.57	3085	4.41	1.4	2.6	18.05	14.15	N
	18.60	11.57	3085	4.48	1.4	2.6	18.49	14.15	Y
	19.04	14.87	3964	3.69	1.3	2.0	18.83	13.61	Y
	19.90	11.10	2959	8.90	1.3	2.0	19.34	9.33	Y
	21.63	11.16	2977	11.32	1.1	1.6	19.35	8.69	Y
	25.96	8.88	2369	10.25	0.93	1.3	17.63	6.08	Y
3.11	4.33	6.48	1728	1.86	1.5	2.8	4.32	7.91	N
	8.65	10.48	2794	2.90	1.8	2.4	8.60	11.13	N
	10.39	12.11	3229	3.23	1.8	2.4	10.31	11.97	N
	12.12	14.68	3916	3.24	1.7	2.2	11.99	13.29	N
	12.98	16.06	1880	3.51	1.8	2.2	12.83	13.79	N
	12.98	7.05	4282	5.43	1.3	2.1	10.96	5.98	Y
	12.98	7.79	2079	5.62	1.4	2.0	11.75	6.85	Y
	15.58	14.89	3971	3.66	1.6	2.2	15.41	13.85	N
	17.31	9.88	2634	3.64	1.2	2.5	17.22	12.67	N
	18.18	17.72	4724	3.73	1.6	2.0	17.93	15.43	N
	21.64	18.30	4880	3.52	1.3	1.7	21.32	14.49	N
	24.23	18.51	4935	4.48	1.5	2.0	23.92	15.68	N
	25.96	7.70	2055	15.18	1.1	1.5	17.27	5.90	Y
5.64	4.33	5.14	1370	2.25	2.1	2.7	4.36	7.18	N
	8.65	7.42	1979	2.98	1.7	2.7	8.65	10.30	N
	12.98	11.44	3050	2.92	1.4	2.5	12.88	12.96	N
	17.31	11.88	3169	3.92	1.5	2.1	17.45	11.30	Y
	21.64	15.42	4111	4.53	1.7	2.5	21.47	16.24	N
	22.50	16.05	4279	4.52	1.7	2.3	22.28	16.59	N
	22.94	16.30	4347	6.04	2.1	2.8	22.78	16.13	N
	23.36	8.66	2310	5.90	1.7	2.5	23.39	11.25	Y
	23.37	15.19	4050	4.94	1.8	2.5	23.15	16.95	N
	24.23	16.20	4320	5.58	2.0	2.6	24.06	16.57	N
	25.96	16.97	4525	4.29	1.5	2.8	25.68	22.73	N
	25.96	10.02	2671	5.56	1.6	2.4	25.92	12.49	Y

APPENDIX G FINITE ELEMENT MODEL IMPACT PARAMETER DATA

Coating Thickness (mm)	Impact Energy (J)	Max Contact Force, F_m (kN)	Max Accel., a_m (m/s^2)	Max displ., δ_m (mm)	Time to Max Force, t_{max}	Duration of impact, Δt (msec)	Max Energy Transferred (J)	Impulse (Ns)
0.00	0.12	3.74	3558	0.12	0.34	0.59	0.12	1.04
	0.24	5.26	5011	0.17	0.34	0.59	0.24	1.47
	0.36	6.34	6035	0.21	0.34	0.59	0.36	1.77
1.32	4.33	11.07	2953	1.05	0.92	1.7	4.35	9.81
	8.65	14.82	3953	1.47	0.89	1.7	8.69	13.43
	12.98	16.13	4302	1.82	0.88	2.1	13.02	16.08
2.33	4.33	7.86	2097	1.22	1.1	2.5	4.36	9.85
	8.65	10.63	2834	1.75	1.1	2.6	8.70	13.41
	12.98	12.83	3421	2.17	1.2	2.3	13.04	16.42
	17.31	14.35	3827	2.55	1.1	2.3	17.37	18.16
3.11	4.33	7.01	1868	1.33	1.3	2.5	4.37	9.78
	8.65	9.13	2436	1.92	1.2	2.5	8.71	13.13
	12.98	10.82	2886	2.41	1.3	2.6	13.05	15.62
	17.31	12.52	3339	2.81	1.2	2.8	17.39	17.83
	21.64	12.45	3321	3.20	1.3	2.7	21.72	19.67
	25.96	14.56	3883	3.54	1.3	2.7	26.05	22.49
5.64	4.33	5.23	1394	1.58	1.5	3.0	4.38	9.83
	8.65	6.45	1720	2.34	1.5	3.6	8.73	12.93
	12.98	7.11	1896	2.98	1.4	3.7	13.08	15.17
	17.31	8.22	2192	3.54	1.7	3.6	17.42	17.61
	21.64	8.64	2304	4.09	1.7	3.9	21.76	19.24
	25.96	8.59	2292	4.60	1.2	3.7	26.11	20.52